

UNCLASSIFIED

AD NUMBER

AD861911

NEW LIMITATION CHANGE

TO

**Approved for public release, distribution
unlimited**

FROM

**Distribution authorized to U.S. Gov't.
agencies and their contractors;
Administrative/Operational Use; OCT 1969.
Other requests shall be referred to Air
Force Flight Dynamics Laboratory, Attn:
FDTE, Wright-Patterson AFB, OH 45433.**

AUTHORITY

AFFDL ltr, 31 May 1973

THIS PAGE IS UNCLASSIFIED

AD 861911

AFFDL-TR-69-63
VOLUME I

**LOW ALTITUDE ATMOSPHERIC TURBULENCE
LO-LOCAT PHASE III INTERIM REPORT**

VOLUME I. DATA ACQUISITION AND ANALYSIS

K. R. MONSON, G. W. JONES, R. H. MIELKE, *et al.*
The Boeing Company

TECHNICAL REPORT AFFDL-TR-69-63, VOLUME I

OCTOBER 1969

This document is subject to special export controls and each transmittal to foreign governments or foreign nationals may be made only with prior approval of the Air Force Flight Dynamics Laboratory (FDTE), Wright-Patterson Air Force Base, Ohio 45433.

AIR FORCE FLIGHT DYNAMICS LABORATORY
AIR FORCE SYSTEMS COMMAND
WRIGHT-PATTERSON AIR FORCE BASE, OHIO

267

NOTICE

When Government drawings, specifications, or other data are used for any purpose other than in connection with a definitely related Government procurement operation, the United States Government thereby incurs no responsibility nor any obligation whatsoever; and the fact that the Government may have formulated, furnished, or in any way supplied the said drawings, specification, or other data, is not to be regarded by implication or otherwise as in any manner licensing the holder or any other person or corporation, or conveying any rights or permission to manufacture, use, or sell any patented invention that may in any way be related thereto.

This document is subject to special export controls and each transmittal to foreign governments or foreign nationals may be made only with prior approval of the Air Force Flight Dynamics Laboratory (FDTE), Wright-Patterson Air Force Base, Ohio, 45433. The distribution of this report is limited because it contains information that would significantly diminish the technological lead time of the United States and friendly foreign nations by revealing formulas, processes, or techniques having a potential strategic or economic value not generally known throughout the world.

2

Copies of this report should not be returned unless return is required by security considerations, contractual obligations, or notice on a specific document.

AFFDL-TR-69-63
VOLUME I

**LOW ALTITUDE ATMOSPHERIC TURBULENCE
LO-LOCAT PHASE III INTERIM REPORT**

VOLUME I. DATA ACQUISITION AND ANALYSIS

K. R. MONSON, G. W. JONES, R. H. MIELKE, et al.

This document is subject to special export controls and each transmittal to foreign governments or foreign nationals may be made only with prior approval of the Air Force Flight Dynamics Laboratory (FDTE), Wright-Patterson Air Force Base, Ohio 45433.

FOREWORD

This report is an interim summary of the low-level critical air turbulence research work conducted from 17 April 1968 through 8 January 1969 under Contract Number F33615-68-C-1468 (LO-LOCAT PHASE III). The report was prepared by The Boeing Company, Wichita Division for the Air Force Flight Dynamics Laboratory, Wright-Patterson Air Force Base, Ohio.

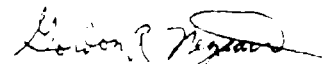
The LO-LOCAT PHASE III Project is part of Advanced Development Program 682E (ALLCAT) and, as such, is under the direction of the ADP 682E Program Director, Mr. E. Brazier, and the Technical Coordinator, Mr. Neal V. Loving. Mr. Jan N. Garrison, FDTE, is the Air Force Project Engineer.

Research is being conducted under the Boeing supervision of Mr. F. K. Atnip, Program Manager. Mr. C. F. Peterson is the Project Pilot. Mr. D. B. Marshall is in charge of Instrumentation; Mr. H. H. Depew is directing the Data Processing; and Mr. J. D. Gault is in charge of Data Analysis; Mr. W. B. Moreland (Boeing-Seattle) is directing meteorological forecasts and analysis; Airplane maintenance and inspection are the responsibility of Mr. J. Strain and Mr. J. Bonawitz, respectively.

Acknowledgment is made for the assistance of the following Boeing-Wichita personnel: Dr. T. Swaney, Structural Loads; Messrs. C. J. Gamm and J. Robertson, Instrumentation; Messrs. D. E. Gunter and J. W. Jones, Data Analysis; Messrs. W. F. Wenzlaff, C. P. Dennis, and L. D. Hager, Data Processing; and Mr. B. Gordon, Industrial Graphics. The following Boeing-Seattle personnel are providing meteorological forecasts and analysis: Messrs. R. Martin, R. Clancy, and K. Knechtel.

This report was submitted by the authors 26 May 1969.

This technical report has been reviewed and is approved.


GORDON R. NEGAARD,
Major, USAF
Chief, Design Criteria Branch
Structures Division
Air Force Flight Dynamics Laboratory

ABSTRACT

The contents of this report describe accomplishments during the first half of the Low-Level Critical Air Turbulence (LO-LOCAT) Phase III program. Data that were obtained during flight over routes near McConnell Air Force Base, Kansas, and Edwards Air Force Base, California, are presented. Also included are time histories of some of the larger magnitude gust velocities recorded over the Peterson Field, Colorado route. Approximately 72 hours of low-level (0-1000 feet) turbulence and associated meteorological data recorded from August 16, 1968, through January 8, 1969, are presented. The turbulence environment is analyzed in terms of gust velocity primary peaks, amplitude samples, rms values, maximum values and derived equivalent gusts. Mathematical expressions for turbulence spectra and scale length statistics, and correlations between atmospheric gust velocities and meteorological and geophysical phenomena are shown. The most predominant characteristics of these data are the increases in rms values, scale lengths, Taylor micro scales and maximum gust values as compared to the LO-LOCAT Phases I and II data. These differences are attributed to the increased speed of the Phase III airplane which is providing a better definition of the longer wavelengths of atmospheric turbulence. This report consists of two volumes. Volume I contains a discussion of data acquisition and quality, along with a preliminary analysis of turbulence and meteorological data. Instrumentation details, calibrations and checks, data processing, gust velocity data (power spectra, peak and amplitude count, etc.) and test logs are presented in Volume II.

(Distribution of this abstract is unlimited)

TABLE OF CONTENTS

	VOLUME I	PAGE NO.
SECTION I	INTRODUCTION	1
SECTION II	DATA ACQUISITION	3
	INSTRUMENTATION	3
	OPERATIONS	5
	TEST PROCEDURE	7
	DATA CATEGORIZATION	8
SECTION III	DATA QUALITY	19
	ANGLE OF ATTACK, SIDESLIP AND AIRSPEED SENSORS	19
	PROBE MOTION SENSORS	20
	GUST PROBE AND BOOM NATURAL FREQUENCY	22
	CALCULATED GUST VELOCITY ERRORS	22
	CALCULATED GUST VELOCITY DRIFT ANALYSIS	25
	NOISE EVALUATION	29
SECTION IV	METEOROLOGICAL DATA ANALYSIS	52
	WIND VELOCITY	52
	RICHARDSON NUMBER	54
	SAMPLING SITES	55
	FORECASTING TECHNIQUES	56
	CASE STUDIES, PHASES I AND II	63
	CASE STUDIES, PHASE III	65
SECTION V	PRELIMINARY TURBULENCE ANALYSIS	94
	PRIMARY PEAK COUNT	94
	AMPLITUDE COUNT	95
	LEVEL CROSSINGS COUNT	95
	COMPARISON OF COUNTING TECHNIQUES	95
	GAUSSIAN DISTRIBUTION CHECK	97
	RUN TEST OF STATIONARITY	97
	COMPARISON OF STANDARD DEVIATIONS	97
	CHARACTERISTIC FREQUENCY	97
	ENSEMBLE AVERAGING	98
	SEVERE AND EXTREME TURBULENCE ENCOUNTERS	99
	GUST VELOCITY RMS VALUES	100
	Gust Velocity RMS Statistical Analysis	101
	Gust Velocity RMS Correlation with Measured Phenomena	104
	Gust Velocity RMS Regression Models	105
	DERIVED EQUIVALENT GUST VELOCITY	109
	TURBULENCE SPECTRA	111
	Instrumentation Anomalies	111
	Low Turbulence Level	111
	Coherency	111

TABLE OF CONTENTS

	<u>PAGE NO.</u>
Homogeneity	112
Isotropy	112
Normalized Spectra	113
Experimental/Mathematical Spectra Comparison	113
Turbulence Scale Length	115
VISCOUS DISSIPATION RATE	121
MICROSCALES	121
SECTION VI BREN TOWER FLYBY	223
SECTION VII SUMMARY	229
REFERENCES	232

VOLUME II

APPENDIX I INSTRUMENTATION DETAILS	1
AIRPLANE AND GUST PROBE INSTRUMENTATION	1
Airspeed	1
Angular Rates	1
Accelerations	1
Pitch, Roll and Yaw Angles	2
Angles of Attack and Sideslip	2
Pressure Altitude	2
Surface Positions	3
Ground Surface Temperature	3
Outside Air Temperature	3
Heading	3
Ground Speed and Drift Angle	3
Absolute Altitude	3
Photographic Coverage	3
Gust Probe Temperatures	4
SIGNAL CONDITIONING AND RECORDING	4
Instrumentation Power Control	4
Signal Conditioning	4
Transducer Power Supply	5
Sub-Carrier Oscillator Package	5
Magnetic Tape Recorder	5
Standardization Control Panel and Preflight Timer	5
Time Coordination	5
MOBILE GROUND STATION - QUICK LOOK SYSTEM	7
Tape Recorder - Reproducer	7
Discriminator System	7
Time Code Reader	7
Oscillograph	7
Communication Radio	7

TABLE OF CONTENTS		PAGE NO.
APPENDIX II	INSTRUMENTATION CALIBRATIONS AND CHECKS	12
	CALIBRATION IN THE LABORATORY AND AT THE AIRPLANE	12
	WIND TUNNEL STATIC CALIBRATION OF THE PROBE	12
	CAMERA BORESIGHT	14
	INFLIGHT CALIBRATION OF GUST PROBE ANGLES OF ATTACK AND SIDESLIP	15
	RADAR ALTIMETER CHECK	17
	GROUND SPEED VERIFICATION	18
	WIND TUNNEL DYNAMIC CALIBRATION OF THE GUST PROBE	18
	GUST PROBE AND BOOM NATURAL FREQUENCY DETERMINATION	20
	AIRSPEED CALIBRATION	21
	RADIOMETER (GROUND SURFACE TEMPERATURE) CALIBRATION	24
	OUTSIDE AIR TEMPERATURE (OAT) CALIBRATION	27
APPENDIX III	DATA PROCESSING	61
	GROUND STATION EQUIPMENT	61
	DATA PLAYBACK	62
	COMPUTER PROGRAMS	65
	MULTIPLE REGRESSION	88
APPENDIX IV	GUST VELOCITY POWER SPECTRA AND ASSOCIATED SPECTRA DATA	105
	POWER SPECTRA	106
	HOMOGENEITY	106
	COHERENCY	106
	EXPERIMENTAL TO MATHEMATICAL COMPARISONS	107
	ISOTROPY	107
APPENDIX V	GUST VELOCITY PEAK, AMPLITUDE AND LEVEL CROSSING COUNT DATA	252
APPENDIX VI	TEST LOG	277
REFERENCES		298

LIST OF ILLUSTRATIONS

<u>FIGURE NO.</u>	<u>VOLUME I</u>	<u>PAGE NO.</u>
	<u>TITLE</u>	
2.1	Instrumentation Equipment Locations	10
2.2	Gust Probe Instrumentation	11
2.3	Gust Probe and Boom Installation	12
2.4	Instrumentation Van Equipment Locations	13
2.5	Test Progress-Number of Flights	14
2.6	Test Progress-Number of Samples	15
2.7	McConnell Route	16
2.8	Edwards Route	17
2.9	Peterson Route	18
3.1	Comparison of Wind Tunnel and "Confetti" Calibration Results	32
3.2	Dynamic Response of Angles of Attack and Sideslip Measurements	32
3.3	Probe and Pilot's Systems Position Errors	33
3.4	Gust Probe Pressure Coefficients for JB-52H, C-131B and T-33A Airplanes	34
3.5	Measured and Calculated Angle of Pitch Comparison-Smooth Air	35
3.6	Measured and Calculated Angle of Roll Comparison-Smooth Air	35
3.7	Measured and Calculated Angle of Yaw Comparison-Smooth Air	35
3.8	Measured and Calculated Angle of Pitch Comparison-Turbulence	36
3.9	Measured and Calculated Angle of Roll Comparison-Turbulence	36
3.10	Measured and Calculated Angle of Yaw Comparison-Turbulence	36
3.11	Measured and Calculated Angle of Pitch Comparison-Simulated Turbulence	37

LIST OF ILLUSTRATIONS

<u>FIGURE NO.</u>	<u>VOLUME I</u>	<u>PAGE NO.</u>
	<u>TITLE</u>	
3.12	Measured and Calculated Angle of Yaw Comparison-Simulated Turbulence	37
3.13	Longitudinal Gust Velocity PSD Calculated Using Inputs From Different Accelerometers	38
3.14	Lateral Gust Velocity PSD Calculated Using Inputs from Different Accelerometers	39
3.15	Vertical Gust Velocity PSD Calculated Using Inputs from Different Accelerometers	40
3.16	Gust Velocity Time Histories of Simulated Turbulence	41
3.17	Drift in True Longitudinal Gust Velocity	42
3.18	Drift in True Lateral Gust Velocity	42
3.19	Drift in True Vertical Gust Velocity	42
3.20	Drift in Indicated Lateral Gust Velocity	43
3.21	Drift in Indicated Vertical Gust Velocity	43
3.22	Drift in Integrated Acceleration - Interval 1	44
3.23	Drift in Integrated Acceleration - Interval 2	44
3.24	Drift in Pitch Angle	45
3.25	Drift in Roll Angle	45
3.26	Drift in Yaw Angle	45
3.27	Time History of Filtered Drift Data	46
3.28	Unfiltered Gust Velocity-Smooth Air	47
3.29	Filtered Gust Velocity-Smooth Air	47
3.30	Unfiltered Gust Velocity-Turbulence	48

LIST OF ILLUSTRATIONS

<u>FIGURE NO.</u>	<u>VOLUME I</u>	<u>PAGE NO.</u>
	<u>TITLE</u>	
3.31	Filtered Gust Velocity-Turbulence	48
3.32	Filtered and Unfiltered Measured Attitude Angle Comparison-Smooth Air	49
3.33	Filtered and Unfiltered Measured Attitude Angle Comparison-Turbulence	49
3.34	Frequency of Occurrence of Irregularly and Regularly Shaped Spectra	50
3.35	Frequency of Occurrence Ratio of Number Regularly to Irregularly Shaped Spectra	51
4.1	Climatological Variances for McConnell Route	66
4.2	Wind Speed Cumulative Probability Associated with Location	67
4.3	Wind Speed Cumulative Probability at McConnell	68
4.4	Wind Speed Cumulative Probability at Edwards	69
4.5	Variation of Wind Speed Cumulative Probability over the Plains with Altitude	70
4.6	Variation of Wind Speed Cumulative Probability over High Mountains with Altitude	71
4.7	Variation of Wind Speed Cumulative Probability over Low Mountains with Altitude	72
4.8	Variation of Wind Speed Cumulative Probability over Desert Terrain with Altitude	73
4.9	Variation of Wind Speed Cumulative Probability at McConnell with Time-of-Day	74
4.10	Variation of Wind Speed Cumulative Probability at Edwards with Time-of-Day	75
4.11	Variation of Wind Speed Cumulative Probability over High Mountains with Time-of-Day	76
4.12	Variation of Wind Speed Cumulative Probability over Low Mountains with Time-of-Day	77
4.13	Variation of Wind Speed Cumulative Probability over Desert with Time-of-Day	78
4.14	Variation of Wind Speed Cumulative Probability at Edwards with Atmospheric Stability	79

LIST OF ILLUSTRATIONS

<u>FIGURE NO.</u>	<u>VOLUME I TITLE</u>	<u>PAGE NO.</u>
4.15	Variation of Wind Speed Cumulative Probability at McConnell with Atmospheric Stability	80
4.16	Wind Speed Cumulative Probability Associated with Terrain Type	81
4.17	Longitudinal Gust Velocity RMS Cumulative Probability Associated with Richardson Number	82
4.18	Lateral Gust Velocity RMS Cumulative Probability Associated with Richardson Number	83
4.19	Vertical Gust Velocity RMS Cumulative Probability Associated with Richardson Number	84
4.20	Gust Velocity RMS versus Richardson Number for 80 Percent Probability	85
4.21	Surface Synoptic Analysis for 13 December 1967, 1500 GMT, Edwards AFB Route.	86
4.22	Surface Synoptic Analysis for 13 December 1967, 1800 GMT, Edwards AFB Route.	87
4.23	850 mb Synoptic Analysis for 14 December 1967, 0000 GMT, Edwards AFB Route.	88
4.24	850 mb Synoptic Analysis for 13 December 1967, 1200 GMT Edwards AFB Route.	89
4.25	Surface Synoptic Analysis for 13 November 1968, 1500 GMT, Edwards AFB Route.	90
4.26	Surface Synoptic Analysis for 13 November 1968, 1800 GMT, Edwards AFB Route.	91
4.27	850 mb Synoptic Analysis for 14 November 1968, 0000 GMT, Edwards AFB Route	92
4.28	850 mb Synoptic Analysis for 13 November 1968, 1200 GMT, Edwards AFB Route.	93
5.1	Peak Count Example	123
5.2	Peak Count Extrapolation Technique	124

LIST OF ILLUSTRATIONS

<u>FIGURE NO.</u>	<u>VOLUME I</u>	<u>PAGE NO.</u>
	<u>TITLE</u>	
5.3	Amplitude Count Example	125
5.4	Level Crossing Count Example	126
5.5	Comparison of Peak and Level Crossing Count Distributions-Longitudinal Gust Velocity	127
5.6	Comparison of Peak and Level Crossing Count Distributions-Lateral Gust Velocity	128
5.7	Comparison of Peak and Level Crossing Count Distributions-Vertical Gust Velocity	129
5.8	Comparison of Probability Distributions of Counting Techniques-Longitudinal Gust Velocity	130
5.9	Comparison of Probability Distributions of Counting Techniques-Lateral Gust Velocity	131
5.10	Comparison of Probability Distributions of Counting Techniques-Vertical Gust Velocity	132
5.11	Terrain Effects on Longitudinal Gust Velocity Peaks	133
5.12	Terrain Effects on Lateral Gust Velocity Peaks	134
5.13	Terrain Effects on Vertical Gust Velocity Peaks	135
5.14	Altitude Effects on Longitudinal Gust Velocity Peaks	136
5.15	Altitude Effects on Lateral Gust Velocity Peaks	137
5.16	Altitude Effects on Vertical Gust Velocity Peaks	138
5.17	Stability Effects on Longitudinal Gust Velocity Peaks	139
5.18	Stability Effects on Lateral Gust Velocity Peaks	140
5.19	Stability Effects on Vertical Gust Velocity Peaks	141
5.20	Chi-Square Test for Statistical Normality	142
5.21	Comparison of Longitudinal Gust Velocity Standard Deviations Calculated by Different Techniques	143
5.22	Comparison of Lateral Gust Velocity Standard Deviations Calculated by Different Techniques	144

LIST OF ILLUSTRATIONS

<u>FIGURE NO.</u>	<u>VOLUME I</u>	<u>PAGE NO.</u>
	<u>TITLE</u>	
5.23	Comparison of Vertical Gust Velocity Standard Deviations Calculated by Different Techniques	145
5.24	Turbulence Spectra Data Calculated from Ensemble Average Time Function	146
5.25	Time History of Gust Velocity Components-Severe Turbulence Encounter	147
5.26	Time History of Gust Velocity Components-Severe Turbulence Encounter	148
5.27	Time History of Gust Velocity Components-Severe Turbulence Encounter	149
5.28	Time History of Gust Velocity Components-Severe Turbulence Encounter	150
5.29	Time History of Gust Velocity Components-Severe Turbulence Encounter	151
5.30	Time History of Gust Velocity Components-Severe Turbulence Encounter	152
5.31	Time History of Gust Velocity Components-Severe Turbulence Encounter	153
5.32	Time History of Gust Velocity Components-Severe Turbulence Encounter	154
5.33	Time History of Gust Velocity Components-Severe Turbulence Encounter	155
5.34	Time History of Gust Velocity Components-Severe Turbulence Encounter	156
5.35	Time History of Gust Velocity Components-Severe Turbulence Encounter	157
5.36	Time History of Gust Velocity Components-Severe Turbulence Encounter	158
5.37	Time History of Gust Velocity Components-Severe Turbulence Encounter	159
5.38	Time History of Gust Velocity Components-Severe Turbulence Encounter	160
5.39	Time History of Gust Velocity Components-Severe Turbulence Encounter	161
5.40	Time History of Gust Velocity Components-Severe Turbulence Encounter	162
5.41	Time History of Gust Velocity Components-Severe Turbulence Encounter	163
5.42	Time History of Gust Velocity Components-Severe Turbulence Encounter	164
5.43	Time History of Gust Velocity Components-Severe Turbulence Encounter	165

LIST OF ILLUSTRATIONS

<u>FIGURE NO.</u>	<u>VOLUME I TITLE</u>	<u>PAGE NO.</u>
5.44	Terrain Profile of Leg 2-Peterson Field Route	166
5.45	Longitudinal Gust Velocity RMS Cumulative Probability During Various Phases of LO-LOCAT	167
5.46	Lateral Gust Velocity RMS Cumulative Probability During Various Phases of LO-LOCAT	168
5.47	Vertical Gust Velocity RMS Cumulative Probability During Various Phases of LO-LOCAT	169
5.48	Gust Velocity RMS Cumulative Probability Associated with Terrain	170
5.49	Gust Velocity RMS Cumulative Probability Associated with Altitude	171
5.50	Gust Velocity RMS Cumulative Probability Associated with Atmospheric Stability	172
5.51	Gust Velocity RMS Cumulative Probability Associated with Time-of-Day	173
5.52	Gust Velocity RMS Cumulative Probability Associated with Location	174
5.53	Effects of Terrain on Cumulative Probability of Gust Velocity RMS Values Obtained at 250 Feet	175
5.54	Effects of Terrain on Cumulative Probability of Gust Velocity RMS Values Obtained at 750 Feet	176
5.55	Effects of Altitude Over High Mountains on Gust Velocity RMS Cumulative Probability	177
5.56	Effects of Altitude Over Low Mountains on Gust Velocity RMS Cumulative Probability	178
5.57	Effects of Altitude Over Desert Terrain on Gust Velocity RMS Cumulative Probability	179
5.58	Effects of Altitude Over Plains on Gust Velocity RMS Cumulative Probability	180
5.59	Variation of Gust Velocity RMS Mean Values With Terrain and Altitude	181
5.60	Standardized Longitudinal Gust Velocity RMS Cumulative Probability Distribution	182
5.61	Standardized Lateral Gust Velocity RMS Cumulative Probability Distribution	183
5.62	Standardized Vertical Gust Velocity RMS Cumulative Probability Distribution	184
5.63	Extrapolated Longitudinal Gust Velocity RMS Cumulative Probability	185

LIST OF ILLUSTRATIONS

<u>FIGURE NO.</u>	<u>VOLUME I</u>	<u>PAGE NO.</u>
	<u>TITLE</u>	
5.64	Extrapolated Lateral Gust Velocity RMS Cumulative Probability	186
5.65	Extrapolated Vertical Gust Velocity RMS Cumulative Probability	187
5.66	Gust Velocity RMS Values Versus Wind Speed at 250 Feet Over High Mountains	188
5.67	Gust Velocity RMS Values Versus Wind Speed at 750 Feet Over High Mountains	189
5.68	Gust Velocity RMS Values Versus Wind Speed at 250 Feet Over Low Mountains	190
5.69	Gust Velocity RMS Values Versus Wind Speed at 750 Feet Over Low Mountains	191
5.70	Gust Velocity RMS Values Versus Wind Speed at 250 Feet Over Desert	192
5.71	Gust Velocity RMS Values Versus Wind Speed at 750 Feet Over Desert	193
5.72	Gust Velocity RMS Values Versus Wind Speed at 250 Feet Over Plains	194
5.73	Gust Velocity RMS Values Versus Wind Speed at 750 Feet Over Plains	195
5.74	Correlation of Gust Velocity RMS Values With Wind Speed as a Function of Terrain and Altitude	196
5.75	Time Histories of Gust Factor	197
5.76	Lateral Gust Velocity RMS Versus Corrected Surface Winds	197
5.77	Cumulative Probability of U_{de} and Maximum Vertical Gust Velocity-High Mountains	198
5.78	Cumulative Probability of U_{de} and Maximum Vertical Gust Velocity-Low Mountains	198
5.79	Cumulative Probability of U_{de} and Maximum Vertical Gust Velocity-Plains	199
5.80	Cumulative Probability of U_{de} and Maximum Vertical Gust Velocity-Desert	199
5.81	Cumulative Probability of U_{de} and Maximum Vertical Gust Velocity-Water	200
5.82	Cumulative Probability of U_{de} and Maximum Vertical Gust Velocity-All Terrain	200
5.83	Gust Velocity Power Spectra of a Data Sample Containing Suspected Instrumentation Irregularities	201
5.84	Gust Velocity Power Spectra of a Data Sample Having Insufficient Signal-to-Noise Ratio	202

LIST OF ILLUSTRATIONS

<u>FIGURE NO.</u>	<u>VOLUME I</u>	<u>PAGE NO.</u>
<u>TITLE</u>		
5.85 Average Gust Velocity Coherency Characteristics		203
5.86 Gust Velocity Power Spectra of Non-Homogeneous Turbulence-Test 170 Leg 2, Category 112143		204
5.87 Turbulence Homogeneity Characteristics-Test 170 Leg 2, Category 112143		205
5.88 Gust Velocity Power Spectra of Homogeneous Turbulence-Test 170 Leg 6, Category 112143		206
5.89 Turbulence Homogeneity Characteristics- Test 170 Leg 6, Category 112143		207
5.90 Average Homogeneity Characteristics		208
5.91 Isotropy Based on von Karman Expressions		209
5.92 Average Isotropy Characteristics		210
5.93 Gust Velocity Average Power Spectra Normalized by σ_t^2		211
5.94 Gust Velocity Average Power Spectra Normalized by $\sigma_t^2 L$		212
5.95 Experimental Gust Velocity Power Spectra/von Karman Mathematical Power Spectra-Normalized by $\sigma_t^2 L$		213
5.96 Experimental Power Spectra/Dryden and von Karman Mathematical Power Spectra Comparisons		214
5.97 Von Karman Longitudinal Scale Length Cumulative Probability		215
5.98 Effects of Altitude on von Karman Longitudinal Scale Length		216
5.99 Effects of Altitude on von Karman Longitudinal Scale Length		217
5.100 Effects of Altitude on von Karman Longitudinal Scale Length		218
5.101 Variation of von Karman Longitudinal Scale Length With Altitude and Terrain		219
5.102 Variation of von Karman Longitudinal Scale Length With Altitude and Stability		220
5.103 Viscous Dissipation Rate Statistics for 750 Foot and 250 Foot Altitudes		221
5.104 Kolmogorov Microscale Statistics for 750 Foot and 250 Foot Altitudes		222

LIST OF ILLUSTRATIONS

<u>FIGURE NO.</u>	<u>VOLUME 1</u>	<u>PAGE NO.</u>
	<u>TITLE</u>	
5.105	Taylor Microscale Statistics for 750 Foot and 250 Foot Altitudes	222
6.1	BREN Tower Location	224
6.2	Gust Velocity Time History for BREN Tower Flyby No. 1	225
6.3	Gust Velocity Time History for BREN Tower Flyby No. 7	226
6.4	Turbulence Spectra Data for BREN Tower Flyby No. 1	227
6.5	Turbulence Spectra Data for BREN Tower Flyby No. 7	228

LIST OF TABLES

VOLUME I

<u>TABLE NO.</u>	<u>TITLE</u>	<u>PAGE NO.</u>
3.1	Comparison of Measured and Calculated Attitude Angles	21
3.2	Comparison of Gust Velocities Computed Using Probe and C.G. Accelerometers	22
3.3	Comparison of Airplane Motion During Actual and Simulated Turbulence	23
3.4	Probable Gust Velocity Errors	24
3.5	Comparison of Drift in Gust Velocity Equation Terms	27
3.6	Minimum Valid Standard Deviation Values	30
4.1	Evaluation of GWC Forecasts (Phase III)	57
4.2	Evaluation of Showalter Index (Phase III)	58
4.3	Evaluation of Richardson Numbers (Phase III)	59
4.4	Turbulence Forecast using Wind Shear (Surface 1000')	60
4.5	Turbulence Forecast using Surface Wind	60
4.6	Turbulence Forecast using Convective Cloud Type	61
4.7	Turbulence Forecast Considering Maximum Value from Wind Shear, Surface Wind or Convective Cloud Type	61
5.1	Comparison of Characteristic Frequencies Calculated from Power Spectra and Peak Count Data	98
5.2	Regression Models Based on B-66B Airplane Low Level Gust Study Data	106
5.3	Regression Models Based on Data Obtained During B-52G/H Airplane Flight Load History Program	107
5.4	Regression Models Based on Phases I and II Data	107
5.5	Regression Models Based on Phases I and II Data	108
5.6	Experimental/von Karman Data	115

LIST OF TABLES

VOLUME I

<u>TABLE NO.</u>	<u>TITLE</u>	<u>PAGE NO.</u>
5.7	LO-LOCAT Scale Lengths for von Karman Expressions Compared to Those Recommended by MIL-F-008785A(USAF)	118
5.8	LO-LOCAT Scale Lengths for Dryden Expressions Compared to Those Recommended by MIL-F-008785A (USAF)	119
5.9	LO-LOCAT Scale Lengths Compared to Those Recommended by AFFDL-TR-67-122	120
6.1	BREN Tower Flyby Data	223

NOTATIONS

Symbols and Abbreviations:

A	Regression coefficient.
A thru H, J, K	Coefficients in the equation for angle of attack.
A' thru H', J', K'	Coefficients in the equation for angle of sideslip.
A(n)	Complex finite transform.
$\tilde{A}(n)$	Complex conjugate of A(n).
a	"Universal Constant" in the longitudinal gust velocity component spectrum expression, constant in α equation; and shape parameter used in spectra mathematical expressions.
B	Air stability ratio.
b	Constant in β equation, also a constant in gust velocity rms distribution equation.
b_n	Real part of Fourier transform.
C	Constant in the Lumley-Panofsky equation.
c	Mean aerodynamic chord.
c.g.	Airplane center of gravity.
C_L	Airplane lift curve slope in 1/radians.
cpf	Cycles per foot.
cps	Cycles per second.
D	Distance from airplane c.g. to measurement location in feet.
d	Degrees of freedom, distance traveled in statute miles, differential.
db	Decibel
E_{AR}	Actual energy per unit area radiated from a real surface.
E_{BB}	Energy per unit area radiated from a black body.

NOTATIONS

E_R	Incoming radiant energy.
E_α	Total crossings of the level α .
F	F-ratio or F-test of significance in regression analysis.
$F(f)$	Fourier transform modulus.
f	Frequency in cps; function.
f_b	Frequency of occurrence in band b.
f_c	The highest frequency of a low-pass filter whose amplitude is passed with unity gain (cutoff frequency) in cps.
f_N	Nyquist or folding frequency in cps.
fps	Feet per second.
f_s	Sampling frequency in samples per second.
f_a	A significant frequency present in the spectrum in cps.
G_f	Gust factor.
G_z	Ground speed in feet per second.
g	Earth's gravitational constant at sea level = 32.174 ft./sec. ²
H	Altitude above the earth's surface in feet, true altitude in feet.
H_c	Calibrated pressure altitude in feet.
$H(f)$	Transfer function of the filter.
Hg	Symbol for the element Mercury.
H_1, H_1'	Indicated pressure altitude in feet.
$\overline{H_N}(f)$	Constrained transfer function.
H_P	Pressure altitude in feet.
h	True heading in degrees.

NOTATIONS

h_m	Magnetic heading in degrees.
h_n	Filter weights at time $t + n \Delta t$.
\bar{h}_n	Constrained filter weights.
$h(t, \tau)$	Time domain weighting function.
h_0	Constant in empirical scale length equation.
i	Counter, time series sample.
ips	Inches per second.
IAS	Indicated airspeed.
IRIG	Inter-range Instrumentation Group
in.	Inches.
j	Square root of minus one.
$K_{a,b}$	Constants.
KIAS	Knots indicated airspeed.
K_g	Gust alleviation factor.
K_t	Ram recovery factor for OAT probe
k	Spatial frequency in cps; also defines order of the derivative of the transfer function $H(\Omega)$.
k_1, k_2, k_3	Truncated standard deviation frequency limits corresponding to 0.04, 0.667 and 10 cps, respectively, in cycles per foot.
L	Turbulence scale length in feet.
L_f	Minimum focal range of the camera lens in feet.
L_h	Constant in empirical scale length equation.
l	Distance from probe tip to accelerometers in feet.
M	True Mach Number.

NOTATIONS

M_s	Magnitude of the center of the step pressure.
m	Maximum lag = $f_N / \Delta f$, slope of a line, number of functions of the input variables, and meters.
mb	Millibar
mm	Millimeter.
N	Total number, conditions, data points, samples, peaks, bands.
NBFM	Narrow band frequency modulation.
N_0	Characteristic frequency from power spectral density - cps.
N_{CL}	Number of crossings of the zero level.
N_p	Total number of peaks per mile. (characteristic frequency).
N_{pe}	Total number of peaks obtained using extrapolation technique.
N_α	Crossings per mile of the level α .
n	Acceleration in g units, also a counter, number of data points, shape parameter in spectra mathematical expressions.
OAT	Outside air temperature in °F.
O_m	Run test observation of the mean.
O_m'	Run test observation of the mean square
PSD	Power spectral density.
P_s	Static pressure in inches of mercury.
P_i	Indicated static pressure in inches of mercury.
P_0	Static pressure at sea level under standard conditions - 29.921 inches of mercury.
P_α	Level crossing probability
Q	Number of independent variables in the regression equation.
q_c	Calibrated impact pressure in inches of mercury.

xxvii

NOTATIONS

q_i	Indicated impact pressure in inches of mercury.
R_A	Radar altitude, feet
R	Richardson number.
$[R]$	Rotation matrix used to transform measurements from the airplane reference axis to the earth reference axes.
R_1	Value of least square line at a given wind speed.
rms	Root mean square.
R_d	Distance from c.g. to camera lens in feet.
$R(\tau)$	Gust velocity covariance function.
$R(\tau)/R(0)$	Gust velocity autocorrelation function where $\tau = 0 \dots \tau_L$.
S	Airplane planform wing area in ft^2 , horizontal distance in miles.
SCO	Subcarrier oscillator
S_T	True solar time of day - hours.
S_{\sin}	Sine of solar elevation.
T	Period of time function in seconds.
T_a	Ambient air temperature in degrees Rankine.
T_{AR}	Actual temperature of real surface in degrees Rankine.
T_{BB}	Temperature of black body in degrees Rankine.
Temp.	Temperature.
T_0	Ground surface temperature in degrees Fahrenheit.
T_i	Calibrated outside air temperature in degrees Rankine.
T_L	Lower time limit of weighting function in seconds.
T_0	Temperature at sea level under standard conditions (518.69 degrees Rankine).

NOTATIONS

T_{rad}	Surface temperature as recorded by radiometer.
T_u	Upper time limit of weighting function in seconds.
t	Time in sec., also standardized variable.
U_{de}	Derived equivalent gust velocity in fps.
U_u U_v U_w	Probe motion terms
u	Longitudinal gust velocity in fps, positive aft.
v	True airspeed or ground speed in fps.
V_e	Equivalent airspeed in fps.
V_f	Confetti fall rate in fps.
V_0	Ground speed in fps
V_i	Indicated airspeed.
V_{SL}	Confetti fall rate at sea level in fps.
V_T	True airspeed in fps.
$\{V\}$	Represents the matrix of true airspeed components and corrections for pitch and yaw rate.
v	Lateral gust velocity in fps, positive to the right.
w	Airplane weight in pounds, wind speed in fps.
WA	Wind angle, angle in degrees between airplane ground track and wind vector.
W_D	Wind direction in degrees azimuth.
$\overline{W_E}$	Average easterly winds in fps.
$\overline{W_N}$	Average northerly winds in fps.
w	Vertical gust velocity in fps, positive upward.

NOTATIONS

x	Amplitude.
x_b	Mid-band value.
x_i	i^{th} value of x , predictors, coefficient of simple linear correlation, and value of gust velocity rms at a given wind speed.
$x(t)$	Amplitude values of the time series.
$x_k(t_1)$	k^{th} record included in the ensemble averaging scheme.
\bar{x}_q	Smoothed values.
$x(t)$	Sampled value of time series.
x_t^*	Filter output data at equi-spaced intervals.
$x^*(t)$	Sampled value of low-pass filtered time series.
$\tilde{x}(t)$	Sampled value of high-pass filtered time series.
X_a	Level of gust velocity - fps.
Y	Dependent variable, regression function
y	Intercept of y axis, random variable.
Z_1	Input variable.
$\%$	Percent.
α	Angle of attack in degrees, levels of gust velocity used in level crossing procedure; confidence limit.
β	Angle of sideslip in degrees.
Γ	Lapse rate in degrees Fahrenheit/ft. (+ indicates temperature decrease with increasing altitude).
Γ_d	Dry adiabatic lapse rate.
γ	Ratio of specific heats for air = 1.40.
$\gamma^2(k)$	Coherency function.
Δ	Incremental or difference.

NOTATIONS

Δf	A change in frequency in cps, also the width between where the filter transfer function equals one and zero.
Δh	Static pressure error in feet.
ΔH	Distance above or below reference point H_{IT} , also difference in terrain elevation-in feet.
ΔN_{zco}	Incremental load factor in acceleration units.
ΔP_s	Static pressure error in inches of mercury.
$\Delta P_s/q_i$	Pressure coefficient - dimensionless
ΔP_{SP}	Static pressure position error correction inches of Mercury.
ΔP_a	Angle of attack differential pressure in inches of mercury.
ΔP_β	Angle of sideslip differential pressure in inches of mercury.
Δt	Time interval between data samples in seconds.
$\Delta W/\Delta H$	Vertical wind gradient in fps/ft.
ΔW_{DH}	Number of degrees of wind direction change between start and end of data sample.
Δw_H	Horizontal wind gradient in ft./sec./mi.
$\Delta \alpha$	Total angle of attack correction in degrees.
$\Delta \alpha_{FR}$	Angle of attack correction due to confetti fall rate in degrees.
$\Delta \alpha_{PL}$	Angle of attack correction due to measurement location in degrees.
$\Delta \alpha_{PR}$	Angle of attack correction due to aircraft rate of pitch in degrees.
$\Delta \beta$	Total angle of sideslip correction in degrees.
$\Delta \beta_{FR}$	Angle of sideslip correction due to confetti fall rate in degrees.

NOTATIONS

$\Delta\theta_{PL}$	Angle of sideslip correction due to measurement location in degrees.
$\Delta\theta_{YR}$	Angle of sideslip correction due to aircraft rate of yaw in degrees.
$\Delta\psi$	Error in angle of yaw.
δ	Drift angle in degrees.
ϵ	Viscous dissipation rate in ft^2/sec^3 ; filter constant, and emissivity factor.
ϵ_c	Emissivity of surface used for calibration.
ϵ_A	Emissivity of a real surface.
η	Kolmogorov microscale.
θ	Pitch angle in degrees.
$\dot{\theta}$	Rate of pitch in degrees/sec.
λ	Taylor turbulence microscale length.
μ	Air viscosity in lb. sec./ft.^2 , also mean value, airplane mass ratio.
μ_1, μ_2	Constant used in gust velocity rms distribution equation.
$\mu_x(t)$	Ensemble average time function
ν	Kinematic viscosity, degrees of freedom.
π	3.1416 . . .
ρ	Air density in slugs/ ft^3
ρ_0	Air density at sea level under standard conditions - .002378 slugs/feet 3 .
σ	Standard deviation of a statistical sample; standard deviation in fps from gust velocity spectra between 0.0416 and 10 cps; air density ratio; Stefan-Boltzman constant.
σ_D	Standard deviation about a least square line.
σ_L	Standard deviation of level crossing distribution.
σ_N	Standard deviation of noise.

NOTATIONS

σ_n	Standard deviation of vertical acceleration.
σ_{p_0}	Standard deviation of primary peaks obtained using extrapolated value of M_{p_0} .
σ_x	Standard deviation of recorded data.
σ_T	Standard deviation in fps obtained from the gust velocity spectra between 0.667 and 10 cps.
σ_t	Standard deviation of the gust velocity time series in fps.
σ_{t_m}	Minimum valid σ_t .
σ_Y	Standard deviation of Y.
σ_y	Standard deviation of y.
σ_a	Standard deviation of angle of attack differential pressure in inches of Hg.
σ_s	Standard deviation of sideslip differential pressure in inches of Hg.
σ_v	Standard deviation (dispersion of the distribution) of gust velocity rms.
σ_{vc}	Corrected standard deviation of gust velocity rms.
σ_1	Standard deviation of the time derivative of the associated function.
σ_2, σ_3	Constant used in rms gust velocity distribution equation.
τ	Lag time for the weighting operation convolution in seconds.
τ_L	Maximum correlation distance where $\tau_L = mV$.
Φ	One-dimensional gust velocity power spectral density.
ϕ	Roll angle in degrees.
χ	Chi statistic.
ψ	Yaw angle in degrees.
$\dot{\psi}$	Rate of yaw in degrees per second.
ω	Frequency in radians per second.
ω_0	Break frequency - radians per second.

NOTATIONS

SUBSCRIPTS AND SUPERSCRIPTS:

b	Band number.
corr.	Corrected value.
D	Based on the Dryden equation.
e	Extrapolated value.
filt.	Filtered value.
H	Horizontal.
i	Sample number.
N	Noise.
n	Counter.
k	Based on the von Karman equation.
max	Indicates maximum value.
min	Indicates minimum value.
P	Peak count or, based on the Lumley- Panofsky equation.
R	Recorded data.
T	Truncated, obtained from wind tunnel instrumentation, obtained from tower.
t	From the gust velocity time series.
u	From the longitudinal gust velocity component.
v	From the lateral gust velocity component.
w	From the vertical gust velocity component.
x	Longitudinal.
y	Lateral.
z	Vertical.

NOTATIONS

SUBSCRIPTS AND SUPERSCRIPTS (CONT.):

- 0 Initial value.
- I Pertaining to quadrant 1
- II Pertaining to quadrant 2
- III Pertaining to quadrant 3
- IV Pertaining to quadrant 4
- a Related to level crossing count; also refers to significant frequency content present in the data.

Primes indicate Hanned estimates unless otherwise noted.

Overbars depict time means.

- 2 Refers to starting point of leg
- 3 Refers to ending point of leg
- 32 Refers to difference between start and end.

xxxx

SECTION I

INTRODUCTION

A model for low altitude atmospheric turbulence is being developed by The Boeing Company in cooperation with the United States Air Force. This is being accomplished through a research program designated LO-LOCAT (Low Altitude Critical Air Turbulence). LO-LCCAT is part of an extensive program known as ALLCAT (Reference 1.1).

The purpose of the LO-LOCAT Program is to determine the turbulence environment below 1,000 feet above the ground utilizing statistically representative samples of turbulence data obtained over a wide range of meteorological, topographical, seasonal, and time-of-day conditions. The data will be used to improve turbulence design criteria for aircraft that are required to operate below 1000 feet above the terrain for extended periods of time.

The LO-LOCAT Program consists of three phases of testing. Phases I and II, which have been completed and are discussed in Reference 1.2, used four C-131B aircraft as instrumentation platforms to obtain the turbulence data. Turbulence wavelengths up to 7,000 feet per cycle were measured during that program. The purpose of Phase III is to extend the statistical definition of the turbulence environment and define wavelengths up to 14,000 feet per cycle through the utilization of a higher-speed (T-33A) airplane as the instrumentation platform.

The T-33A aircraft was instrumented to measure both meteorological and gust velocity data. A radar altimeter, a Doppler radar system, a radiometer, and an outside air temperature (OAT) probe comprise the basic instrumentation used to obtain the meteorological data. Atmospheric turbulence in the 0.04 to 10 cps frequency range is sensed by instrumentation contained in a Boeing-designed gust probe mounted on the airplane. The gust probe head being used is the one that was installed on a B-52H probe during the testing discussed in References 1.3 through 1.5. This probe head has been both statically and dynamically calibrated in a wind tunnel at Mach numbers including the range of the Phase III recording requirements. The head was mated with the body of a gust probe used during Phases I and II. The boom, on which the gust probe is mounted, was designed for optimization between air flow and vibration characteristics.

Airplane attitude and roll rate instrumentation are installed at the base of the boom. Instrumentation contained inside the gust probe senses the following:

- Differential pressures due to sideslip and attack angles
- Vertical, lateral, and longitudinal accelerations
- Static and impact pressures
- Pitch and yaw rates

A Narrow Band Frequency Modulated (NBFM) system is used to record the data. During a one-year flight period, the T-33A is being flown over test routes located in New York, Kansas, Colorado, and California. These routes were established to give a wide range of possible

topographical and climatological conditions, and were selected such that populated areas would be avoided. The routes are situated in the same vicinity of those routes used during Phases I and II. Each route consists of eight straight legs. The legs are approximately 30 nautical miles in length. They are traversed in the same direction on each flight. Prior to flying each leg, meteorological survey conditions are flown at 100 and 1,000 feet above the terrain. These conditions are performed over the start point of each test leg. Normally, three missions are scheduled every other day; one at dawn, one at mid-morning, and one at mid-afternoon. This is varied as necessary when weather conditions, aircraft maintenance problems, or other factors interfere. Two specific altitudes, 250 feet and 750 feet above the terrain, are used for the gust data gathering position of the flights. The pilot follows the terrain contour, as closely as safety will allow, using a radar altimeter to maintain a constant absolute altitude.

A turbulence sample consists of four and one-half minutes of flight over a leg. In the gust velocity calculations, airplane motion effects are removed giving three orthogonal, space oriented gust velocity components. High-pass numerical filtering of the gust velocity time function and dynamic calibration of all measurements is accomplished to ensure valid gust data, especially at the lower frequencies.

Frequency of exceedance and the probability of exceeding given levels of gust velocity are determined from amplitude count, peak count, and level crossing count data. Gust velocity standard deviations, determined from peak count, amplitude samples, and level crossing data are compared. Cumulative probability and probability density distributions are calculated for these data. Their distributions are being analyzed and compared to a normal distribution. Magnitudes of the gust velocity rms values are investigated as a function of numerous variables.

The properties of turbulence are evaluated by power spectral density (PSD) techniques. The PSD's are calculated and plotted for selected conditions. The spectra are normalized by the gust velocity variance σ_t^2 and by $L \sigma_t^2$. The shapes of the spectra are then analyzed. Mathematical representation of the spectra is being investigated by comparing the experimental spectra with several mathematical expressions as suggested by von Karman, Dryden, and others. The integral scale lengths of the turbulence are also being analyzed.

Certain characteristics of selected turbulence samples such as homogeneity, isotropy, and coherency are calculated and plotted versus spatial frequency. Correlations between turbulence and meteorological phenomena are being studied, and turbulence forecasting techniques are being investigated.

This report summarizes the program accomplishments during the first half of the LO-LOCAT Phase III Program. The data being analyzed are those obtained during flight over the routes near McConnell Air Force Base, Kansas, and Edwards Air Force Base, California. This includes testing through 8 January 1969. Time histories of some of the larger magnitude gust velocities being recorded over the Peterson Field, Colorado, route are also presented. Flying was initiated on 16 August 1968 and will be completed on 15 August 1969.

SECTION II

DATA ACQUISITION

INSTRUMENTATION

Contractual authorization for the LO-LOCAT Phase III Program was received on 15 April 1968. The test airplane, T-33A, AF 57-6550, arrived at Boeing-Wichita from Holloman Air Force Base, New Mexico, on 17 April 1968.

Airplane modification and instrumentation installation began on 23 April 1968. The modification consisted of removal of airplane equipment not required during this testing and relocation of other equipment to permit instrumentation installation. Among those items removed were the instructor pilot's seat, control stick, instrument panel, and other miscellaneous equipment in the same general area. This provided room for the installation of a magnetic tape recording system, signal conditioning equipment, Doppler receiver transmitter unit, and other smaller instrumentation items. The APX-25 control was moved to the pilot's left side panel to provide space for the Doppler radar control on his center panel. The aircraft batteries were removed from the gun bay area and relocated to the engine compartment in partial compliance with T.O. iT-33A-663, "Conversion of T-33A-5LO Navigational Trainer to AT-33A-20LO Attack Trainer." Relocation of the batteries provided space for the gust boom and sideslip camera installations. Two additional inverters were installed in the engine compartment to provide 60 and 400 cycle instrumentation electrical power. All modification and installation work was completed by 8 August 1968.

In order to increase "visibility" of the airplane while flying at low altitude, conspicuity paint was applied per T.O. 1-1-4, "Exterior Finishes, Insignia, and Markings Applicable to Aircraft and Missiles."

The design of the instrumentation system was simplified by using, primarily, equipment which had previously been used on the C-131B airplanes during LO-LOCAT Phases I and II. The major area of design involved modification and installation of this equipment. However, a special radome was designed and fabricated and installed on the underside of the airplane to house the Doppler radar antenna.

Instrumentation equipment locations for the LO-LOCAT Phase III Program are shown in Figure 2.1. The radar altimeter, Doppler, radiometer, and outside air temperature (OAT) probe are used basically to obtain meteorological data. The sideslip camera shown in Figure 2.1 was used only during the inflight calibrations of the probe. Atmospheric turbulence in the frequency range from 0.04 to 10 cycles per second is sensed by instrumentation installed in the probe. Instrumentation contained inside the gust probe is shown in Figure 2.2. Note that fine and coarse measurements are provided to improve resolution. To ensure accuracy, the temperature of each transducer is closely regulated to 135 degrees Fahrenheit with thermostatically controlled heaters. Pitch and yaw angular rate sensors are installed in the probe in close proximity to the gust sensors. The attitude and roll rate gyros are installed at the base of the boom.

Design of the boom on which a gust probe is to be mounted requires optimization between airflow and vibration characteristics. The probe must be placed far enough in front of the airplane to minimize the fuselage influences on airflow. On the other hand, the effects of boom flexure on probe instruments must be considered. To achieve this end, a tapered wall thickness was incorporated in the LO-LOCAT boom design. The ratios of pressure port distances from the fuselage to effective fuselage diameter are 1.62 and 1.16 for the α and ρ ports and for the static pressure ports, respectively. The gust boom and probe installation is shown in Figure 2.3.

The boom originally used on C-131B, AF53-7822, was shortened and a mounting was fabricated for installation on the T-33A test airplane. Since the probes used on the C-131B airplanes during Phases I and II were not calibrated for speeds in the range to be flown during Phase III, a probe head previously used on JB-52H, AF 61-023 (Reference 1.3) was installed on the T-33A. This probe head had been previously calibrated both statically and dynamically in the 8-foot transonic wind tunnel at Cornell Aeronautical Laboratory, Buffalo, New York. The B-52 probe head was then fitted to the improved probe body and instrumentation carriage previously used on C-131B, AF 53-7795.

A solid state Narrow Band Frequency Modulation (NBFM) system is used for data recording. This system is the same as that used during Phases I and II. The Inter-Range Instrumentation Group (IRIG) Telemetry Standards were used as a guideline in the design of the system. The system is compatible with remote base ground stations meeting IRIG standards.

Excluding transducers, the NBFM system consists of the following basic components:

- Signal conditioners to control transducer excitation and bias and for switching in standardization signals.
- Subcarrier oscillators (SCO) to provide frequency deviations from center frequency that are proportional to the conditioned transducer output voltages.
- Mixer amplifiers which combine the outputs of several SCO's of different frequency bands into a mixed or composite signal.
- An oscillator to provide a stable reference for tape flutter compensation. Transducer power supplies to provide stable DC voltages for transducer excitation and system correction signals. A magnetic tape recorder to record the analog outputs of the mixer amplifiers.
- A standardization control panel to provide the required system standardization.
- A control system installed at the pilot's station to enable the data gathering sequences to be performed with a minimum of pilot effort.
- A time code generator to provide elapsed time on the magnetic tape for time correlation.

The maximum error of the NBFM data recording system is 0.67 percent of full scale with a confidence of 95 percent (Reference 2.1) for the following recording equipment less transducers:

- Airborne data acquisition System
- FM playback and discrimination system
- Analog to digital converter system

This statement was verified by a test program of 13 flights with two different acquisition systems covering IRIG Bands 2 through 11.

During remote operations, a playback system in a mobile van is used to make "quick-look" checks of data recorded during flight. This system consists of a tape recorder/reproducer, discriminators, time decoder, oscilloscope, frequency counter, digital voltmeter, and a multichannel oscillograph recorder (Figure 2.4). This system is used after each flight to establish validity of the recorded data, perform quality assurance checks, and to determine maximum airplane accelerations. The equipment installed in this van is also used during instrumentation preflight and maintenance checks. A command radio is installed in the van to provide communication with the test airplane.

Instrumentation details are given in Appendix I.

OPERATIONS

Airplane and instrumentation checkout and calibration flights began on 9 August 1968. These flights consisted of tower flybys for airspeed calibration, flights over Cheney Lake, located in south central Kansas, for radiometer and radar altimeter checks, stabilized and maneuvering flight in smooth air for gust probe checks, and angle of attack and sideslip calibrations using the confetti cloud technique. With the exception of angle of attack and sideslip calibrations, these checkout and calibration flights were all completed prior to start of turbulence research testing which began on 16 August 1968. Details of these calibrations are given in Appendix II.

The angle of attack and sideslip calibration flights were not accomplished until 4 September 1968 due to delayed availability of a C-135 support airplane. The C-135, AF 55-3129, and crew were provided by the Air Force, Aeronautical Systems Division, located at Wright-Patterson AFB, Ohio. This airplane arrived at Boeing-Wichita on 3 September 1968, and the confetti hopper was installed in the cargo area. The following day the C-135 provided two support flights to dispense confetti particles into the flight path of the T-33A test airplane.

Turbulence data were obtained over the McConnell AFB, Kansas, route during the period 16 August to 25 September 1968. A total of 348 turbulence samples were recorded during 44 flights. During this same period, 66 samples were not recorded due to adverse weather. These 66 samples include complete flights as well as individual legs which were not flown due to fog or cloud cover. Of the 44 flights flown, 21 were flown at 250 feet absolute altitude and 23 at 750 feet. No attempt was made to obtain an equal number of flights at each altitude other than to schedule alternate flight altitudes each succeeding flight day.

The airplane was moved to Edwards Air Force Base, California, and data were obtained during the period 8 October 1968 to 8 January 1969. A total of 637 turbulence samples were recorded during 100 flights over this route. During Edwards' testing, 255 samples were not recorded

because of adverse weather. Complete tests as well as individual legs were not flown. Legs 2 and 7 were frequently not flown due to smoke and haze cover and leg 4 was frequently omitted due to fog. Of the 100 flights accomplished, 49 were flown at 250 feet absolute altitude and 51 at 750 feet.

One flight was made in the area of the BREN Tower near Lathrop Wells, Nevada, on 8 January 1969 (See Section VI). The purpose of this flight was to obtain turbulence data for comparison with that obtained from the instrumented tower.

Turbulence research flights over the Peterson Field, Colorado, route were started on 20 January 1969. A safety-chase airplane, T-33A, AF 58-0546, was bailed to Boeing by the Air Force to support the turbulence flights over the high mountains. This airplane will be utilized until completion of research over the Peterson route. It will then be returned to the Air Force. It is anticipated that flying over the Peterson route will be completed on 2 May 1969.

Upon completion of flying over the Peterson route, the research airplane will be moved to Tinker AFB, Oklahoma. The airplane will then be used for approximately two weeks to record turbulence data in the vicinity of thunderstorms. This flying will be performed in support of research being performed by the National Severe Storms Laboratories at Norman, Oklahoma.

The airplane will be moved to Griffiss Air Force Base, New York, in the latter part of May after completion of severe storms research. Turbulence research flying will be performed over the Griffiss route until completion of the flight period for LO-LOCAT Phase III, which will be approximately 15 August 1969. The airplane will then be returned to Boeing-Wichita for instrumentation removal and airplane restoration.

Figures 2.5 and 2.6 show the cumulative number of flights and samples recorded versus calendar time. As of 31 March 1969, 90 percent of the scheduled flights had been flown and 77.5 percent of the scheduled samples had been obtained. The schedule was based on 8 samples per flight and no allowance was made for legs not flown due to clouds, smoke, haze, or fog cover. The percentage of scheduled samples recorded was lower than the percentage of scheduled flights accomplished.

The actual number of flights flown have been less than those scheduled for various reasons. As discussed previously, several flights have been canceled due to adverse weather. Also, due to late availability of a C-135 support airplane, the angle of attack and sideslip calibrations were performed after turbulence research testing had begun. Because of these calibrations, the T-33A airplane was not available for turbulence research flights for three days.

Unexpected maintenance problems have also caused the airplane to be grounded. For example, the airplane was grounded at Edwards Air Force Base for 11 days while awaiting a replacement engine. Four flights have been canceled at Peterson Field due to maintenance problems causing unavailability of the safety-chase airplane. One flight was not flown due to preparations for flyby of the BREN Tower.

TEST PROCEDURE

Prior to each mission a complete check of the instrumentation is performed. If the instrumentation is acceptable for data recording, the pilot is then briefed by the Boeing meteorologist concerning the weather conditions over the route. The pilot decides whether or not to proceed with the mission based on the weather conditions over the majority of the route. The airplane is not flown in clouds, rain, etc., to preclude moisture accumulation in the gust probe. The pilot considers any operational or flying safety hazards that might exist and has final authority to ground the aircraft if he deems it necessary.

The routes consist of eight straight legs, each of which is approximately 30 nautical miles in length. The McConnell, Edwards, and Peterson routes are shown in Figures 2.7 through 2.9. On data gathering flights the routes are flown beginning with the starting point of leg 1 and continuing to the end point of leg 8. Each leg is traversed in the same direction on every flight and every effort is made to stay exactly on course while flying each leg.

Normally, data flights are scheduled every other day. This is varied as necessary when weather conditions, aircraft maintenance problems, or other factors interfere. On each flying day three missions are flown, one at dawn, one at mid-morning, and one at mid-afternoon. Two specific altitudes are used for the gust data gathering portion of the flights. These altitudes are 250 feet and 750 feet above the terrain. The pilot follows the terrain contour, as closely as safety allows, using the radar altimeter to maintain a constant absolute altitude. Only one altitude is used for any one flying day and it is alternated on successive flight dates.

The following procedures are adhered to as closely as possible during data gathering flights:

1. The pilot stabilizes the aircraft at 1,000 feet altitude above the terrain, and flies over the starting point of the first leg of the course. He then actuates a sequencing switch to initiate the automatic data recording sequence.
2. Atmospheric survey data are recorded for 10 seconds.
3. An instrumentation standardization cycle is then initiated automatically. During the standardization cycle, the pilot begins a descending turn to an altitude of 100 feet above the terrain.
4. The pilot stabilizes the aircraft at an altitude of 100 feet above the terrain on a course that will pass over the starting point of the first leg.
5. After the standardization cycle is completed, atmospheric survey data are again recorded for 10 seconds. These data are recorded, as near as possible, in the same vertical air column as that for Step 2.
6. The pilot makes a climbing turn to the appropriate data gathering altitude and aligns the aircraft with the first leg of the course.
7. When the aircraft passes over the starting point of the leg, gust data recording is initiated by again actuating the sequencing switch. A turbulence sample, 4 minutes 30 seconds in length, is recorded. During this period the airspeed is maintained at approximately 360 knots.
8. These procedures are repeated for each leg.

DATA CATEGORIZATION

All data are categorized according to terrain features, altitude, atmospheric stability, time-of-day, season, and geographic location.

The categories are divided into precise elements as indicated in the following list:

Terrain Features

1. High mountain
2. Low mountain
3. Desert
4. Plains
5. Swamp (not used)
6. Water

Altitude

1. 250 feet
2. 750 feet

Atmospheric Stability

1. Very stable $\Gamma < 2$
2. Stable $2 \leq \Gamma < 5$
3. Neutral $5 \leq \Gamma < 6$
4. Unstable $6 \leq \Gamma$

Time-of-Day

TAKEOFF TIMES - LOCAL TIME ± 30 MINUTES

	<u>Summer</u>	<u>Spring-Fall</u>	<u>Winter</u>
1. Dawn	Sunrise	Sunrise	Sunrise
2. Mid-morning	0900	0930	1000
3. Mid-afternoon	1500	1430	1400

Season

1. Spring - March 21 to June 20
2. Summer - June 21 to September 20
3. Fall - September 21 to December 20
4. Winter - December 21 to March 20

Geographic Location

1. Edwards Air Force Base, California
2. Griffiss Air Force Base, New York
3. Peterson Field, Colorado
4. McConnell Air Force Base, Kansas

Data processing is accomplished primarily by the use of digital computing equipment. The compensation for inadequate frequency response of angle of attack and sideslip measurements is accomplished with an analog computer. Analog compensation networks are spot-checked on the digital computer for accuracy verification.

The data processing equipment provides precise time correlation through the use of linear phase filters, sample and hold features to assure simultaneous sampling and time correlation of data during analog-to-digital conversion, reduced tape playback time, and automatic plotting and printing. Automatic methods are employed that precisely correct the data for undesirable transducer frequency response characteristics, transducer zero drift, and data system zero drift and sensitivity changes. Data processing details are given in Appendix III.

The category for each turbulence sample is indicated on every item (listing or plot) of data by a code number. This number consists of six digits in the order of classification as given in the preceding list. The number preceding each item is the code number for that item. The following example illustrates this method:

Code No. 422324

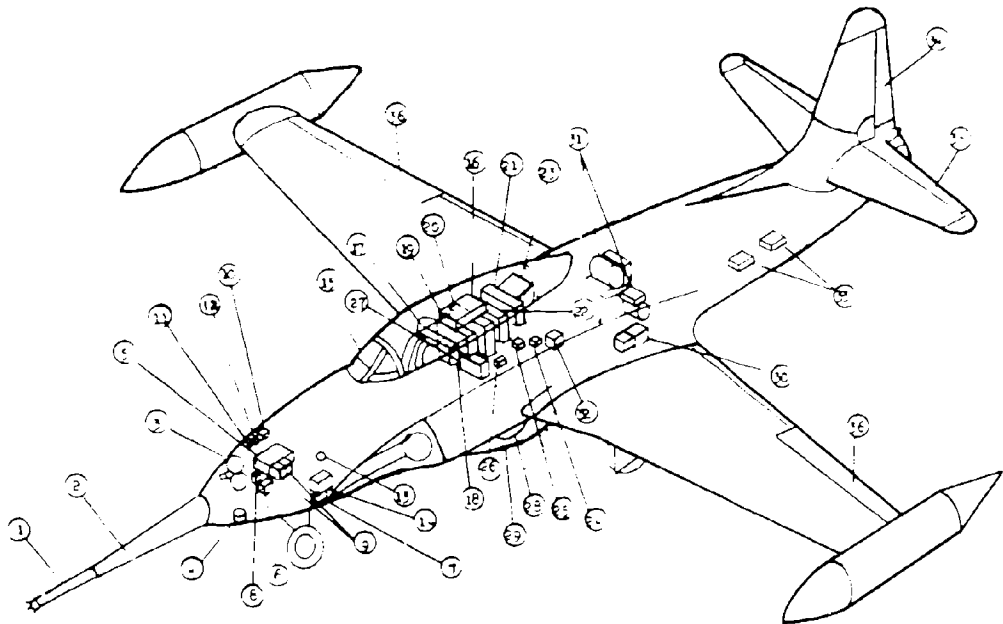
- 4 - Terrain Feature, plains
- 2 - Altitude, 750 feet
- 2 - Atmospheric stability, stable
- 3 - Time-of-Day, afternoon
- 2 - Season, summer
- 4 - Location, McConnell AFB

The categories are reduced to a minimum by pooling the data for categories which show like characteristics. The number zero is used to indicate that all data under a given heading is pooled. An example to illustrate the pooling technique follows:

Code No. 114000

- 1 - Terrain feature, high mountain
- 1 - Altitude, 250 feet
- 4 - Atmospheric stability, unstable
- 0 - Time-of-Day, all pooled
- 0 - Season, all pooled
- 0 - Location, all pooled

All category numbers, except stability, are assigned when the data request is prepared. The number for stability is assigned during data processing after lapse rate has been computed. A description of this computation is given in Appendix III.



1 Gust Probe	19 Signal Cond Rack
2 Gust Boom	20 Dual Pwr Supply
3 Sideslip Camera	21 Signal Cond Rack-Special
4 Radiometer Optics	22 Time Code Generator
5 Stable Platform Gyro ASN-50	23 Circuit Breaker Panel
6 Stable Platform Gyro Amp-Pwr Supply ASN-50	24 Control Pwr Relays
7 Stable Platform Gyro Controller ASN-50	25 Group Selector
8 Stable Platform Gyro Compensator ASN-50	26 Auto-Cal Network Box
9 Probe Heater Control	27 AN/APN 153 Doppler Radar RT Unit
10 Stable Platform Gyro Roll rate Cutoff Sw ASN-50	28 AN/APN 153 Doppler Radar Antenna
11 Rate Gyro Electronics	29 Radome
12 Roll Rate Gyro	30 Battery
13 OAT Probe	31 400 & 60 Cycle Inverters
14 Radiometer Electronics	32 HG9050 Radar Altimeter RT Unit
15 Pilots Instr Panel	33 HG9050 Radar Altimeter Antenna
16 14 Track Tape System	34 Rudder Position
17 SCO Assembly	35 Elevator Position
18 Standardization Control	36 Aileron Position

Figure 2.1 Instrumentation Equipment Locations

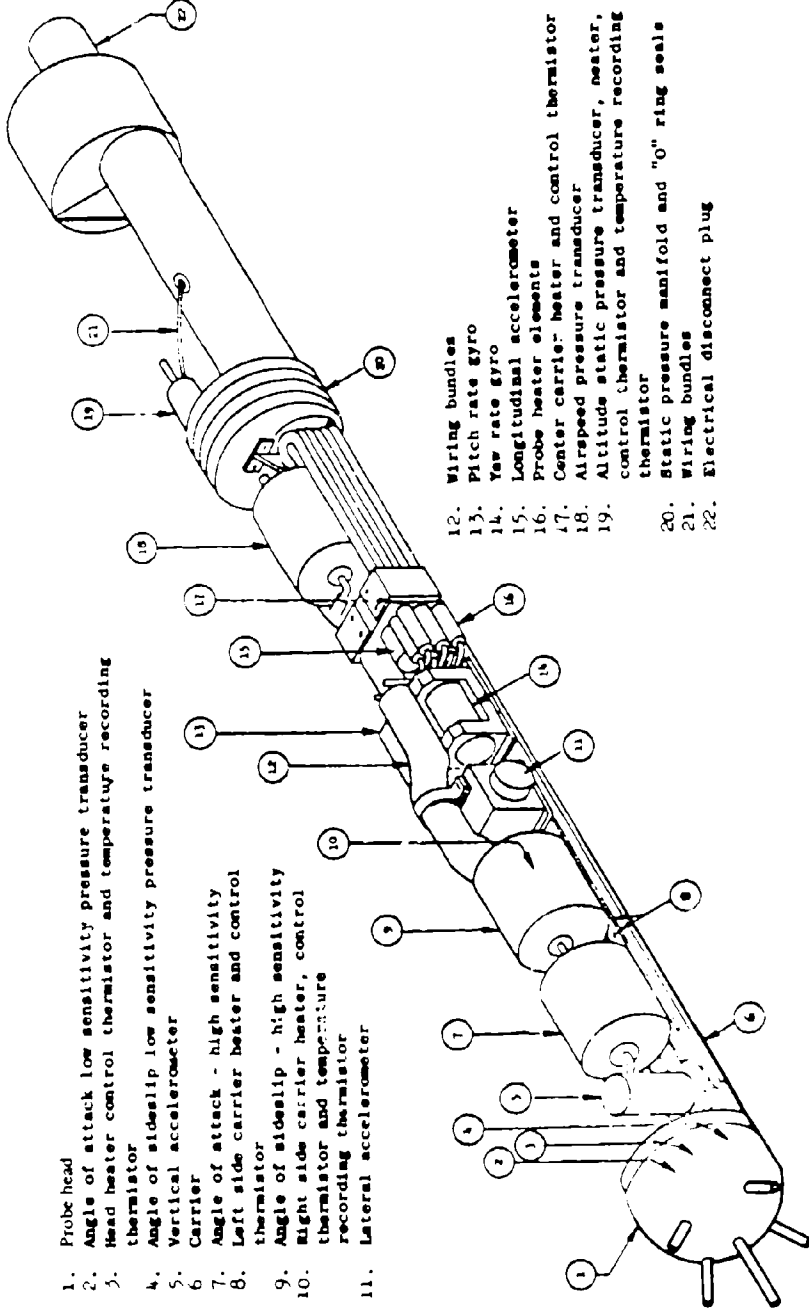


Figure 2.2 Gust Probe Instrumentation

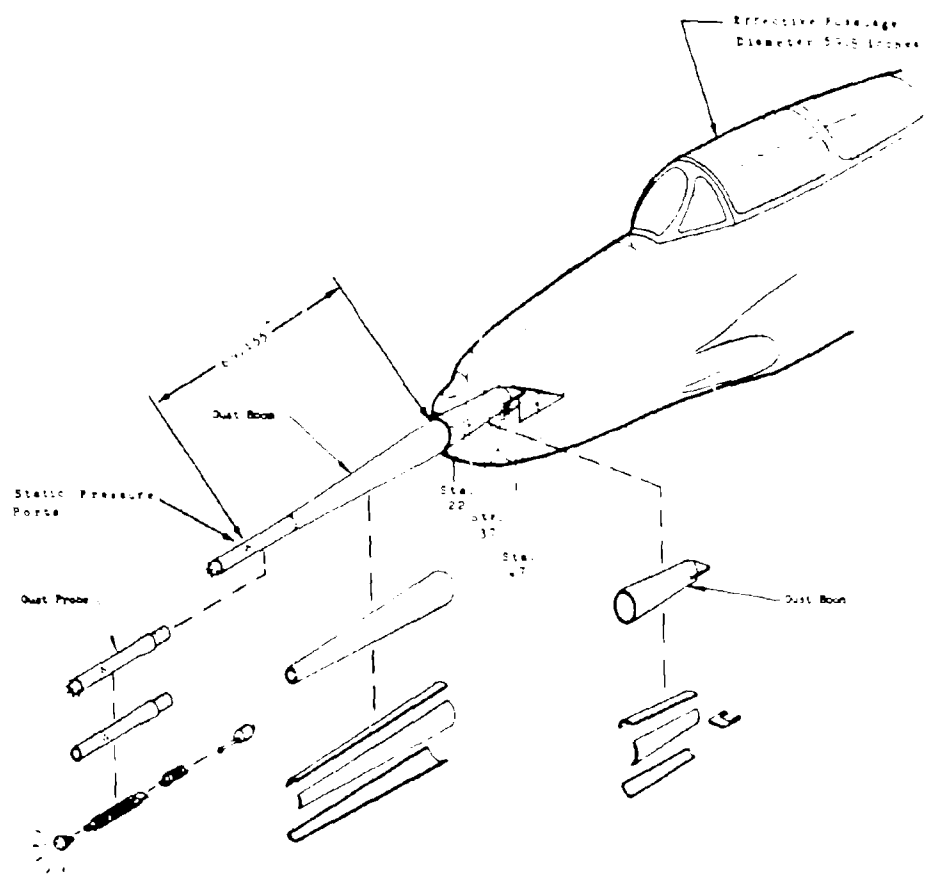


Figure 2.3 Gust Probe and Boom Installation

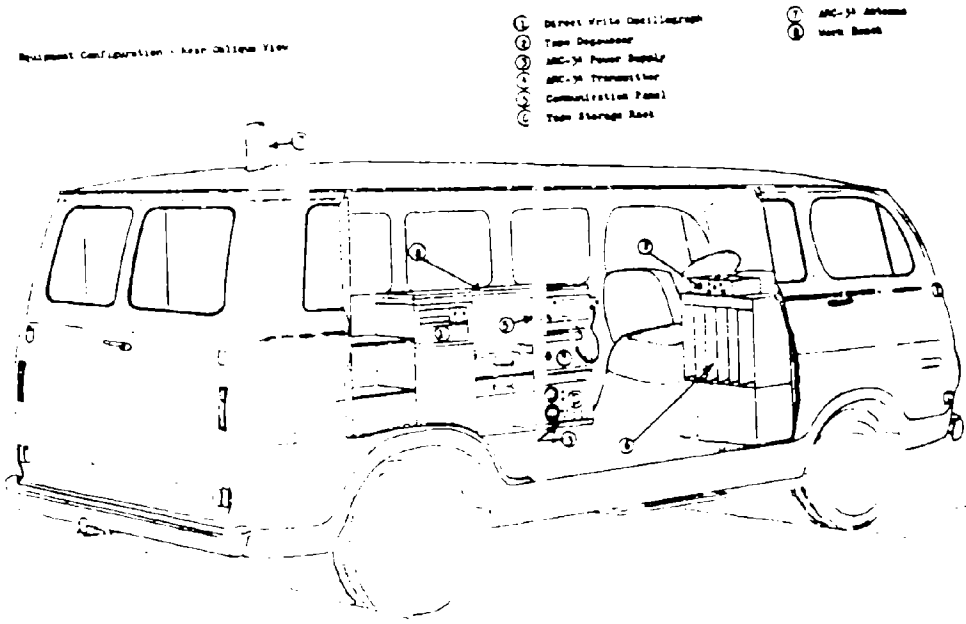
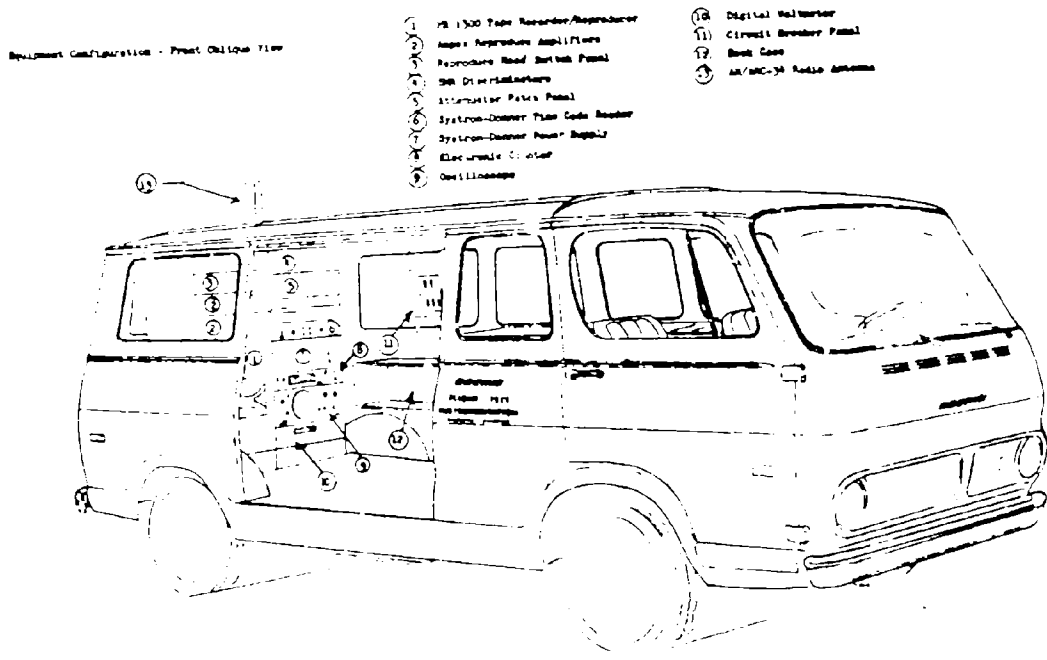
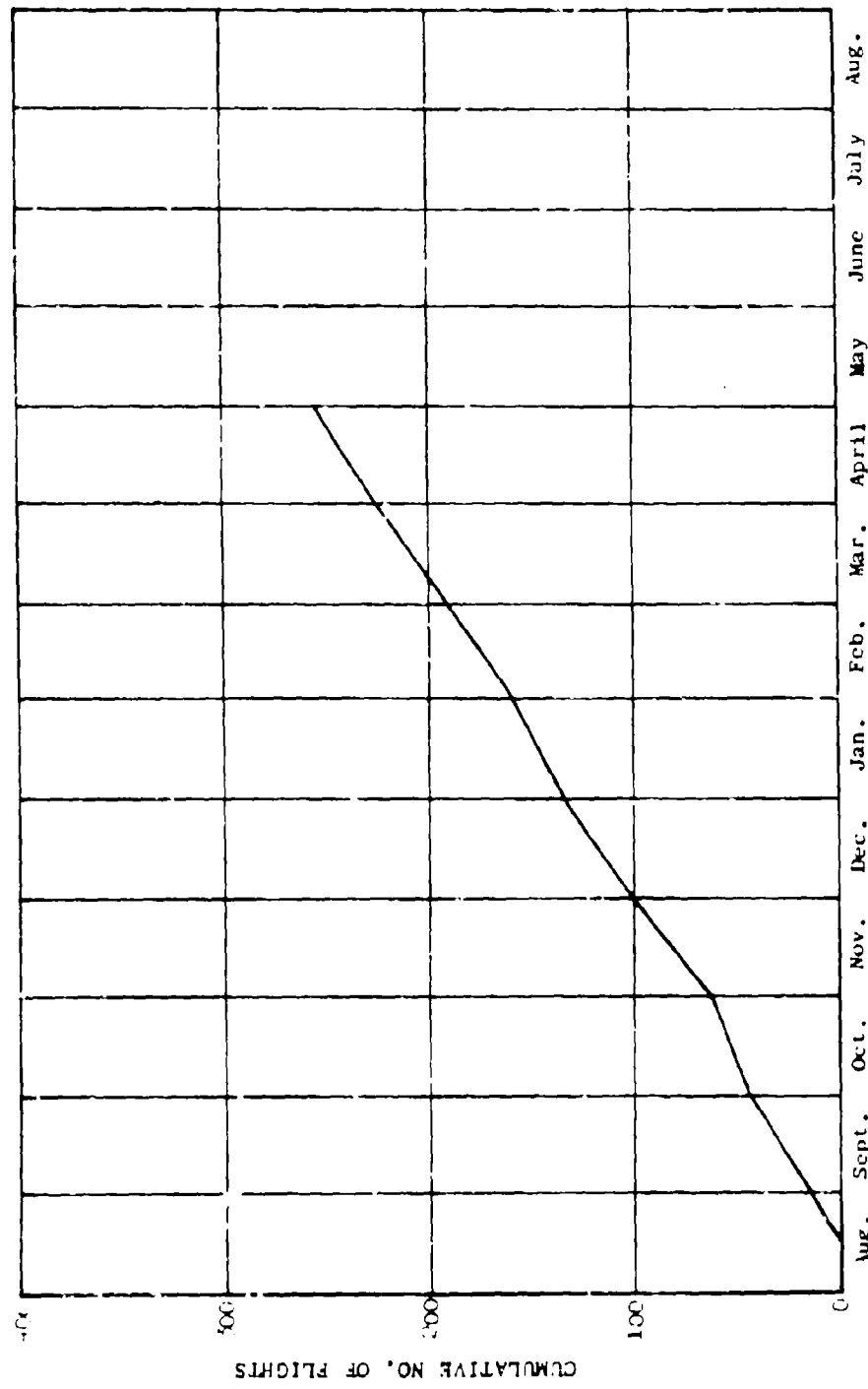


Figure 2.4 Instrumentation Van Equipment Locations



CALENDAR TIME - 1948 and 1949

Figure 2.5 Test Progress - Number of Flights

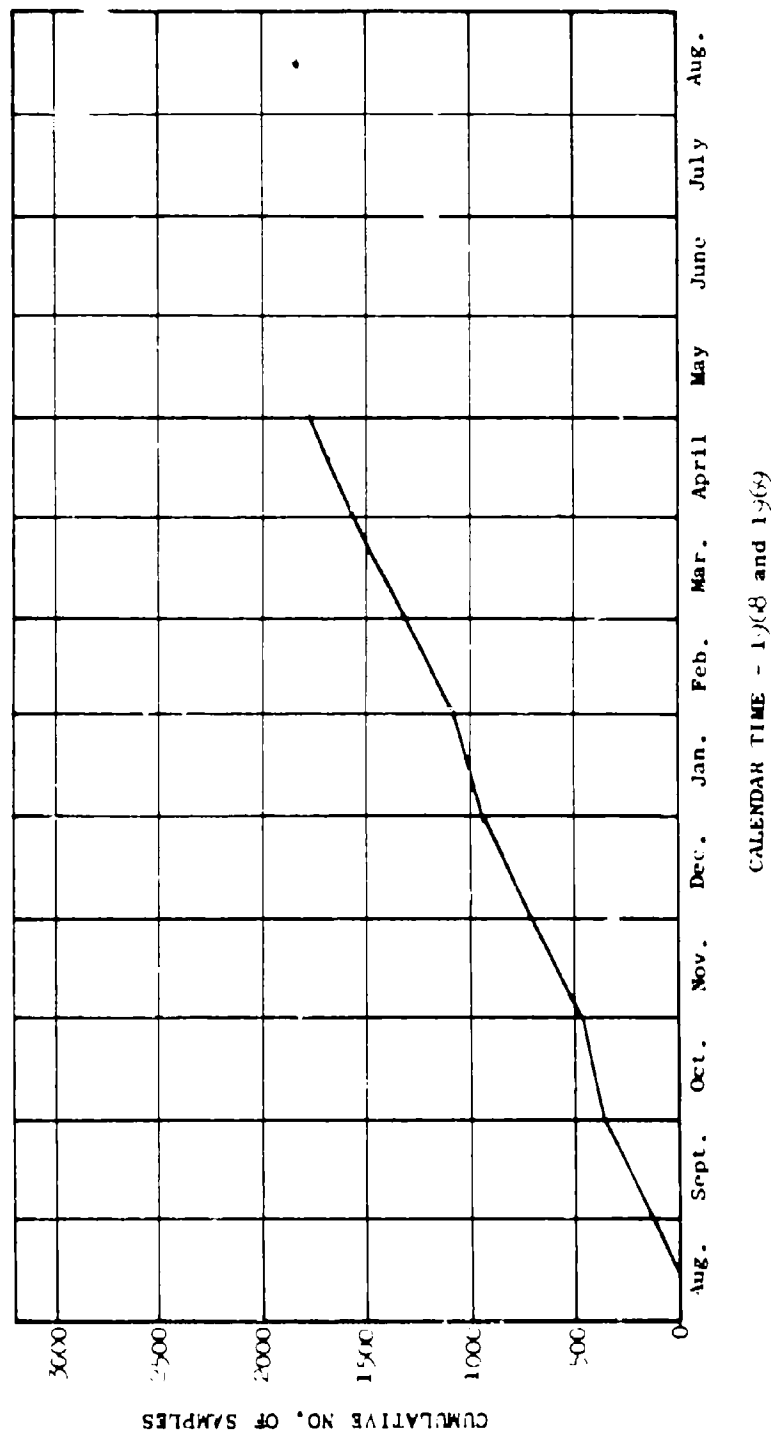


Figure 2.6 Test Progress - Number of Samples

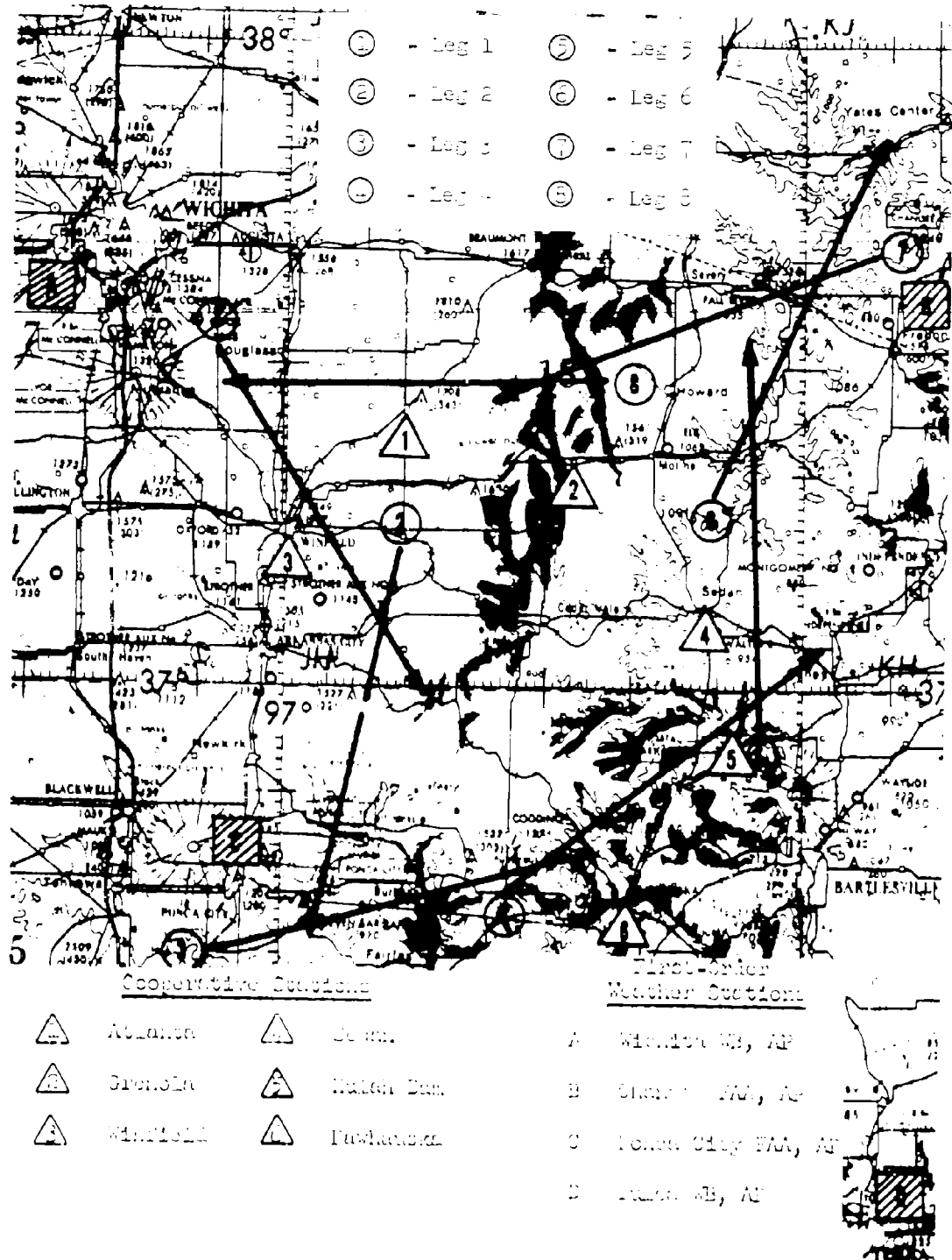


FIGURE 8. McCormick Route

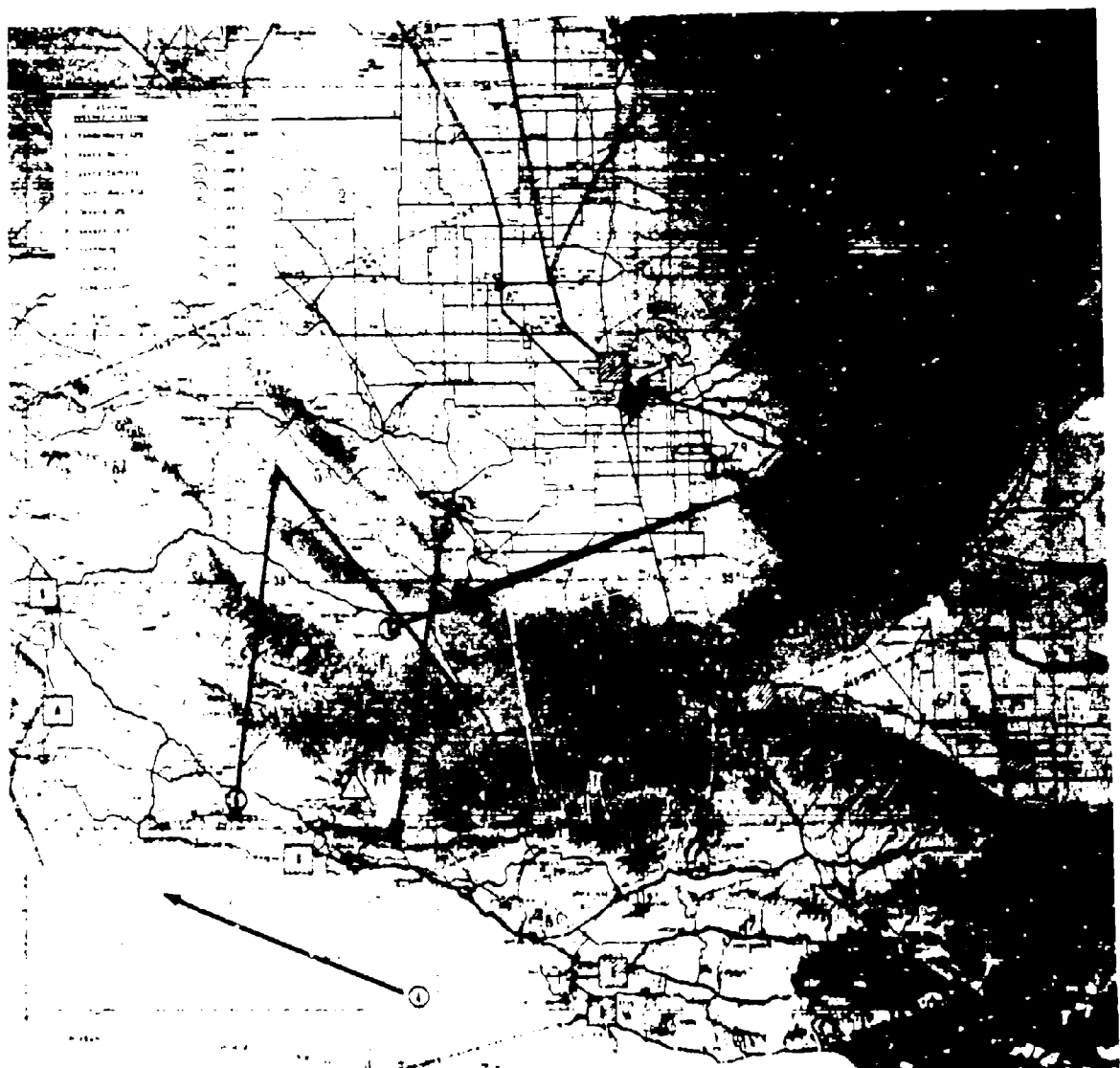


Figure 11.3 Estimated Route

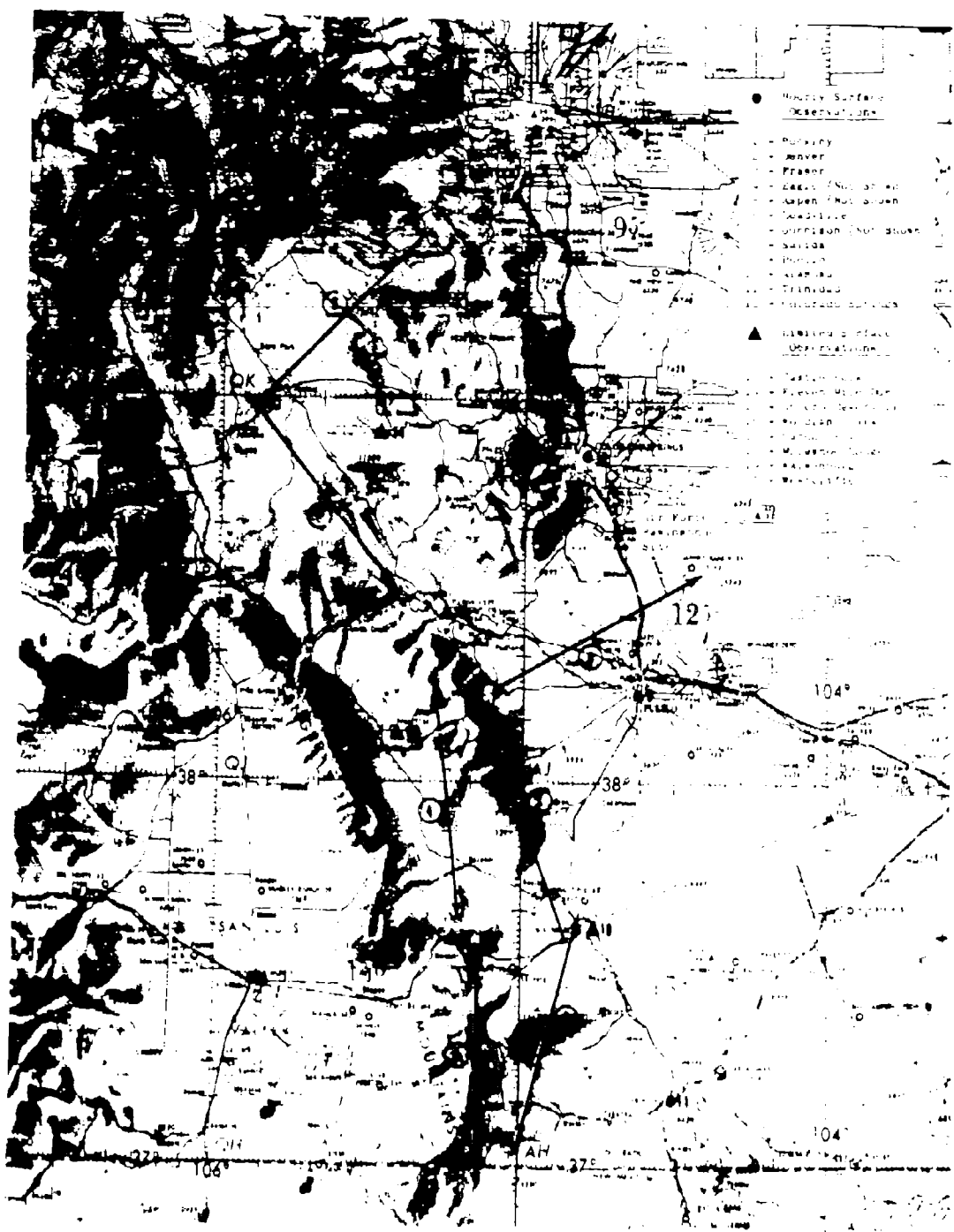


Figure 2.3 Peterson Ranch

SECTION III

DATA QUALITY

A detailed consideration of the qualitative aspects of atmospheric data is necessary if it is to be applied in an effective manner. The development of these data involves the application of many optimizations and engineering judgments. Individual measurements are characterized by certain inaccuracies, noise content, and other limitations. The combination of these variables in the many calculations involved results in a composite of characteristics. Results of special tests and analyses are presented to show characteristics of LO-LOCAT data and to provide insight into the reasoning for approaches being taken during the program.

ANGLE OF ATTACK, SIDE SLIP AND AIRSPEED SENSORS

The following items were accomplished in order to accurately determine α and β from the probe pressure measurements:

- The probe was statically and dynamically calibrated in the wind tunnel to determine sensitivity and frequency response.
- The wind tunnel static calibration results were verified and fuselage generated pressure field effects were checked in flight by the confetti cloud calibration technique.
- That portion of the gust probe overall frequency response due to transduction effects was determined by subjecting the probe pressure system to step inputs.

The probe was statically and dynamically calibrated in 1964 in the Cornell Aeronautical Laboratory's eight-foot transonic wind tunnel. The static wind tunnel calibration was performed to calibrate the probe, to verify design criteria, and to determine Mach number and Reynold's number effects on the pressure sensing elements over wide angle displacements and large speed ranges. The results of the static wind tunnel calibration are given in Reference 1.3 and Appendix II.

A dynamic wind tunnel calibration was performed to determine frequency response of the angles of attack (α) and sideslip (β). The tests were conducted over a Mach number range from 0.50 to 0.95 and for frequencies from 2 to 12 cps. It was found that measured gust velocity frequency characteristics were affected by probe aerodynamics and transduction (tubing and transducer) effects. These results are also given in Reference 1.3 and Appendix II.

Ground testing was accomplished with the gust probe installed on the airplane (a B-52H airplane, Reference 1.3) to isolate the aerodynamic effects from the transduction effects. Results from the wind tunnel dynamic calibration provided the overall frequency response, i.e., the response due to combined aerodynamics and transduction effects. Step pressure inputs were applied to the probe pressure ports to determine the frequency response characteristics of the tubing and transducers. The difference between the frequency response functions obtained from the wind tunnel and the ground test established that portion of the overall frequency response attributable to aerodynamic effects.

Since the probe head being used during LO-LOCAT Phase III had thus been previously calibrated statically and dynamically, it was not necessary to repeat this procedure. The probe shell, which was used on the C-131B aircraft during LO-LOCAT Phases I and II, is mated to this calibrated head and is identical in exterior dimensions to the one used in the wind tunnel. Therefore, the aerodynamic effects previously determined from the wind tunnel and ground tests are applicable to the probe-shell combinations used on the T-33A airplane. To check for any effects on α and β caused by the pressure field generated by the airplane fuselage, the wind tunnel results were checked at the beginning of the Phase III program by the confetti cloud calibration technique (Appendix II). Results of this testing verified the wind tunnel static calibration results. Figure 3.1 shows the agreement of the results from these two methods of testing. The results indicate that α and β measurements are not affected by the T-33A fuselage. Therefore, wind tunnel derived equations of α and β are being used in processing the LO-LOCAT Phase III data. These equations are given in Appendix II.

The frequency response characteristics due to transduction effects were determined for LO-LOCAT Phase III testing. With the probe installed on the T-33A airplane, the probe pressure system was subjected to step inputs. The transduction effects were determined from the resultant data by utilizing Fourier transform techniques. This method of testing and analysis is detailed in Appendix II.

The transduction effects thus determined were then combined with the known aerodynamic effects obtained from wind tunnel and ground testing. The addition of these two effects determined the overall frequency response characteristics of the probe. This overall frequency response was found to be the same as that for the Reference 1.3 testing. The gain factor is shown plotted versus frequency in Figure 3.2. The reciprocal of this gain factor is used as the frequency response compensation for α and β in processing the Phase III LO-LOCAT data. The value of compensating the probe pressures for frequency response characteristics is discussed in Reference 1.2.

In addition to the testing and analysis done for the probe angles of attack and sideslip, static pressure position error was also investigated. The airspeed systems of both the probe and airplane (pilot's airspeed system) were calibrated during flight by a tower. The techniques of this airspeed calibration method are discussed in Appendix II.

The pressure coefficients for the probe and for the pilot's airspeed systems are plotted versus indicated Mach number, as shown in Figure 3.3. It was determined from these data that a value of 0.045 for the probe pressure coefficient, $\Delta P_s / q_1$, was appropriate for the T-33A gust probe. Further substantiation of this pressure coefficient was established by comparison to coefficients from other installations of this same probe. The comparison is shown in Figure 3.4 for the B-52, C-131B, and T-33A. This figure illustrates that for the T-33A installation, a value of 0.045 is very close to the expected value. Impact pressure, q_1 , and true static pressure, P_s , are then calculated as shown in Appendix III.

PROBE MOTION SENSORS

LO-LOCAT instrumentation and computer programs are designed such that probe attitude angles may be obtained from either attitude gyro data (measured angles) or by integrating the output of the rate gyros (calculated angles). Also, vertical and lateral accelerations may be obtained either from accelerometers installed in the probe or at the airplane center of gravity (c.g.). Since these

parameters are interchanged in the event of a malfunction, an investigation was accomplished to evaluate their equality. This evaluation was made using data obtained during flight in smooth air, turbulence, and simulated turbulence. The effects of the turbulence were simulated by maneuvering the airplane in smooth air.

Power spectra of measured and calculated angles were computed for each of these samples. They are presented in Figures 3.5 through 3.12. As can be seen from these data, the agreement between the two measurements is very good. The largest difference in the spectra occurred for angle of yaw for the smooth air sample. However, the power level is low and the difference in the standard deviation is small, as can be seen from the data in Table 3.1.

TABLE 3.1

COMPARISON OF MEASURED AND CALCULATED
ATTITUDE ANGLES

Sample Type	Variable	Standard Deviation (degrees)	
		Calculated Variable	Measured Variable
Smooth Air	Pitch	0.28	0.26
	Roll	0.79	0.74
	Yaw	0.37	0.23
Turbulence	Pitch	0.89	0.79
	Roll	2.60	2.50
	Yaw	0.95	0.90
Simulated Turbulence	Pitch	0.96	0.93
	Roll	*	*
	Yaw	0.91	0.84

* Roll rate exceeded the limitations of the recording system during this test, therefore, roll angle comparisons cannot be made.

Since the accelerometers installed at the probe and c.g. are in different vibration environments, the effect of using these accelerometers in calculating gust velocities was evaluated by comparing the gust velocities calculated using the output from each set of instruments.

Power spectra of gust velocity calculated using accelerations measured at both the probe and c.g. were calculated for a turbulence condition and are presented in Figures 3.13 through 3.15. The time series standard deviations obtained from these data are tabulated in Table 3.2.

TABLE 3.2
COMPARISON OF GUST VELOCITIES COMPUTED USING
PROBE AND C.G. ACCELEROMETERS

Sample Type	Component	Component Standard Deviation (σ_t)	
		Probe Acceleration	C.G. Acceleration
Turbulence	u	3.98	3.99
	v	3.89	4.19
	w	3.29	3.13

As can be seen from Table 3.2 data, there is little effect caused by the interchange in the accelerometer measurements in either the σ_t values or the spectra shape. It was determined that calculated and measured angles, and probe and c.g. accelerations may be interchanged with no harmful effect on the final data.

GUST PROBE AND BOOM NATURAL FREQUENCY

The gust probe-boom assembly was designed to have a natural frequency greater than 10 cps since the frequency range of interest for LO-LOCAT is 0.04 to 10 cps.

The probe and boom assemblies used during Phases I and II of the LO-LOCAT Program had natural frequencies of approximately 15.6 cps (Reference 3.1). Since the boom used during Phases I and II was shortened, for the use on the T-33A, it was expected that the natural frequency of the Phase III assembly would be greater than 15.6 cps. The rigidity of the boom attachment to the airplane has a large influence on vibrational characteristics; therefore, a check was made to determine the natural frequency of the assembly for the Phase III Program. Details of this check and associated plots of the vibration characteristics are presented in Appendix II.

The results of this test show that two predominant frequencies are present. These frequencies are 16.7 and 18.5 cps in both the vertical and lateral directions (see Appendix II). There was not any significant vibration between the frequencies of 0.04 and 10 cps.

CALCULATED GUST VELOCITY ERRORS

Longitudinal, lateral, and vertical gust velocity components are computed using the equations given in Appendix III. Earth-referenced probe motion is sensed in terms of acceleration. Probe velocities are computed by integrating the acceleration signals. A small bias error in the integrand will produce a large ramp function error in the resultant integral over a long time period. This error is alleviated by establishing a zero mean for the integrand prior to integration. Results of a test designed to demonstrate the effect of mean removal are discussed in Reference 1.2.

Maneuvers were performed in relatively smooth air to evaluate the effectiveness of motion instrumentation in the removal of probe motion effects in computed gust velocities. The maneuvering used to simulate airplane motion in turbulence was comparable to the gust motion experienced during the movement of an actual turbulence sample where gust velocities reached 55 fps, and their average σ_t was 7.4 fps. Maximum excursions of probe attitude angles and rates of change of attitude for the two cases are shown in Table 3.3.

TABLE 3.3
COMPARISON OF AIRPLANE MOTION DURING
ACTUAL AND SIMULATED TURBULENCE

Variable	PEAK TO PEAK VALUES	
	Turbulence Sample	Simulated Turbulence Condition
Pitch Angle-deg.	16.7	8.8
Roll Angle-deg.	18.4	16.7
Yaw Angle-deg.	10.1	9.4
Pitch Rate-deg/sec	29.0	28.7
Roll Rate-deg/sec	25.1	30.8
Yaw Rate-deg/sec	29.0	16.7

Plots of the gust velocity data calculated from the simulated turbulence sample are presented in Figure 3.16. As evidenced by this data, the incremental fluctuations are generally ± 2 fps with 4.7 fps as the maximum. Time history plots of gust velocities for the turbulence sample (Test 170, Leg 1) are presented in Section V, Figure 5.32.

An analysis of errors, other than drift, involved in the gust velocity calculations was accomplished. Negligible airplane motion and small angles were assumed to obtain simplified equations for the probable error of the three gust velocity components:

$$\Delta \alpha \approx .6745 \Delta v \quad (3.1)$$

$$\Delta v \approx .6745 [(\nu \Delta \beta)^2 + (\beta \Delta v)^2 + (\nu \Delta \psi)^2 + (\psi \Delta v)^2]^{1/2} \quad (3.2)$$

$$\Delta v \approx .6745 [(\nu \Delta \alpha)^2 + (\alpha \Delta v)^2 + (\nu \Delta \theta)^2 + (\theta \Delta v)^2]^{1/2} \quad (3.3)$$

Error in the measurement of airspeed was determined to be 3.2 fps from the mean square of the various terms in the differential of the true airspeed equation (Appendix III) assuming:

$$\begin{array}{ll}
 P_s = 25 \text{ in. Hg} & \Delta P_s = \pm 0.13 \text{ in. Hg} \\
 q_s = 6.3 \text{ in. Hg} & \Delta q_s = \pm 0.06 \text{ in. Hg} \\
 T_a = 540^\circ\text{R} & \Delta T_a = \pm 2^\circ\text{R} \\
 K_t = 0.996 & \Delta K_t = \pm 0.004
 \end{array}$$

Gust velocity errors were then determined using this error ($\Delta V = \pm 3.2$ fps) and the following errors assumed for angular measurements:

$$\Delta \psi \text{ and } \Delta \theta = \pm 0.5 \text{ Deg.}$$

$$\Delta \beta \text{ and } \Delta \alpha = \pm 0.20 \text{ Deg.}$$

In addition, the following constant values were used:

$$\alpha \text{ and } \beta = 6 \text{ Deg.} \quad \psi = 5 \text{ Deg.}$$

and

$$V = 620 \text{ fps} \quad \theta = 10 \text{ Deg.}$$

The greatest value of the above calculations is in the study of the relative contribution of various errors in the computation. Errors determined by the analysis are shown in Table 3.4.

TABLE 3.4
PROBABLE GUST VELOCITY ERRORS

Gust Velocity Component	Error - fps	Contributions
Longitudinal	± 3.0	$\Delta V = 100\%$
Lateral	± 3.9	$\Delta \psi = 66\%$ $\Delta \beta = 27\%$ $\Delta V = 7\%$
Vertical	± 3.9	$\Delta \theta = 66\%$ $\Delta \alpha = 27\%$ $\Delta V = 7\%$

The estimates shown in Table 3.4 are probably pessimistic due to the fact that it is impossible to account for the cancelling effects of errors associated with individual terms in the gust velocity equation. In fact, the maximum gust velocity values calculated for several routine turbulence samples, where the air happened to be smooth, have been considerably less. During one such sample, for example, longitudinal gust velocity varied from -2.7 to +1.8 fps; lateral from -0.9 to +1.2 fps; and vertical from -1.4 to +1.2 fps.

Based on these data, it is concluded that the probable error in LO-LOCAT Phase III data is ± 2 fps with a maximum error of ± 4 fps for extreme turbulence.

CALCULATED GUST VELOCITY DRIFT ANALYSIS

An evaluation of the low frequency drift in unfiltered calculated gust velocity was accomplished.

The test consisted of performing a normal instrumentation preflight and recording data for two five minute intervals spaced two hours apart. During testing the airplane was in a hangar and isolated so that no actual physical inputs to the instrumentation would occur. The data were then processed through the gust velocity equations. Both measured (attitude gyro output) and calculated (integrated rate gyro output) probe attitudes were used in the calculations to evaluate the drift caused by each set of measurements. All parameters that form the gust velocity equations were used as recorded except for q_1 (airspeed), P_{st} (static pressure), and T_a (temperature). These parameters were set equal to constants that would yield a V_T (true airspeed) equal to a value representative of the inflight airspeed.

The unfiltered data obtained from these calculations are presented in Figures 3.17 through 3.19. The letter designations on the figures indicate whether calculated (C) or measured (M) attitude angles were used. The subscripts one and two refer to the first and second recording intervals. The data obtained show that the drift increased with an increase in instrumentation operating time when using calculated angles. The drift in the data using measured angles was generally more linear than the data obtained using calculated angles.

To further evaluate the effects of drift and determine where its greatest influence occurs, the gust velocity equation was divided into three parts: probe motion terms, indicated gust velocity terms, and constant terms. The probe motion terms define the changes in the longitudinal, lateral, and vertical probe velocities in relation to the earth axes. Their computations involve the integration of acceleration information obtained from probe acceleration measurements and rotation to the earth axes using probe attitude measurements. The constant terms define the initial conditions and remove the earth gravitational effects from probe vertical acceleration measurement. They cannot, therefore, contribute to the drift. The indicated gust velocity terms define the longitudinal, lateral, and vertical components as a combination of probe velocity and gust velocity in relation to the earth axes. Their computation involves attack, sideslip, and probe attitude angles and true airspeed.

The drift in each gust velocity component was found to be almost totally caused by the probe motion terms. They are not shown because they did not vary significantly from the true gust velocity data presented in Figures 3.17, 3.18, and 3.19. The drift in the indicated gust velocity terms, Figures 3.20 and 3.21, did not exceed 10 fps and was somewhat cyclic in nature. The drift in indicated longitudinal gust velocity is not presented because the maximum change was less than one fps.

The high drift experienced in the probe motion terms was due to very low amplitude drifting in the instrumentation. This drift varied in amplitude in a periodic manner. Plots of integrated accelerometer signals and calculated and measured angles are presented in Figures 3.22 through 3.26

As the drift experienced in the individual parameters was less than 0.2 fps for the integrated accelerometers and less than 0.7 degree for the calculated angles, it was not readily apparent how this small drift could build up to high values. The probe motion terms were further segmented as follows and each segment analyzed separately:

$$U_u = g \int_0^t a_u dt \quad (3.4)$$

where: $a_u = \gamma_1 + \gamma_2 + \gamma_3$

$$\gamma_1 = -n_x \cos \psi \cos \theta$$

$$\gamma_2 = n_y (\sin \psi \cos \phi - \cos \psi \sin \theta \sin \phi)$$

$$\gamma_3 = n_z (\sin \psi \sin \phi + \cos \psi \sin \theta \cos \phi)$$

$$U_v = g \int_0^t a_v dt \quad (3.5)$$

where: $a_v = \mu_1 + \mu_2 + \mu_3$

$$\mu_1 = n_x \sin \psi \cos \theta$$

$$\mu_2 = n_y (\cos \psi \cos \phi + \sin \psi \sin \theta \sin \phi)$$

$$\mu_3 = n_z (\cos \psi \sin \phi - \sin \psi \sin \theta \cos \phi)$$

$$U_v = g \int_0^t a_v dt \quad (3.6)$$

where: $a_v = \tau_1 + \tau_2 + \tau_3$

$$\tau_1 = n_x \sin \theta$$

$$\tau_2 = -n_y \sin \phi \cos \theta$$

$$\tau_3 = n_z \cos \phi \cos \theta$$

The data selected for presentation were obtained using calculated angles and exhibited the maximum drift amplitude. The data which may be found in Table 3.5 show that the effect of γ_1 , γ_2 , μ_1 , μ_2 , τ_1 and τ_2 is insignificant and that γ_3 , μ_3 and τ_3 contribute almost all of the drift.

TABLE 3.5
COMPARISON OF DRIFT IN GUST VELOCITY EQUATION TERMS

Recording Interval No.	Gust Velocity Component	Equation Variable	Variable Mean (\bar{x})	$g \int_0^t x dt$
2	u	γ_1	-6.88×10^{-8}	-6.64×10^{-4}
		γ_2	2.88×10^{-8}	2.20×10^{-4}
		γ_3	6.58×10^{-2}	6.35×10^2
	v	μ_1	-2.21×10^{-8}	-2.13×10^{-4}
		μ_2	5.20×10^{-8}	5.02×10^{-4}
		μ_3	2.38×10^{-2}	2.29×10^2
	w	τ_1	-1.75×10^{-7}	-1.69×10^{-3}
		τ_2	-7.43×10^{-7}	-7.17×10^{-3}
		τ_3	-3.00×10^{-3}	-2.90×10^1

It is believed that, since vertical acceleration is common to all three equations, it is the primary source of drift. This is caused in part by the reduced resolution of the vertical acceleration measurement when compared to lateral or longitudinal acceleration. The resolution of the reduced data is approximately .005 g's/digital count for vertical acceleration, .002 g's/digital count for lateral acceleration, and .001 g's/digital count for longitudinal acceleration. It should be noted that, in Figures 3.22 and 3.23, integrated vertical acceleration exhibited the maximum amount of drift. It should also be noted that roll angle is common to all three equations (γ_3 , μ_3 , and τ_3); however, the resolution of roll angle is the same as for pitch and yaw.

A comparison of the drift in u , v , and w revealed that u and v generally drifted to higher amplitudes than w . The w drift never exceeded 30 ips whereas v drifted to values greater than 125 ips and u drifted to values in excess of 500 ips. These characteristics have been consistent in all gust velocity calculations.

The drift frequencies observed in the unfiltered data were never greater than .04 cps and were generally much lower. Drift frequencies were generally .02 cps or less.

Example plots illustrating the removal of drift from the ground test data are presented in Figure 3.27. This figure contains the C_2 data of Figures 3.17, 3.18, and 3.19, after filtering with the LO-LOCAT digital filter. Figures 3.28 and 3.29 contain time history plots of unfiltered and filtered data obtained in smooth air. Figures 3.30 and 3.31 are unfiltered and filtered data from a turbulence sample. As can be seen from these data, the removal of the undesirable drift in unfiltered gust velocity is successfully achieved through the use of the LO-LOCAT high-pass digital filter. Details of the digital filter may be found in Appendix III.

In summary, drift, to some degree, is inevitable in the present state-of-the-art processes required to compute gust velocity. Low frequency ($f < 0.04$ cps), high amplitude drift in calculated gust velocity is generated by small amounts of drift in the individual recorded parameters, coupled with the mathematical operations required to compute gust velocities, especially integration. The primary source of drift is attributed to the vertical acceleration measurement. The variation of this drifting with time is unique for each individual gust velocity calculated. Drift in gust velocities computed using attitude gyro data appears to be more linear than the drift which occurs when computations are based on attitude angles calculated from rate gyro information. Successful drift removal may be attained by accurate application of a digital filter.

NOISE EVALUATION

A study of instrumentation system noise levels was made to evaluate the effects on calculated gust velocities. For the purposes of this study, noise was defined as all spurious oscillations, at high and low frequencies, which appear in the data. During LO-LOCAT Phases I and II, it was determined that some type of processing technique must be employed to remove noise from the static pressure, OAT, and attitude gyro measurements (Reference 1.2).

A 100-point, moving time averaging technique was developed to reduce the noise on static pressure and temperature. Evaluation of this technique was accomplished using data obtained during flight in smooth air. It was determined that by smoothing these two parameters no distortion occurred in the longitudinal spectra at low frequencies and there was a reduction of noise levels in the high frequency end of the spectra. No smoothing effects were observed in vertical and lateral gust spectra. As a result of this test, OAT and static pressure data are also being smoothed during Phase III using the 100-point, time-averaging routine.

During Phases I and II, it was also determined that high frequency noise must be eliminated from the measured attitude angles. This was accomplished by calculating $\Delta\sigma_t$, i.e., $[\sigma_t - \bar{\sigma}_t]$ for the gust velocity data. An evaluation of $\Delta\sigma_t$ gives an indication of the amount of turbulence that exists between frequencies of 10 and 20 cps, assuming no noise. This occurs because σ_t is calculated from the truncated spectrum from 0.04 to 10 cps and $\bar{\sigma}_t$ is calculated from the time series. Time series data, considering the high-pass digital filter and the low-pass ground station analog filter, contain frequencies from 0.04 to 20 cps. In addition, it was further proved during Phases I and II that the measured attitude angles were contributing significant noise to the gust data at frequencies less than 10 cps. This was proven by comparing the σ_t values for gust velocity spectra calculated both with measured and with calculated angles. It was found that significant noise existed in the attitude measurement at frequencies greater than five cps. A low-pass filter was therefore developed to remove noise above four cps. The filter is an Ormsby low-pass (See Appendix III) with a cutoff frequency of 4 cps. During Phase III, the filter cutoff frequency was changed to three cps to permit removal of more noise. The effect of this filter can be seen in Figures 3.32 and 3.33 which show the noise level on measured angles both before and after filtering. Since the frequency of airplane motion is one cps and lower, only noise is removed by this filter and the frequencies in the airplane motion range were not affected.

The complete instrumentation system was evaluated using both ground and flight data to determine the level of turbulence below which LO-LOCAT Phase III data could no longer be considered valid due to low signal-to-noise ratio.

The ground test data consisted of the same data used during the drift analysis. The drift data in Figures 3.17 through 3.19 were processed through the high-pass filter, described in Appendix III, and power spectra and standard deviations were calculated. The minimum valid σ_t was calculated assuming that 10 decibels (db) is the minimum signal-to-noise power ratio required for valid data. This minimum value, σ_{t_m} , was calculated by increasing σ_t by a factor of the square root of 10 or:

$$\sigma_{t_m} = (10 \sigma_t^2)^{1/2} \quad (3.8)$$

Since σ_t^2 and the power spectral density function are related by

$$\sigma_t^2 = \int_0^\infty \Phi(k) dk \quad (3.9)$$

increasing σ_t^2 by a factor of 10 is equivalent to increasing the power level of the spectra by 10 db and integrating the new function to obtain the minimum σ_t^2 .

The result of this test is presented in Table 3.6.

TABLE 3.6
MINIMUM VALID STANDARD DEVIATION VALUES

Recording Interval	Attitude Angles Used	Variable	σ_t	σ_{t*}
1	Calculated	u	0.01	0.03
		v	0.02	0.38
		w	0.06	0.19
	Measured	u	0.03	0.05
		v	0.52	1.64
		w	0.48	1.52
2	Calculated	u	0.02	0.06
		v	0.11	0.35
		w	0.07	0.22
	Measured *	u	0.03	0.09
		v	0.10	0.32
		w	0.49	1.55

*Measured angles of pitch and roll, calculated angle of yaw.

The lower σ_t value for the lateral measurement during the second interval using measured angles is probably the result of using calculated instead of measured yaw angle. Calculated angles apparently contribute less error than measured angles to the standard deviation values. This is a result of the smoothing effect of integration on high frequencies [$f > 1/(2\pi)$] when using rates, and the additional high frequency noise associated with the attitude gyros.

It would appear from the above table that there are some cases when σ_t should have a value of at least 1.64 fps to be assured of valid turbulence data. However, it must be realized that the noise

varies slightly from time to time. This is readily seen in the fact that σ_t values as low as 0.34, 0.28, and 0.28 for u, v, and w, respectively, have been observed in the flight data. This would yield σ_{t_e} values on the order of 1.07 fps for valid data.

The shape of the power spectral density function of any variable will be degraded if the signal-to-noise ratio becomes too low. It will also be degraded if the time (or space) function is clearly nonhomogeneous. Therefore, the turbulence data which had irregularly shaped spectra (i.e., did not have a well defined inertial subrange with a -5/3 slope) were compared with the turbulence data having a well defined inertial subrange (regularly shaped spectra). Figure 3.34 contains frequency histograms of the standard deviations of both sets of data. In developing the histograms, only turbulence data having $\sigma_t \leq 2.0$ fps were used. A plot of the ratio of the frequency of occurrence of irregularly shaped to regularly shaped spectra for each band of σ_t is presented in Figure 3.35. As indicated by this curve, there are twice as many irregularly shaped spectra σ_t values of approximately 1.2 fps. At $\sigma_t = 1.4$ fps there are an equal number of both sets.

Considering the ground test data, inflight standard deviations, and power spectra data, it is believed that a minimum value $\sigma_{t_e} = 1.4$ fps will yield good results in the final data with the small number of noisy samples contained in the final data having little effect on the results.

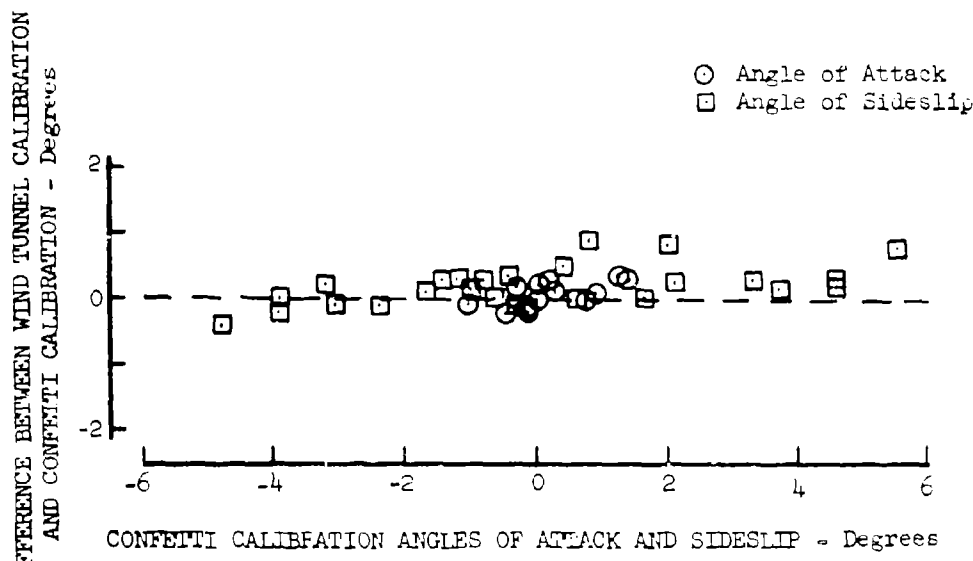


Figure 3.1 Comparison of Wind Tunnel and "Confetti" Calibration Results

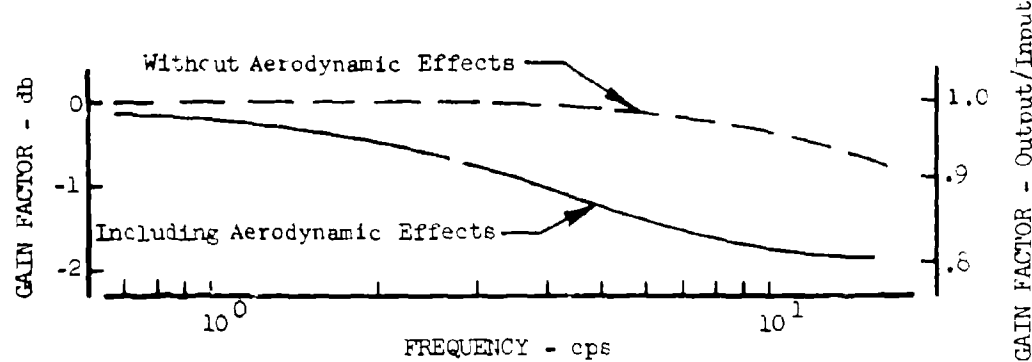


Figure 3.2 Dynamic Response of Angles of Attack and Sideslip Measurements

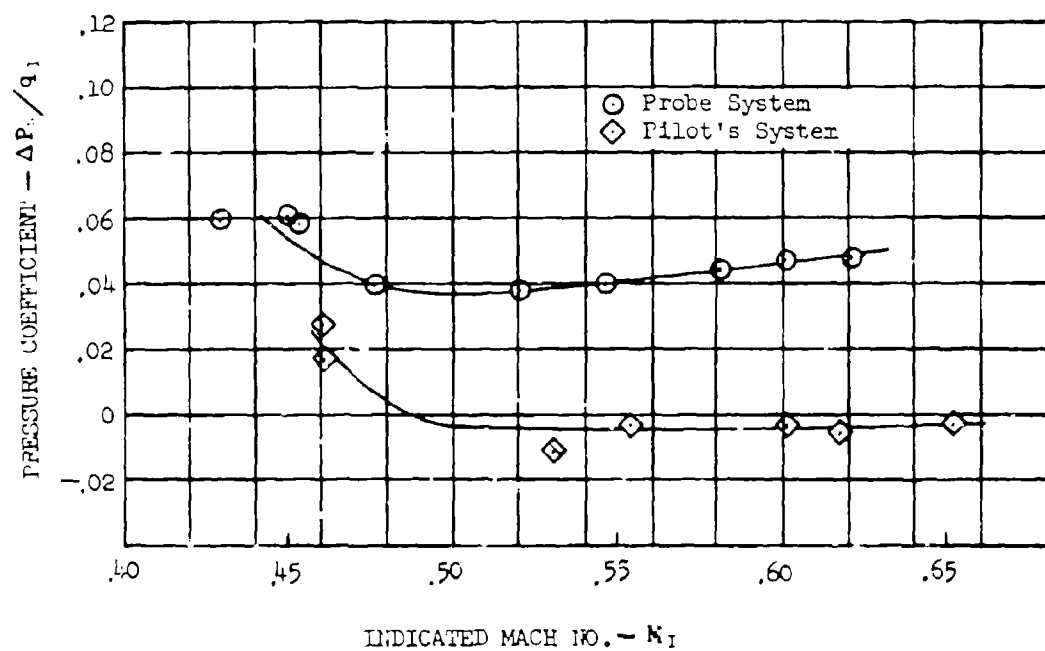


Figure 3.3 Probe and Pilot's Systems Position Errors

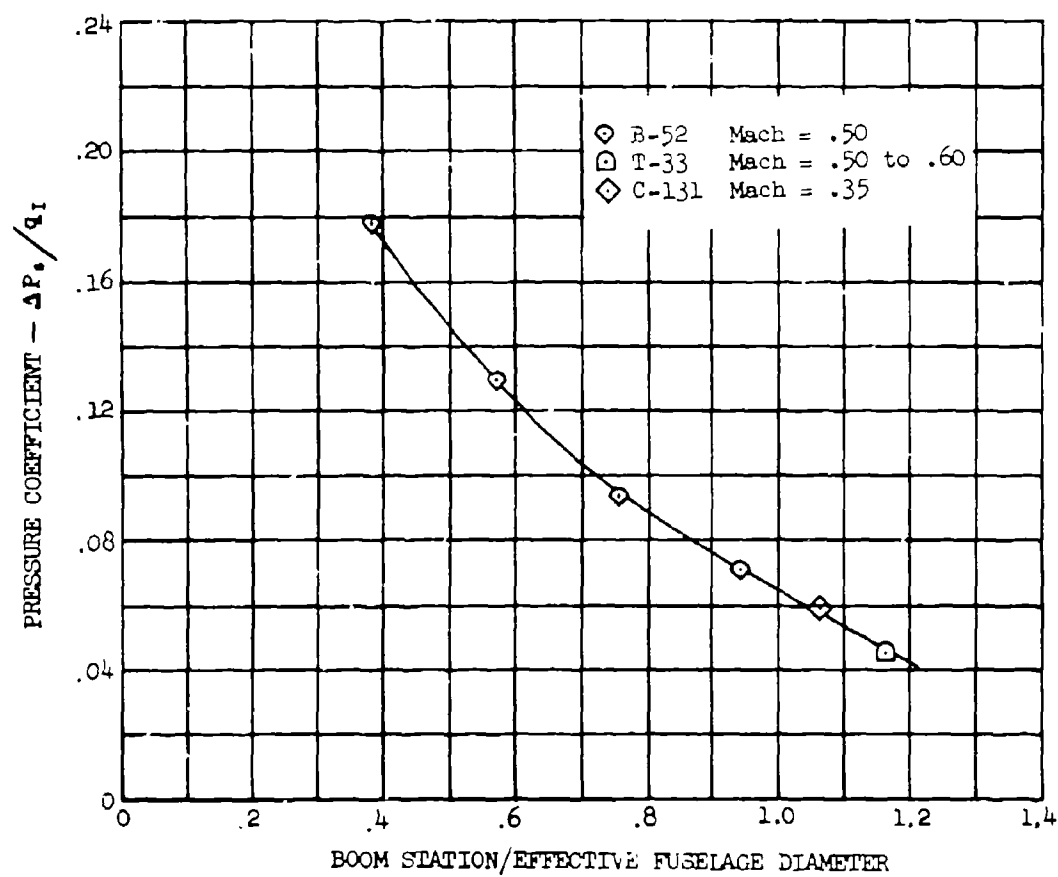


Figure 3.4 Gust Probe Pressure Coefficients for
JB-52H, C-131B, and T-33A Airplanes

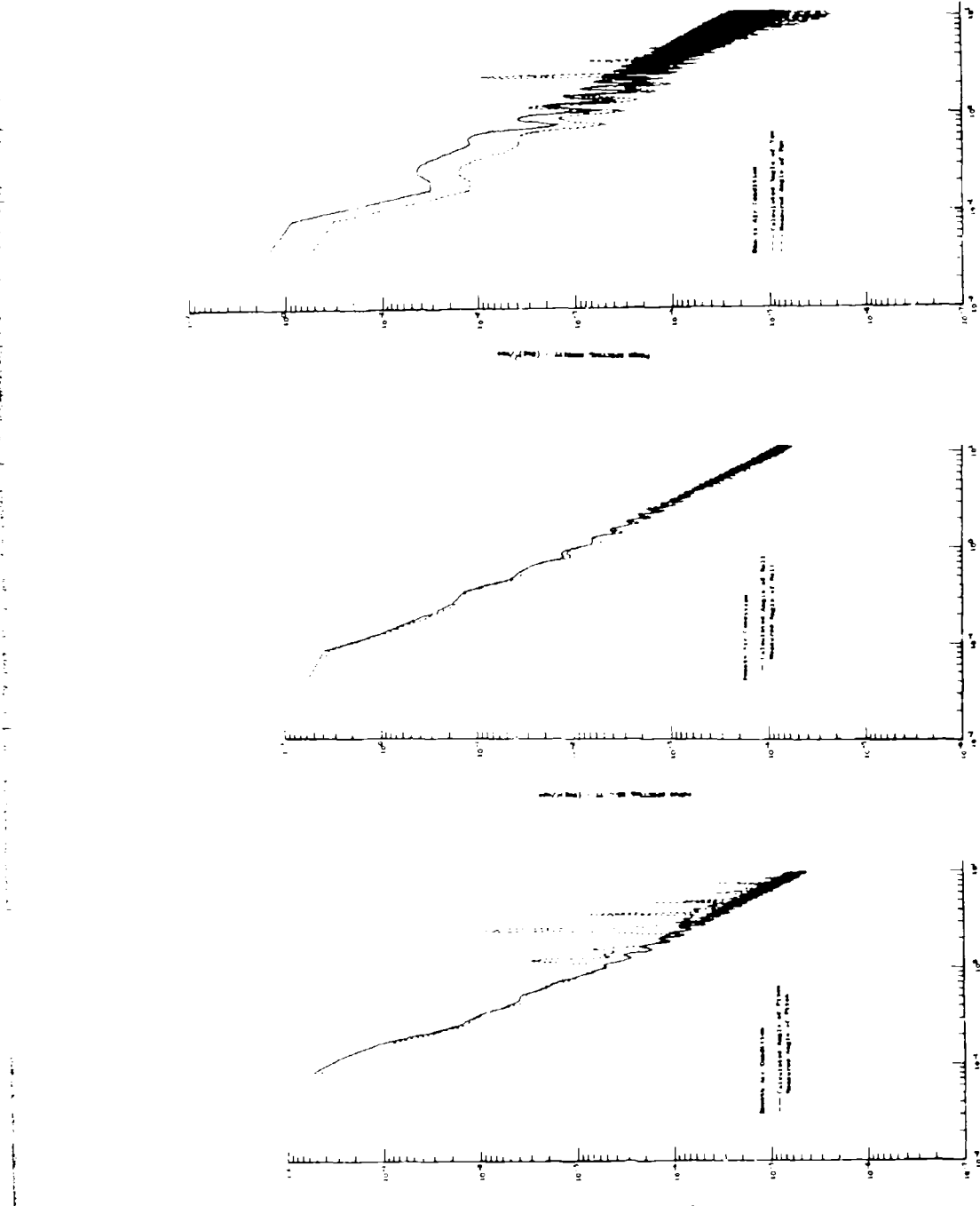


Figure 3.5
Measured and Calculated
Angle of Pitch Comparison -
Smooth Air

Figure 3.6
Measured and Calculated
Angle of Roll Comparison -
Smooth Air

Figure 3.7
Measured and Calculated
Angle of Yaw Comparison -
Smooth Air

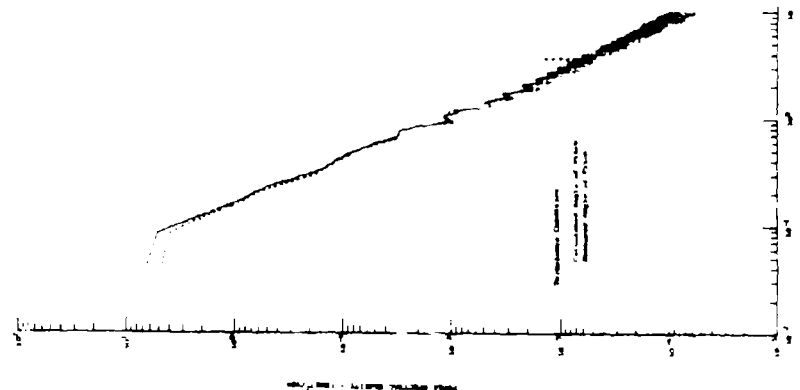


Figure 3.8
Measured and Calculated
Angle of Pitch Comparison -
Turbulence

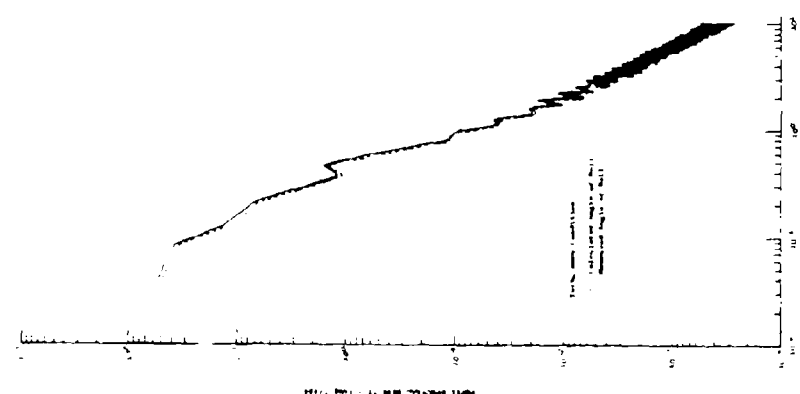


Figure 3.9
Measured and Calculated
Angle of Yaw Comparison -
Turbulence

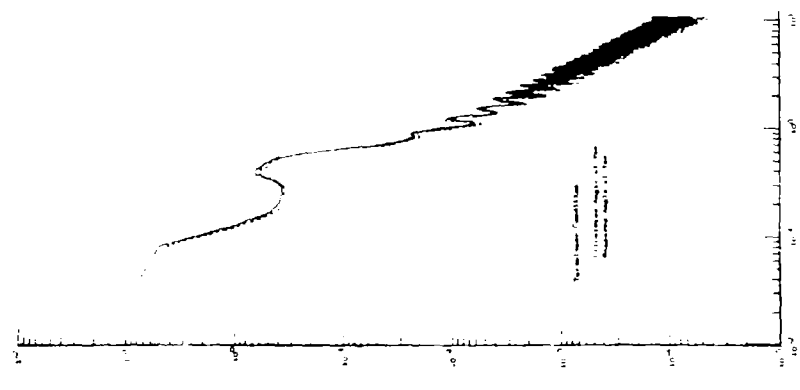


Figure 3.10
Measured and Calculated
Angle of Roll Comparison -
Turbulence

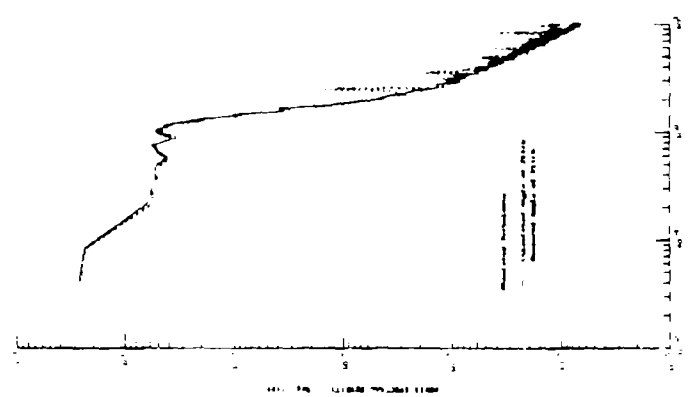


Figure 3.11
Measured and Calculated
Angle of Pitch Comparison -
Simulated Turbulence

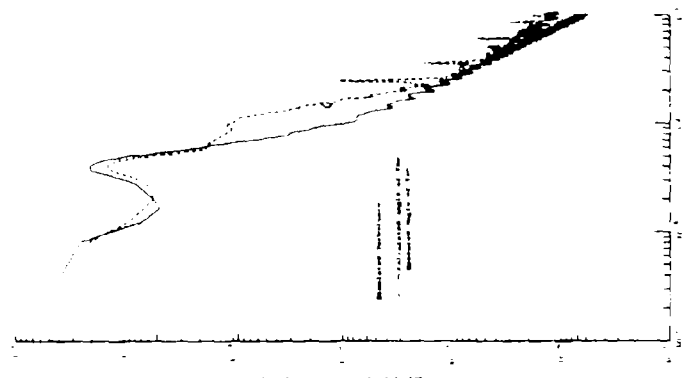


Figure 3.12
Measured and Calculated
Angle of Yaw Comparison -
Simulated Turbulence

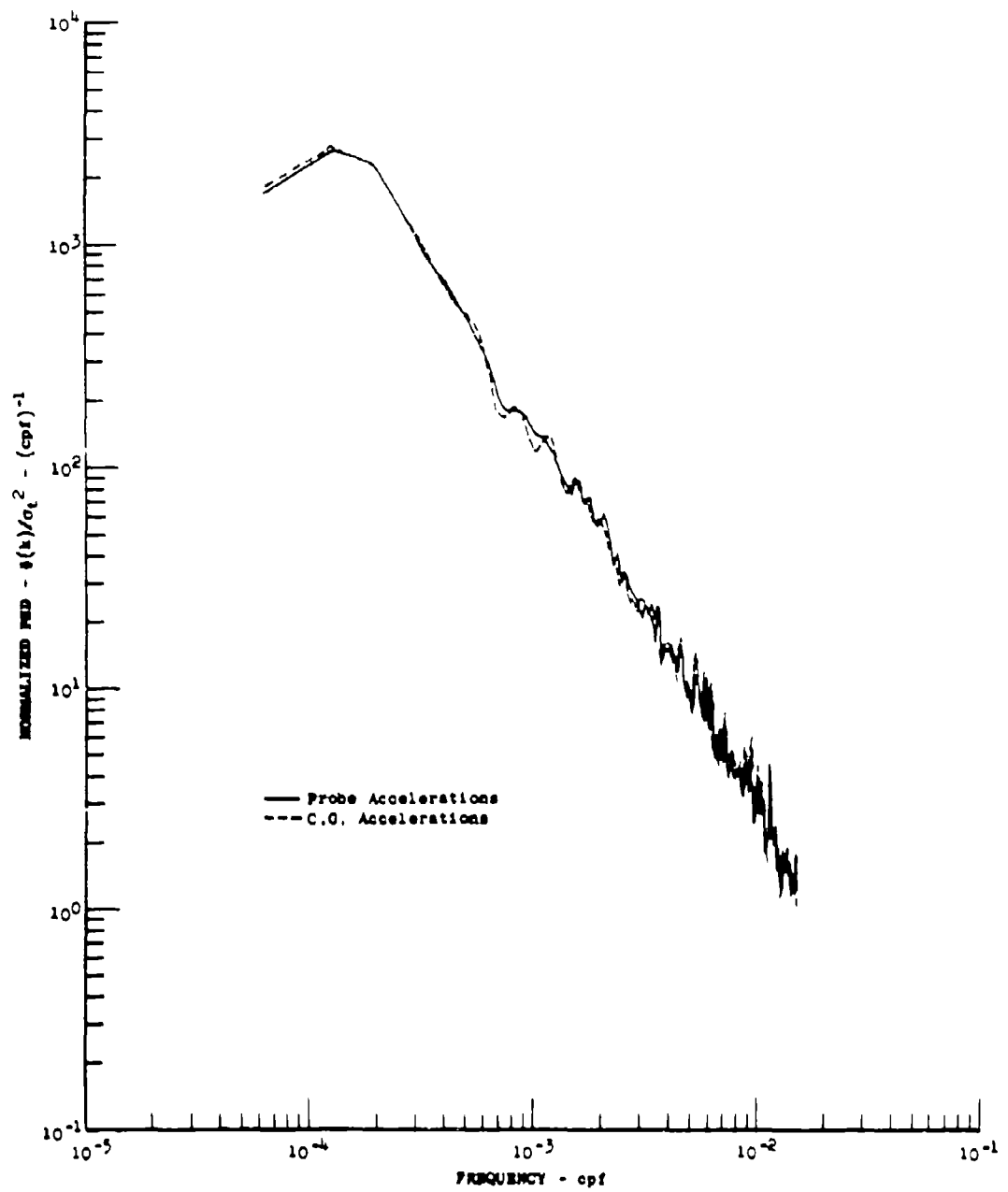


Figure 3.13 Longitudinal Gust Velocity PSD Calculated Using Inputs from Different Accelerometers

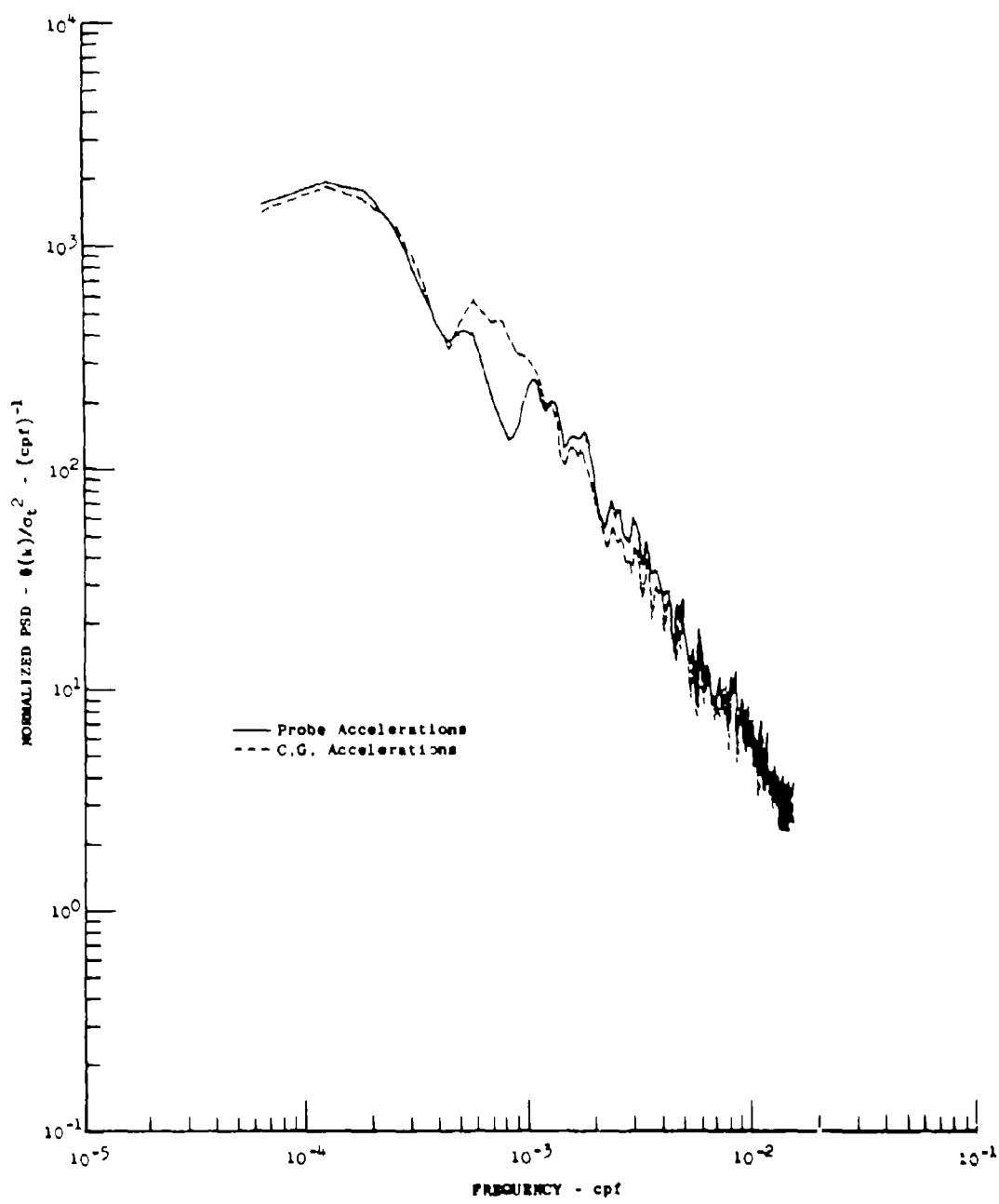


Figure 3.14 Lateral Gust Velocity PSD Calculated Using Inputs from Different Accelerometers

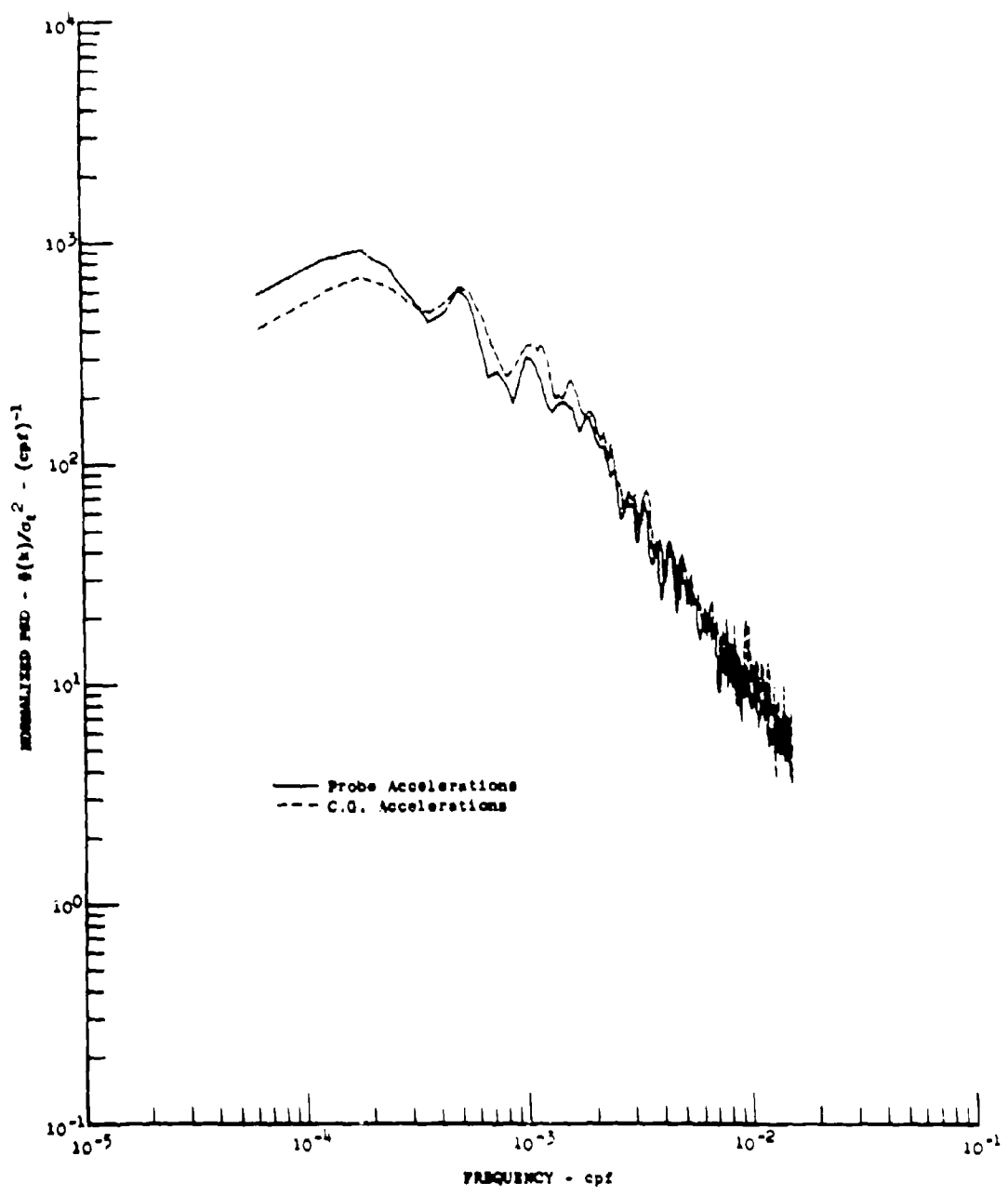


Figure 3.15 Vertical Gust Velocity PSD Calculated Using Inputs from Different Accelerometers

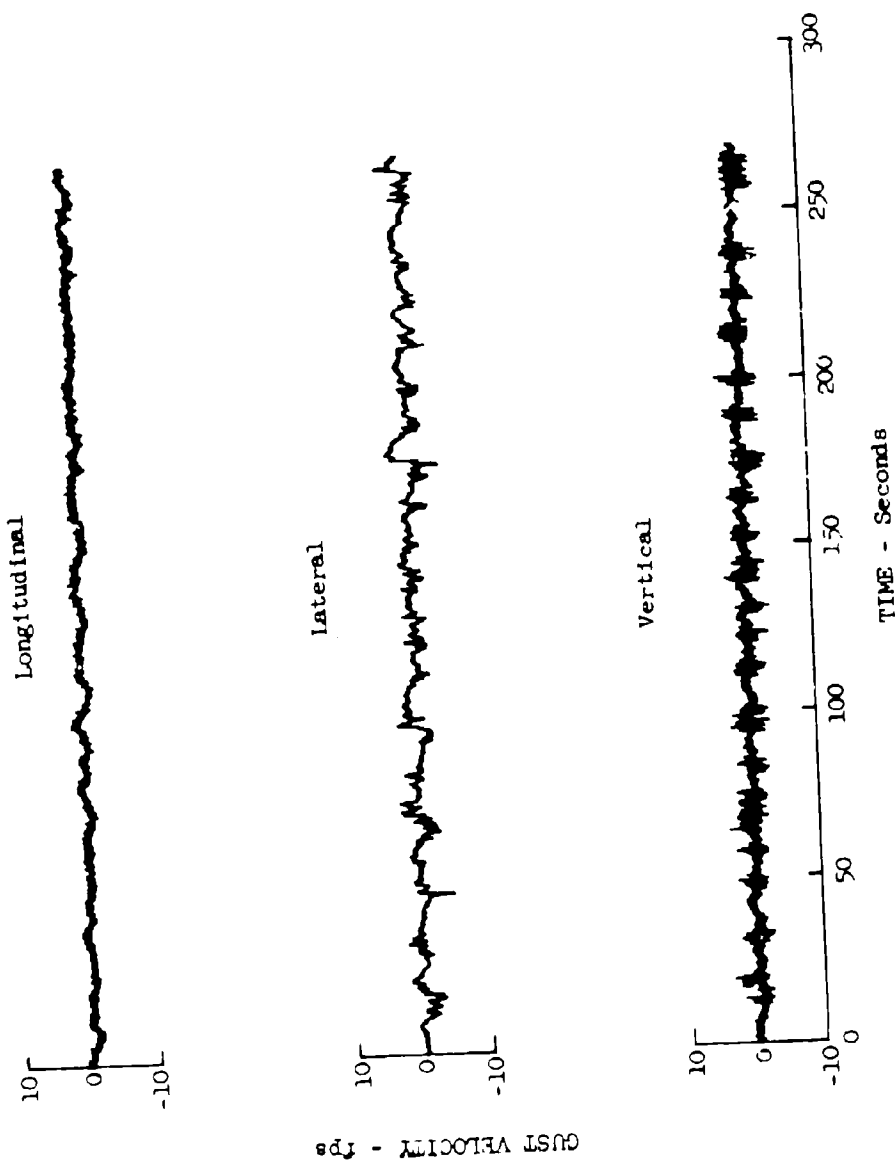


Figure 3.16 Gust Velocity Time Histories of Simulated Turbulence

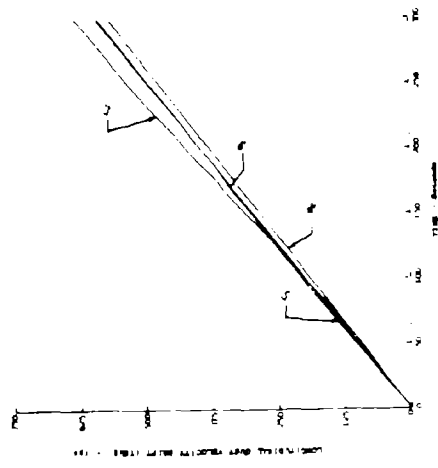


Figure 3.17 Drift in True Longitudinal Gust Velocity

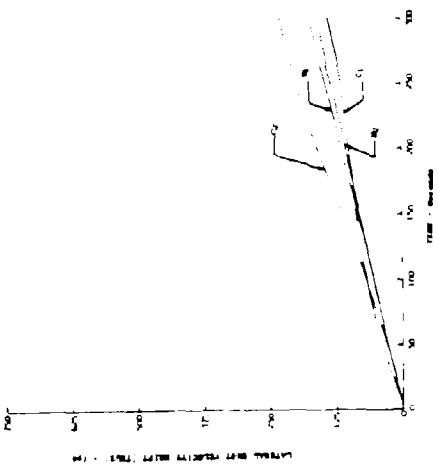


Figure 3.18 Drift in True Lateral Gust Velocity

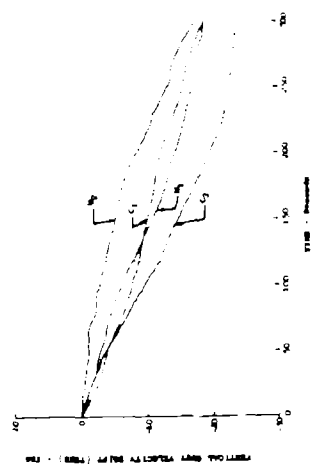


Figure 3.19 Drift in True Vertical Gust Velocity

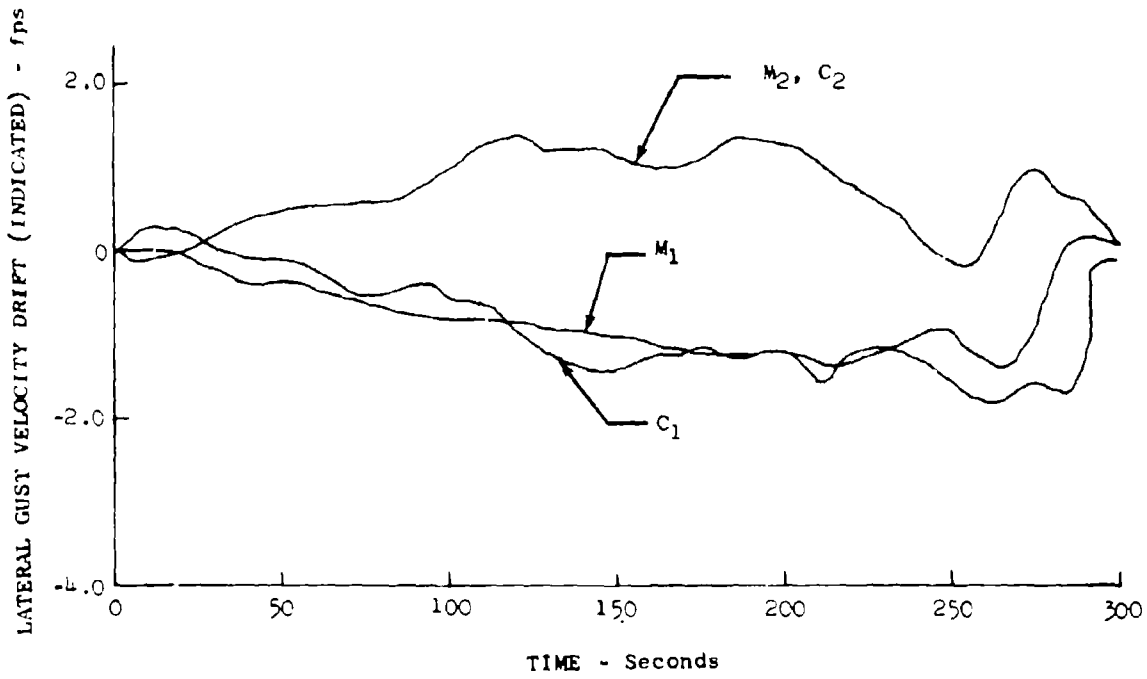


Figure 3.20 Drift in Indicated Lateral Gust Velocity

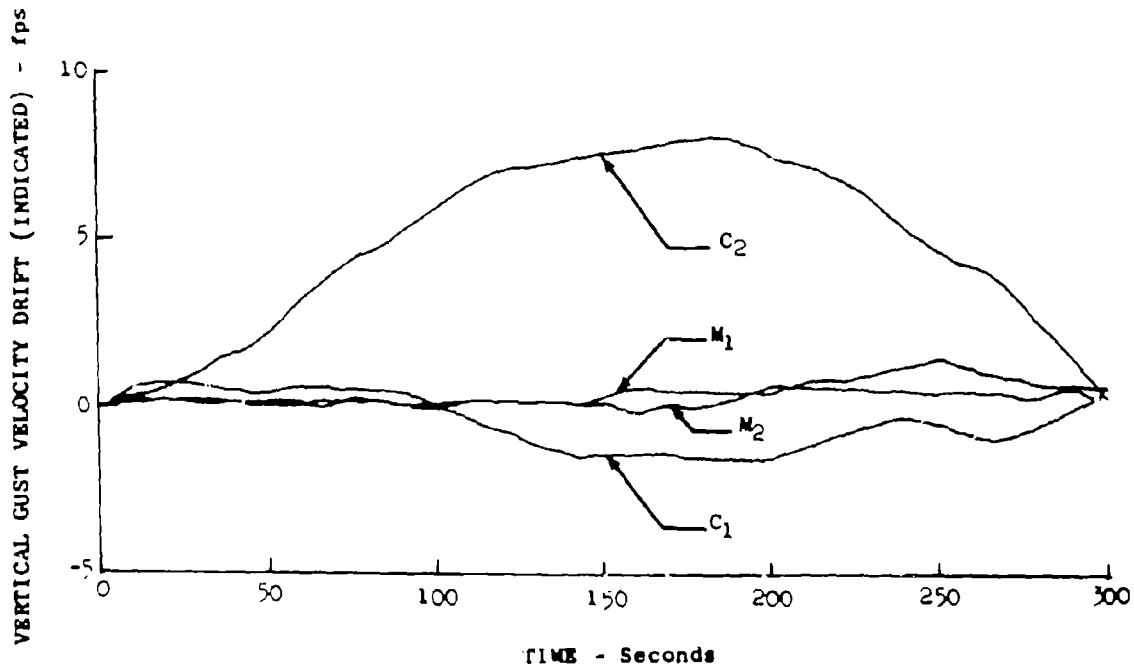


Figure 3.21 Drift in Indicated Vertical Gust Velocity

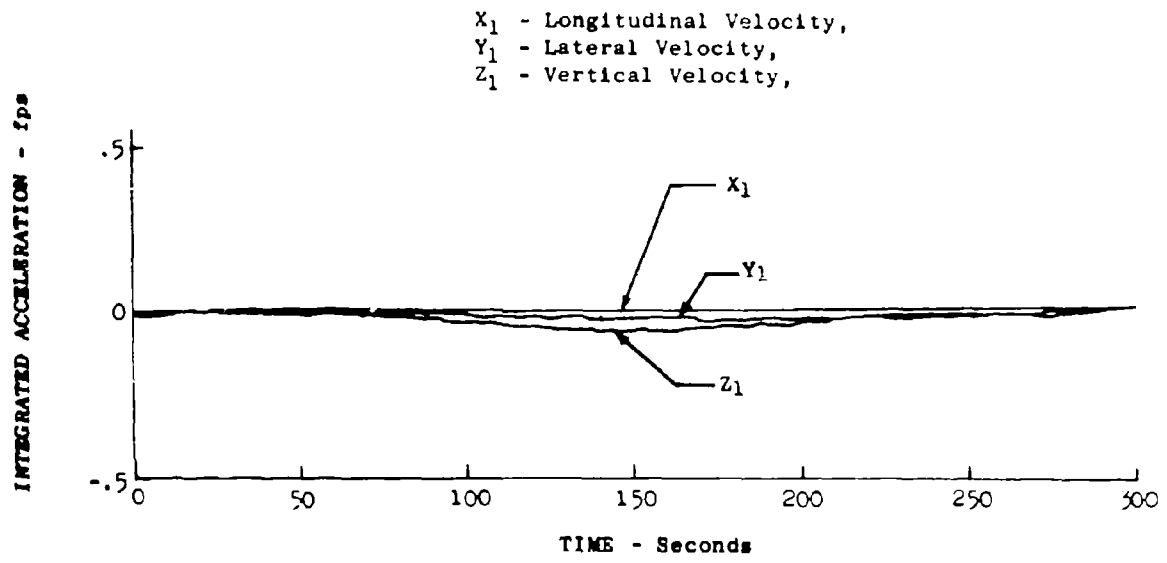


Figure 3.22 Drift in Integrated Acceleration - Interval 1

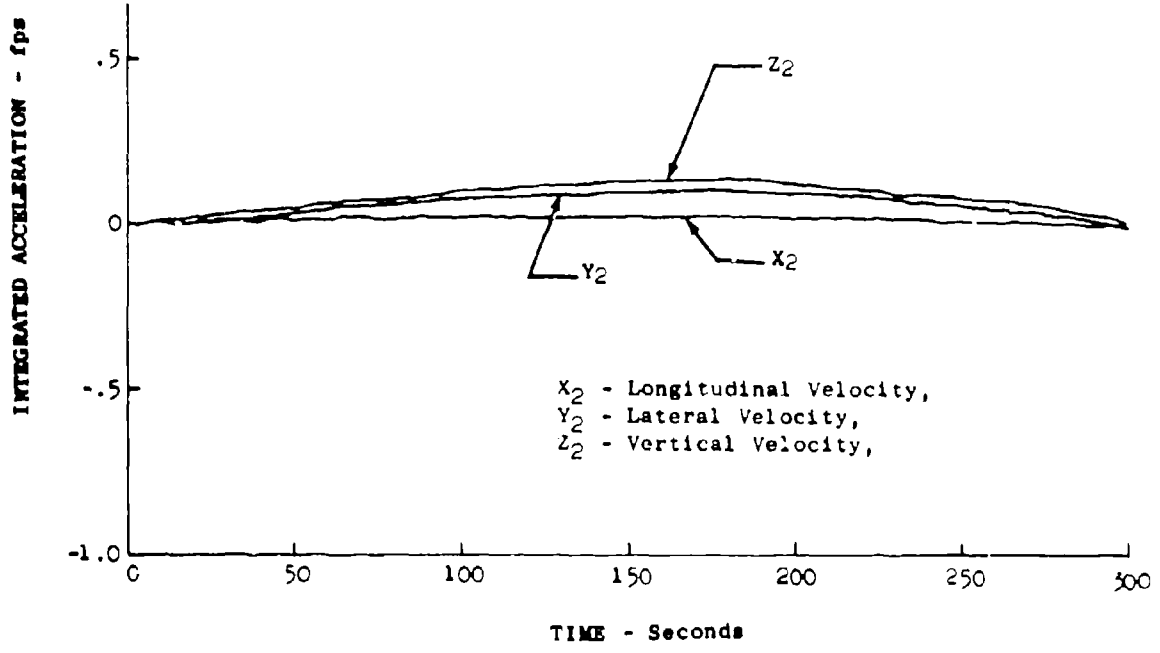


Figure 3.23 Drift in Integrated Acceleration - Interval 2

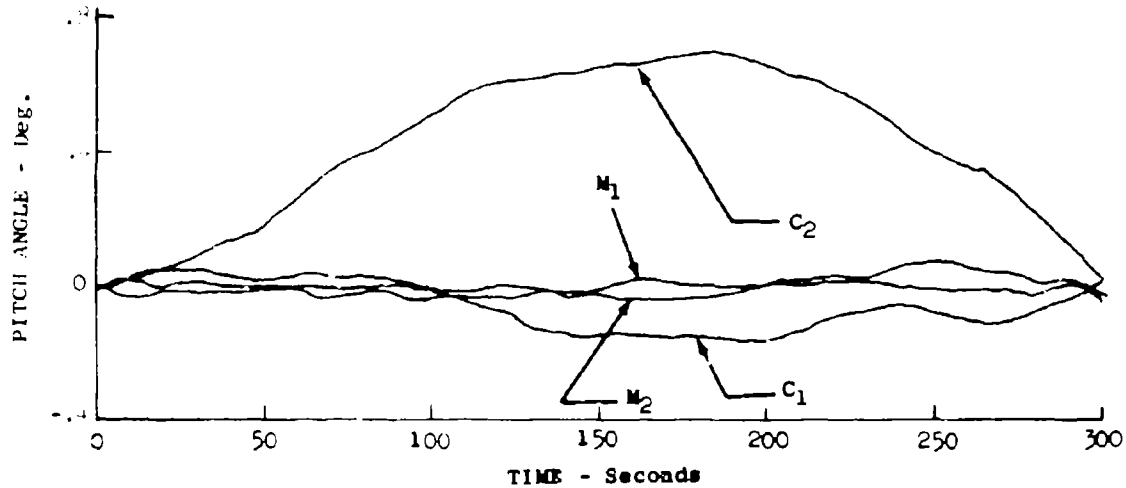


Figure 3.24 Drift in Pitch Angle

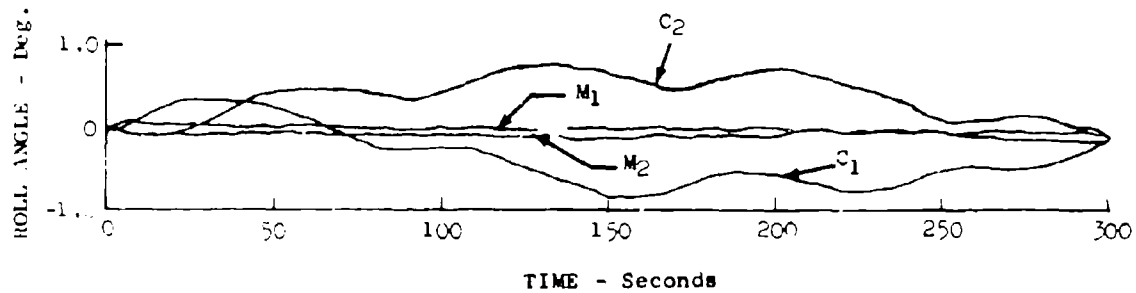


Figure 3.25 Drift in Roll Angle

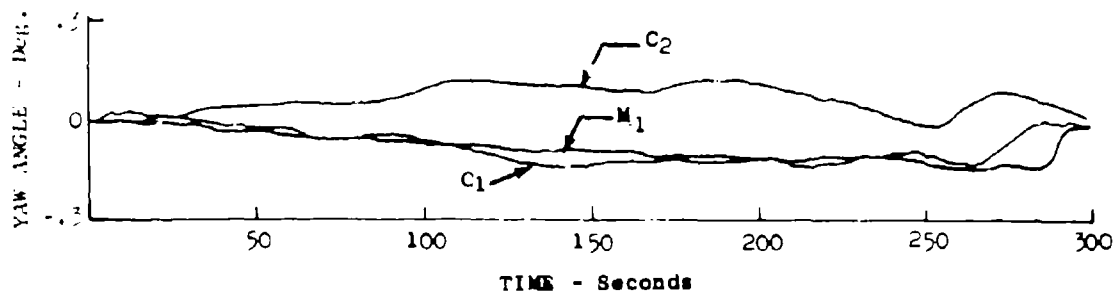


Figure 3.26 Drift in Yaw Angle

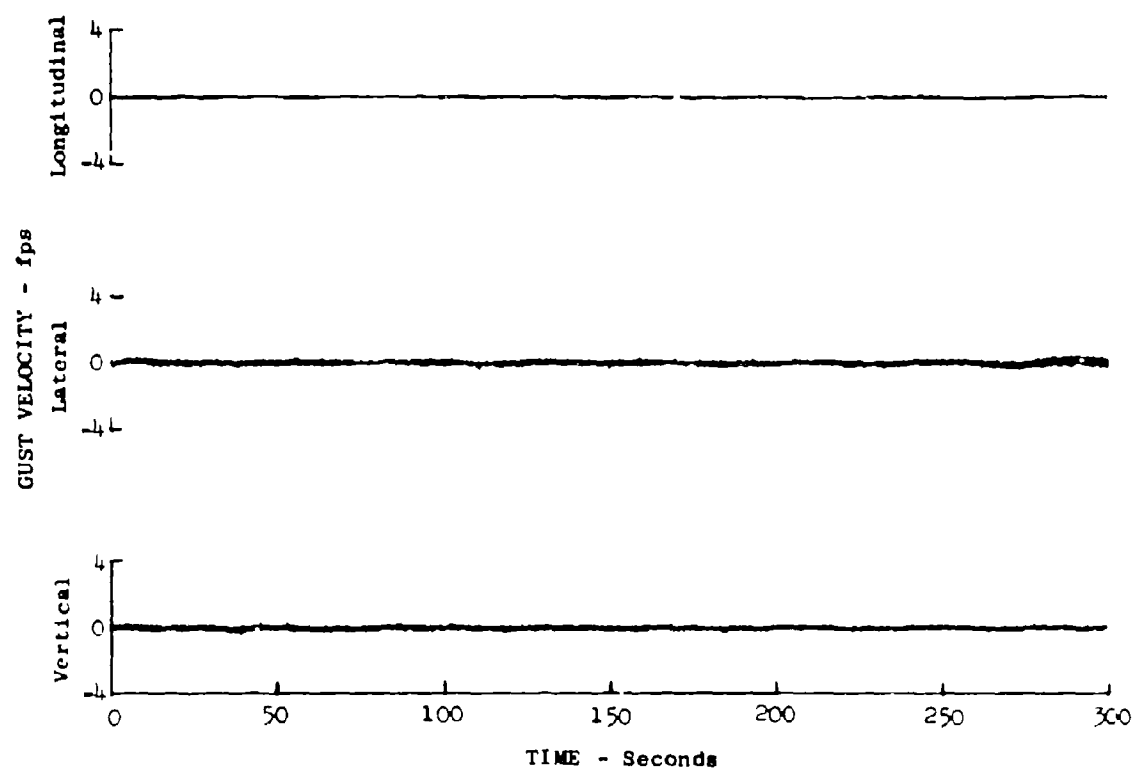


Figure 3.27 Time History of Filtered Drift Data

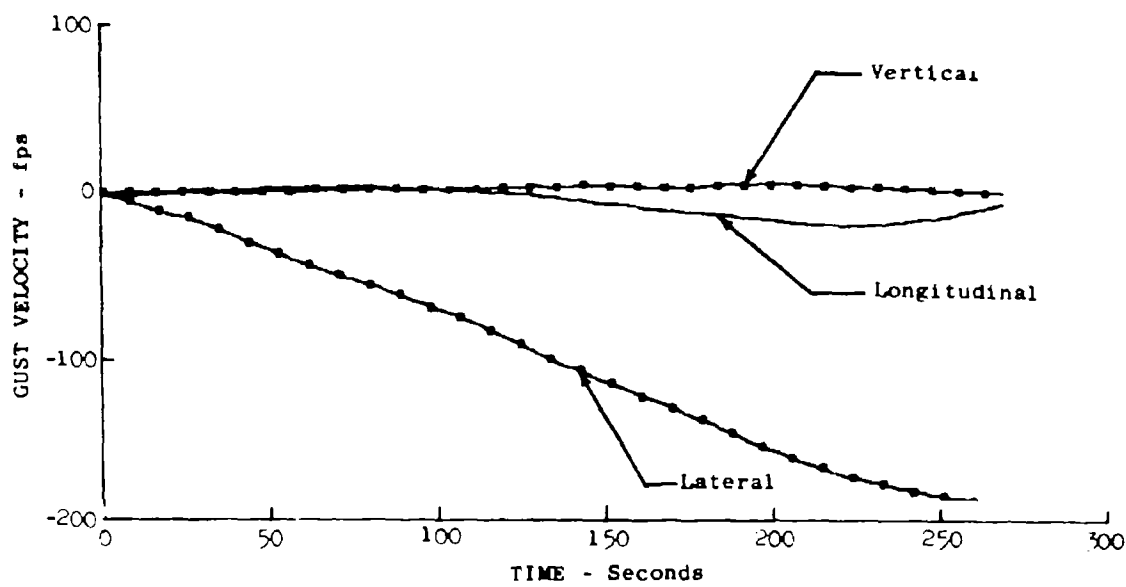


Figure 3.28 Unfiltered Gust Velocity - Smooth Air

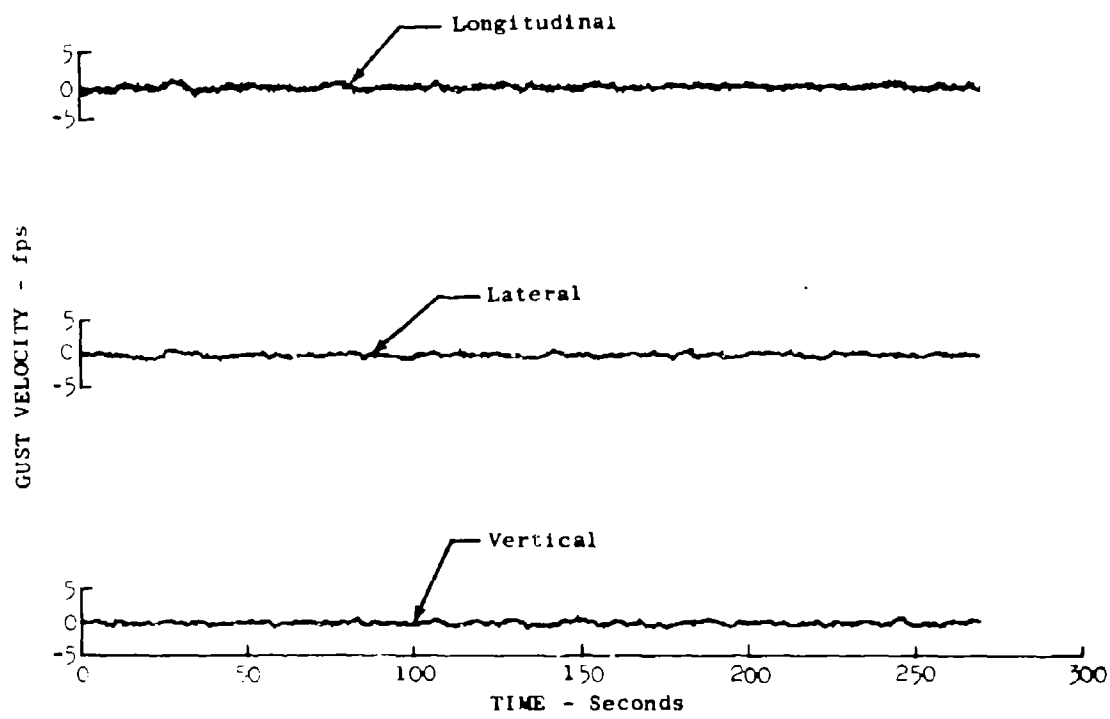


Figure 3.29 Filtered Gust Velocity - Smooth Air

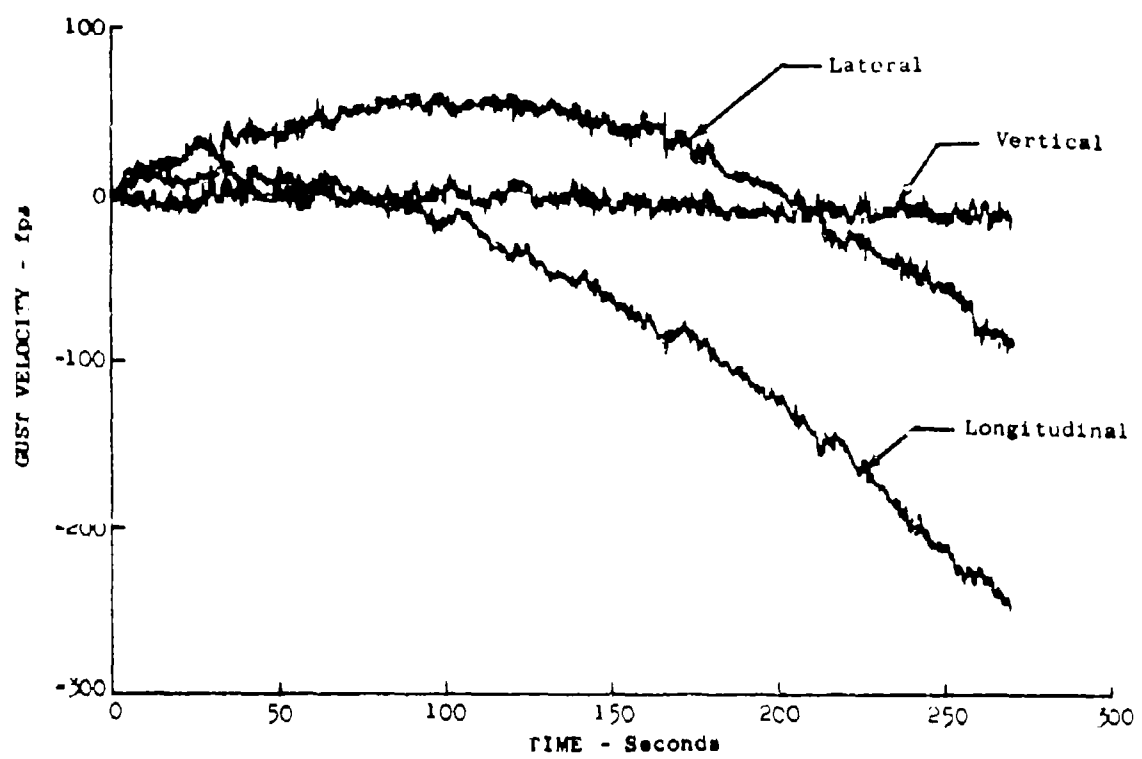


Figure 3.30 Unfiltered Gust Velocity - Turbulence

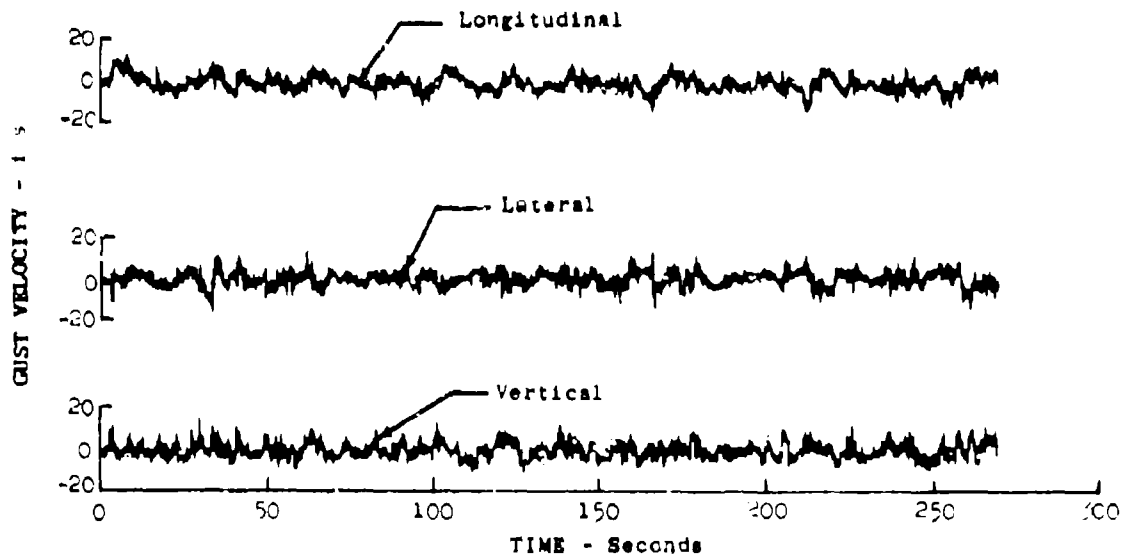


Figure 3.31 Filtered Gust Velocity - Turbulence

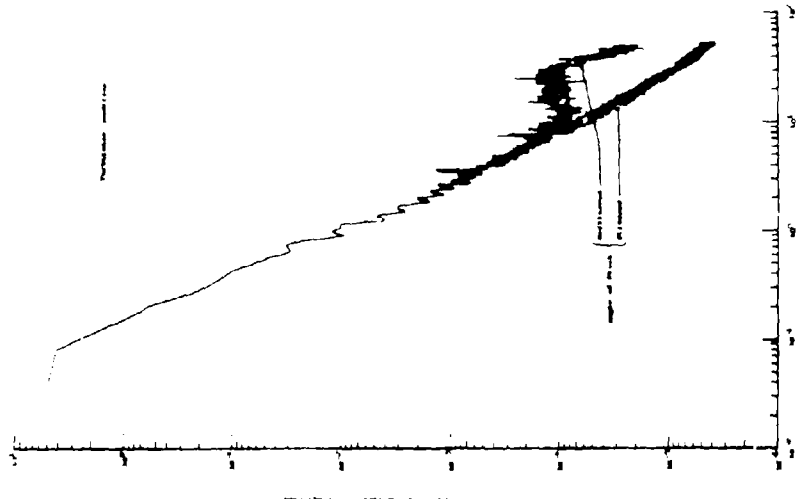


Figure 3.33
Filtered and Unfiltered Measured
Attitude Angle Comparison -
Turbulence

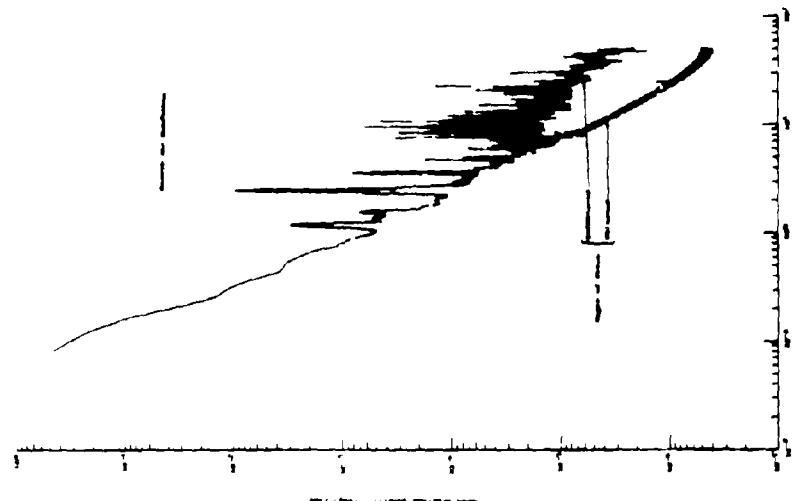


Figure 3.32
Filtered and Unfiltered Measured
Attitude Angle Comparison - Smooth
Air

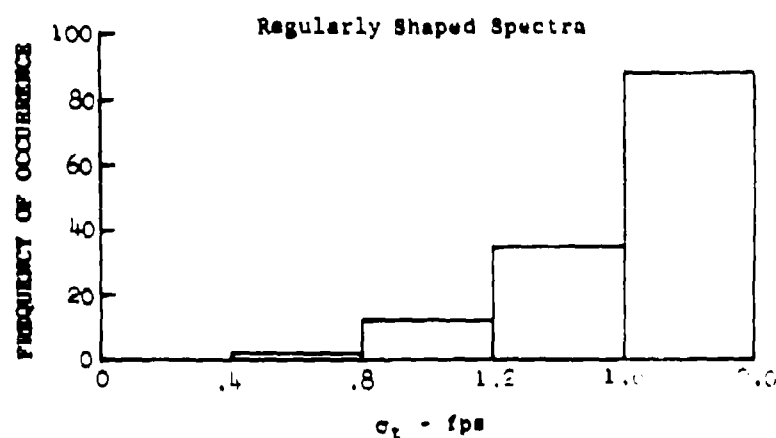
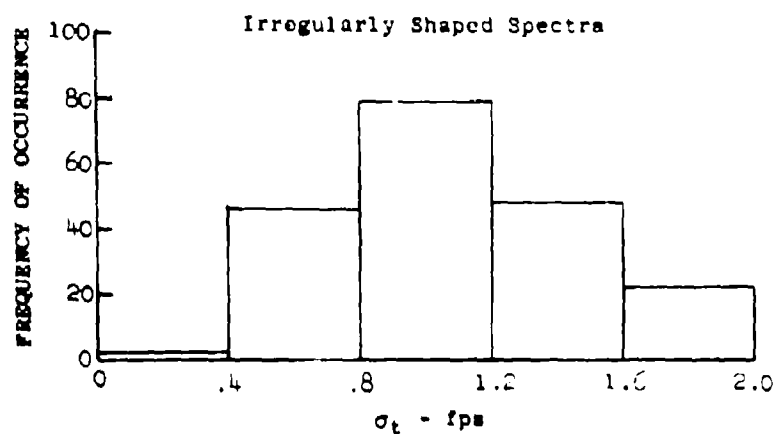


Figure 3.34 Frequency of Occurrence of Irregularly and Regularly Shaped Spectra

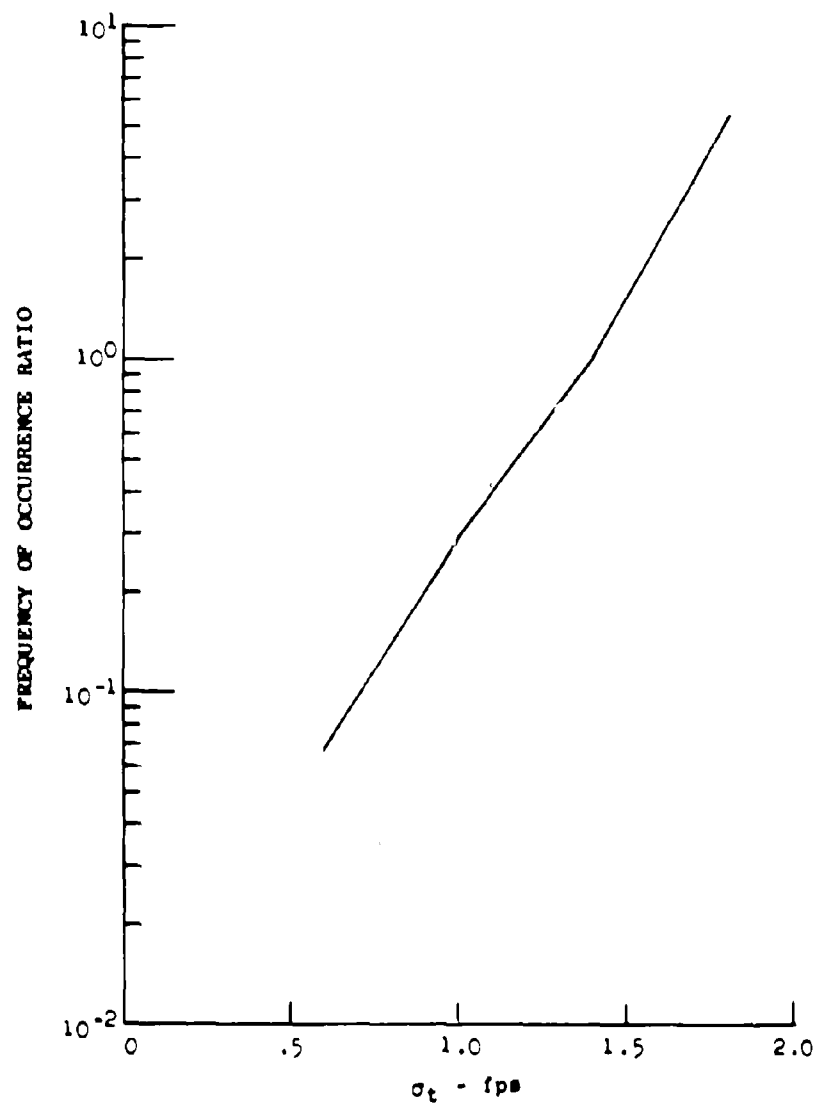


Figure 3.35 Frequency of Occurrence Ratio of Number of Regularly to Irregularly Shaped Spectra

SECTION IV

METEOROLOGICAL DATA ANALYSIS

Meteorological parameters are being recorded to determine their relationship to turbulence. This effort includes development of forecasting models, correlation of observed turbulence and meteorological data, and statistical analysis of certain basic parameters. Global Weather Center (GWC) forecasts are compared to Phase III gust velocity rms values. This report contains Phase III data collected at the McConnell and Edwards Air Force Base locations and selected Phases I and II data.

Three types of meteorological data are being recorded: that recorded by the airplane in flight, that recorded by rawinsonde, and that derived from surface observations. The meteorological data recorded by the airplane are primarily obtained during the surveys performed prior to the recording of each 4.5-minute turbulence sample. During these surveys, air temperature, ground surface temperature, wind speed and direction, absolute and pressure altitude, airplane speed and heading, and pilot comments concerning the state of the atmosphere are recorded. Using the survey data, vertical gradients are determined to define lapse rate, wind shear, and atmospheric stability parameters. Standard Weather Bureau and Air Force rawinsonde observations are utilized whenever applicable; however, the greatest reliance is placed on the special observations provided at each base by the 6th Weather Squadron (Mobile). A Boeing meteorologist at each base of operations provides weather and turbulence forecasts and records pertinent data for subsequent analyses. Flight weather conditions are forecast in cooperation with the Air Force base weather personnel. Hourly surface observations are received by teletype from adjacent first order weather stations and special surface observations are provided by cooperative observers.

A summary of the climatological record during each flight period is given to compare the average observed conditions during the period to the past record (or normal). Records from the nearest U.S. Weather Bureau station were used for this comparison. These stations are located at the Wichita, Kansas Municipal Airport for the McConnell route and at the Kern County Air Terminal, Bakersfield, California, for the Edwards route. The Bakersfield data were not available for this report. McConnell data presented in Fig. 4.1 show the departure of observed data from the normal.

Adverse weather was responsible for cancellation of 14% of the scheduled turbulence sampling at the McConnell route and 30% at the Edwards route.

Selected meteorological data recorded by the airplane instrumentation are listed in the Test Log, Appendix VI. After completion of the program, the rawinsonde observations and the specially prepared large scale synoptic charts for each Phase III flight will be available from the USAF Environmental Technical Applications Center (Data Processing Division) in Asheville, North Carolina.

WIND VELOCITY

The relationship between wind velocity and gust velocity rms values is being investigated (See Section V). In conjunction with this investigation, the variation of wind speed for different geophysical situations is being studied using a statistical approach. This method could be a valuable aid to forecasting wind speeds for low level flights into geographic areas where observations are not available.

The north and east components of airplane measured wind velocities are computed at the rate of 100 times per second, or 27,000 times during a sample. These data are then averaged as follows:

$$\bar{W}_N = \frac{1}{27,000} \sum_{i=1}^{27,000} W_{N,i} \quad (4.1)$$

$$\bar{W}_E = \frac{1}{27,000} \sum_{i=1}^{27,000} W_{E,i} \quad (4.2)$$

From these average wind components, the average wind during the sample is then calculated. The equations for these calculations are shown in Appendix III.

The data are grouped into bands of wind speed, each band having a width of 5 fps. The cumulative probability is plotted versus the lower band limit. The wind analysis includes a total of 741 samples. Of this total, 232 samples were recorded at McConnell and 509 at the Edwards location. For each category presented, a minimum of 30 wind sampler was used for establishing a cumulative probability curve with adequate reliability. Because of the need for a representative number of samples in each category, various combinations of geophysical situations could not be analyzed. However, the data presented here indicate the wind speed trends as they vary with the most pertinent individual category components.

During LO-LOCAT Phases I and II (Reference 1.2), the category components which showed the greatest effects on wind cumulative probabilities were location and season. Effects of altitude above the terrain and time-of-day were also found to be present, but were dependent upon the type of terrain over which the data were obtained and the geographic location.

For the Phase III data, an analysis by both season and location was not made because the two category components are redundant. At McConnell Air Force Base, Kansas, approximately 50 percent of the data were obtained during the summer and only 10 percent during the fall. At Edwards Air Force Base, California, data obtained during the fall accounted for approximately 80 percent of the total. Approximately 20 percent of the Edwards data were obtained during the winter. The cumulative probability of wind speed was not analyzed, therefore, as a function of season. The wind cumulative probability is presented as a function of location in Figure 4.2. As can be seen, the probability of encountering wind of a given speed is greater for the McConnell route than for Edwards. This same result was also found during Phase I and II of the program. In fact, during Phase I and II the highest winds were recorded at McConnell and the lowest at Edwards.

Although the data during Phases I and II were obtained during all four seasons at each location, the McConnell data agree well with the data obtained at that location during Phase III (Figure 4.3). The Phase III winds recorded at McConnell during the summer are of slightly greater magnitude than those recorded during Phases I and II. The wind speeds recorded at Edwards during Phase III are somewhat less than those recorded at that location during Phases I and II (Figure 4.4).

The probability of encountering a given wind speed was higher at 750 feet absolute altitude than at 250 feet for data recorded over the plains (Figure 4.5). For data recorded over the high mountain, low mountain, and desert terrain, there is very little difference in wind speed cumulative probabilities at 750 and 250 feet. These results are shown in Figure 4.6, 4.7, and 4.8. For the data included in this analysis, all of the plains legs are located at the McConnell route and all high mountain, low mountain, and desert legs are located at the Edwards route.

Time-of-day effects on wind cumulative probability are shown in Figure 4.9 through 4.13. For the data recorded over the McConnell route (Figure 4.9), the cumulative probability for a given wind speed is greater at dawn than either mid-morning or mid-afternoon. Winds recorded over the Edwards route showed a different tendency. As during Phases I and II, these wind speeds increased slightly as the time-of-day progressed from dawn to mid-morning to mid-afternoon (Figure 4.10). As shown in Figures 4.11, 4.12, and 4.13, time-of-day did not have as great an effect on wind over any of the terrains of the Edwards route as was observed for the plains data at McConnell.

The variation of wind cumulative probability with atmospheric stability is different for each geographical location. At Edwards (Figure 4.14), the general trend is for the wind cumulative probability to increase for a given wind speed as the atmosphere becomes more unstable. This trend does not appear in the McConnell data (Figure 4.15). For these data, there appears to be very little change in the expected wind speed as the stability changes.

The greatest wind velocities obtained during this part of the program were over the plains. Figure 4.16 presents an overall view of the relative wind speed cumulative probabilities as a function of the terrain over which the data were obtained.

Wind speed and direction are listed in Appendix VI for each gust velocity sample. The corresponding geophysical category for each sample is also listed.

RICHARDSON NUMBER

The following equation is used to calculate the values of Richardson number presented in this report:

$$R = \left(\frac{g}{T_s} \right) \frac{(F_q - \Delta T / \Delta H)}{(\Delta W / \Delta H)^2} \quad (4.3)$$

Probabilities of encountering given gust velocity rms values were determined for each of 20 bands (0.6 wide) of Richardson number from -2.0 to +10.0. Approximately 11 percent of the Richardson number values were greater than +10, and 2 percent were less than -2. They were not included for this analysis. The data analyzed are presented in Figures 4.17 through 4.19. The gust velocity rms values having 80 percent probability of occurrence were plotted versus mid-band Richardson number (Figure 4.20). This figure compares Phase I and II to the Phase III data and indicates that the probability of occurrence of a given rms level is greater for the Phase III data at equivalent Richardson number values. These data are consistent with the higher rms gust velocities being recorded during Phase III because of the increased airspeed of the T-33A airplane compared to the C-131B airplanes.

The data presented here for Richardson number statistics must be considered preliminary because of the small number of turbulence samples, and their distribution in the Richardson number bands. The number of data points in each Richardson number band should be at least 30 for a good statistical sample. For this interim report, only the three bands from -0.2 to +1.6 contained over 30 data points.

SAMPLING SITES

Hourly surface observations and rawinsonde soundings provide data used to support the LO-LOCAT Phase III flights. Special rawinsonde soundings are being provided by the USAF Sixth Weather Squadron (Mobile). These special soundings, which are being provided for each flight, include soundings from the surface to 500 mb (400 mb at McConnell). Additionally, they are providing the pressure, temperature, dew point, and wind velocity at levels of 250, 750, and 1,000 feet above the ground. The balloon is underinflated so as to rise at the rate of 500 feet per minute. Azimuth and elevation data are recorded every 30 seconds. Whenever available, standard rawinsonde observations from nearby fixed installations are also being recorded.

Cooperative observers in the vicinity of each route are asked to provide additional observations. The observers are provided with sling psychrometers, thermometers, hand-held anemometers, observing guidelines, and special recording forms. They provide wet and dry-bulb temperatures, surface winds, and visual observations of cloud cover, dust devils, and precipitation.

Meteorological information derived from debriefing of the pilot is also recorded.

McConnell Air Force Base, Kansas - 15 August 1968 to 25 September 1968

For the McConnell route, the mobile rawinsonde was located at Cedar Vale, Kansas, which is approximately equidistant from all the flight legs. Since all the flight legs were over plains, one sounding was considered representative of a given flight. Hourly surface observations were obtained from Wichita, Chanute, and McConnell Air Force Base, Kansas, and Ponca City, Oklahoma. Weather radar reports were available continuously from McConnell Air Force Base and hourly from the Wichita Weather Bureau. Periodic observations were received from Bartlesville, Oklahoma. Six cooperative weather observers volunteered to participate in the program, located as shown in Figure 2.7. Surface wind data were available on call from the TITAN II missile sites near legs 1, 2, 7, and 8.

Edwards Air Force Base, California - 8 October 1968 to 8 January 1969

The mobile rawinsonde site was first located about six miles north of Oxnard Air Force Base, California, on 8 October 1968 and was later removed to Oxnard Air Force Base on 22 October 1968. Edwards Air Force Base also provided special rawinsonde soundings for each flight (prior to 23 October 1968, only wiresonde observations were provided). In addition to these special observations, the routinely provided rawinsonde data from Vandenberg Air Force Base, California, for 0400, 1000, and 1600 PST were analyzed to assist in characterizing the upper air situation. The terrain in the overall test area is so complex that it would have taken several mobile rawinsonde sets to obtain representative soundings for all the flight legs. However, this was not feasible for budgetary reasons. Hourly surface observations were obtained from the first order weather station shown on Figure 2.8. Only one cooperative observer (located at Juncal Dam) participated in the program.

FORECASTING TECHNIQUES

Subjective Forecasting Techniques

The Second Weather Squadron at Offutt Air Force Base, Nebraska, Global Weather Center, provided special low-level turbulence forecasts for the Phase III LO-LOCAT flights. These forecasts were based on forecast values of the vertical wind shears, wind speeds from the surface to 1,000 feet, pressure changes, and a value for terrain type. Forecasts were prepared for each type of terrain and specifically for the dawn, mid-morning, and mid-afternoon flights. The forecast consisted of a nondimensional number corresponding to a specific degree of turbulence as follows:

<u>GWC Numerical Forecast</u>	<u>Expected Turbulence</u>
Less than 80	No Turbulence
80 to 119	Light Turbulence
Greater than or equal to 120	Moderate Turbulence

An evaluation of the GWC turbulence forecast was performed by computing the correlation of GWC numbers to observed gust velocity rms values. The correlation was computed for the general case (all values) by using regression analysis with inputs of either linear (L) or squared (S) terms. The resulting correlation coefficients are listed in Table 4.1, a value of zero indicating no correlation and a value of 1.0 perfect correlation. The mean error between the actual gust velocity rms and that predicted from the regression equation is listed in Table 4.1. Also listed are the errors for regression equations of rms values greater than a selected threshold value, which is of interest in defining how well the forecast predicts only the higher rms values. The best forecasts are shown to have been made for the plains terrain with errors of as much as 42 percent in some other categories.

Another forecasting tool, the Showalter stability index, was compiled for each flight and the same type of regression analysis performed as was done for the GWC forecasts. This index is an indication of either a stable or unstable atmospheric condition between the 850 to 500 mb level. The results are shown in Table 4.2 and indicate that the Showalter stability index is poorly correlated with the gust velocity rms values.

For comparison, Table 4.3 lists the results of regression analysis equations to evaluate Richardson number as a forecast tool. The errors are quite large and the correlation coefficients are near zero.

The evaluations represented by Table 4.1 through 4.3 emphasize the difficulty being experienced in the forecasts of low level turbulence. These results indicate the importance of the need for improved methods and procedures in the performance of low level turbulence forecasting, and in evaluating forecasting techniques.

TABLE 4.1
EVALUATION OF GWC FORECASTS (PHASE III)

Vertical rms Gusts					
Terrain	Input Terms (L or S)	Correlation Coefficients	Overall Error (%)	Error Above Threshold (%)	rms Threshold (fps)
High Mountains	L	-0.0505	40.00	34.18	4.5
Low Mountains	S	0.1981	40.82	46.36	4.0
Desert	L	0.3039	47.36	47.36	2.5
Plains	L	0.6285	31.00	20.00	4.0

Lateral rms Gusts					
Terrain	Input Terms (L or S)	Correlation Coefficients	Overall Error (%)	Error Above Threshold (%)	rms Threshold (fps)
High Mountains	S	0.0447	30.21	19.07	4.5
Low Mountains	L	0.2974	30.63	16.81	4.0
Desert	L	0.4581	30.13	29.79	2.5
Plains	L	0.6087	27.26	14.77	4.0

TABLE 4.2
EVALUATION OF SHOWALTER INDEX (PHASE III)

Vertical rms Gusts					
Terrain	Input Terms (L or S)	Correlation Coefficients	Overall Error (%)	Error Above Threshold (%)	rms Threshold (fps)
High Mountains	S	-0.0865	39.80	35.14	4.5
Low Mountains	L	0.1372	43.92	45.27	4.0
Desert	L	-0.0428	57.93	57.93	2.5
Plains	S	-0.2964	41.06	32.43	4.0

Lateral rms Gusts					
Terrain	Input Terms (L or S)	Correlation Coefficients	Overall Error (%)	Error Above Threshold (%)	rms Threshold (fps)
High Mountains	S	-0.0657	30.11	35.14	4.5
Low Mountains	L	0.2023	31.02	49.15	4.0
Desert	L	-0.0663	31.98	31.98	2.5
Plains	S	-0.3384	34.33	36.27	4.0

TABLE 4.3
EVALUATION OF RICHARDSON NUMBERS (PHASE III)

Vertical rms Gusts					
Terrain	Input Terms (L or S)	Correlation Coefficients	Overall Error (%)	Error Above Threshold (%)	rms Threshold (fps)
High Mountains	L	-0.1790	33.73	44.25	4.5
Low Mountains	L	-0.0540	44.08	46.02	4.0
Desert	L	-0.1508	56.97	34.29	2.5
Plains	S	-0.3344	44.59	36.0	4.0

Lateral rms Gusts					
Terrain	Input Terms (L or S)	Correlation Coefficients	Overall Error (%)	Error Above Threshold (%)	rms Threshold (fps)
High Mountains	L	-0.1683	26.39	34.62	4.5
Low Mountains	L	-0.0726	31.38	37.96	4.0
Desert	L	-0.1206	31.89	31.39	2.5
Plains	L	-0.3292	36.49	34.81	4.0

McConnell Air Force Base, Kansas

Turbulence forecasting at McConnell Air Force Base was accomplished using guidelines of the Air Weather Service Manual 55-8, Volume 1. The forecasts were primarily based upon the intensity of the surface winds, the vertical wind shear from the surface to 1,000 feet above the ground, and the type of convective clouds observed or forecast for the period of a given flight. For wind shears of 3 to 5 knots per 1,000 feet, light turbulence was forecast; 6 to 9, moderate; and 10 or higher, severe. For surface winds greater than 15 knots but less than 25, light turbulence was forecast if the air was neutrally stable or unstable. Similarly, moderate turbulence was forecast for winds greater than 25 knots. When cumuliform clouds were forecast, the following turbulence was forecast in that vicinity: fairweather cumulus, light turbulence; thunderstorms or towering

cumulus, moderate; mature or rapidly growing thunderstorms, severe; and severe thunderstorms, extreme turbulence. The forecast turbulence level compared to the pilot's estimate of the turbulence (Tables 4.4 through 4.7) indicates that of the methods used, wind shear (Table 4.4) was the best indicator. The tendency to underestimate at lower turbulence levels, and overestimate at higher levels, is evident.

TABLE 4.4

TURBULENCE FORECAST USING WIND SHEAR (SURFACE-1000')

FORECAST	OBSERVED BY PILOT			
	NONE	LIGHT	MODERATE	SEVERE
NONE	1	12	4	0
LIGHT	4	2	0	0
MODERATE	5	4	1	0
SEVERE	3	4	0	0

TABLE 4.5

TURBULENCE FORECAST USING WIND SPEED

FORECAST	OBSERVED BY PILOT		
	NONE	LIGHT	MODERATE
NONE	14	19	4
LIGHT	0	6	1
MODERATE	0	0	0

TABLE 4.6
TURBULENCE FORECAST USING CONVECTIVE CLOUD TYPE

FORECAST	OBSERVED BY PILOT	
	LIGHT	Moderate
LIGHT	3	1
Moderate	3	0

TABLE 4.7
TURBULENCE FORECAST CONSIDERING MAXIMUM
VALUE FROM WIND SHEAR, SURFACE WIND, OR
CONVECTIVE CLOUD TYPE.

FORECAST	OBSERVED BY PILOT			
	NONE	LIGHT	Moderate	SEVERE
NONE	1	12	13	0
LIGHT	4	4	1	0
Moderate	5	6	1	0
SEVERE	3	4	0	0

Edwards Air Force Base, California

Turbulence occurrences from leg to leg for a given flight varied considerably. During the period from 8 October 1968 to 8 January 1969, atmospheric conditions in the area were characterized as stable, except for brief occurrences of post-frontal instability; however, showers and low clouds over the mountains usually prevented flights during these times.

The most useful subjective forecasting aid for turbulence over the flight legs was wind direction and speed in relation to the terrain covered by each leg. Particularly useful in determining low-level wind conditions from the surface to about 2,000 feet above the terrain were upper-air soundings from Vandenberg Air Force Base, Oxnard Air Force Base, and Edwards Air Force Base, and surface observations from Sandberg, California. Sandberg was the only observing station which reported wind velocities in the mountains.

The turbulence occurrences appeared to be highly related to terrain. The pilot observed that the most severe encounters occurred near the higher peaks of legs 3 and 5. For this reason, the subjective techniques are categorized by flight leg.

- Legs 1 and 8: The pilot reported that any low altitude wind speed over 10 knots normally produced at least light turbulence over these legs. A low-altitude wind direction from west-southwest through north-northwest or from east-northeast through south-southeast with speeds in excess of 25 knots resulted in moderate or greater turbulence. On several occasions, turbulence was encountered over the desert to the southeast of the mountains in an apparent lee wave effect.
- Legs 2 and 7: Turbulence was reported on only a few flights over these legs. The low altitude flight path above the valley floor was apparently somewhat sheltered, even from possible effects of strong northerly winds down the valley.
- Legs 3 and 5: The most severe turbulence encounters occurred on these legs. From a forecast standpoint, any low altitude wind speed over 10 knots resulted in reports of at least light turbulence by the pilot over one of the legs. A low altitude wind direction from northwest through northeast or from southwest through southeast, accompanied by speeds in excess of 25 knots, resulted in moderate or greater turbulence. An interesting feature is that the reported turbulence occurred in a different position relative to the terrain, depending on the wind direction. The position of the hardest strikes was generally to the lee of a major terrain feature.
- Leg 6: Turbulence was reported by the pilot on this leg less often than on legs 3 and 5. In general, low altitude wind speeds of 20 knots or more produced at least light turbulence on this leg.
- Leg 4: Turbulence was rarely reported on this leg over the coastal water. Occasions on which light turbulence was reported over this leg were associated most often with a strong offshore pressure gradient and strong Santa Ana wind channeled down the Santa Clara River Valley.

Major emphasis was placed on the low altitude wind from the surface to about 2,000 feet above the surface, since this appeared to be a key factor related to reports of turbulence. From a forecast standpoint, low altitude wind in both direction and speed must be forecast over the flight area from available soundings and observations prior to the turbulence forecast. Understanding of synoptic conditions and resulting wind conditions is useful in this regard, but this was not attempted since it involves, essentially, a case study approach. Given an accurate low altitude wind velocity forecast for the seasonal period of Phase III LO-LOCAT flights, one can, through terrain considerations, prepare a subjective low altitude turbulence forecast.

Objective Forecasts

The objective forecast models being developed are based on multiple regression analysis (Section V and Appendix III). Because most models developed use the gust velocity rms as the dependent variable, an analysis of maximum gust velocities was conducted to determine if a turbulence index based on maximum gust velocity could prove more significant. It was found that the maximum gust velocities occurred frequently over the same legs of a particular course. This indicates that

some local terrain feature or combination of terrain feature and wind pattern was responsible for the maximum gusts. For instance, legs 7 and 8 at Edwards AFB (Phases I and II routes) were subject to highly localized lee wave turbulence under certain stability and wind conditions, whereas the remaining legs would have light or no turbulence. Therefore, only the gust velocity rms values are being evaluated to develop forecast models. It was also determined that the lower rms values are present so often that they constitute a form of "noise", and as such correlate poorly with the forecast data. In a case study of twelve of the highest rms values for each base, for example, it was found that variables such as vertical wind shear and Richardson number were better indicators of turbulence than when all of the data were used in this regression analysis. Therefore, it was decided to eliminate the lower gust velocity rms values from the Phases I and II data. Analysis indicated that 240 fps was a suitable cutoff point for all but the water leg. The small amount of data precluded the possibility of eliminating the lower gust velocity rms values for this leg. All the Phase III data will be retained since there are fewer data than was the case with Phases I and II.

The input variables used in the regression analysis are tabulated in Appendix III.

CASE STUDIES, PHASES I AND II

Case Studies of Phases I and II data have been completed for the twelve highest vertical gust velocity rms values from each of the four bases. Although rms gust velocities have quite a limited range, the maximum vertical gust velocities for these flights range from about 16 to 50 fps, with an average of about 27 fps. No consistent synoptic pattern could be discerned.

The most striking features noted were the vertical wind shears. The low-mountain legs had an average wind shear of 3.29 knots per 100 feet; for high mountains and plains, the values are 1.94 and 1.53 knots per 100 feet, respectively.

The next most consistent feature is the low value of the Richardson numbers. For the low mountain legs, the Richardson number (R) never exceeded 0.015. The R over the high mountain legs are small negative values, with the exception of one case where it is plus 0.49. Over the plains there is less consistency: there is a high value of 2.42, three values between one and two, one value between one-half and one, and seventeen values less than one-half.

The mountain legs have higher vertical gust velocity average rms values than do the plains legs (high mountains 6.59 fps; plains 4.94 fps). The lowest gust velocity rms value over the mountains is also higher than the average for the plains. These same relationships also hold true for the maximum vertical gust velocities (average: high mountains 33.49 fps; low mountains 32.31 fps; plains 21.81 fps).

There is some tendency for these high vertical gusts to occur during the spring season. Over the plains, this is true for 16 out of 26 cases; over the low mountains, it is true for 6 out of 14 cases.

A diurnal trend appears only for the plains legs: mid morning and afternoon flights account for 24 out of the 26 cases. This could be the result of convective activity, especially since the sine of the solar elevation is greater than 0.55 for these 24 cases. However, the high wind shears recorded for these cases and the fact that unstable lapse rates are in the minority indicate that convective activity is not responsible for the diurnal trend.

It is probably a coincidence that the ratio of the average wind speeds for the mountains and plains is fairly close (1.40 versus 1.33) to the ratio of the respective average gust velocity rms values. Over the plains, the range of wind speeds (3 to 35 knots) combined with the low average value (15 knots) suggest that, for these flight samples at least, wind speed by itself is not causally related to high rms gusts. Over the mountains, the average wind speeds (21 knots) is submarginal for producing full scale lee waves; however, this is high enough to produce mechanical turbulence. The higher winds (up to 30 knots) could of course produce lee waves given the proper stability profile and terrain orientation.

An example case study follows. This case was chosen because five out of a total of twelve large gust velocity rms values occurred on the same day. In addition, a maximum gust velocity of 50 fps was recorded.

Edwards Air Force Base (13 December 1967)

General Synoptic Situation

An extensive and intense high pressure area was centered over British Columbia with a ridge line extending southward into California. A low pressure area was located south of the flight route as shown in the surface analysis for 1500 GMT in Figure 4.21. This synoptic pattern is frequently associated with Santa Ana winds, (relatively strong, warm and dry off-shore winds observed along the southern California coast). A fast-moving cold front had passed through the area the previous night, bringing very dry air. The cold front then became stationary for several hours near the Mexican border (see Figure 4.21). Throughout the flight route area (outlined by dotted lines) the surface pressure gradient gradually increased and therefore, the winds were expected to increase. The surface winds, which varied in direction from northwest to northeast, were considerably influenced by topography. The temperature pattern isotherms of 5° C are represented by the dashed lines and was similarly strongly influenced by topography. Figure 4.22 shows the surface conditions at 1800 GMT.

The synoptic patterns at 850 mb for 0000 and 1200 GMT are shown in Figure 4.23 and 4.24 where the pressure-height gradient is not unusual. The flow as represented from vertical soundings is northeasterly in contrast to the more easterly flow suggested by the pressure gradient. At this height (about 2500 feet above lowest ground), the effects of terrain are still present. Low pressure at both the 850 and 700 mb levels was centered over San Diego.

Dawn Flight

Turbulence was encountered over legs 6, 7 and 8, with maximum vertical gusts of 50 fps over legs 7 and 8. Neutrally stable air and scattered clouds existed over the route. Winds at flight altitude were 20 knots over leg 6 and 28 knots over leg 7. Legs 6 and 7 lie over the Santa Clara River valley directly in the lee of the coastal mountains. Without consulting a radiosonde sounding, it cannot be known that lee waves were present in the valley. However, the flow at 850 mb, corresponding approximately to the heights of the mountains, was about 35 knots. This is more than adequate for the generation of lee waves if a stable layer is present at higher levels. This could explain the difference of 20 fps in the maximum gust velocity over legs 6 and 7. Leg 8 lies partly in the same valley so that lee waves could also be experienced there. Leg 8 also crosses part of the mountain range making it vulnerable to lee effects from some of the higher isolated peaks.

The wind shears were 1.4 knots per 100 feet over leg 6 and 1.3 over leg 7. The Richardson numbers were small and negative.

Mid-Morning Flight

Turbulence was encountered over legs 7 and 8, with maximum vertical gusts of 50 fps on leg 7. Unstable lapse rates were recorded. Winds at flight altitude were 22 knots over leg 7 and 28 knots over leg 8. Wind shears were 2.6 knots per 100 feet over leg 7 and 2.3 over leg 8. The Richardson numbers were small and negative.

CASE STUDIES, PHASE III

Edwards Air Force Base (13 November 1968)

General Synoptic Situation

Figures 4.25 and 4.26 show the surface synoptic analysis for 1500 and 1800 GMT, respectively. Through this three-hour time period in which the flights were conducted, very little variation was noted in the synoptic pattern. A large high pressure system was centered in the eastern Pacific Ocean at 37°N and 135°W from which a broad ridge extends eastward into Oregon and towards Colorado. A minor ridge was observed to develop through central California and south towards Yuma, Arizona. The effects of this ridge were noticed in a generally high pressure gradient through the flight area. Winds through this area were mostly from the north to east and increased through the time period from 8 to 10-15 knots. The temperature pattern shown by the dashed isotherms was generally influenced by the topographical variation in surface heights.

Aloft at 850 mb for 0000 and 1200 GMT as indicated in Figures 4.27 and 4.28 a low pressure center occurred over the southern California border. This was associated with a surface low pressure cell and frontal system which extended through Arizona. Winds at 850 mb through the flight area were north to northeast. During the 12-hour period presented, little change was observed in the pattern of pressure-heights through the flight area. At 500 mb, a broad trough having a north-south axis along the coastal states intensified during the 12-hour period examined. Such development is generally reflected in a slow-down of movement of surface systems.

Mid-Morning Flight

Stable and relatively dry atmospheric conditions prevailed over the flight legs in Test No. 87. The pilot reported moderate to severe turbulence over legs 3 and 5 with the hardest strikes occurring to the lee of major terrain features. The north winds, in some local cases exceeding 25 knots at flight altitudes, are approximately crossing the coastal mountains. Considerable variation was observed between the wind directions and speeds observed over individual legs, and it was concluded that this variation is closely correlated with the resulting turbulence. Legs 3 and 5 have the largest wind speed components along or against the wind, respectively, which when combined with the cross-ridge effects contributes to the resulting rms gust velocities observed of 11.46 and 8.50 feet per second. This compares with rms gusts less than 3.5 feet per second in the other legs of this flight. It is interesting to note that flight along leg 4 resulted in the lowest rms gust velocity of this test (1.24 fps). This leg is essentially parallel to and in the lee of the coastal ridge but out over the water. It must be concluded that the terrain perturbations of the winds do not extend nor travel far downwind under this synoptic pattern.

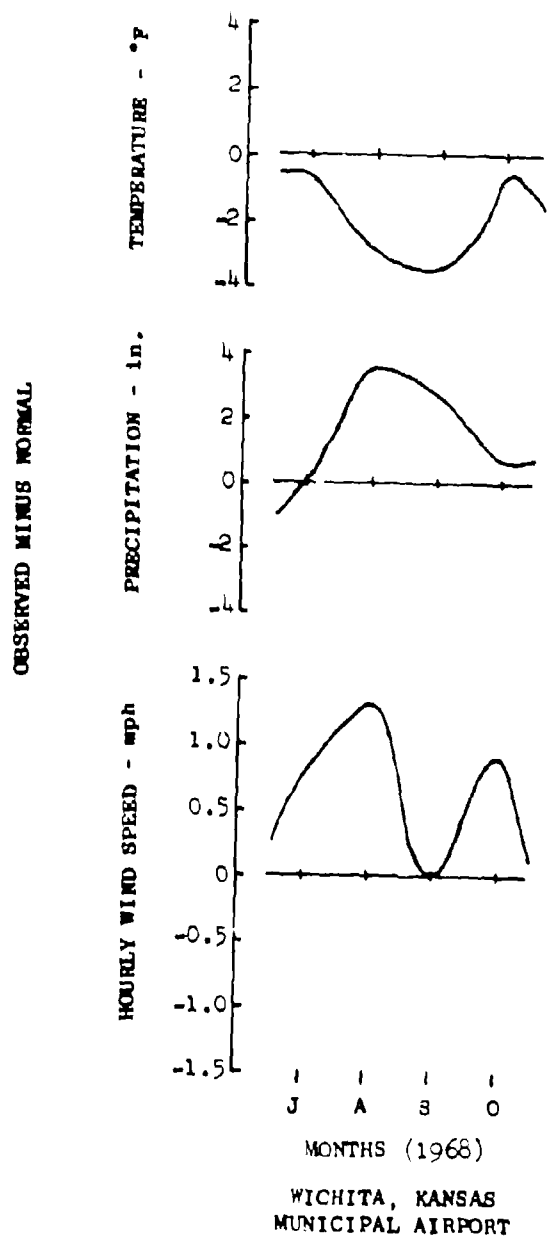


Figure 4.1 Climatological Variances for McConnell Route

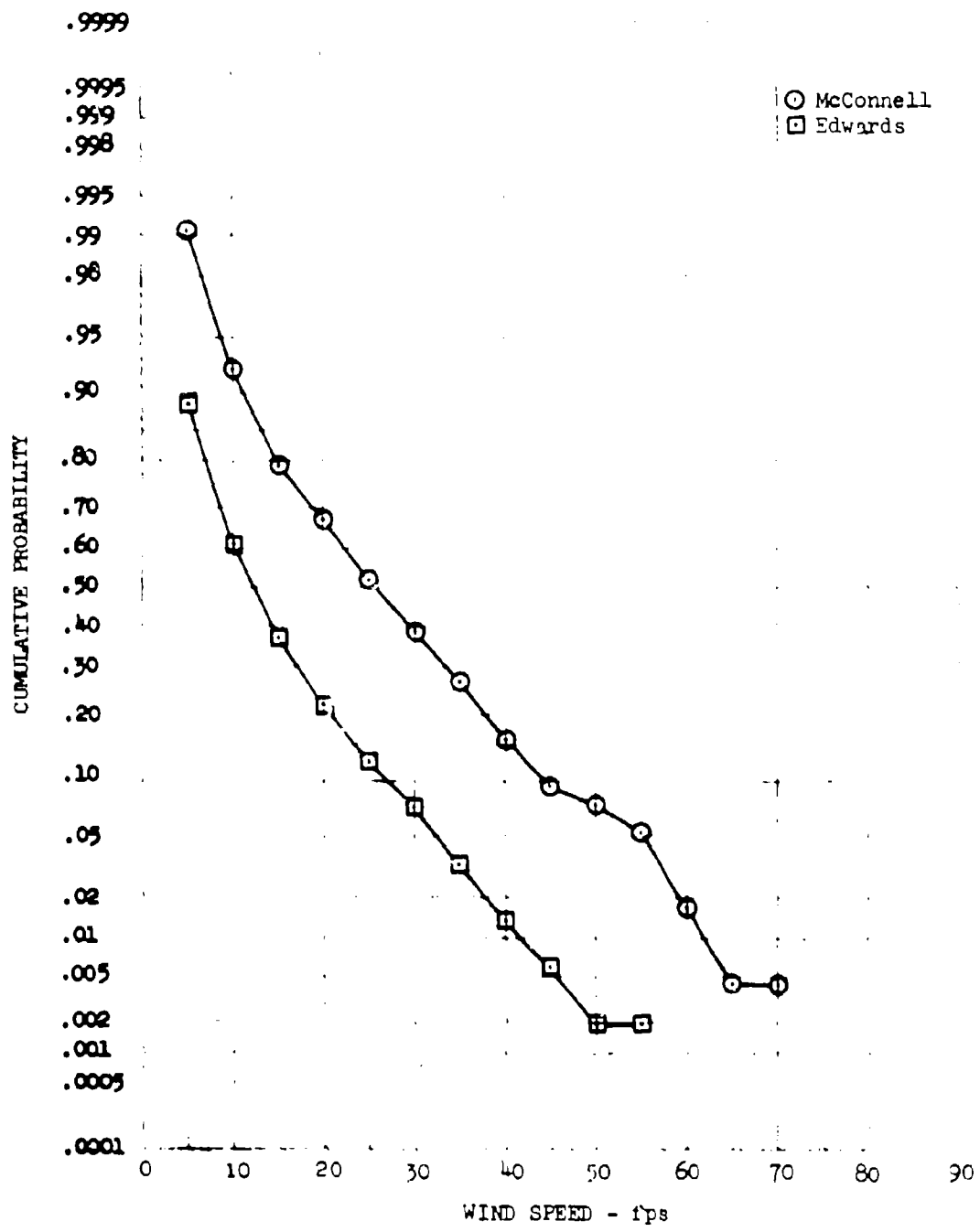


Figure 4.2 Wind Speed Cumulative Probability Associated with Location

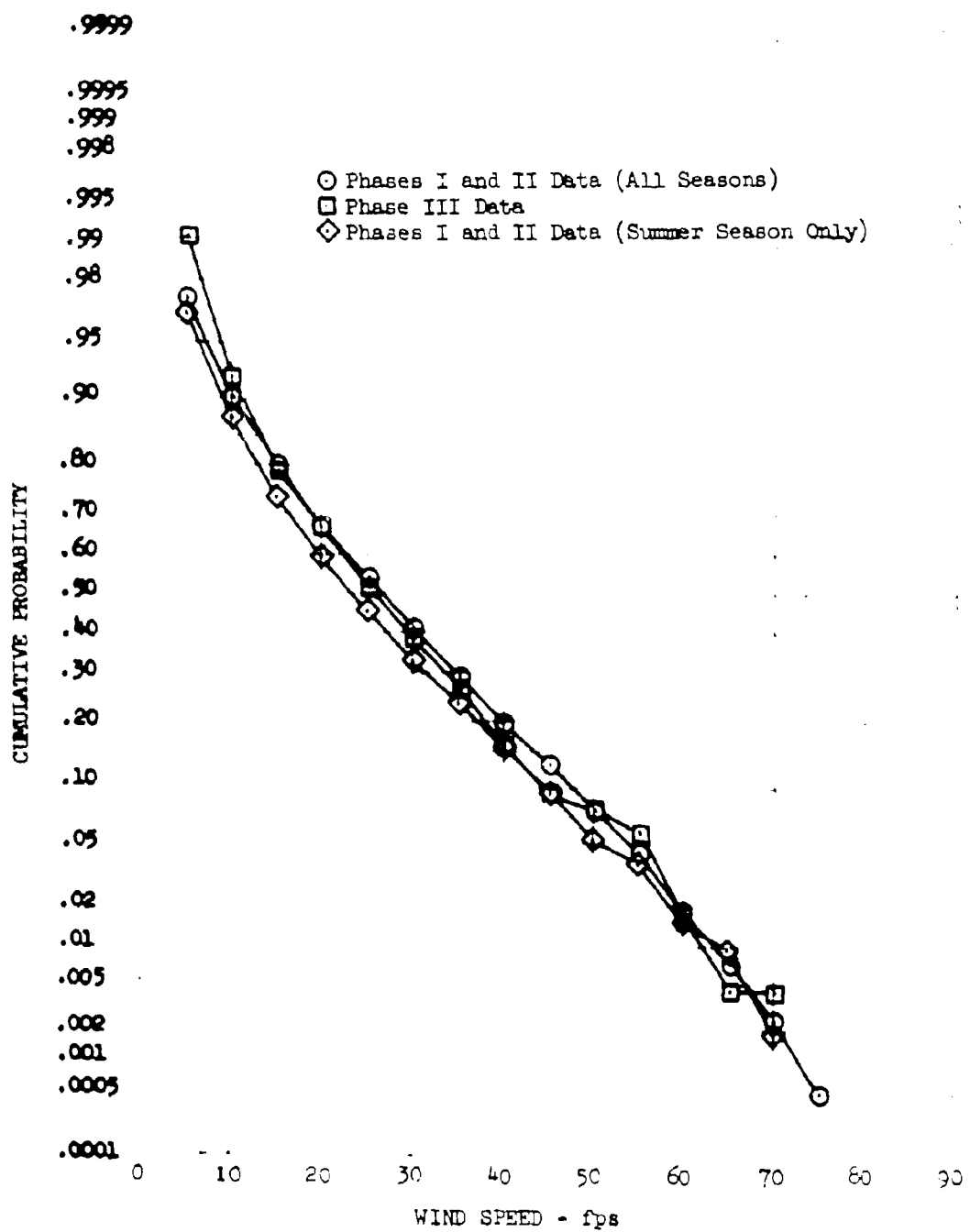


Figure 4.3 Wind Speed Cumulative Probability at McConnell

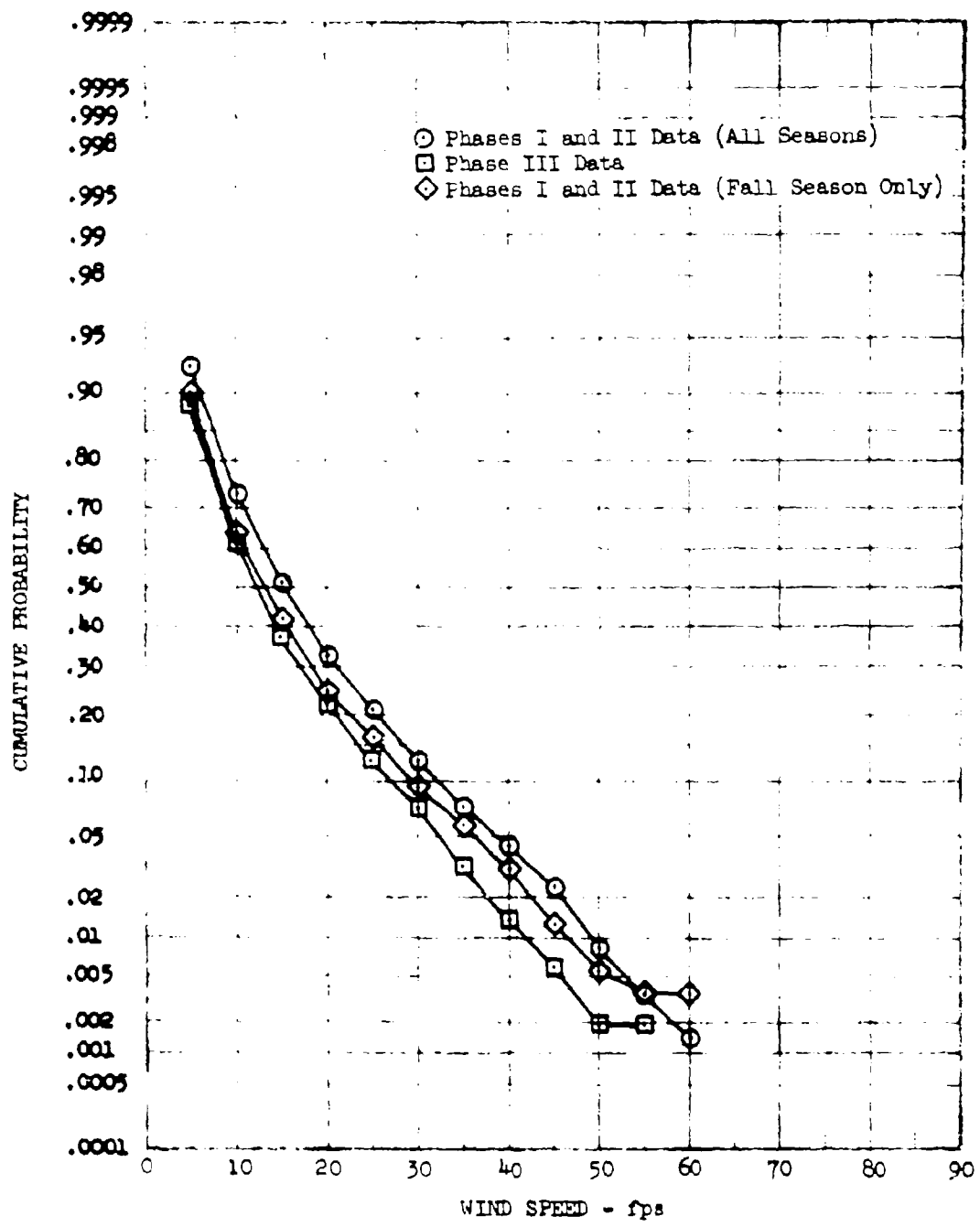


Figure 4.4 Wind Speed Cumulative Probability at Edwards

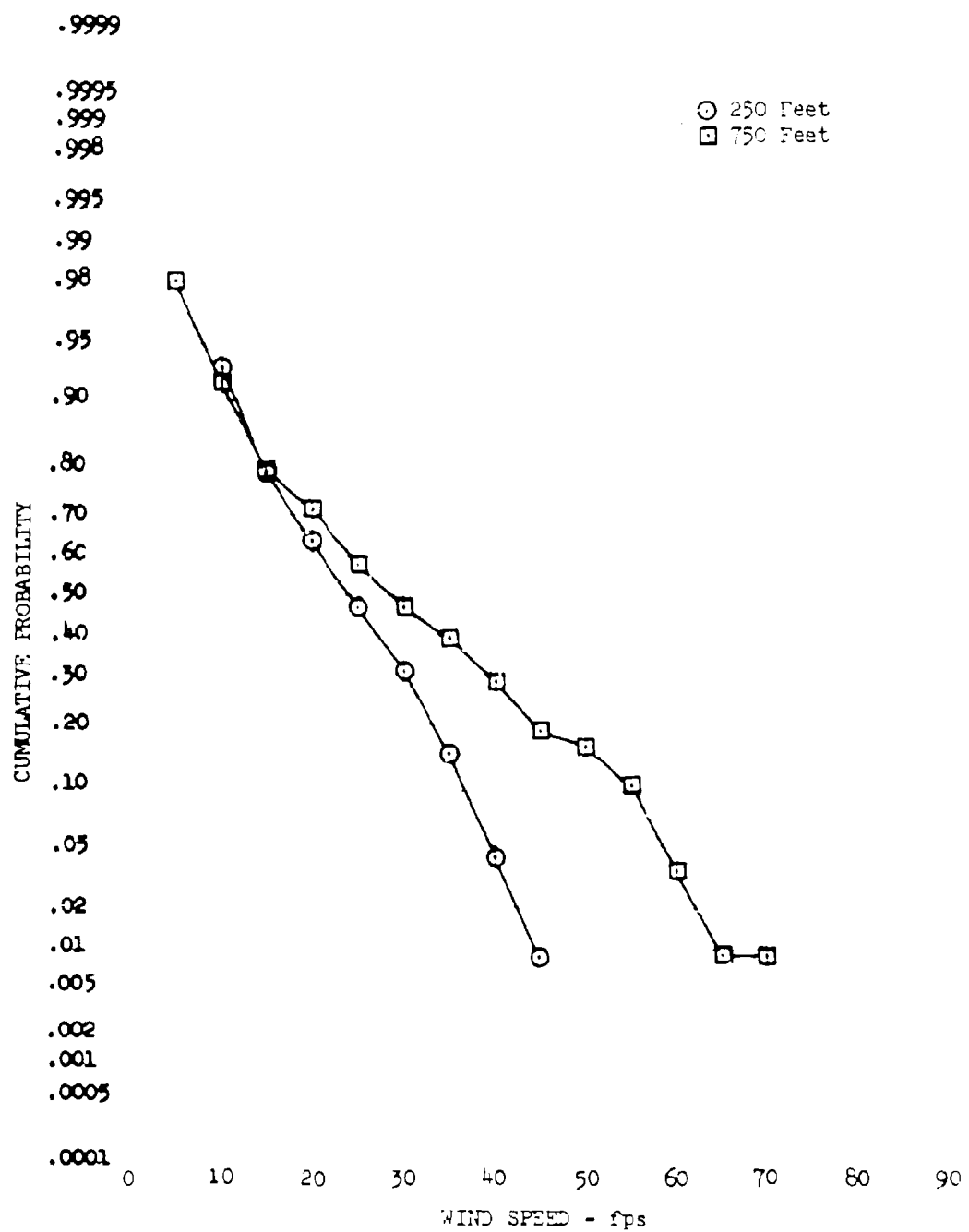


Figure 4.5 Variation of Wind Speed Cumulative Probability over the Plains with Altitude

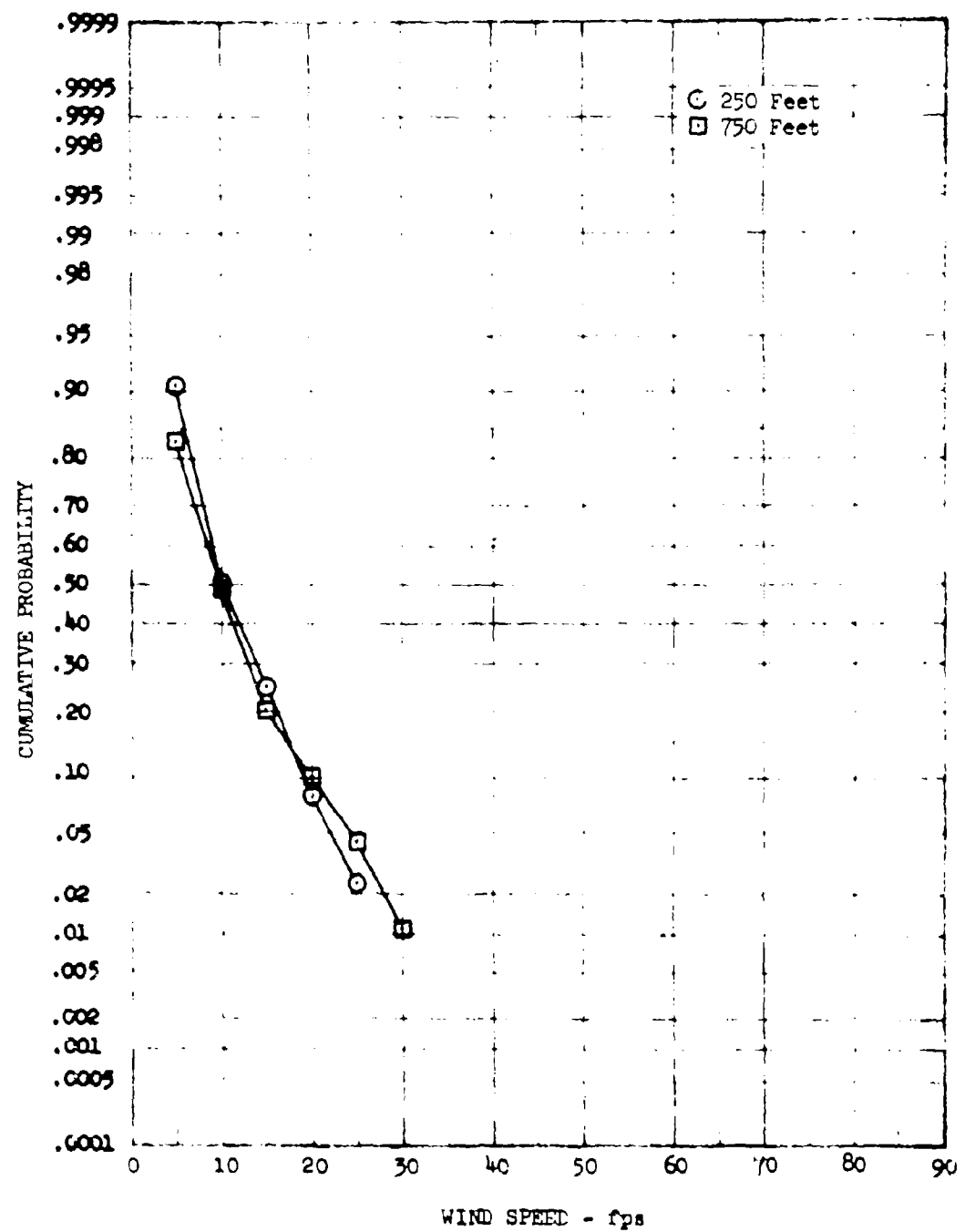


Figure 4.6 Variation of Wind Speed Cumulative Probability over High Mountains with Altitude

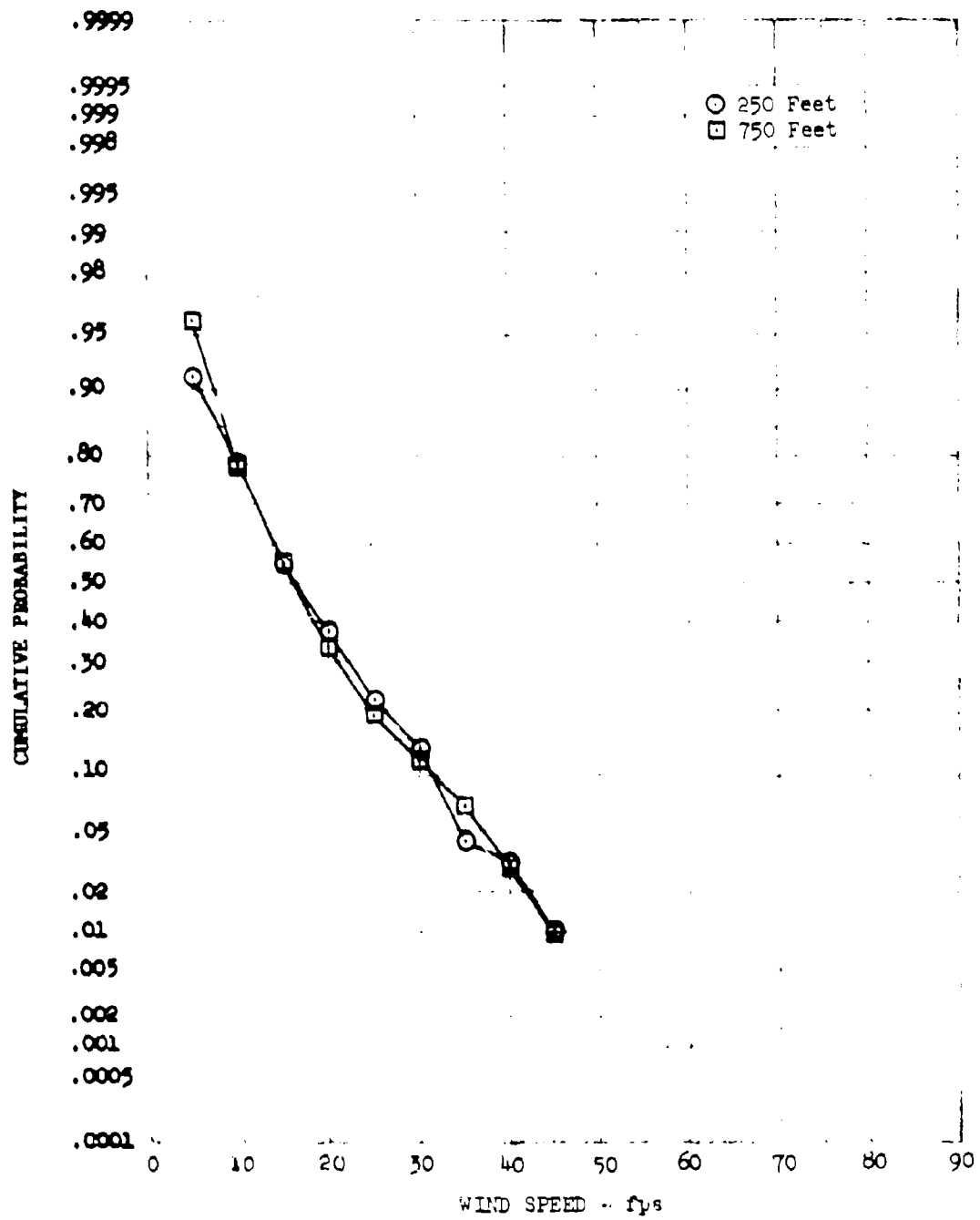


Figure 4.7 Variation of Wind Speed Cumulative Probability over Low Mountains with Altitude

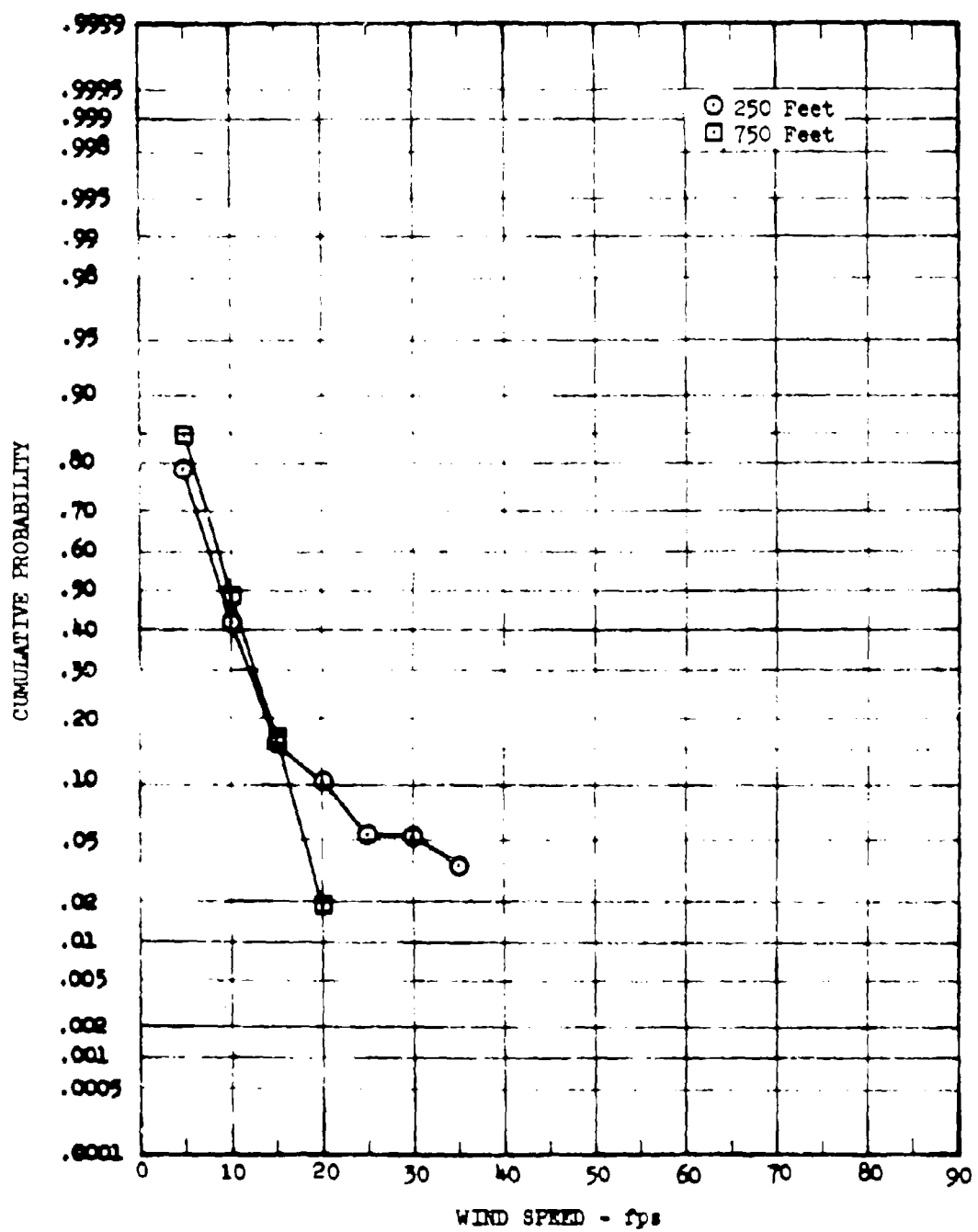


Figure 4.8 Variation of Wind Speed Cumulative Probability over Desert Terrain with Altitude

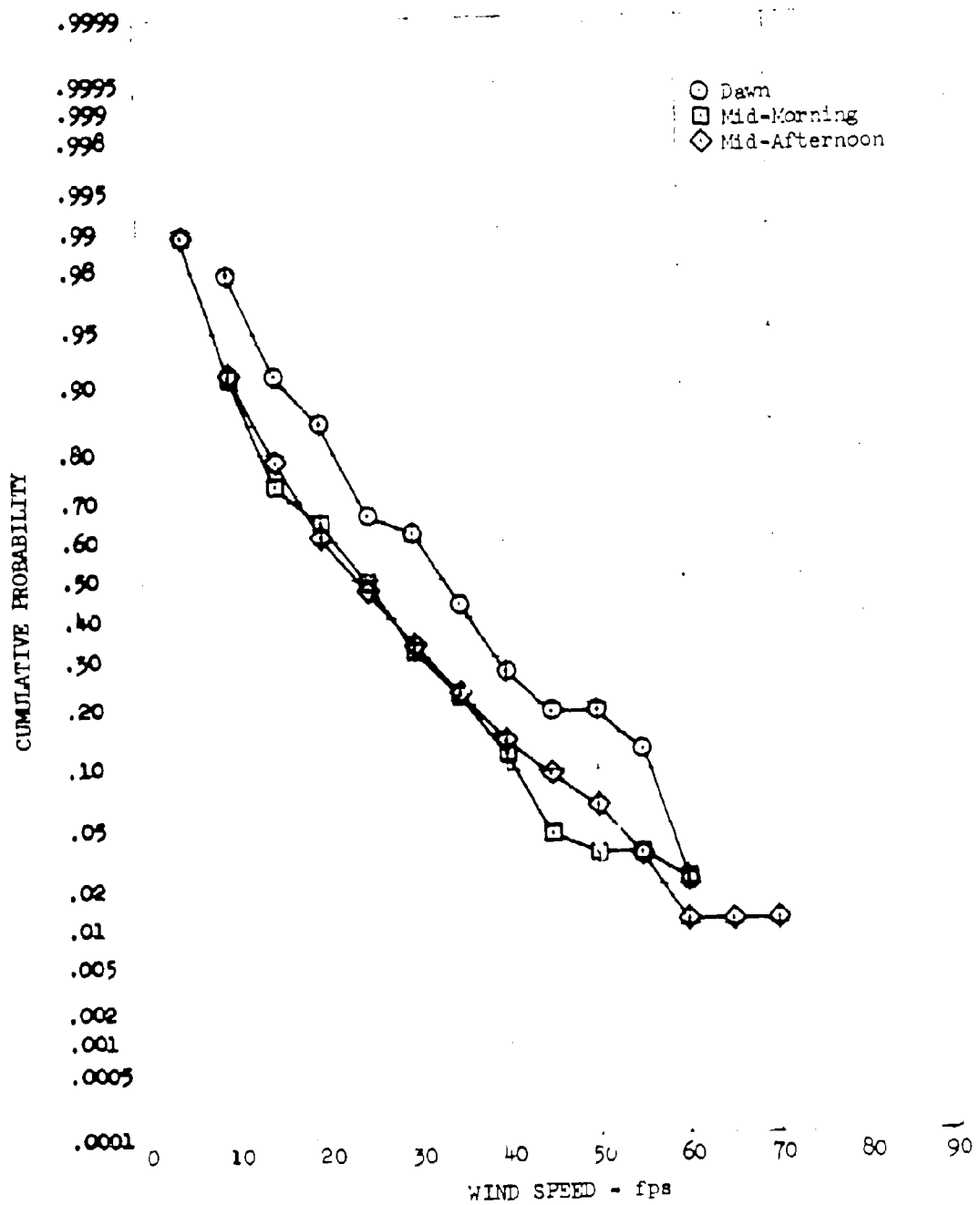


Figure 4.9 Variation of Wind Speed Cumulative Probability at McConnell with Time-of-Day

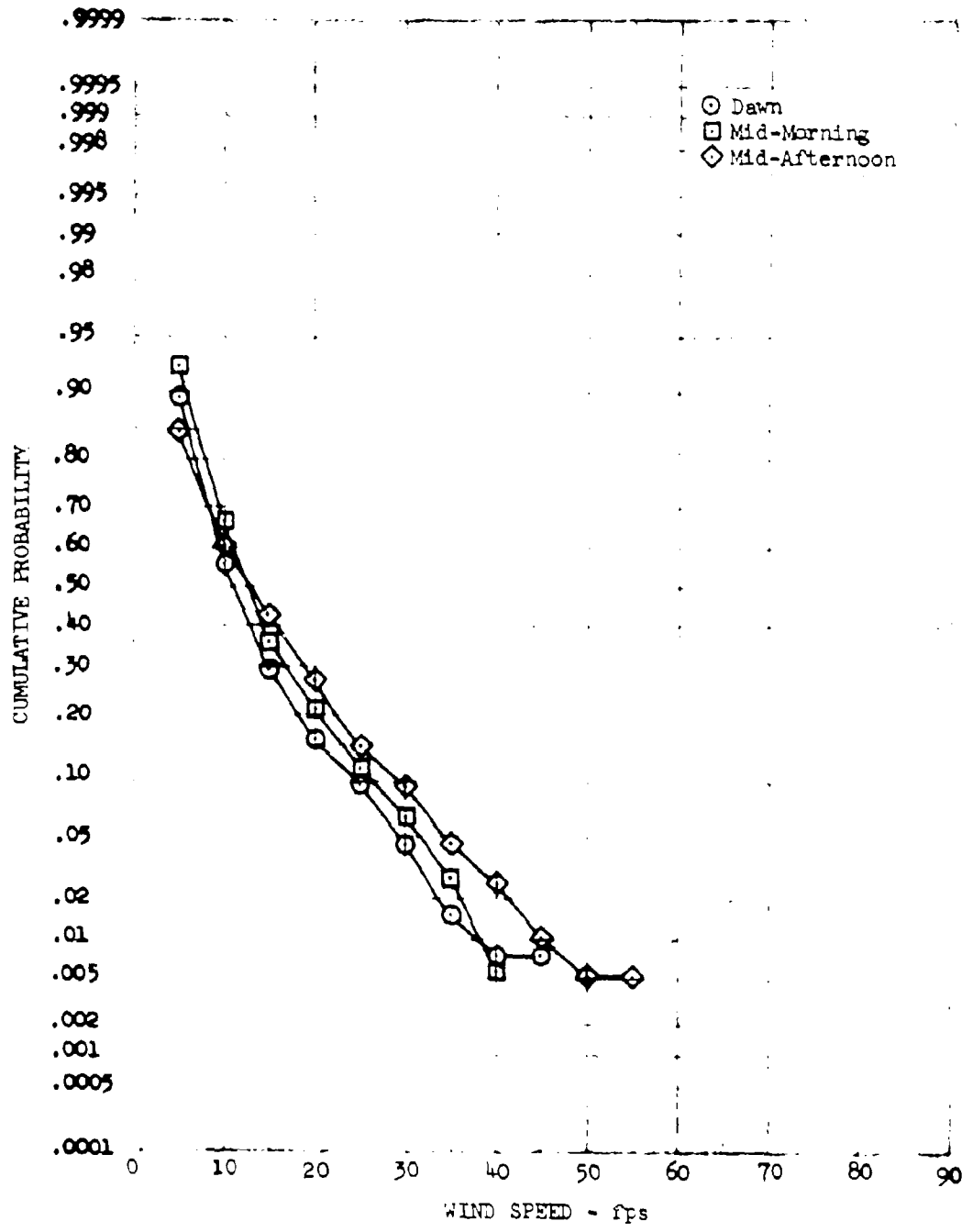


Figure 4.10 Variation of Wind Speed Cumulative Probability at Edwards with Time-of-Day

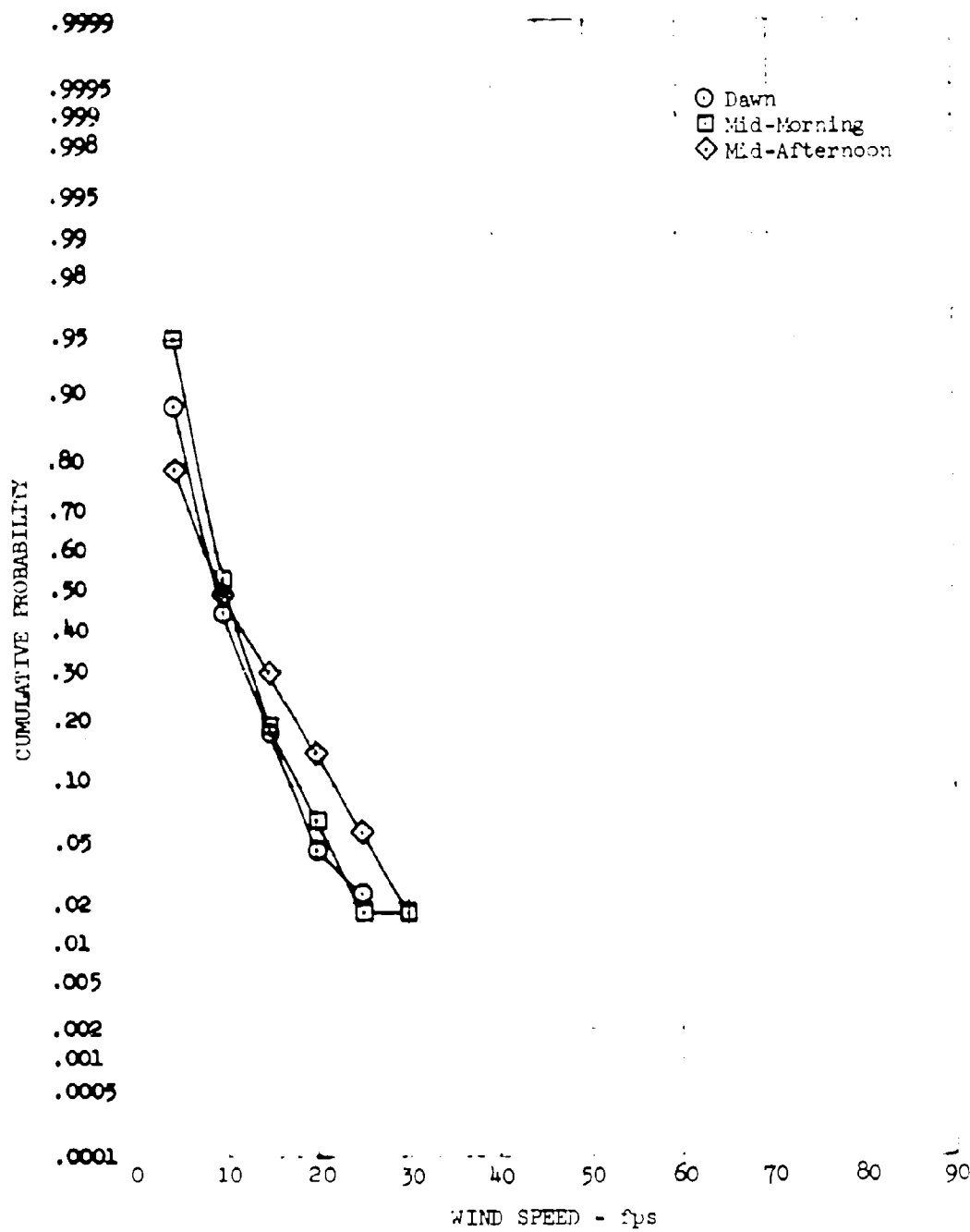


Figure 4.11 Variation of Wind Speed Cumulative Probability over High Mountains with Time-of-Day

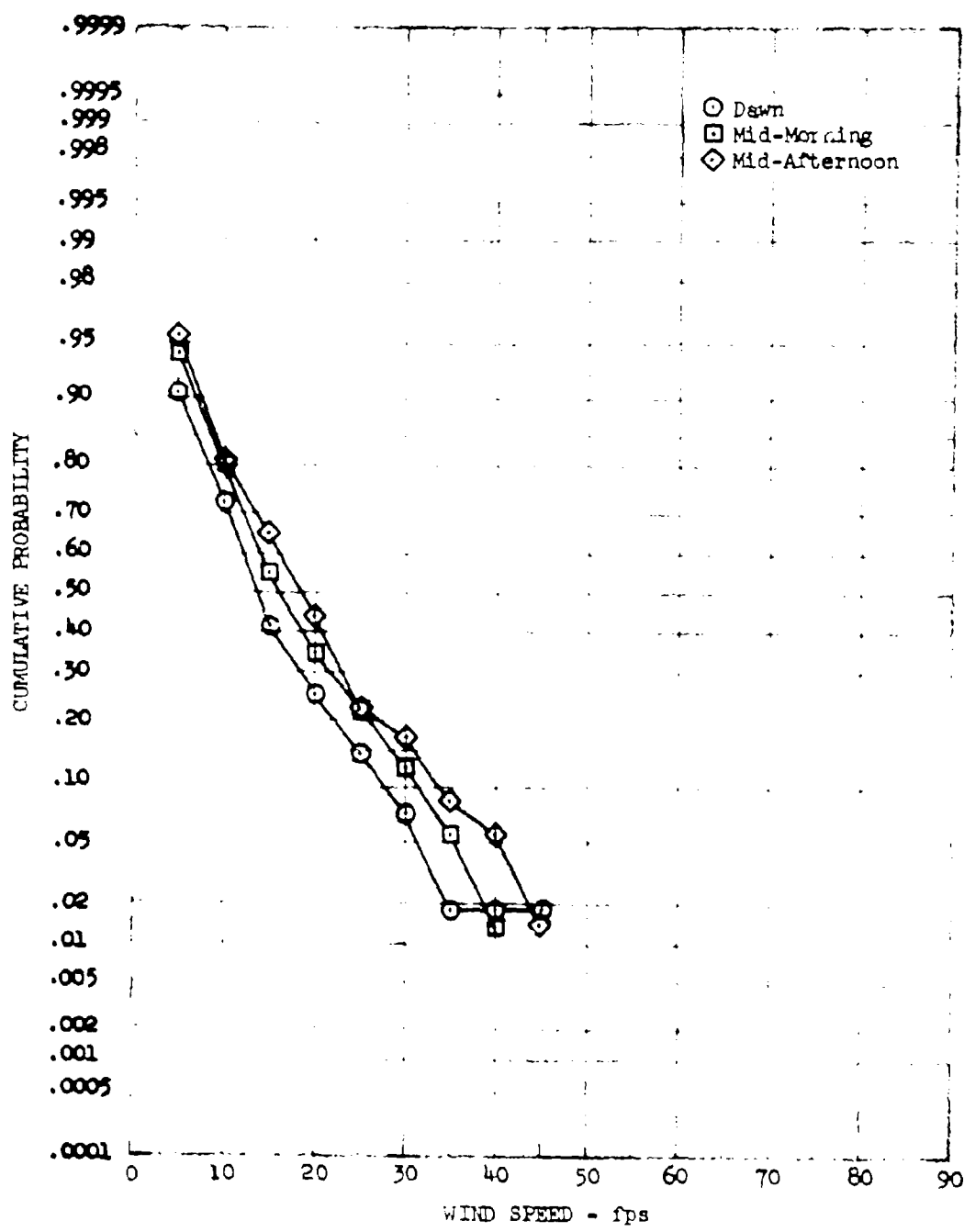


Figure 4.12 Variation of Wind Speed Cumulative Probability over Low Mountains with Time-of-Day

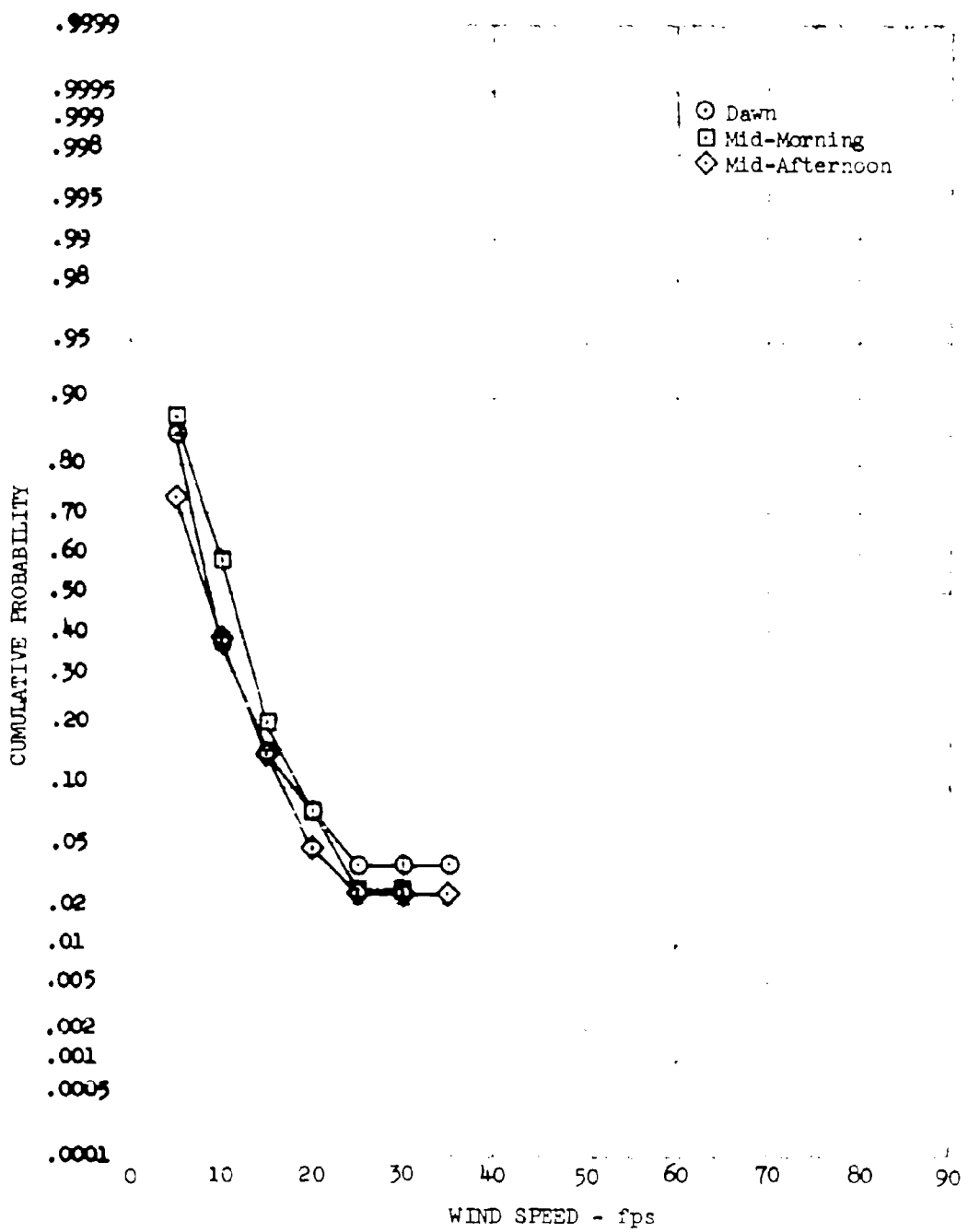


Figure 4.13 Variation of Wind Speed Cumulative Probability
over Desert with Time-of-Day

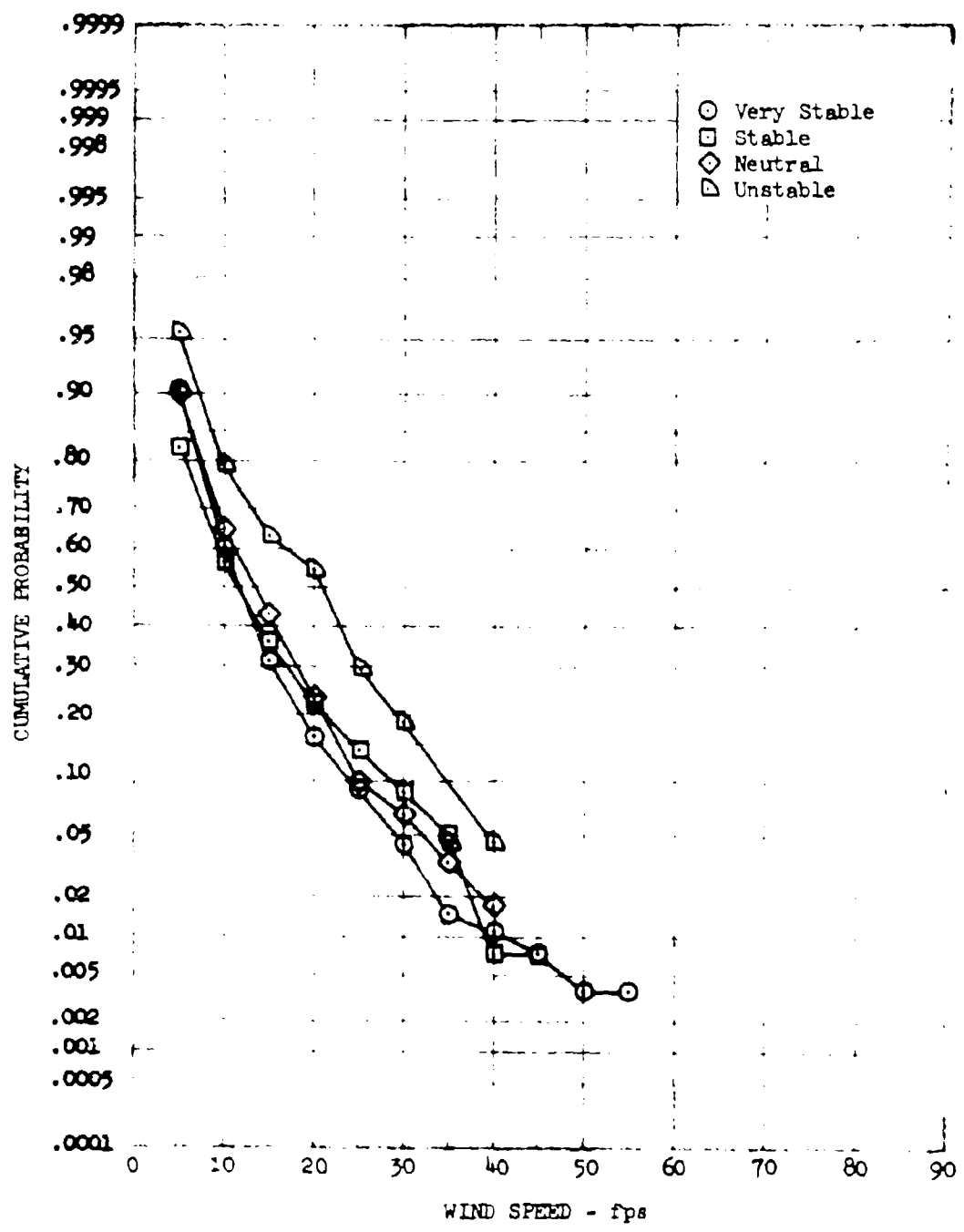


Figure 4.14 Variation of Wind Speed Cumulative Probability at Edwards with Atmospheric Stability

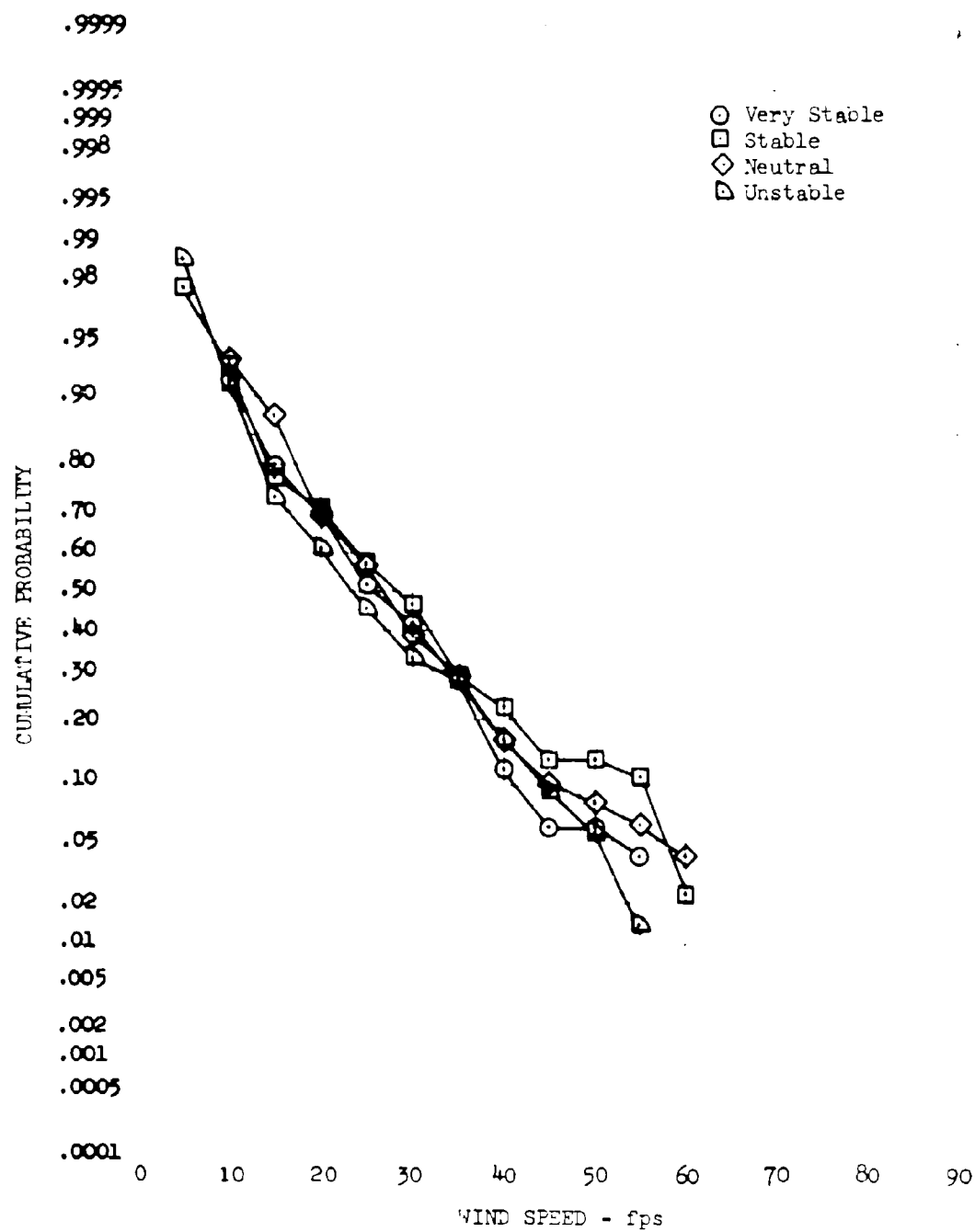


Figure 4.15 Variation of Wind Speed Cumulative Probability at McConnell with Atmospheric Stability

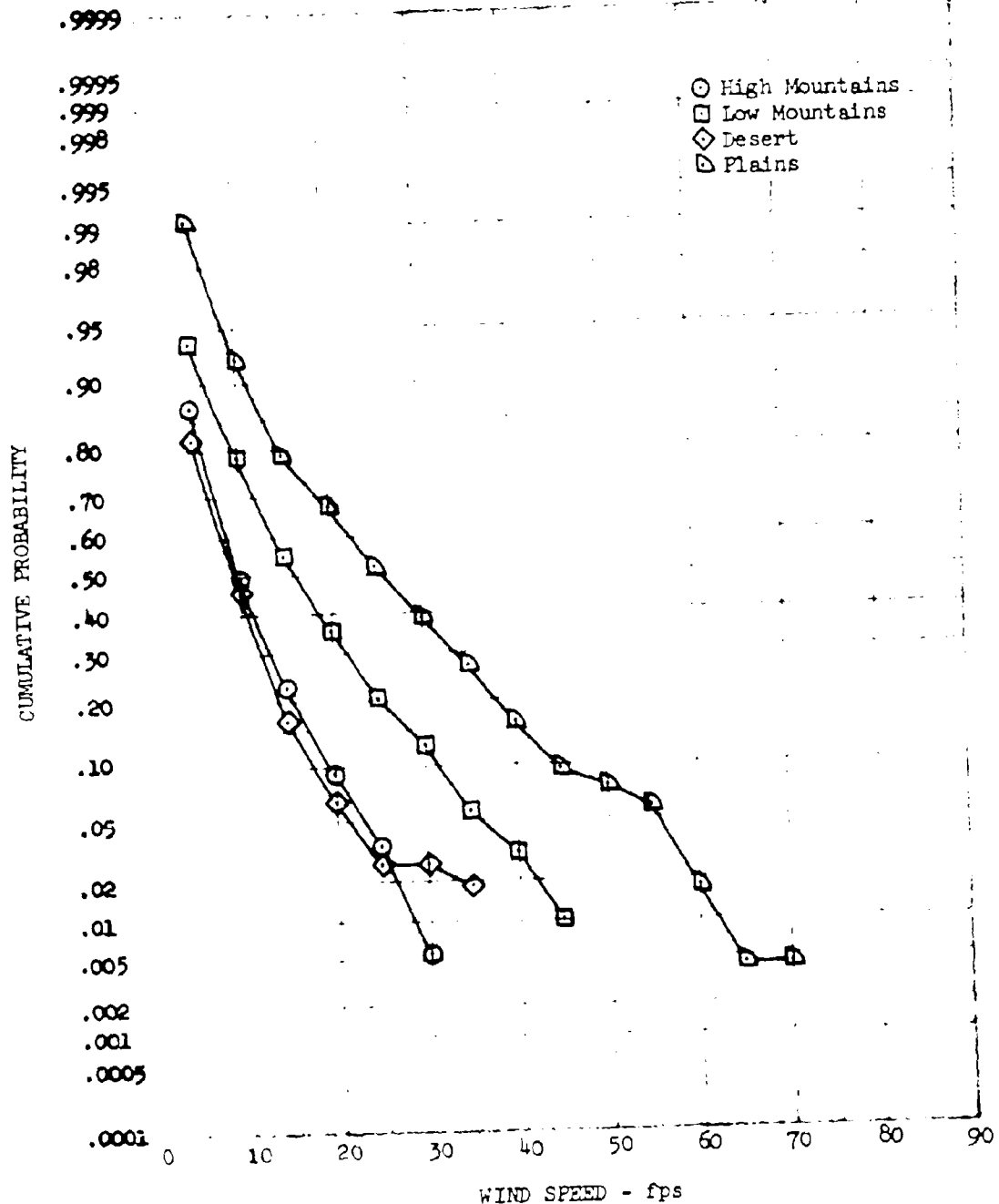


Figure 4.16 Wind Speed Cumulative Probability Associated with Terrain Type

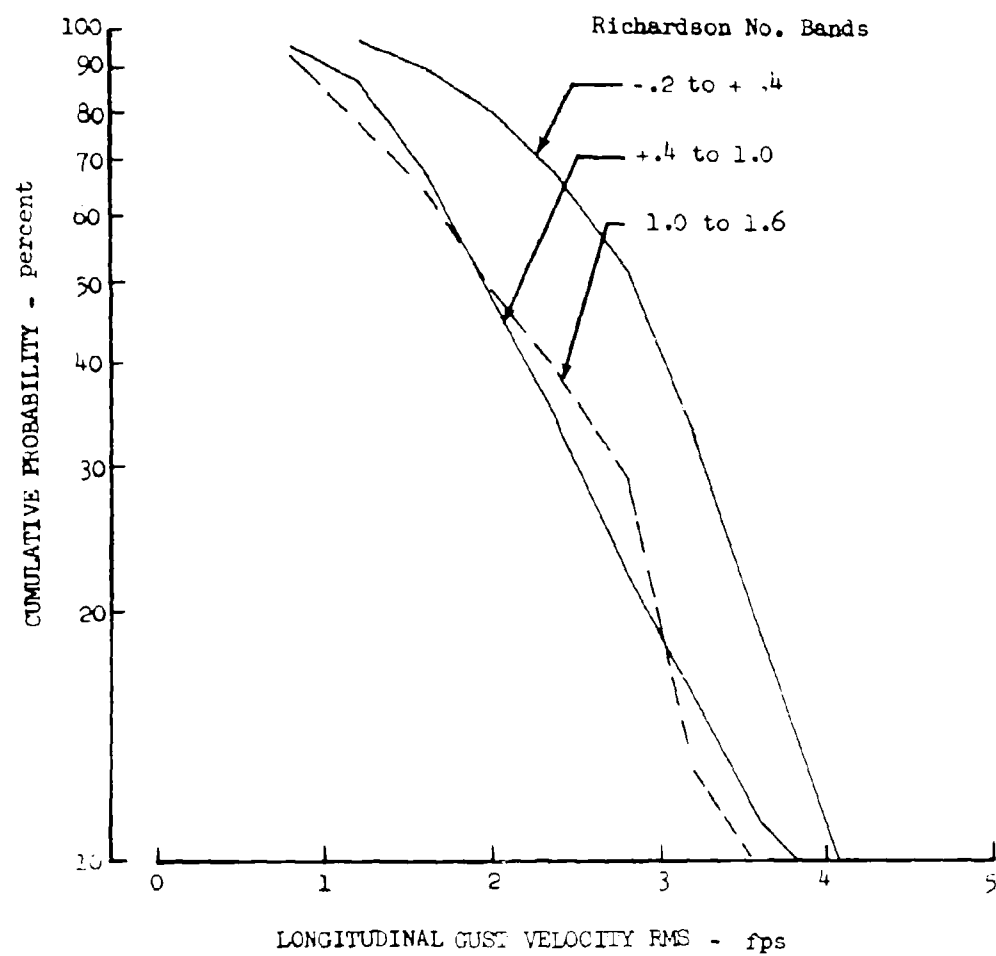


Figure 4.17 Longitudinal Gust Velocity RMS Cumulative Probability Associated with Richardson Number

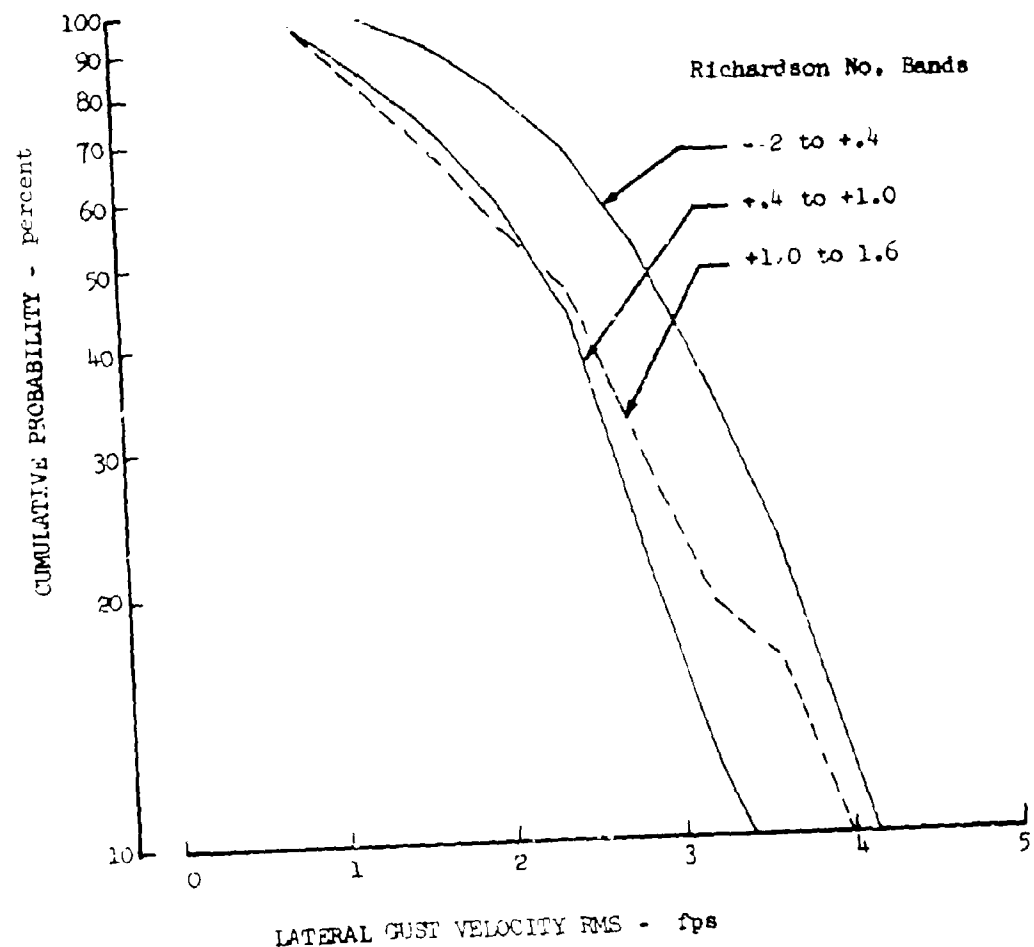


Figure 4.18 Lateral Gust Velocity RMS Cumulative Probability
Associated with Richardson Number

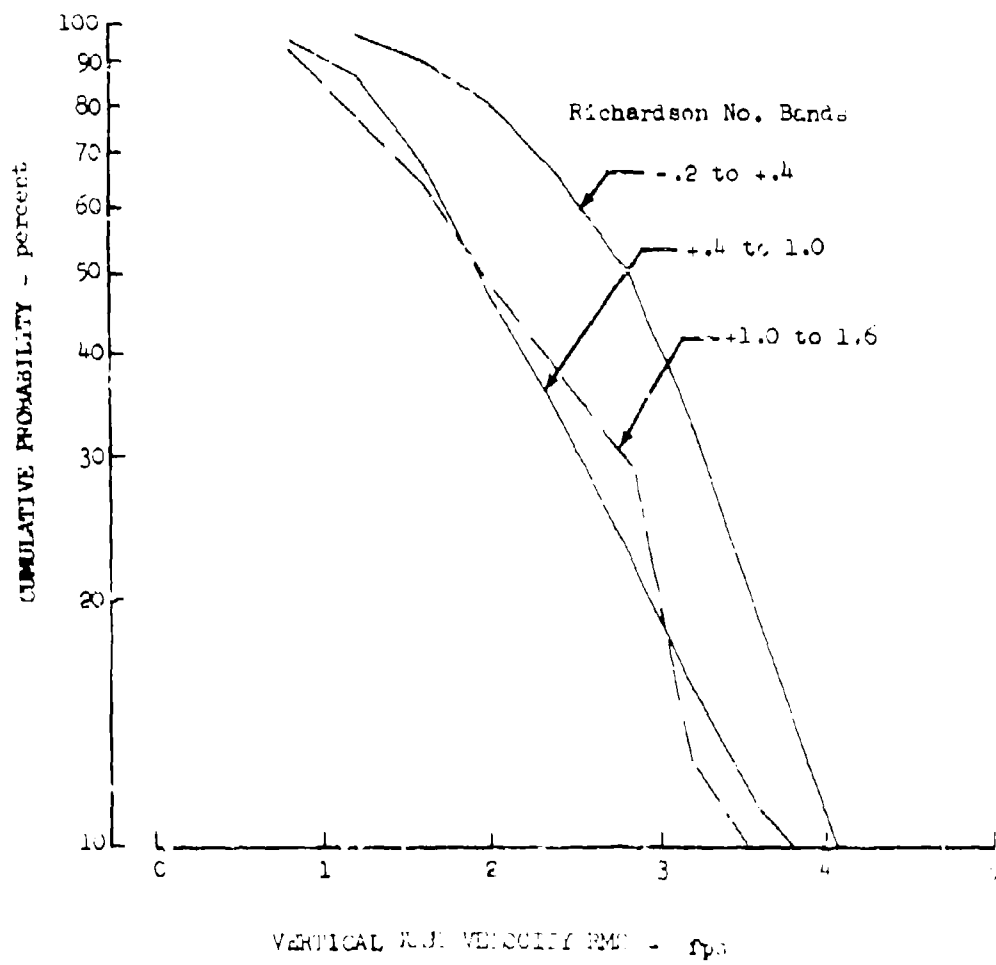


Figure 6 - Vertical Shear Velocity (M) Cumulative Probability Associated with Richardson Number

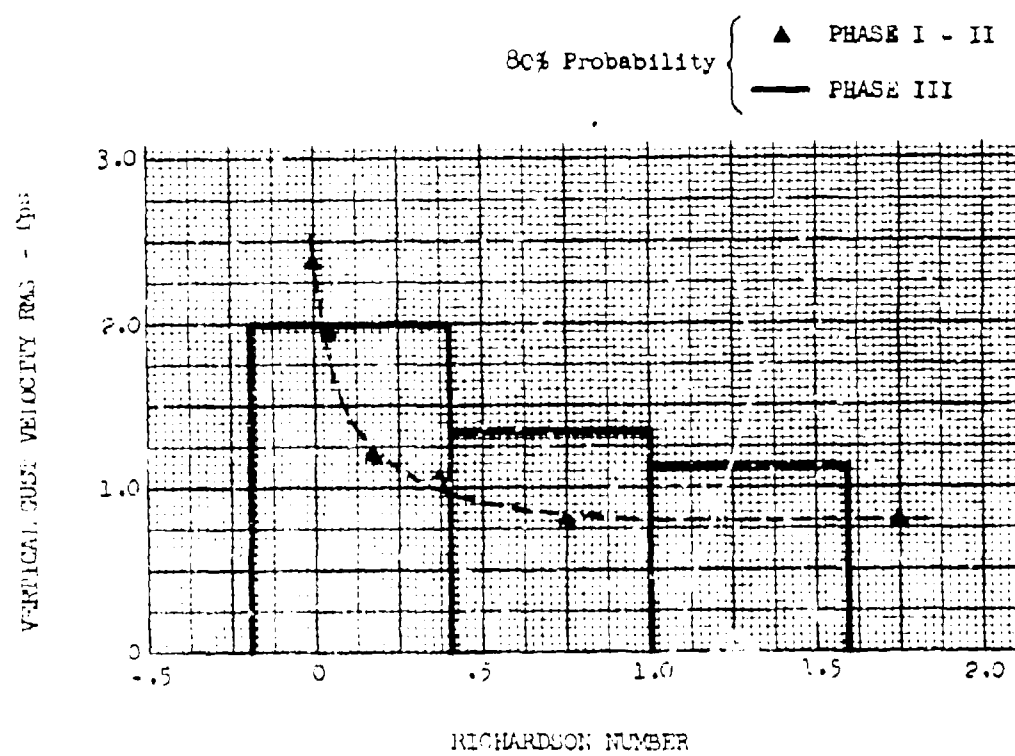
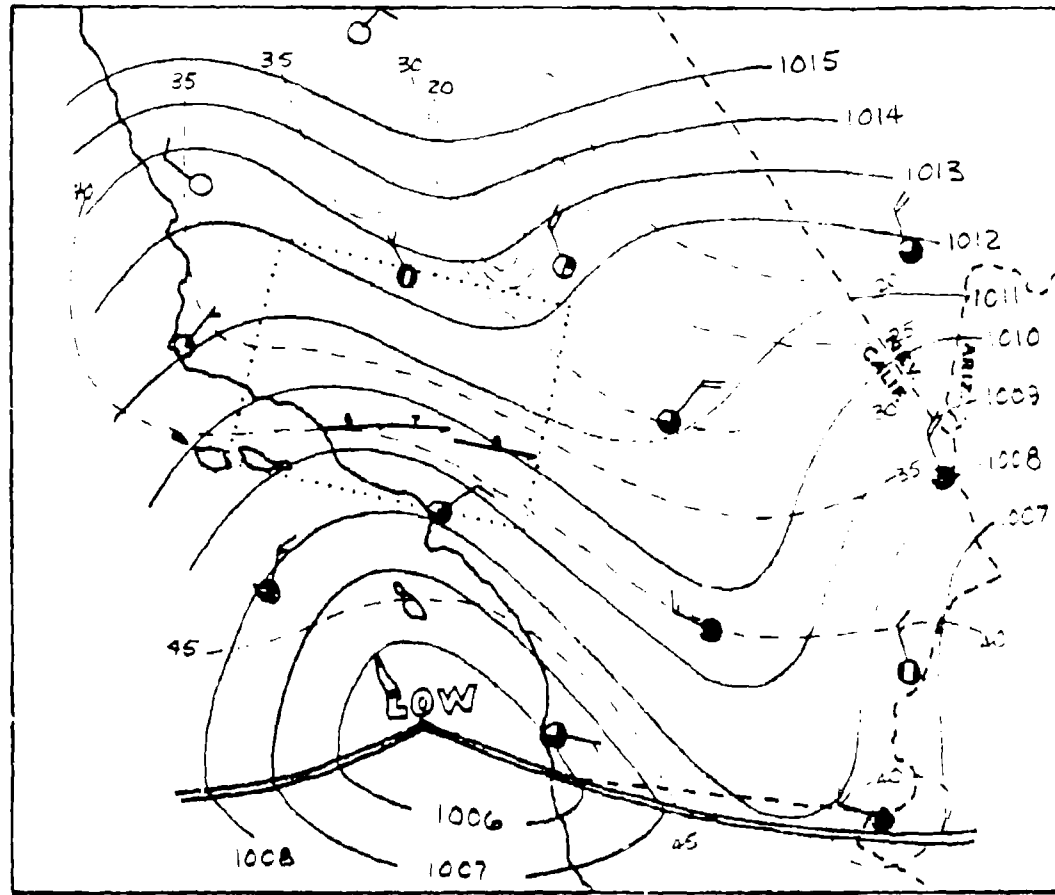


Fig. 10.20. Gust Velocity, RMS Vertical Velocity over 10 minutes
versus Richardson Number.



LEGEND

CLOUD COVER

- (○) - CLEAR
- (◐) - .2 to .3
- (◑) - .4
- (●) - .7 to .8
- (▀) - .9 to 1.0
- (■) - OVERCAST

WIND ARROWS

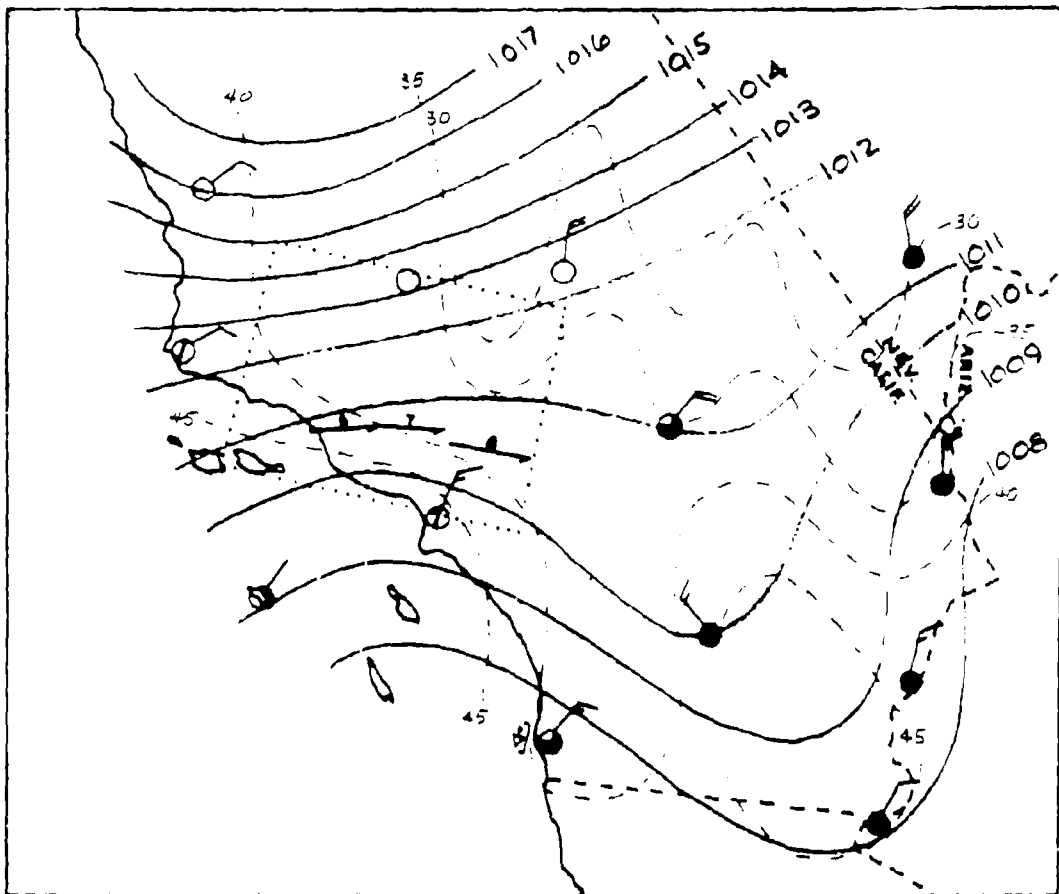
- - CALM
- (HALF BARB) - 5 knots
- (WHOLE BARB) - 10 knots

Arrow extends toward the direction from which the wind is blowing.

— ISOBARS (mb)

— — — ISOTHERMS (°F)

Figure 4-21 Surface Synoptic Analysis for 13 December 1967, 1500 GMT, Edwards AFB Router.



LEGEND

CLOUD COVER

- - CLEAR
- ◐ - .2 to .3
- ◑ - .4
- - .7 to .9
- ◐ - .9 to 1.0
- - OVERCAST

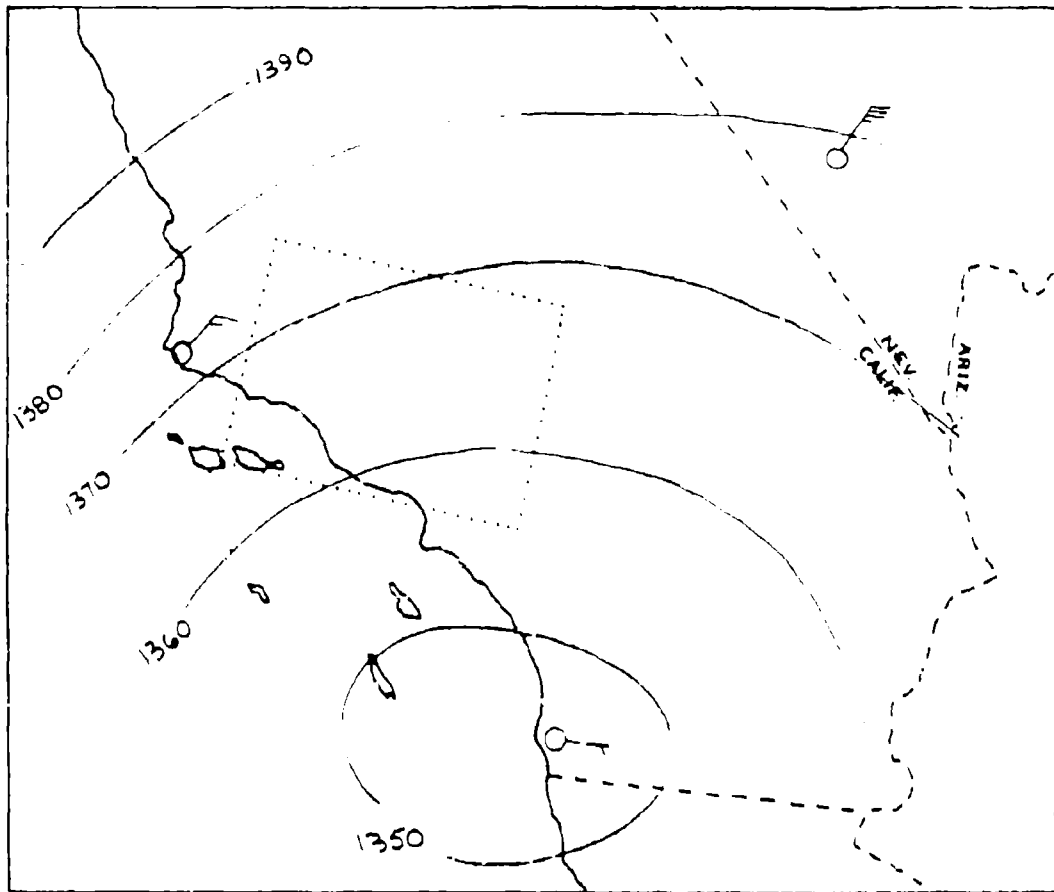
WIND ARROWS

- - CALM
- (HALF BARB) - 5 knots
- (WHOLE BARB) - 10 knots
- Arrow extends toward the direction from which the wind is blowing.

— ISOBARS (mb)

- - - - ISOTHERMS (°F)

Figure 5.72 Surface Synoptic Analysis for 13 December 1967, 1800 GMT,
Edwards AFB Route.



LEGEND

CLOUD COVER

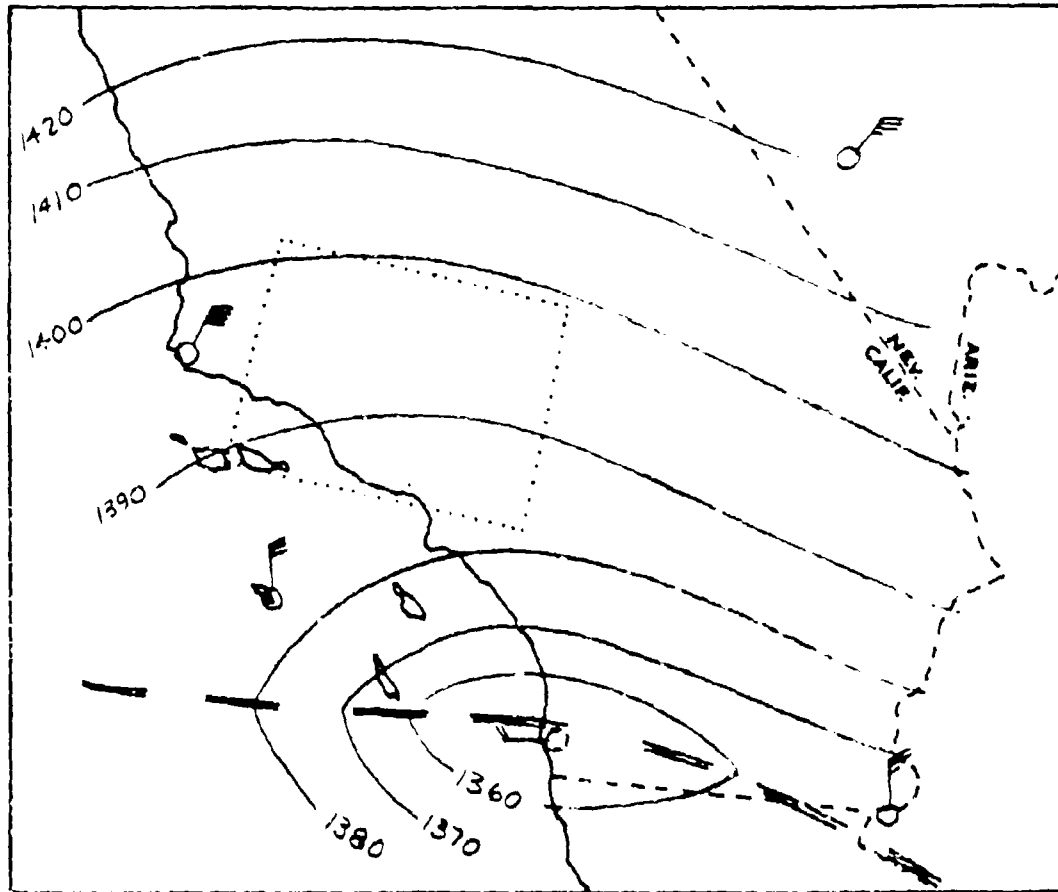
- - CLEAR
- ◐ - .2 to .3
- ◑ - .4
- - .7 to .8
- - .9 to 1.0
- - OVERCAST

WIND ARROWS

- - CALM
- (HALF BARB) - 5 knots
- (WHOLE BARB) - 10 knots
- Arrow extends toward the direction from which the wind is blowing.

— 850 mb HEIGHTS (m)

Figure 4.23 850 mb Synoptic Analysis for 14 December 1967, 0000 GMT,
Edwards Air Force Base Route.



LEGEND

CLOUD COVER

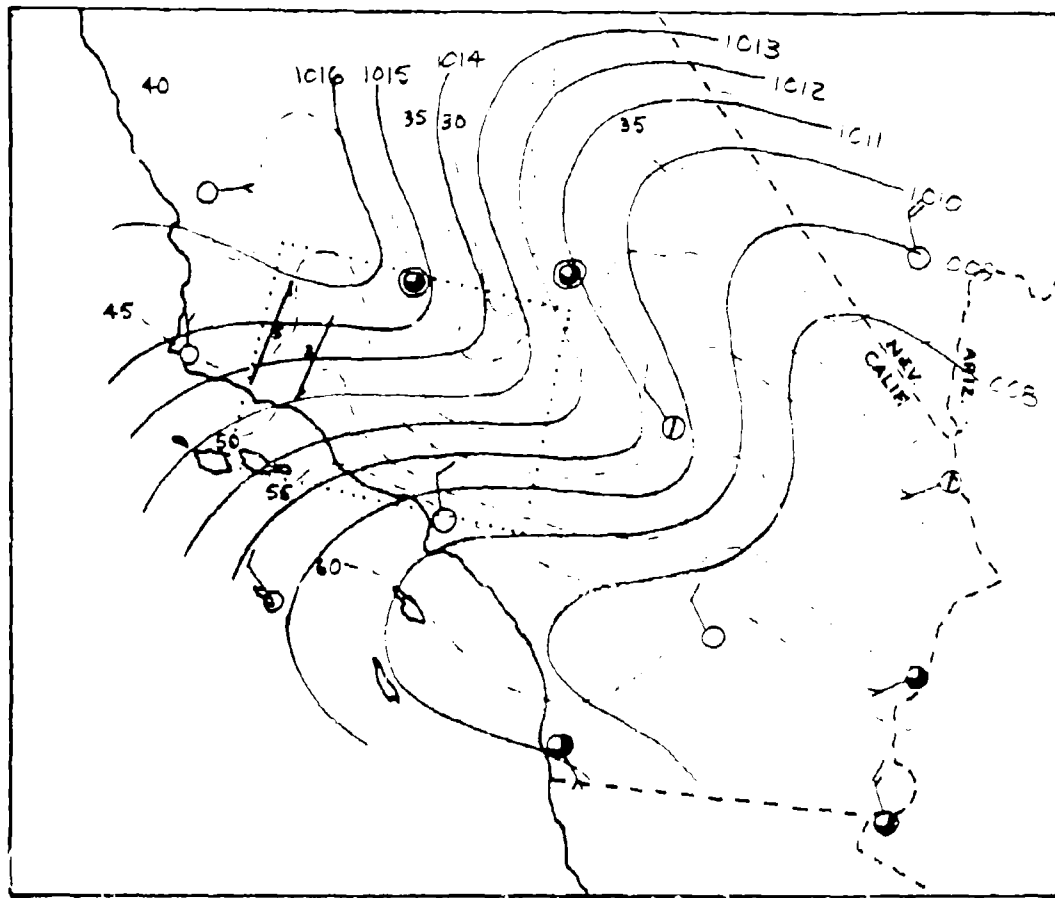
- - CLEAR
- ◐ - .2 to .3
- ◑ - .4
- - .7 to .8
- ◐ - .9 to 1.0
- - OVERCAST

WIND ARROWS

- - CALM
- (HALF BARB) - 5 knots
- (WHOLE BARB) - 10 knots
- Arrow extends toward the direction from which the wind is blowing.

— 850 mb HEIGHTS (m)

Figure 4.24 850 mb Synoptic Analysis for 13 December 1967, 1200 GMT, Edwards AFB Route.



LEGEND

CLOUD COVER

- - CLEAR
- ◐ - .2 to .3
- ◑ - .4
- - .7 to .8
- ◐ - .9 to 1.0
- - OVERCAST

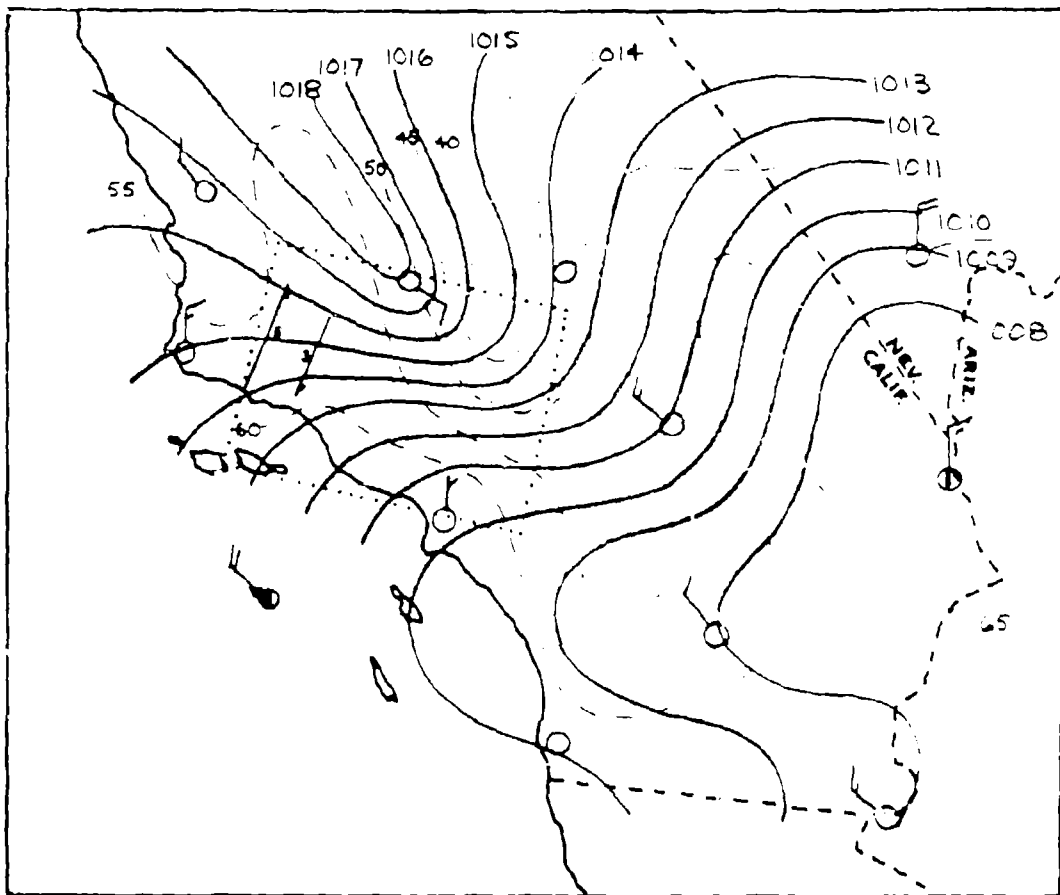
WIND ARROWS

- - CALM
- (HALF BARB) - 5 knots
- (WHOLE BARB) - 10 knots
- Arrow extends toward the direction from which the wind is blowing.

— ISOBARS (mb)

— — — ISOETHERMS ('F)

Figure 4.25 Surface Synoptic Analysis for 13 November 1968, 1500 GMT,
Edwards AFB Route.



LEGEND

CLOUD COVER

- - CLEAR
- ◐ - .2 to .3
- ◑ - .4
- - .7 to .8
- ◐ - .9 to 1.0
- - OVERCAST

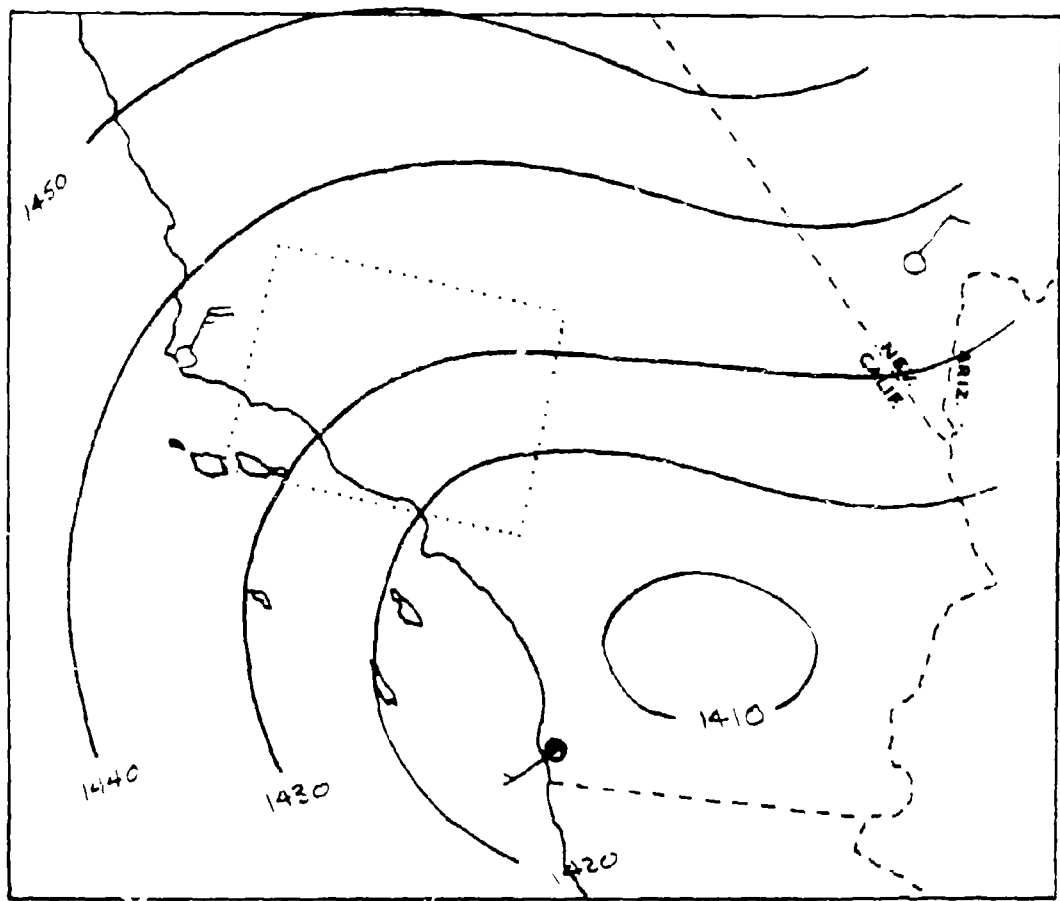
WIND ARROWS

- - CALM
- ━ (HALF BARB) - 5 knots
- ━ (WHOLE BARB) - 10 knots
- Arrow extends toward the direction from which the wind is blowing.

— ISOBARS (mb)

- - - - ISOTHERMS (°F)

Figure 4.26 Surface Synoptic Analysis for 13 November 1968, 1800 GMT,
Edwards AFB Route.



LEGEND

CLOUD COVER

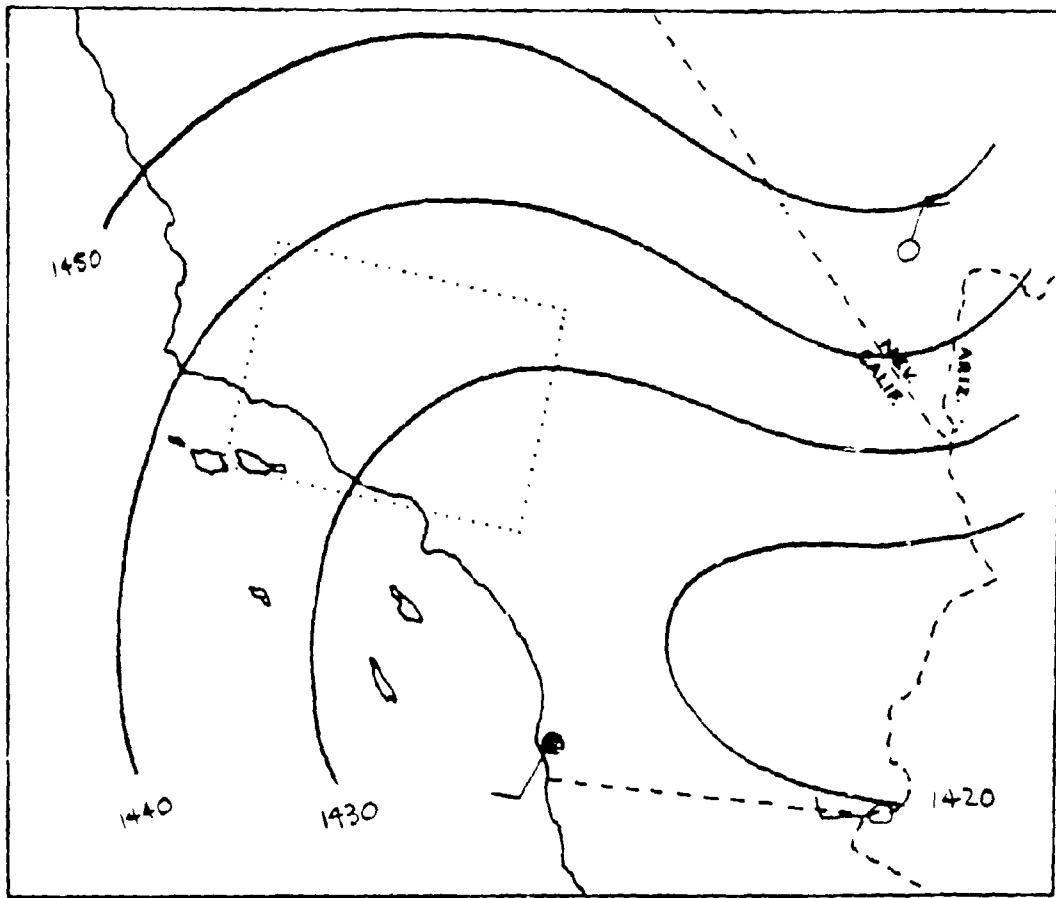
- - CLEAR
- ◐ - .2 to .3
- ◑ - .4
- - .7 to .8
- - .9 to 1.0
- - OVERCAST

WIND ARROWS

- - CALM
- (HALF BARB) - 5 knots
- (WHOLE BARB) - 10 knots
- Arrow extends toward the direction from which the wind is blowing.

— 850 mb HEIGHTS (m)

Figure 4.27 850 mb Synoptic Analysis for 14 November 1968, 0000 GMT, Edwards AFB Route.



LEGEND

CLOUD COVER

- - CLEAR
- ◐ - .2 to .3
- ◑ - .4
- - .7 to .8
- ◐ - .9 to 1.0
- - OVERCAST

WIND ARROWS

- - CALM
- ↖ (HALF BARB) - 5 knots
- ↖ (WHOLE BARB) - 10 knots
- Arrow extends toward the direction from which the wind is blowing.

— 850 mb HEIGHTS (m)

Figure 4.28 850 mb Synoptic Analysis for 13 November 1968, 1200 GMT,
Edwards AFB Route.

SECTION V

PRELIMINARY TURBULENCE ANALYSIS

Preliminary turbulence analysis was accomplished on data obtained during the first half of the Low-Level Critical Air Turbulence Phase III program. Approximately 72 hours of low-level (0-1000 feet) turbulence and associated meteorological data were recorded from 16 August, 1968, through 8 January, 1969. The data were obtained during flight over routes near McConnell Air Force Base, Kansas and Edwards Air Force Base, California. Also included are time histories of some of the larger magnitude gust velocities recorded over the Peterson Field, Colorado route.

During the LO-LOCAT Phase III program, gust velocities are not being computed for data samples where the level of turbulence is low, which reduces computer effort on data which would eventually be discarded due to a low signal-to-noise ratio. The standard deviations of the angles of attack and sideslip differential pressures, as sensed by the gust probe pressure ports, were the criteria used in determining which samples fall into this category. Data were not processed when $\sigma_\alpha \leq 0.07$ in. Hg or $\sigma_\beta \leq 0.05$ in. Hg. For this situation, the standard deviations of gust velocities were nearly always less than 1.0 fps. The values of σ_α and σ_β are determined from the calibration program (see Appendix III). When these small values are obtained, then all of the data processing, including plotting, that involves gust velocities is halted early in the data processing sequence. Thus, this criteria results in a savings, while assuring processing of the meaningful turbulence data. The manner in which this low turbulence level data are included in the various statistical analyses is explained in each appropriate section.

Three different types of counting techniques are being used to evaluate gust velocity data. These techniques are the peak count, amplitude count, and level crossings count. A description will be given of each of these techniques. Following the descriptions, results will be presented and comparisons made.

PRIMARY PEAK COUNT

In the peak count procedure each maximum positive or negative excursion between adjacent crossings of the mean is defined as a primary peak. As shown in Figure 5.1, secondary peaks are not considered. The number of primary peaks which fall in each 2 fps wide amplitude band are counted.

In the peak count procedure, high frequency, low amplitude data (or noise) occur as primary peaks in the lowest band. Figure 5.2 shows a peak count distribution and illustrates how it was extrapolated to eliminate the undesirable peaks in the lowest band. The shaded points indicate the cumulative number of peaks in the lowest band as they were originally counted. The unshaded points are the extrapolated values. This curvilinear extrapolation is performed based on the shape of the distribution curve. This is done by fitting, by computer, a curve through the data points and extrapolating it to zero gust velocity. The new value of N_{pe} and f_1 obtained by this extrapolation is then used in computation of the standard deviation: σ_{pe} .

$$\sigma_{pe} = \left[\sum_{b=1}^N \frac{f_b(x_b)^2}{N_{pe}} \right]^{1/2} \quad (5.1)$$

Also, N_{pe} is used for calculation of the cumulative probability.

AMPLITUDE COUNT

The amplitude count technique of amplitude analysis was performed on computed values of the gust velocity components. Each component was computed at 100 samples per second. In this procedure, amplitude bands 2 fps wide are placed on either side of the mean. The number of samples which fall in each band is determined, then corresponding positive and negative bands are added together. This procedure is illustrated in Figure 5.3. These data are used to compute cumulative distributions, cumulative probabilities, and probability density distributions. The time series standard deviation (σ_t) is computed using the following equation:

$$\sigma_t = \left[\frac{1}{N} \sum_{i=1}^N (x_i - \bar{x})^2 \right]^{1/2} \quad (5.2)$$

LEVEL CROSSINGS COUNT

Another method of amplitude analysis utilizes the level crossing technique. Levels of gust velocity are established at 2 fps intervals from the zero mean. Only crossings with a positive slope are counted. Figure 5.4 illustrates the level crossings technique. Crossings of corresponding positive and negative levels are combined and zero level crossings are doubled. The number of level crossings per mile of the level $x(t) = \alpha$ is computed for each level crossed by:

$$N_\alpha = \frac{E_\alpha}{d} \quad (5.3)$$

A level crossings standard deviation (σ_L) is calculated using the following equation:

$$\sigma_L = \left[\sum_{i=1}^N \frac{E_\alpha X_\alpha^2}{N_{OL}} \right]^{1/2} \quad (5.4)$$

COMPARISON OF COUNTING TECHNIQUES

The three counting techniques used to analyze gust velocity time series are compared in the following paragraphs. Only data obtained during Phase III over the McConnell and Edwards routes were considered. For these data, individual turbulence samples were originally classified into categories as discussed in Section II. Terrain, altitude, and atmospheric stability were found to be the primary categories and all samples were grouped into them for this analysis.

It should be noted that the effects of removing samples where turbulence level was low has not been taken into account for these data presented in this report. A computer program is being modified to incorporate these samples for further analysis.

Cumulative distributions of peaks per mile and level crossings per mile were calculated for comparison. Figures 5.5, 5.6, and 5.7 show comparisons of the occurrences per mile of peak count and level crossings for the three gust velocity components of the all-data category (McConnell and Edwards). These figures show that the occurrences per mile for level crossing are always higher than for peaks, except at the highest gust velocities. If the peak count data had not been extrapolated, these distribution curves would have agreed at zero gust velocity. The reason for extrapolating is explained in the peak count discussion.

Probabilities of encountering a value equal to or greater than a given value of gust velocity for the three counting techniques are shown for the three gust velocity components in Figures 5.8, 5.9, and 5.10. The category represented in these figures includes all McConnell and Edwards data. The relationship of the probability distributions of these three counting techniques varies somewhat from one gust component to another. However, in general, the amplitude count distributions are lowest and the level crossing distributions are the highest. The probability distributions for the peak count technique are consistently lower than the level crossing technique except at the higher gust velocities where they are higher.

The amplitude and peak count distributions given in the LO-LOCAT Phases I and II final report were more nearly a straight line than those given here. The Phase III distributions now being calculated are curving up and showing higher probabilities of encountering given gust velocities at the larger gust velocities. The reason for this is believed to be due to the increased speed of the Phase III test aircraft which permitted measurement of the longer wavelength higher amplitude gusts. These gusts have the effect of making the distribution curve turn up slightly at the higher gust velocity values.

Since the relationship between peak count, amplitude count, and level crossings has already been shown, only peak count data will be shown to illustrate the effect of different geophysical conditions. Figures 5.11, 5.12, and 5.13 show the terrain effects on peak count distributions. The relationship of these distributions are similar to those for LO-LOCAT Phases I and II data except that the difference between high and low mountain data is more pronounced. These plots show that the number of peaks per mile exceeding a given value is, in general, larger for high mountain data and decreases for low mountain, plains, desert, and water, in that order.

Figures 5.14, 5.15, and 5.16 show the altitude effects on peak count distributions. These figures indicate a higher frequency of occurrence of gust velocity peaks at 250 feet altitude than at 750 feet. Here again the relationship of these distributions agrees well with those for Phases I and II.

Figures 5.17, 5.18, and 5.19 show the effect of atmospheric stability on peak count distributions. These plots show that in general very stable data have the lowest distribution, then stable and neutral, in that order. The distribution of unstable data has a much steeper slope than the distributions of the other stabilities. Unstable data did not show this characteristic for Phases I and II data. It is possible that this relationship will change when the Peterson Field high mountain data are included.

Plots showing the relationship of the three components of gust velocity for all three counting techniques are given in Appendix V.

GAUSSIAN DISTRIBUTION CHECK

Amplitude count data obtained for each turbulence sample were checked for normality using the chi-squared goodness-of-fit test. This test compares the actual distribution with a normal distribution.

A chi-squared test was performed on each four and one-half minute turbulence sample using 28 bands (N_b) with widths of constant probability. The degrees of freedom for each sample were ($N_b - 1$). Two hundred gust velocity amplitude values were used in the calculation:

$$\chi^2 = .14 \sum_{b=1}^{28} f_b^2 - 200 \quad (5.5)$$

A cumulative probability distribution of the chi-square values for all McConnell and Edwards data is shown in Figure 5.20. Levels of significance based on the number of degrees of freedom for these data are shown. Inspection of this figure shows that approximately 83 percent of the vertical, 84 percent of the longitudinal and 88 percent of the lateral gust velocity samples were accepted as Gaussian at the 0.02 level of significance. Approximately 10 percent more samples were accepted during Phases I and II. This is attributed to the fact that turbulence samples are being taken over a 60 percent longer distance during Phase III.

RUN TEST OF STATIONARITY

To thoroughly analyze clear air turbulence data, the proof of stationarity is required. When a single time history record is referred to as being stationary, this generally means that statistical properties computed over short time intervals do not vary more than would be expected due to normal sampling variations. Only a limited analysis of stationarity was accomplished prior to this interim report, however, results thus far have shown reasonable agreement with homogeneity checks. Run test results will be presented in the final report.

COMPARISON OF STANDARD DEVIATIONS

Gust velocity standard deviations from amplitude count, peak count, and level crossings were calculated as shown by equations 5.1, 5.2, and 5.4. Figures 5.21, 5.22, and 5.23 show comparisons of the cumulative distributions of these standard deviations for the three gust velocity components. All McConnell and Edwards data are included. Time series standard deviations show a lower probability of occurrence than peak count or level crossing standard deviations.

CHARACTERISTIC FREQUENCY

It should be noted that the characteristic frequency, N_s , as referred to in this report is not the actual characteristic frequency of the turbulence but is equivalent to the intercept of the peak count cumulative distribution function. Measurement of the actual characteristic frequency of the turbulence would require calculation out to very high frequencies (around 30,000 cps).

Values of the characteristic frequency were obtained by two different methods. In the first method, N_o (in cycles per foot) was obtained from PSD data using equation 5.6.

$$N_o = \sigma_1 / \sigma \quad (5.6)$$

In the second method, N_p (peaks per mile) was determined by extrapolation of the peak count distribution curve as previously described under peak count. Values of N_p were determined by this method for each turbulence sample.

In order to compare characteristic frequencies calculated by both methods, N_o values were converted to occurrences per mile and averaged. Average values for each method are given in Table 5.1.

TABLE 5.1
COMPARISON OF CHARACTERISTIC FREQUENCIES CALCULATED FROM
POWER SPECTRA AND PEAK COUNT DATA

	Longitudinal	Lateral	Vertical
N_o (occurrences/mile)	26.39	31.73	34.72
N_p (peaks/mile)	23.30	30.81	38.36

These averages represent McConnaugay and Edwards data. Power spectra (and hence, N_o values) were calculated for approximately 50 percent of the data processed. In addition, characteristic frequency values were not calculated for irregularly shaped spectra (i.e. non-homogeneous turbulence or low signal-to-noise ratio). Extraneous N_p values which deviated more than four standard deviations from the mean were also removed before averaging.

Characteristic frequency for the longitudinal component is the smallest and vertical is the largest. This is true for both N_o and N_p . Comparison of corresponding N_o and N_p values shows reasonable agreement between the two methods of computation.

ENSEMBLE AVERAGING

Atmospheric turbulence, over long periods of time, must be considered to be nonstationary. Stationarity implies that statistical properties computed over short time intervals do not vary more than would be expected due to normal sampling errors. The fact that turbulence is nonstationary is seen by comparing mean square values computed from turbulence samples for different days. Also, in mountainous regions where the terrain is not homogeneous and the wind currents vary considerably, mean square values for adjacent 4.5-minute turbulence samples have been found to vary from 3 to 75 (fps)².

Nonstationary data are segmented into lengths which are stationary and ensemble averaged. The turbulence data are automatically segmented by the sampling routine of recording only 270 seconds of continuous data. These data segments, for the most part, are stationary (i.e. homogeneous); however, only samples which have been proven to be self-stationary are used in the ensemble averaging technique.

Ensemble averaging was accomplished by taking an ensemble (group) of stationary records and averaging the ensemble at corresponding times. That is, individual points of the ensemble average time function $\mu_x(t)$ is calculated by:

$$\mu_x(t_1) = \frac{1}{N} \sum_{k=1}^N x_k(t_1) \quad (5.7)$$

Ensemble averaging was accomplished for a total of twenty-three 4.5-minute turbulence samples for three different categories. Power spectra and associated data (discussed later in this report) for category 424000, consisting of 12 samples, are presented in Figure 5.24. Data for the other categories are not presented due to the limited number of samples and, hence, low statistical confidence.

Due to the limited quantity of data analyzed thus far, no definite conclusions can be expressed. However, certain consistent observations have been noted. These are: (1) As the number of ensemble samples increases, the standard deviation of the ensemble average time function decreases, (2) the scale lengths of the ensemble average time function calculated from the power spectra are approximately equal to the average of the scale lengths for the ensemble records, (3) the ensemble average time function is both stationary and normally distributed, and (4) the ensemble average data are isotropic, homogeneous, incoherent, and in good agreement with von Karman mathematical spectra.

SEVERE AND EXTREME TURBULENCE ENCOUNTERS

Time histories of longitudinal, lateral, and vertical gust velocities are being plotted for turbulence samples during which the pilot reported severe or extreme turbulence and where the value of one or more of the gust velocities exceeded 50 feet per second.

The above criteria were met on one turbulence sample from the Edwards route and on no samples from the McConnell route. Eighteen turbulence encounters meeting or exceeding the above criteria occurred during flights at Peterson Field during the time period from 20 January 1969 to 15 February 1969.

The time histories of gust velocities for the single Edwards encounter are presented in Figure 5.25 and those for the Peterson occurrences are shown in Figures 5.26 through 5.43. A data block included on each figure identifies the test and leg during which the severe turbulence was encountered. Also tabulated in the data block are the maximum and minimum gust velocities, gust σ_t 's, average wind direction and velocity, average ambient air temperature, average true airspeed, average radar altitude, and category number.

The vertical gust velocity component in Figure 5.25 should be particularly noted because of the long wavelengths of approximately 14,300 feet and the high magnitudes of 74.5 fpm and -65 fpm of the turbulence. The long wavelength component appears at a frequency of approximately 0.04 cps in the time history. This same long wavelength turbulence, if encountered during the Phases I and II testing, would have appeared as 0.02 cps data due to the lower speed at which the C-131

aircraft were flown. Phases I and II gust velocity measurements in this frequency regime would have been attenuated approximately 80 percent due to the low frequency data filtering techniques utilized to alleviate the effects of instrumentation drift. This is a cogent example of the fact that there is turbulence at low altitudes that contains wavelengths longer than 7000 feet, and this is the reason why, in comparing Phase III results with Phases I and II for equivalent categories, that (1) the probability distributions of peak gust velocities are higher, (2) the probability distributions for rms gust velocities are higher, (3) integral scale lengths are longer, (4) Taylor's microscales are longer, and (5) viscous dissipation rates are less.

The striking similarity between Figure 5.33, 5.37, and 5.41 should also be noted. These turbulence samples were gathered over leg 2 of the Peterson route on three separate flights conducted on the same day. Leg 2 starts approximately one mile southwest of Elk Creek Acres and proceeds in a southwesterly direction over Tarryall Reservoir toward Antero Junction. The terrain profile of this particular leg is shown in Figure 5.44. The elapsed time between the first turbulence sample gathered during the dawn flight (Figure 5.33) and the last turbulence sample gathered during the mid-afternoon flight (Figure 5.41) is approximately seven hours.

GUST VELOCITY RMS VALUES

Another method of investigating turbulence magnitude is to analyze the standard deviation of the gust velocities. The standard deviation (σ_t) of each of the three gust velocity components was calculated by using equation 5.2.

The values of x_i are taken from the time histories of gust velocities which are computed at the rate of 100 samples per second giving 27,000 values for each four and one-half minute turbulence sample. Therefore, for this particular calculation, $N = 27,000$. The mean gust velocity value is indicated by \bar{x} .

Since the mean value, \bar{x} , is made essentially equal to zero by high-pass filtering, the standard deviation is actually equal to the root-mean-square (rms) value as shown in equation 5.8. The two terms are used interchangeably in this report.

$$\sigma_t = \left[\frac{1}{N} \sum_{i=1}^N (x_i - \bar{x})^2 \right]^{1/2} = \text{rms with } \bar{x} = 0 \quad (5.8)$$

The gust velocity rms values are being analyzed in a number of ways. Primarily these involve analysis of rms magnitude on a statistical basis, a study of the gust velocity rms values as a function of wind speed, and investigation of various turbulence forecasting models (discussed in Section IV) using gust velocity rms values and regression techniques. Since the gust velocity rms values are being investigated within the realm of the categorization technique described in Section II, then any relationship with these geophysical categories also becomes apparent.

Gust Velocity RMS Statistical Analysis

Probabilities of gust velocity rms values being a given value or greater are computed. The rms values are grouped into bands 0.5 fps in width and the cumulative probabilities calculated. The cumulative probabilities determined for all data recorded thus far during Phase III are presented in Figure 5.45 through 5.47. For comparative purposes, the data obtained during Phases I and II of the program are also presented. As can be seen, the Phase III gust velocity rms values are greater in magnitude than the corresponding seasonal-location Phases I and II data. This is attributed to the fact that the longer turbulence wavelengths are being measured more accurately.

A statistical analysis of rms values by geophysical category is being accomplished. In order to assure a good statistical sampling, a minimum of 30 data samples within the category being analyzed was established as the criteria for a valid analysis of this type. Therefore, all of the various combinations of geophysical categories being used during this program cannot be analyzed. There are not enough data for such an extensive investigation. However, those categories which have the greatest effect on gust velocity rms magnitudes are being analyzed.

The results analyzed for this report are shown in Figures 5.48 through 5.58. Season of the year has not been analyzed separately in any of these plots. As mentioned previously, it is redundant with location for the Phase III testing.

As can be seen in these figures, the results are similar for all three gust velocity components. A discussion of general effects related to individual category components is presented below.

Figure 5.48 shows the effects of terrain over which the data were obtained. Turbulence over the rougher terrains produced the highest gust velocity rms values. Data recorded over the water leg show the lowest turbulence magnitudes.

The data were recorded at the two nominal test altitudes of 250 and 750 feet above the terrain. Resultant gust velocity rms probabilities are shown in Figure 5.49 and, as can be seen, the rms values are greater at the lower altitude. As shown in Appendix VI, the average radar altitude did not always correspond with the 250 and 750 foot category altitudes as far as exact magnitude is concerned. For the greater part, this occurs for flight over the rougher terrains. Small crevices and canyons into which the airplane cannot maneuver to maintain absolute contour flight increase the average radar altitude.

Effects of atmospheric stability on gust velocity rms values are shown in Figure 5.50. The lowest rms values were recorded when the atmospheric stability was very stable. The cumulative probability increases with decreasing atmospheric stability.

As the time-of-day during which the data were recorded varies from dawn to mid-morning or to mid-afternoon, the cumulative probability of encountering an rms gust of a given magnitude increases. This is shown in Figure 5.51.

Figure 5.52 shows the gust velocity rms cumulative probability curves for data from each of the two locations associated with this report.

During Phases I and II all combinations of terrain, altitude, and stability were analyzed. This involves 40 different category combinations. For the Phase III data, however, only six of these combinations contained 30 or more data samples. Therefore, for this interim report the effects of terrain and altitude were determined by studying the combinations of these two category components. Cumulative probability plots for the combinations are shown in Figures 5.53 through 5.58. A summary of these plots is shown in Figure 5.59 where the gust velocity rms mean values are plotted as a function of terrain and altitude.

These data show how the turbulence level increases as altitude decreases for all types of terrain. Also, the turbulence level is seen to increase with the rougher terrains. The one exception to this is with regard to the plains and desert terrain. Although the desert terrain is rougher than for the plains, larger gust velocity rms magnitudes were recorded over the plains.

It has been found that the effects of noise are significant at the lower gust velocity rms magnitudes. According to theory for normal distributions:

$$\sigma_R^2 = \sigma_t^2 + \sigma_N^2 \quad (5.9)$$

Where: σ_t = standard deviation of the turbulence

σ_N = standard deviation of the noise

σ_R = standard deviation of the recorded data

If σ_t is assumed constant for a given category, this value becomes a greater and greater percentage of σ_R as σ_N becomes smaller and smaller. Therefore, at lower turbulence levels the distribution is distorted by the high percentage of noise content in the data where the noise has a greater effect on the distribution than does the turbulence.

Because of the low signal-to-noise ratio criteria and the results from the noise analysis discussed in Section III, the cumulative probability distribution plots in Figures 5.45 through 5.58 do not extend below a gust velocity rms value of 1.5 fps. However, so that no error will occur through evaluation of these data, the rms values below 1.5 feet per second have been used in computing the probabilities for the data above 1.5 fps. Those samples that were not processed due to the low turbulence levels have been assumed to have gust rms values below 1.5 fps and are included in the cumulative probability distribution calculations by being added into the total number of data samples within the category being investigated.

Addition of these low turbulence level conditions does, of course, have an effect on the mean values of the data. These mean values were corrected by assuming that 1/3 of the samples added are contained in each of the three bands below 1.5 fps (i.e., 1/3 in the 0 to 0.5 fps band, 1/3 in the 0.5 to 1.0 fps band, and 1/3 in the 1.0 to 1.5 fps band). The average value of the added samples within each of the bands is then assumed to be the middle value of the band. The values plotted in Figure 5.59 were corrected in this manner.

The distribution shape, or form, of all gust velocity rms values recorded during Phases I and II of the LO-LOCAT program was determined to be a sum of two normal distributions (see Reference 1.2). Distributions of the data obtained so far during the Phase III program and those from Phases I and II, are shown together in Figures 5.60, 5.61, and 5.62 for comparison. In these figures, the cumulative probabilities are plotted versus a standardized variable t , where t is computed as follows:

$$t = \frac{\text{Gust Velocity rms} - \mu}{\sigma} \quad (5.10)$$

In this manner, the effects of turbulence intensity, as represented by the mean (μ) and the dispersion of the distribution (σ) are removed and the data are compared on the basis of distribution form only.

The rms values which were not calculated because of low turbulence levels were accounted for in the calculation of μ and σ by estimating the distribution of these values within the gust velocity rms bands below 1.5 fps. These estimations were made by extrapolating the cumulative probability curves to zero (Figures 5.63, 5.64, and 5.65). The number of samples within each of the lower bands can then be determined. The mean value of the data can then be calculated by assuming that the mean value of the samples within each of these lower three bands (0.0 - 0.5, 0.5 to 1.0, and 1.0 to 1.5 fps) is at the mid-point value of each respective band. The dispersion of the distributions is corrected by noting that:

$$\sigma_{e_1} = \left[\frac{1}{N_1} \sum_{i=1}^{N_1} (\sigma_{t_{i1}} - \mu_1)^2 \right]^{1/2} \quad (5.11)$$

and

$$\sigma_{e_2} = \left[\frac{1}{N_2} \sum_{i=1}^{N_2} (\sigma_{t_{i2}} - \mu_2)^2 \right]^{1/2} \quad (5.12)$$

where the subscript 1 represents the set of estimated rms values and the subscript 2 represents the calculated set of rms values. It can be shown that the dispersion of the distribution (σ_e) for the combination of both sets of data is:

$$\sigma_e = \left\{ \frac{1}{N_1 + N_2} \left[\sum_{i=1}^{N_1} \sigma_{t_{i1}}^2 + \sum_{i=1}^{N_2} \sigma_{t_{i2}}^2 \right] - \left[\frac{N_1 \mu_1 + N_2 \mu_2}{N_1 + N_2} \right]^2 \right\}^{1/2} \quad (5.13)$$

After these corrections were made, the values of the standardized variable, t , were calculated, and Figure 5.60, 5.61, and 5.62 were prepared. The distribution shapes of the different Phases match well at the higher cumulative probability values but seem to vary at some of the lower probabilities of the higher gust velocity rms magnitudes.

Gust Velocity RMS Correlation with Measured Phenomena

Gust Velocity RMS Versus Inflight Measured Wind Speed

The effects of wind velocity on gust velocity rms values are being investigated during Phase III testing. Because of the mechanical generation of turbulence caused by wind blowing across the terrain, the relationship between gust velocity rms values and recorded inflight wind velocity has been investigated with relation to type of terrain and altitude above the terrain associated with the data.

The gust velocity rms values were plotted versus the wind velocity and the first-order least square line which best fit the data was computed. The slope of the least-square line indicates the amount of correlation between rms gusts and wind velocity. As the slope increases, a greater correlation is indicated. Calculation of the y-intercept then allows calculation of the equation of the line using the point-slope method.

$$\sigma_t = y_0 + m W \quad (5.14)$$

where:

m = slope of line

y_0 = y intercept

The standard deviation of the data about the least-square line is calculated as follows:

$$\sigma_D = \left[\frac{1}{N} \sum_{i=1}^N (x_i - R_i)^2 \right]^{1/2} \quad (5.15)$$

where:

x_i = value of gust velocity rms at a given wind speed

R_i = value of least square line at the given wind speed

The standard deviation of the data about the line indicates the degree of data scatter. The results are shown in Figures 5.66 through 5.73. Figure 5.74 summarizes the wind-turbulence relationship by showing the slopes of the least-square lines plotted as a function of terrain and altitude.

Certain trends apparent in these data are as follows:

- The turbulence level increases at a greater rate with increasing wind velocity at the 250-foot altitude over high mountains than for any of the other terrain-altitude combinations studied. At 750 feet, the greatest correlation occurs for data obtained over low mountains. The correlation between turbulence and wind speed is less over plains and desert terrains. At 750 feet, over desert terrain there is a decrease in turbulence intensity with an increase in wind speed.

- The effect of altitude varies depending upon the type terrain involved. Over high mountains, the correlation between turbulence level and wind velocity is considerably greater at 250 feet than at 750 feet. Over the plains, the effect of wind speed on rms values is small and approximately the same regardless of altitude. The gust velocity rms values increase at a greater rate with increasing wind speed for data obtained at 750 feet than for 250 feet over low mountains. This is the only type of terrain over which this phenomena occurs. These trends appear to be the same for all three components of turbulence.

Gust Velocity RMS Correlation with Surface Wind Measurements

An attempt was made to define a relationship between routine meteorological data from established U.S.W.B. stations and the rms of observed gust velocities. The following assumptions and simplifications were made:

- The stations were sufficiently close to the flight routes.
- The wind recorded at the 3-hour time period nearest the flight time was representative of the wind at flight time.

A gust factor was computed (similar to reference 5.12) by dividing the maximum wind speed by the average wind speed for one day as follows:

$$G_f = \frac{\text{MAX. WIND FOR 24 HOURS}}{\text{AVG. WIND FOR 24 HOURS}} \quad (5.16)$$

Daily gust factors are plotted versus time in Figure 5.75. For the McConnell route, the mean value is approximately 1.9, with extreme values as high as 7.0.

The 3-hour winds for each test were multiplied by the gust factor and compared to the maximum rms value recorded as shown in Figure 5.76. It appears that there is a relationship of increasing gust velocity rms with increases in the product of gust factor and wind speed.

Gust Velocity RMS Regression Models

Correlation of the Phase III gust velocity rms values with some of the regression models from other turbulence studies is currently being investigated. Results of some of these studies using the LO-LOCAT Phases I and II data have been prepared and are presented herein. These analyses are for the vertical component of turbulence only.

The regression models presented in Tables 5.2 through 5.5 have been tested with the LO-LOCAT Phases I and II data. These tables show the average percent difference between the actual recorded gust velocity rms value and the value predicted by the model. They were determined by computing the percentage difference between each sample and the value predicted by the applicable regression model, and then averaging the absolute values for all these percentage differences.

It should be pointed out that the Phases I and II data utilized in this analysis do not contain any gust velocity rms values below 2.40 fps. As explained in the discussion of Forecasting Techniques in Section IV, rms values below this magnitude have shown poor correlation with the forecast data. Thus, these lower gust velocity rms values have been excluded from the data included in this regression model study. Exclusion of these data decreased the percentage difference values.

In Reference 5.1, regression models are presented for flight over each of three different types of terrain: smooth, low mountains, and high mountains. In these equations, gust velocity rms value is expressed as a linear function of mean wind speed. The equations are based on the B-66B Low-Level Gust Study. The results using these models are shown in Table 5.2.

TABLE 5.2
REGRESSION MODELS BASED ON B-66B AIRPLANE LOW LEVEL GUST STUDY DATA

Terrain Type	Model	Percent Different
High Mountains	$\sigma_{t_w} = 5.91 + 0.1W$	114.038
Low Mountains	$\sigma_{t_w} = 4.27 + 0.07 W$	64.028
Desert	$\sigma_{t_w} = 2.45 + 0.12 W$	39.046
Plain	$\sigma_{t_w} = 2.45 + 0.12 W$	86.474

As can be seen, the percentage differences are quite large.

Table 5.3 presents some of the regression models derived from data obtained during the B-52G/H Flight Load History Program (Reference 5.2) from May 1963 to May 1964. Not all the models were tested with the Phases I and II data because the height difference between the 700 and 850 mb levels, which occurs as a variable in some of the models, was not measured. In addition, some of the models tested are not presented in the table because of redundancy. Although more than 1200 hours of usable data were obtained, the B-52 program was limited by the lack of meteorological instrumentation and by the fact that accelerations were used to estimate the gusts.

TABLE 5.3

REGRESSION MODELS BASED ON DATA OBTAINED DURING B-52G/H AIRPLANE
FLIGHT LOAD HISTORY PROGRAM

Terrain Type	Model	Percent Difference
Plains	$\sigma_{t_v} = 3.258 + 0.830 \exp\left[\frac{(S_T - 12.3)^2}{13}\right] - 1.031 \times 10^{-4} H + 1.758 \times 10^{-4} (W)^2 + 0.167 \Gamma$	33.091
High Mountains	$\sigma_{t_v} = 3.316 + 1.070 (S_{SE})^2 - 1.264 \times 10^{-4} H + 7.372 \times 10^{-3} W$	14.378
Low Mountains	σ_{t_v} = Same as High Mountains	16.926
High Mountains	$\sigma_{t_v} = 3.345 + 0.735 \exp\left[\frac{(S_T - 12.3)^2}{8}\right] - 1.241 \times 10^{-4} H + 4.875 \times 10^{-3} W$	17.327
Low Mountains	σ_{t_v} = Same as High Mountains	19.102
High Mountains	$\sigma_{t_v} = 3.195 + 1.720 S_{SE}$	14.570
Low Mountains	σ_{t_v} = Same as High Mountains	20.951

The equations presented are in terms of absolute altitude (H), in feet, true solar time-of-day (S_T), in hours, and sine of the solar elevation (S_{SE}).

Table 5.4 presents some derived regression models, based on Phases I and II data, that are analogous to the Reference 5.1 models previously shown, in that the only independent variable is the mean wind speed.

TABLE 5.4
REGRESSION MODELS BASED ON PHASES I AND II DATA

Terrain Type	Model	Percent Difference
High Mountains	$\sigma_{t_v} = 3.4198 + 0.02356 W$	17.324
Low Mountains	$\sigma_{t_v} = 3.3361 + 0.01779 W$	17.816
Desert	$\sigma_{t_v} = 3.4857 + 0.004203 W$	13.257
Plains	$\sigma_{t_v} = 2.9269 + 0.04086 W$	15.311

The models of Table 5.4 indicate an acceptably low percentage error but they should be used with caution. The equations indicate that gust velocity rms values can be considered constant except for a small correction. This is not a bad assumption most of the time, but these models fail in predicting high gust values. Since the regression coefficients are quite small, very strong winds would be required to predict even moderate rms values.

In conjunction with this reasoning, it must be pointed out that wind speed and terrain are obviously not the only factors which determine gust velocity magnitude. In Reference 1.2, altitude above the terrain and atmospheric stability were shown to be very important influences on the magnitude of gust velocity rms values at low altitudes. Other factors influencing turbulence level include time-of-day, season of the year, geographic location, wind gradients, temperature gradients, synoptic weather patterns, and other variables. Thus, any analysis of turbulence levels as a function of wind only will not, under most circumstances, provide the exact values of gust velocity rms recorded, although trends can be established from the relationships. It should also be pointed out that in Reference 1.2, the slopes and intercepts of the gust velocity rms-wind linear relationships for Phases I and II data are presented as a function of terrain, absolute altitude, and atmospheric stability. All of the gust velocity rms values recorded are included in that analysis, (i.e., even those rms values < 2.4 fps).

The equations in Table 5.3 present gust velocity rms values as a function of more than just terrain and wind speed. As previously discussed, absolute altitude is included as well as solar time-of-day and sine of solar elevation. These latter two variables do relate to season of the year and atmospheric stability. The relationship between time-of-day and stability for the Phases I and II data is presented in Reference 1.2.

The Phases I and II data have also been analyzed with respect to the combination of wind speed and sine of solar elevation. Some preliminary regression models for vertical gust velocity rms magnitudes are presented in Table 5.5.

TABLE 5.5

REGRESSION MODELS BASED ON PHASES I AND II DATA

Terrain Type	Model	Percent Difference
Desert	$\sigma_{t_v} = 1.97 (S_{SE})^2 + 2.65$	10.3
Low Mountains	$\sigma_{t_v} = 1.58 (S_{SE})^2 + 3.24$	16.6
Low Mountains	$\sigma_{t_v} = 1.46 (S_{SE})^2 + .014 (W) + 2.94$	16.0
High Mountains	$\sigma_{t_v} = 0.663 [(W)^{0.25} (S_{SE})^{0.80}] + 2.05$	13.8

DERIVED EQUIVALENT GUST VELOCITY

An approximate value of derived equivalent gust velocity (U_{de}) was calculated for each turbulence sample. These values were used to establish the approximate turbulence level encountered and as an immediate guideline in determining if gust encounters were of a magnitude to warrant an airplane structural inspection. Maximum incremental acceleration from a one g mean was determined from "quick-look" strip charts of vertical acceleration at the airplane center of gravity. Computation of U_{de} was accomplished using the equation:

$$U_{de} = \left[\frac{2W}{C_L \rho_0 S V_e K_g} \right] \Delta N z_{cg} \text{ (feet/second)} \quad (5.17)$$

where K_g , the gust alleviation factor, is expressed as:

$$K_g = \frac{.88\mu}{5.3 + \mu} \quad (5.18)$$

and μ , the dimensionless airplane mass ratio is defined by:

$$\mu = \frac{2W}{C_L \rho_0 g S} \quad (5.19)$$

Using the equation of state, ρ (air density) may be expressed as:

$$\rho = \frac{\rho_0 T_0}{P_0} \left(\frac{P_0}{T_0} \right) = .0412 \frac{P_0}{T_0} \left(\frac{lb \ sec^2}{ft^3} \right) \quad (5.20)$$

The values of U_{de} equation constants for the T-33A airplane are defined below:

c = mean aerodynamic chord = 6.72 feet

g = gravitational constant = 32.2 feet/sec²

ρ_0 = standard day air density = .002378 slug/feet³

S = wing area = 238 feet²

Constant values were determined for the U_{de} equation variables ($C_{L_0} P_s/T$, W and V_e) to facilitate U_{de} calculations in the field. This was accomplished by using an average gross weight (W) for the airplane over the test route, an equivalent airspeed (V_e) approximated by target test airspeed, and the slope of the lift coefficient versus angle of attack curve (C_{L_a}) for a Mach number equivalent to the target airspeed and the average altitude. The ratio of static pressure to ambient temperature (P_s/T_a) was estimated from data obtained during the LO-LOCAT Phases I and II Program. Values for P_s/T_a were calculated by averaging the Phases I and II data over a corresponding seasonal time period for each similar route leg. The values for these variables are listed below:

$$C_{L_a} = 5.95/\text{radian}$$

$$W = 12,500 \text{ lbs.}$$

$$V_e = 591.15 \text{ feet/sec.}$$

$$P_s/T_a = .0534 \frac{\text{in. hg.}}{\text{°R}} \text{ McConnell (all legs)}$$

$$P_s/T_a = .0500 \frac{\text{in. hg.}}{\text{°R}} \text{ Edwards (legs 1, 3, 5, and 8)}$$

$$P_s/T_a = .0550 \frac{\text{in. hg.}}{\text{°R}} \text{ Edwards (legs 2 and 4)}$$

$$P_s/T_a = .0528 \frac{\text{in. hg.}}{\text{°R}} \text{ Edwards (legs 6 and 7)}$$

Substitution of the above constants in Equation (5.17) gives the following equations for calculations of U_{de} from "quick-look" strip charts of N_{ZCG} :

$$U_{de} = 16.31\Delta N_{ZCG} \text{ (McConnell, all legs)} \quad (5.21)$$

$$U_{de} = 16.18\Delta N_{ZCG} \text{ (Edwards, legs 1, 3, 5, and 8)} \quad (5.22)$$

$$U_{de} = 16.37\Delta N_{ZCG} \text{ (Edwards, legs 2 and 4)} \quad (5.23)$$

$$U_{de} = 16.29\Delta N_{ZCG} \text{ (Edwards, legs 6 and 7)} \quad (5.24)$$

The values of U_{de} are tabulated in Appendix VI for each turbulence sample. The maximum vertical gust velocity for each turbulence sample is also tabulated.

Values of U_{de} and maximum vertical gust velocity were categorized with respect to terrain and cumulative probability calculated for each parameter. These data are shown in Figures 5.77 through 5.81 for the high mountain, low mountain, plains, desert, and water terrain categories, respectively. The cumulative probability of the maximum calculated vertical gust velocity and U_{de} for the combined McConnell and Edwards routes were also computed and the two cumulative probability distributions are presented in Figure 5.82.

These distributions indicate that U_{de} consistently underestimated the maximum vertical gust velocities for the higher gust velocities and overestimated them at the lower gust velocities.

TURBULENCE SPECTRA

Power spectra were calculated for 429 out of 985 four and one-half minute turbulence samples. These samples were evaluated for instrumentation anomalies, low signal-to-noise, high coherency, and nonhomogeneous turbulence. Approximately 150 samples not falling in these categories were analyzed for conformance to isotropic theory, comparison to mathematical spectra models, and scale lengths.

Instrumentation Anomalies

An example of power spectra, with suspected instrumentation problems, is presented in Figure 5.83. Here it is quite obvious that the spectra are suspect due to the large hump in the lateral spectra, which occurs at the airplane short period mode, and due to the irregular shape of the vertical spectra. Experience has shown that when spectra such as that shown in Figure 5.83 are obtained, it can ultimately be proven to be caused by instrumentation problems.

Low Turbulence Level

An example plot of power spectra where the turbulence level was low is presented in Figure 5.84. Turbulence data samples obtained during Phase III containing low signal-to-noise ratios typically have σ_t values less than 1.5 fps, irregularly shaped spectra (i.e., spectra which do not have a definite -5/3 slope and in which the power turns upward at the higher frequencies), and uncommonly large integral scale lengths.

Coherency

The statistical independence of the gust components u , v , and w , is evaluated using the coherency function. The coherency function between u and v , and v and w , is calculated, e.g.,

$$\gamma_{uv}^c(k) = \frac{[\Phi_{uv}(k)]^2}{\Phi_u(k) \Phi_v(k)} \quad (5.25)$$

Two parameters are said to be completely dependent (coherent) if their coherency function is equal to 1.0 and completely independent (not coherent) if the coherency is equal to zero. Due to statistical variations in the recorded data, electronic noise, etc., a coherency of zero is impossible to achieve. The gust velocity components are therefore considered to be independent if the coherency function approaches zero.

The coherency function is used as an aid in defining those turbulence samples which are invalid. Electronic noise and instrumentation malfunctions such as sensitivity changes will increase coherency since the same measurements are used in calculating the three gust velocity components.

The average coherency function is presented in Figure 5.85. Also presented is a band representative of the scatter in the data. The average coherency function was calculated by determining the value of the coherency function of each sample at spatial frequencies of 7×10^{-5} , 1×10^{-4} , 1.5×10^{-4} , 2×10^{-4} , 3×10^{-4} , 4×10^{-4} , 6×10^{-4} , 1×10^{-3} , 1.5×10^{-3} , 2×10^{-3} , 4×10^{-3} , 7×10^{-3} , 1×10^{-2} , and 1.5×10^{-2} cpf. The values obtained at each of these frequencies were then averaged and the standard deviation calculated. The average line in Figure 5.85 was obtained by plotting the average value obtained at each of the above spatial frequencies. The scatter band was obtained by plotting the mean plus and minus the standard deviation of the data at each point.

Homogeneity

To accurately define valid scale lengths and spectra shape only turbulence samples considered to be homogeneous can be used.

Homogeneity is the property which in space coordinates corresponds to the stationarity property in time coordinates. The entire analyses of time histories of gust velocities as recorded by an airplane are based upon the validity of Taylor's hypothesis. Assuming Taylor's hypothesis to be valid, then the stationarity of the time history is indicated by the spatial homogeneity of the turbulence sample. Detailed discussions of Taylor's hypothesis may be found in References 5.3 and 5.11. An indication of turbulence homogeneity was obtained by dividing the spectrum of the middle third of a data sample by the spectrum of the entire sample. Complete homogeneity is indicated when the spectra ratio averages approximately 1.0.

Example spectra and homogeneity plots for data considered to be nonhomogeneous are presented in Figures 5.86 and 5.87. Similar plots for homogeneous data are presented in Figures 5.88 and 5.89. Time history plots of the nonhomogeneous and homogeneous data are presented in Figures 5.33 and 5.34.

Data showing average homogeneity for the turbulence data considered to be homogeneous is presented in Figure 5.90. The data plotted consists of a mean line and the scatter band. The latter band was developed in the same manner as for the coherency function.

Isotropy

A turbulent field which is isotropic is one in which there is no preferred direction and therefore all average functions describing this field must remain unchanged regardless of the rotation of the coordinate system.

Theoretical considerations and experimental evidence have shown that most fine or small scale structure of actual anisotropic turbulence is nearly isotropic (local isotropy). The four and one-half minute data samples obtained during this program are considered to be "local" with respect to large scale turbulence and have been analyzed for isotropic characteristics.

According to References 5.3, 5.4, and 5.11, the isotropic characteristics will follow $\Phi_v(k)/\Phi_v(k) = 1$ and $\Phi_u(k)/\Phi_v(k)$ will vary from 2.0 to 0.75 with frequency and scale length. The characteristics of the experimental data were established by dividing the unnormalized power spectra of u and w by the power spectrum of v .

In this manner, if the turbulence is isotropic, the w/v spectra ratio will be equal to 1.0 and the u/v ratio will approach a form similar to that in Figure 5.91. The data in Figure 5.91 illustrate how the u/v ratio varies with scale length and was calculated by taking the ratio of the longitudinal to lateral von Karman equations for turbulence spectra.

Data showing the average isotropic characteristics and the scatter band for Phase III homogeneous turbulence samples are presented in Figure 5.92

Normalized Spectra

The power spectra for each condition were normalized by dividing the power magnitude by σ_t^2 . Since turbulence spectra shift up and down in power with a respective increase or decrease in σ_t^2 , normalizing the data in this manner permits a comparison of the spectra shape without having shifts due to amplitude changes. The power spectra were also normalized by $\sigma_t^2 L$, that is, the power magnitude was divided by the $\sigma_t^2 L$ product. By normalizing the data in this manner and plotting the data versus kL , variations due to both σ_t and L are removed.

Power spectra normalized by σ_t^2 and $\sigma_t^2 L$ are presented in Figures 5.93 and 5.94, respectively. The data in Figure 5.93 represent the average of turbulence spectra for the McConnell and Edwards routes. The data normalized by $\sigma_t^2 L$ in Figure 5.94 are based on an average of 52 turbulence samples except for the very low frequencies where the number of samples decrease to a minimum of 5. The turbulence spectra agree very well with the -5/3 logarithmic relationship expressed by Kolmogorov's theory. In general, the shape of the spectra agree very well with the von Karman mathematical spectra except at the lowest frequencies. This is more readily seen in Figure 5.95 which is a plot of the ratio of the experimental and von Karman spectra. As can be seen, the value of the PSD is greater for the experimental data than for the von Karman relationship at low f . This difference was also observed in the Phases I and II data. Only moderate confidence can be placed on the data at the lowest kL values due to the low number of values averaged. It is anticipated that flight at higher speeds which has been performed over leg 8 of the Peterson route will produce additional data in the lower kL region.

Experimental/Mathematical Spectra Comparison

Use of the power spectral density approach in aircraft design is predicated upon the availability of a mathematical model of the PSD curve. Many mathematical expressions have been proposed to represent the atmospheric turbulence spectra. The expressions most widely used in the aircraft industry at the present time include expressions suggested by Theodore von Karman (Reference 5.5) and by H. L. Dryden (Reference 5.6). These expressions vary according to the gust velocity component being represented and are as follows.

von Karman Vertical and Lateral -

$$\left[\frac{\Phi_v(k)}{\sigma_t} \right]_K = \frac{L_K \cdot [2 + 377.5(L_K, k)^2]}{[1 + 70.78(L_K, k)^2]^{11/6}} \quad (5.26)$$

von Karman Longitudinal -

$$\left[\frac{\Phi_u(k)}{\sigma_t^2} \right]_K = \frac{4L_{Ku}}{[1 + 70.78(L_{Ku}k)^2]^{5/6}} \quad (5.27)$$

Dryden Vertical and Lateral -

$$\left[\frac{\Phi_v(k)}{\sigma_t^2} \right]_D = \frac{L_{Dv} [2 + 6(2\pi L_{Dv} k)^2]}{[1 + (2\pi L_{Dv} k)^2]^2} \quad (5.28)$$

Dryden Longitudinal -

$$\left[\frac{\Phi_u(k)}{\sigma_t^2} \right]_D = \frac{4L_{Du}}{1 + (2\pi L_{Du} k)^2} \quad (5.29)$$

As suggested in Reference 5.7, the equations may be represented by the following general forms

Vertical and Lateral -

$$\frac{\Phi_v(k)}{\sigma_t^2} = \frac{2L[1 + 8\pi^2 a^2 k^2(n+1)]}{(1 + 4\pi^2 a^2 k^2)^{n+3/2}} \quad (5.30)$$

Longitudinal -

$$\frac{\Phi_u(k)}{\sigma_t^2} = \frac{4L}{(1 + 4\pi^2 a^2 k^2)^{n+1/2}} \quad (5.31)$$

where a is related to the scale of turbulence, L , as follows:

$$a = \frac{L[(n-1)!]}{[\sqrt{\pi}(n-\frac{1}{2})!]} \quad (5.32)$$

Thus, depending upon the value of n chosen, various expressions for the power spectral density may be derived. If $n=1/2$ these general equations produce the Dryden expressions. The von Karman equations are the special form of the general equations when $n=1/3$.

These expressions are being compared to the experimentally determined spectra from the LO-LOCAT program in order to investigate the validity of using the von Karman or Dryden expressions in design. These comparisons are made by dividing each experimental spectrum by the mathematical expression in question and plotting this ratio versus spatial frequency. A ratio of 1.0 indicates perfect correlation of the experimental and mathematically defined spectra. These plots are shown in Appendix IV.

Average values of these experimental to mathematical ratios have been computed and plotted. This is done by determining the value of the ratios for each turbulence sample at certain values of spatial frequency. These ratios are then averaged at each of the chosen frequencies. Approximately 150 turbulence samples determined to be homogeneous were used in calculating the averages. The results are shown in Figure 5.96.

Figure 5.96 also shows the good agreement of the von Karman expressions and experimentally determined spectra. This fact is supported by examining the standard deviations of the ratios for the individual sample about the average values. These data are shown in Table 5.6.

TABLE 5.6
EXPERIMENTAL/VON KARMAN DATA

Spatial Frequency (cpf)	Longitudinal		Lateral		Vertical	
	Average	Std. Dev.	Average	Std. Dev.	Average	Std. Dev.
0.0005	0.86	0.18	1.36	0.34	1.29	0.42
0.0007	0.95	0.18	1.44	0.34	1.37	0.41
0.00010	1.10	0.14	1.46	0.29	1.39	0.34
0.00015	1.24	0.14	1.40	0.24	1.33	0.24
0.0002	1.15	0.18	1.13	0.20	1.08	0.20
0.0003	1.05	0.20	0.88	0.20	0.88	0.23
0.0004	0.99	0.20	0.78	0.22	0.81	0.22
0.0006	0.92	0.17	0.70	0.20	0.79	0.18
0.0010	0.94	0.17	0.86	0.21	0.88	0.20
0.0015	1.00	0.18	0.94	0.17	0.96	0.20
0.002	0.99	0.18	0.99	0.19	1.08	0.22
0.004	1.06	0.23	1.12	0.21	1.09	0.21
0.007	1.06	0.19	1.14	0.23	1.13	0.24
0.010	1.05	0.21	1.17	0.22	1.12	0.20
0.015	1.01	0.18	1.10	0.24	1.18	0.29

The Dryden expressions do not agree well with the experimental data, especially at the higher frequencies. The basic disagreement is in the inertial subrange where the Dryden expressions have a -2 logarithmic slope rather than the -5/3 slope of the data.

The results discussed here are similar to those obtained during LO-LOCAT Phases I and II. During that program, expressions suggested by U. O. Lappe (Reference 5.8) and Lumley and Panofsky (Reference 5.11) were investigated. The Lumley and Panofsky expression, which is for the longitudinal component only, agreed well with the experimental data. The Lappe expression, however, showed the same type of disagreement as that discussed above for the Dryden expressions. During the latter half of the Phase III program, the Lumley and Panofsky expression for the longitudinal, and an expression suggested by Busch and Panofsky for the vertical and lateral components, are also being studied.

Turbulence Scale Length

The atmospheric turbulence integral scale length, L , is an indication of the average eddy size associated with the longitudinal gust velocity component. The value of the scale length must be known in order to determine the power spectral density from either the von Karman or Dryden

mathematical expressions (Equations (5.26) through (5.29)).

Scale lengths can be computed from either the autocorrelation function or the power spectrum (Reference 5.4). Scale lengths are computed from power spectra in the following manner. A standard deviation, σ_T , covering only the high frequency range of the spectrum is defined, i.e.,

$$\sigma_T = \left[\int_{k_2}^{k_3} \Phi(k) dk \right]^{1/2} \quad (5.33)$$

For calculations of L using the von Karman expressions, Equations 5.26 and 5.27 are simplified by noting that, in the inertial subrange, $(Lk)^2$ and $70.78(Lk)^2 \gg 1$. The expression for $\Phi(k)$, from either Equation 5.26 or 5.27 is inserted in Equation 5.33 and the integration is carried out and solved for scale length, yielding Equations 5.34 and 5.35, respectively.

$$L_{kv} = .110 \left(\frac{\sigma_t}{\sigma_T} \right)_v^3 \left(\frac{1}{k_2^{2/3}} - \frac{1}{k_3^{2/3}} \right)^{3/2} \quad (5.34)$$

$$L_{ku} = .0717 \left(\frac{\sigma_t}{\sigma_T} \right)_u^3 \left(\frac{1}{k_2^{2/3}} - \frac{1}{k_3^{2/3}} \right)^{3/2} \quad (5.35)$$

Scale lengths to be used in the Dryden expressions are determined in the same manner. Equations 5.28 and 5.29 are simplified by noting that $(2\pi Lk)^2 \gg 1$ in the inertial subrange. The resulting equations obtained by inserting these simplified equations into Equation 5.33 and integrating are:

$$L_{Dv} = .152 \left(\frac{\sigma_t}{\sigma_T} \right)^2 \left(\frac{1}{k_2} - \frac{1}{k_3} \right) \quad (5.36)$$

$$L_{Du} = .101 \left(\frac{\sigma_t}{\sigma_T} \right)^2 \left(\frac{1}{k_2} - \frac{1}{k_3} \right) \quad (5.37)$$

Equations 5.34 and 5.36 are expressions for longitudinal scale length as computed from either the vertical or lateral gust velocity components while Equations 5.35 and 5.37 represent longitudinal scale length as computed from the longitudinal component of gust velocity.

Scale lengths may also be calculated by using the area under the gust velocity autocorrelation curve (Reference 5.3) where:

$$L = G_s \int_0^{\tau_L} [R(\tau)/R(0)] d\tau \quad (5.38)$$

The autocovariance function $R(\tau)$ is normalized by dividing it by $R(0)$, where:

$$R(0) = \int_0^{\infty} \Phi(k) dk = \sigma_t^2 \quad (5.39)$$

During Phases I and II of the LO-LOCAT Program, scale lengths were calculated from the autocorrelation function for selected data. The results of this method were compared to scale lengths obtained for the same data from Equations 5.34 and 5.35. The results agreed very well, lending credence to the assumptions made in deriving Equations 5.34 and 5.35.

Since the von Karman expressions give an accurate representation of the experimental spectra, the scale lengths from these expressions are being analyzed statistically. The cumulative probability distributions of these data are shown in Figure 5.97.

As mentioned above, the scale lengths tend to increase in magnitude as altitude increases. The scale length cumulative probability is plotted in Figures 5.98, 5.99, and 5.100 to illustrate this point. As can be seen in these figures, the scale length computed from the vertical component is more sensitive to altitude changes.

During Phases I and II of the LO-LOCAT Program, scale length was found to be a function of more than just height above the ground. At the 250-foot altitude, scale length was found to increase with increasing terrain roughness. At the 750-foot altitude, atmospheric stability appeared to have an effect on scale length. As the atmosphere became more unstable, scale length showed a tendency to increase in magnitude. These trends were more evident for scale length computed from the vertical component than from the other two components.

The Phase III data are being investigated for the same types of trends. Figure 5.101 shows variations of mean scale length values with terrain and altitude. Scale lengths at the 250-foot altitude tend to increase with increasing terrain roughness, while those recorded at 750 feet are somewhat inconsistent with relationship to terrain.

The mean values of scale length are plotted as a function of atmospheric stability for each of the test altitudes in Figure 5.102. No consistent relationships are apparent in these particular data.

The average scale length values recorded thus far during the Phase III program are 664, 572, and 462 feet for the longitudinal, lateral, and vertical components, respectively. Average corresponding values for all data recorded during Phases I and II were 387, 409, and 367 feet. As mentioned in the gust velocity rms discussion in this section, the values of σ_t being recorded during Phase III are greater in magnitude than the corresponding values recorded during Phases I and II. This is due to the longer wavelength turbulence being measured during Phase III. These larger gust velocity rms values increase the scale length values appreciably as can be seen in Equations (5.34) and (5.35)

The scale lengths analyzed in this report are for homogeneous turbulence conditions only. This is, of course, a preliminary analysis of these data. At the conclusion of Phase III, scale lengths from all three phases of the LO-LOCAT Program will be analyzed to provide values based upon large statistical samples.

According to Reference 5.9, the scale lengths for clear air turbulence below an altitude of 2,500 feet for use in von Karman equations are to be calculated as:

$$L_{K_v} = H \quad (5.40)$$

$$L_{K_v} = L_{K_x} = 184H^{1/3} \quad (5.41)$$

A comparison between the scale lengths recommended by these equations and those obtained so far during the LO-LOCAT Phase III Program are shown in Table 5.7.

TABLE 5.7

LO-LOCAT SCALE LENGTHS FOR VON KARMAN EXPRESSIONS COMPARED
TO THOSE RECOMMENDED BY MIL-I-008785A (USAF)

Absolute Altitude ~ Ft.	Reference 5.9 Recommended Scale Length ~ Ft.			Average LO-LOCAT Phase III Scale Length ~ Ft.		
	L_{K_x}	L_{K_y}	L_{K_z}	L_{K_x}	L_{K_y}	L_{K_z}
250	1159	1159	250	557	539	373
750	1670	1670	750	670	611	556

Although the Dryden expressions do not fit the LO-LOCAT data as well as the von Karman expressions, the Dryden expressions are used in aircraft design. Reference 5.9 states that use of the Dryden expressions is permissible when it is not feasible to use the von Karman forms. According to this reference, the scales of turbulence to be used in the Dryden equations for flight below 1,000 feet are:

$$L_{D_v} = H \quad (5.42)$$

$$L_{D_v} = L_D = 100H^{1/3} \quad (5.43)$$

Table 5.8 shows how the Phase III data are comparing with values calculated from Equations 5.42 and 5.43.

TABLE 5.8
LO-LOCAT SCALE LENGTHS FOR DRYDEN EXPRESSIONS COMPARED
TO THOSE RECOMMENDED BY MIL-F-008785A (USAF)

ABSOLUTE ALTITUDE ~ FT	REFERENCE 5.9 RECOMMENDED SCALE LENGTH ~ FT.			AVERAGE LO-LOCAT PHASE III SCALE LENGTH ~ FT.		
	L_{D_v}	L_D	L_D	L_{D_v}	L_D	L_D
250	630	630	250	470	468	366
750	909	909	750	479	512	478

As can be seen, the Phase III scale lengths included in this analysis do not agree well with those recommended in Reference 5.9. In general, scale lengths calculated from Equations 5.40 and 5.41 overestimate the Phase III experimentally determined scale lengths. The only exceptions to this overestimation occur for the longitudinal scale length computed from the vertical component for both the von Karman and the Dryden expressions. There is some increase in scale length with increasing altitude, as predicted by Equations 5.40 through 5.43.

According to Lappe in Reference 5.1, type of terrain may be taken into consideration by using the following formula for calculating L :

$$L = h_0 + H L_h \quad (5.44)$$

where L_h and h_0 are determined as follows:

Terrain Class	$\frac{L_h}{h}$	h_0
Smooth	2/3	135
Low Mountains	1/2	300
High Mountains	1/8	675

Values from Equation 5.44 are compared to Phase III scale lengths obtained over the McConnell and Edwards routes in Table 5.9.

TABLE 5.9
LO-LOCAT SCALE LENGTHS COMPARED TO THOSE
RECOMMENDED BY AFFDL-TR-67-122

Absolute Altitude ~ Ft	Type of Terrain	L FROM EQUATION 5.44 ~ FT	Average LO-LOCAT Phase III Scale Length ~ Ft		
			L_{K_u}	L_{K_v}	L_{K_w}
250	Smooth	402	621	472	282
250	Lo. Mount.	425	674	543	426
250	Hi Mount.	706	819	728	567
750	Smooth	635	635	581	550
750	Lo Mount.	675	722	688	506
750	Hi Mount.	769	742	628	627

It should be pointed out that L, as calculated in Reference 5.1, is designed for use in the mathematical spectra expression suggested therein, not for use in the von Karman equations. The Reference 5.1 mathematical expression was evaluated during Phases I and II. Those experimental data did not correlate well with that expression. However, the fact that terrain is considered in the calculation of L is in harmony with the results obtained for the 250-foot data during the LO-LOCAT Program. The results from Equation 5.44 agree better with the experimentally determined data than did results from Equations 5.40 and 5.41, where only altitude is considered.

VISCOUS DISSIPATION RATE

Dissipation of kinetic energy present in the atmosphere plays an important role in a complete atmospheric model. In the past, several investigators, using the dissipation of smoke clouds (or puffs), have estimated the viscous dissipation. The numerical results of these investigations vary considerably (Reference 1.2, Figure 4.75). Following the method shown in Reference 1.2, dissipation rates were calculated using the following equation:

$$\epsilon = .761 \sigma_t^3 / L_{K_1} \quad (5.45)$$

The small number of samples (277) were not categorized into stability classes. Figure 5.103 shows the cumulative probability of encountering a value equal to or greater than a given dissipation rate for each altitude. These data indicate that the dissipation rate decreases as the altitude increases from 250 feet to 750 feet, as expected. The mean for these data is somewhat less than that for Phases I and II.

MICROSCALES

It has been suggested by Kolmogorov that turbulence spectra should generally be a function of the kinematic viscosity and the rate at which the energy is dissipated. From a dimensional analysis approach, a length can be formulated as follows (Reference 5.10):

$$\eta = \left(\frac{v^3}{\epsilon} \right)^{1/2} \quad (5.46)$$

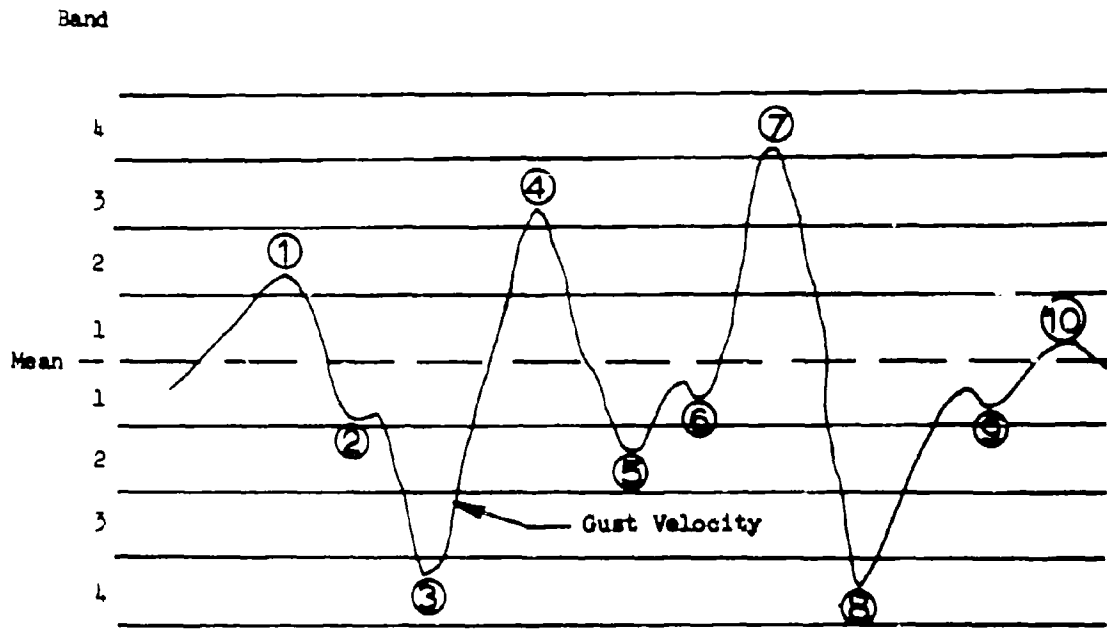
This length represents the eddy size at which the viscous dissipation forces become very strong. The value of η calculated for Phase III of LO-LOCAT is approximately one mm, which agrees well with other estimates for dissipation in the lowest layers of the atmosphere (Reference 5.11). Figure 5.104 shows the distribution of η for each test altitude. Increases in the scale length are suggested to be a function of altitude from this figure.

The Taylor microscale is also a measure of the smallest eddies responsible for viscous dissipation, and is given by the following equation:

$$\lambda = 4.4309 \left[\left(\frac{\mu}{\rho} \right) \left(\frac{L_{K_1}}{\sigma_t} \right) \right]^{1/2} \quad (5.47)$$

This value is the intercept of the parabola drawn to coincide with the vertex of the autocorrelation function. This length lies between the Kolmogorov microscale and the integral scale as reported by Lumley and Panofsky (Reference 5.11). Figure 5.10S shows the properties of the Taylor microscale for each test altitude.

Stability does not seem to influence this length to the extent which was observed for η . The microscales being measured during Phase III of LO-LOCAT are somewhat larger than those measured during Phases I and II. This is in line with the fact that Phase III integral scale lengths too are somewhat larger. The larger scale lengths are also attributed to the fact that the long turbulence wave lengths are being measured better during Phase III.



Band No.	Plus Peak Ident.	Minus Peak Ident.
1	10	
2	1	5
3	4	
4	7	3 8

② ⑥ ⑨ - Secondary Peaks
Not Counted

Figure 5.1 Leak Count Example

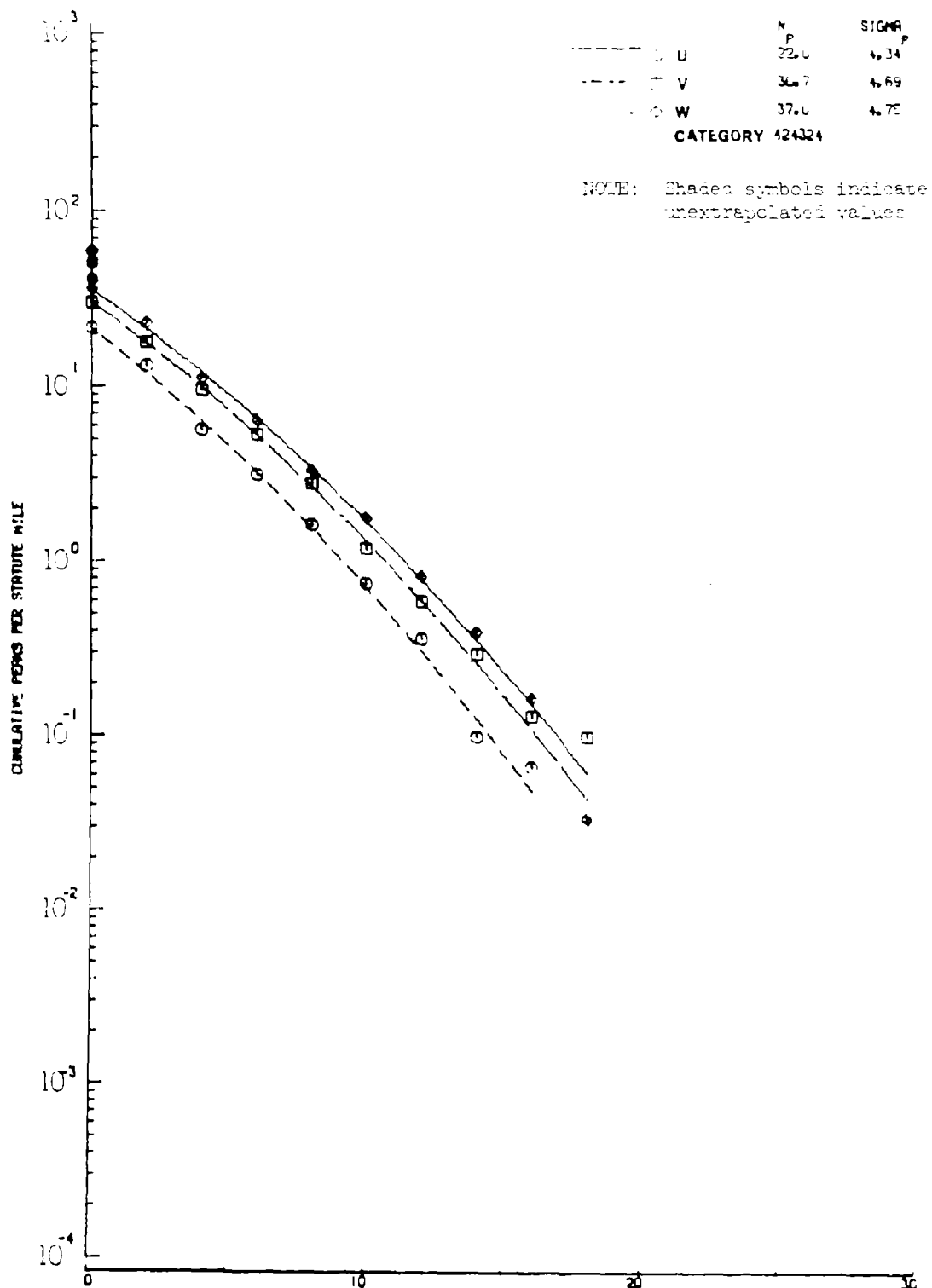
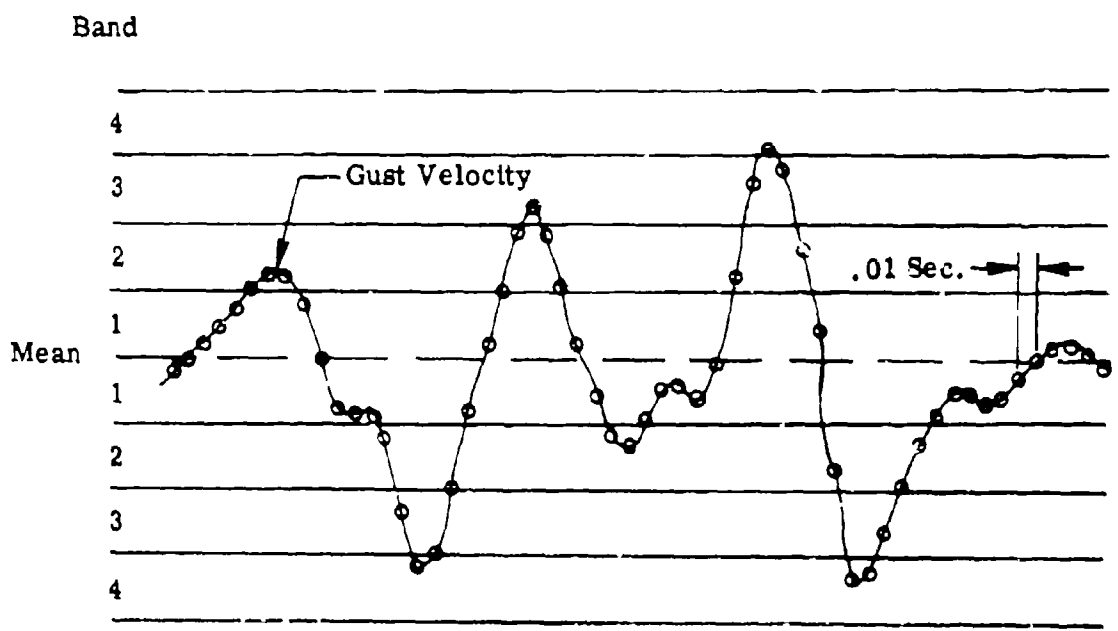


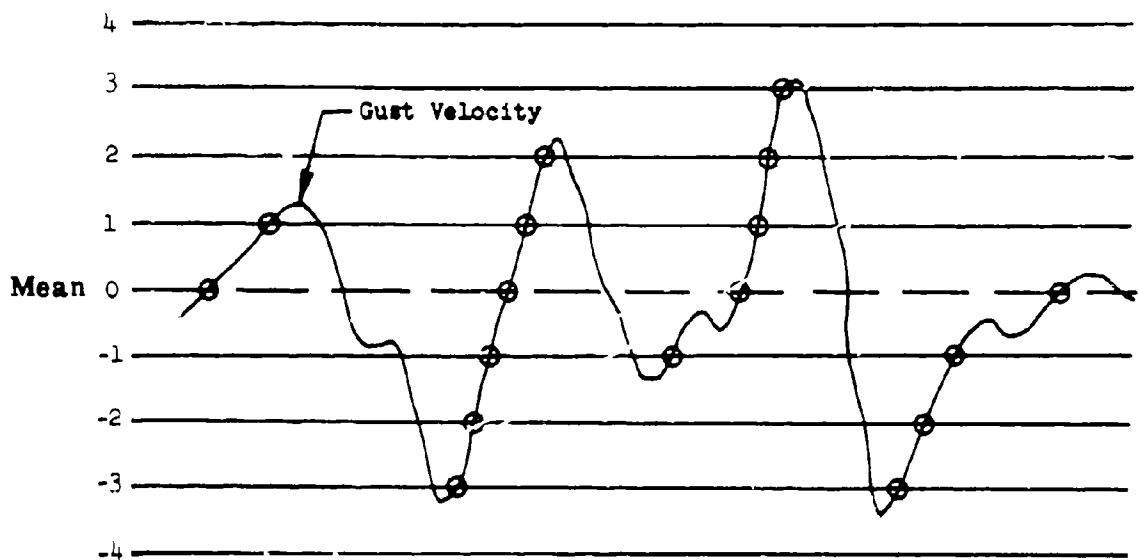
Figure 5.2 Peak Count Extrapolation Technique



Band No.	Occurrences
1	31
2	16
3	6
4	4

Figure 5.3 Amplitude Count Example

Gust Level ~ips



Level	Number of Crossings	Folded Number of Crossings
4	0	0
3	1	3
2	2	4
1	3	6
0	4	8
-1	3	
-2	2	
-3	2	
-4	0	

Figure 5.4 Level Crossing Count Example

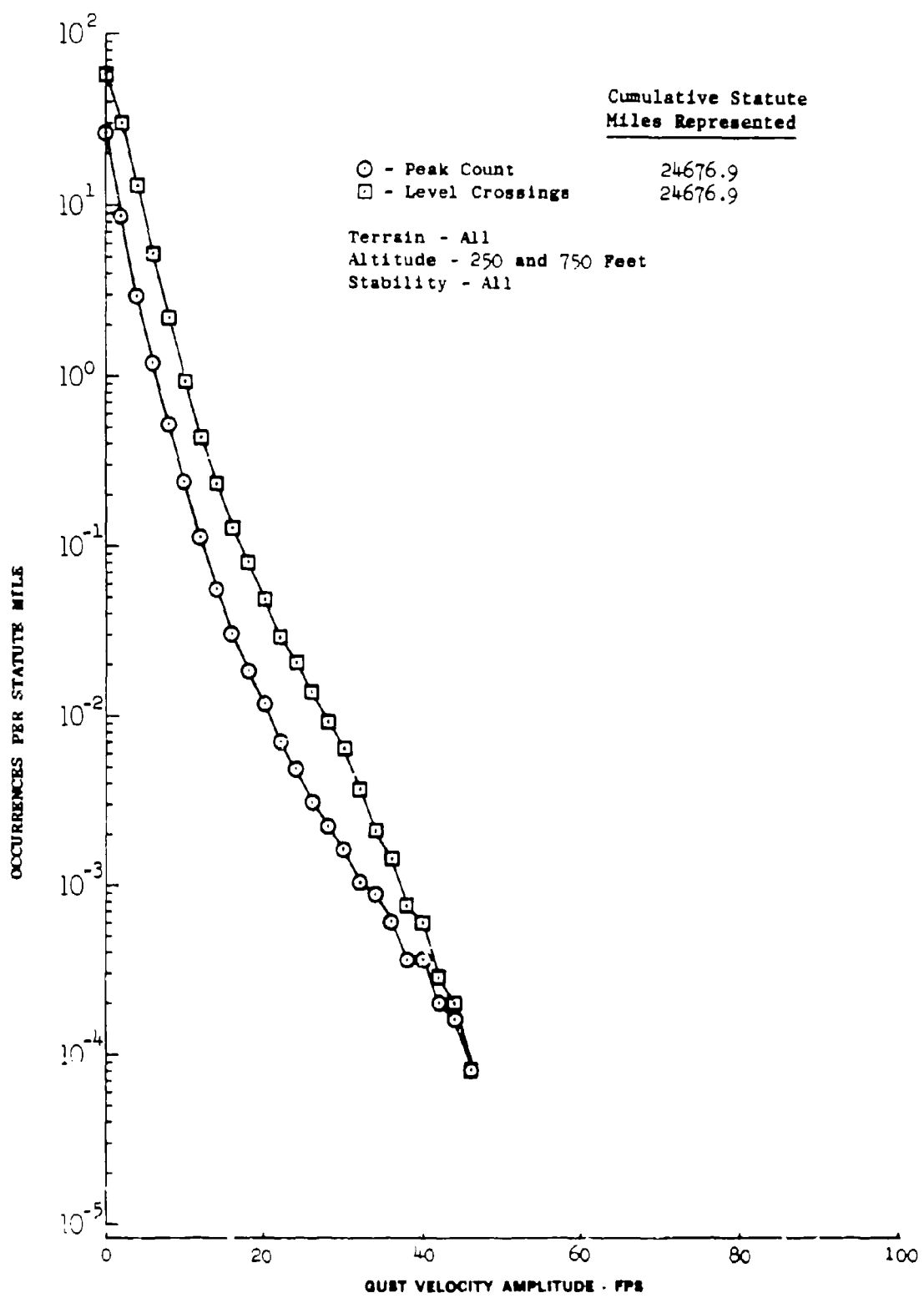


Figure 5.5 Comparison of Peak and Level Crossing Count Distributions - Longitudinal Gust Velocity

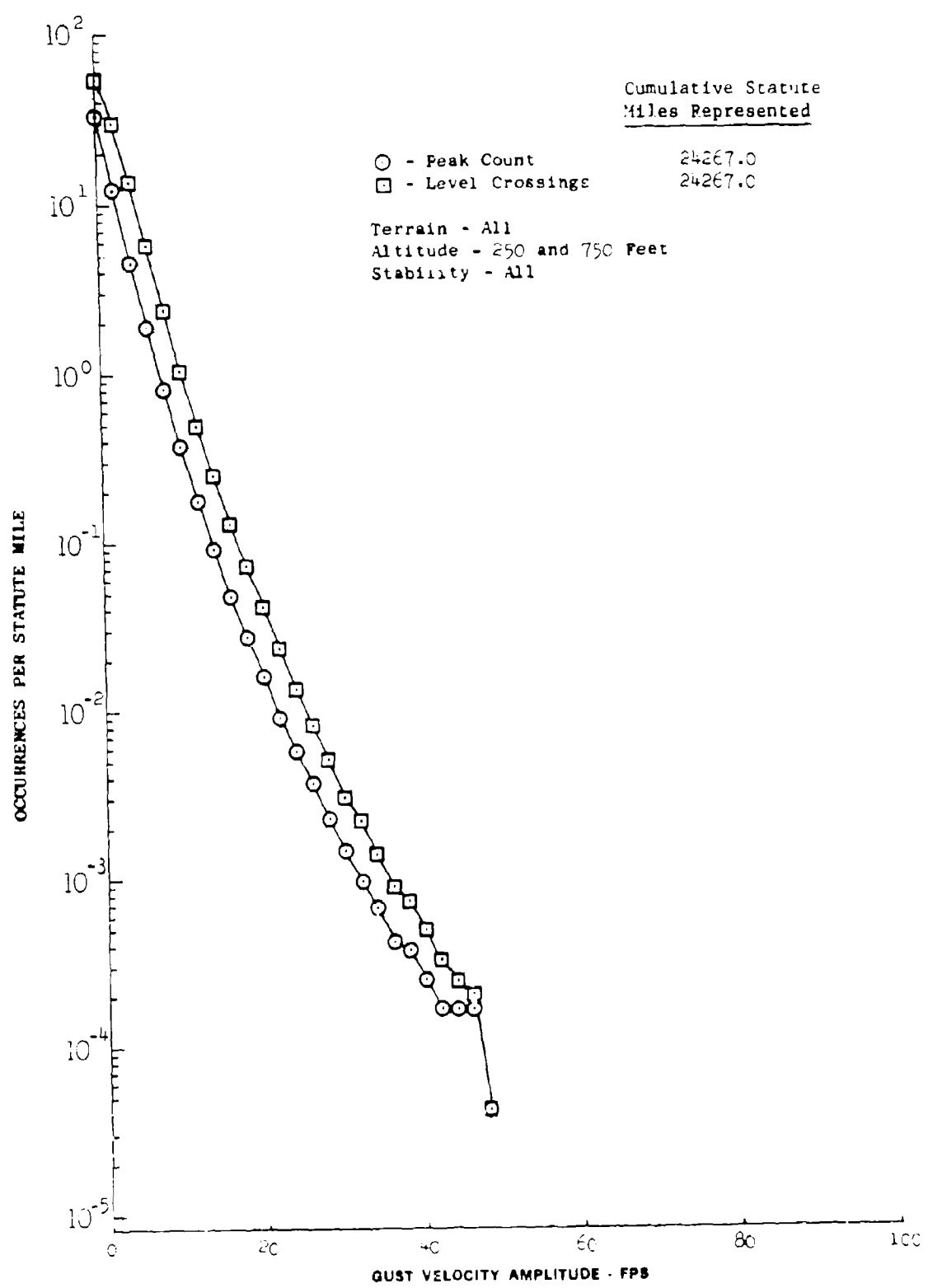


Figure 5. Comparison of Peak and Level Crossing Count Distributions - Lateral Gust Velocity

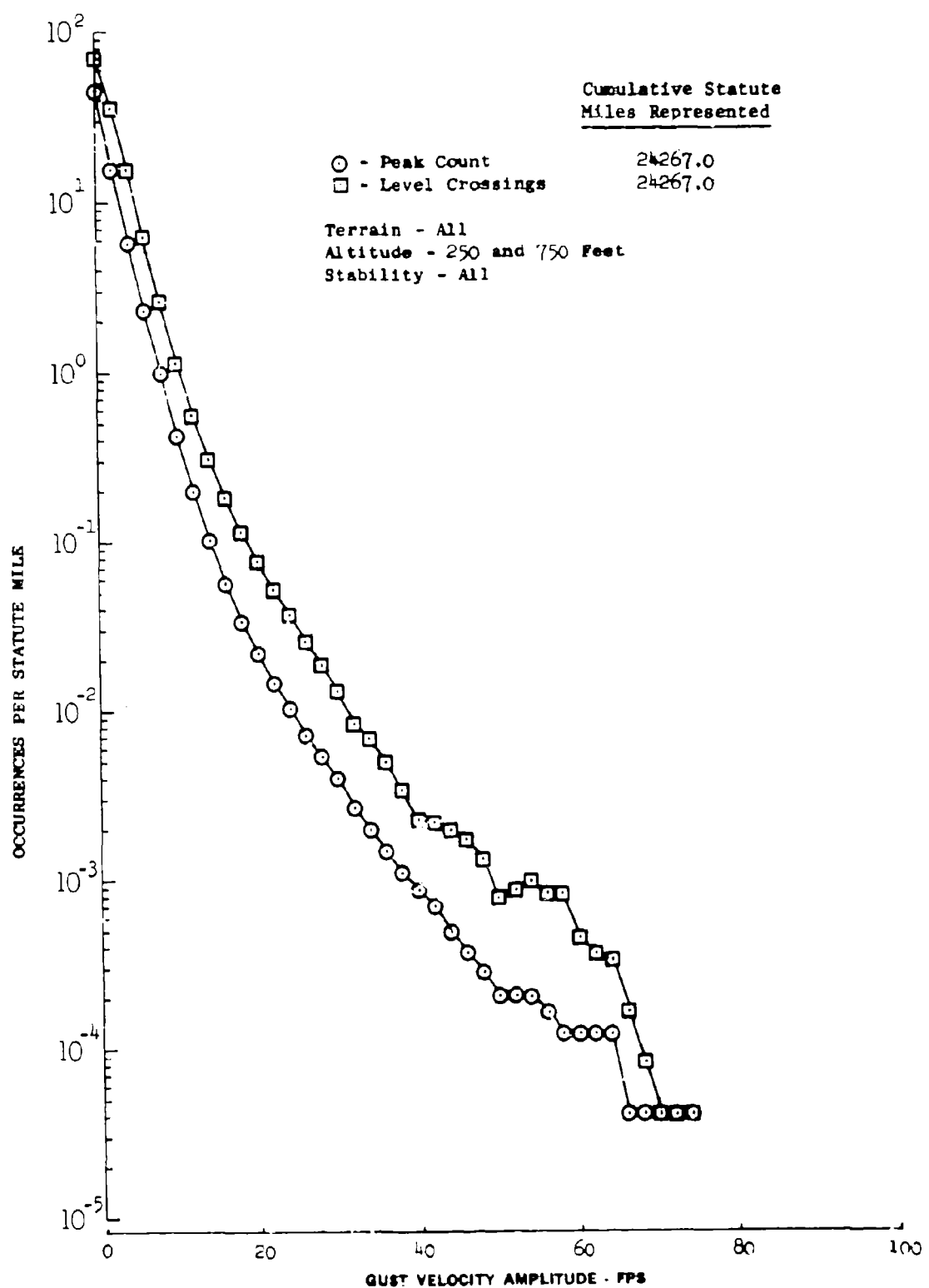


Figure 7 Comparison of Peak and Level Crossing Count Distributions - Vertical Gust Velocity

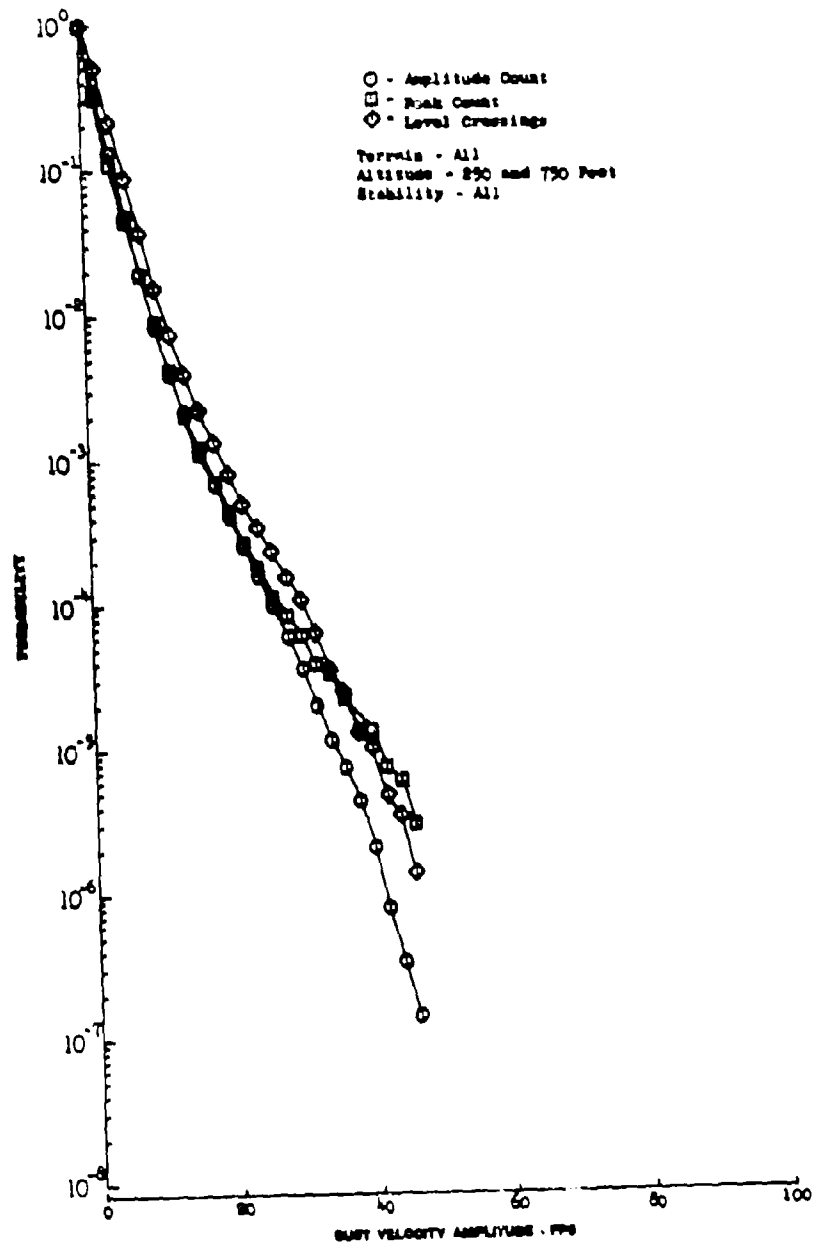


Figure 5.8 Comparison of Probability Distributions of Counting Techniques -
Longitudinal Gust Velocity

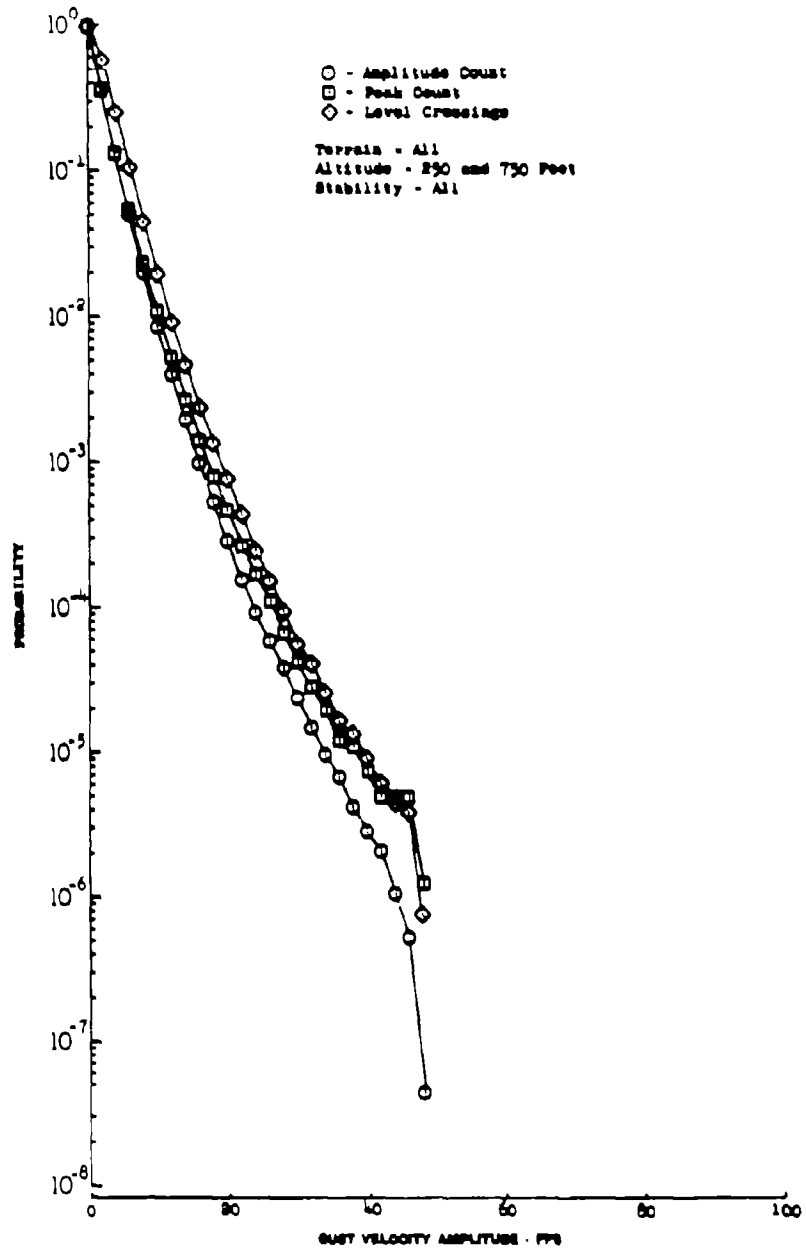


Figure 5.3 Comparison of Probability Distributions of Counting Techniques - Lateral Gust Velocity

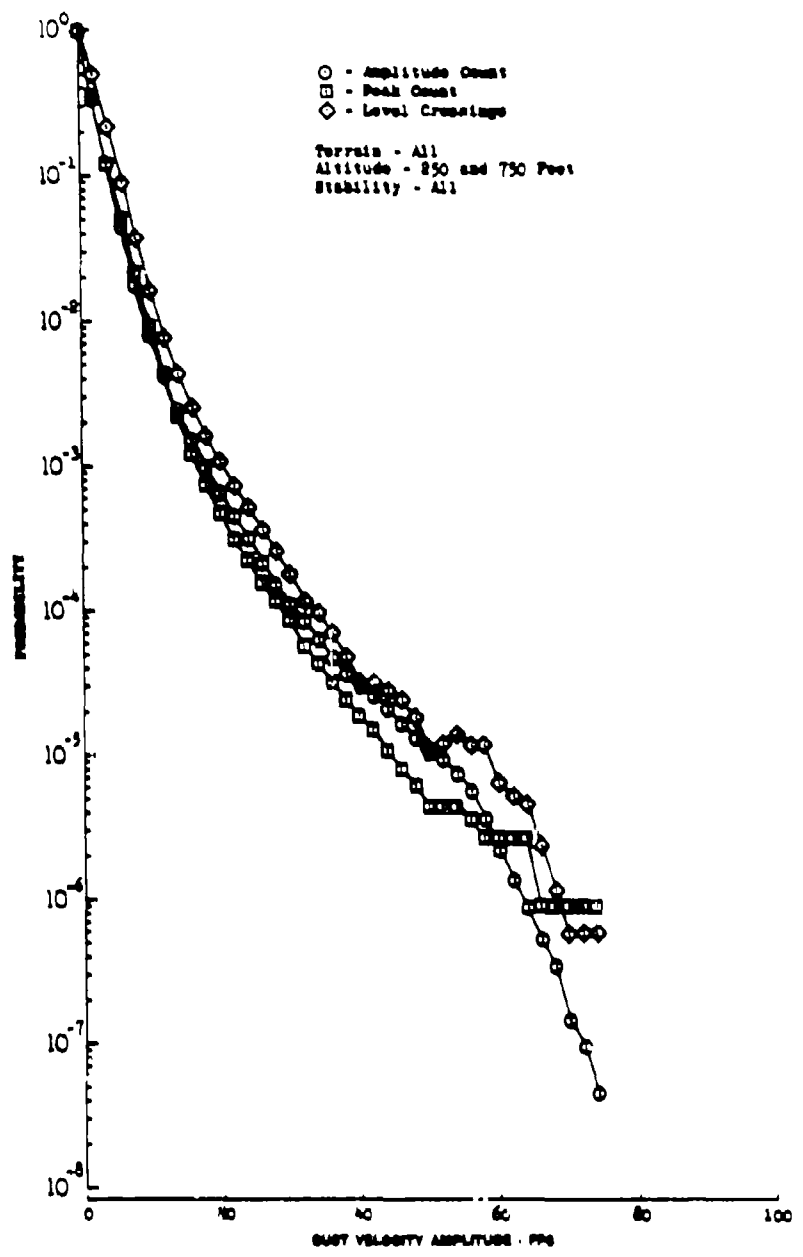


Figure 5.10 Comparison of Probability Distributions of Counting Techniques - Vertical Gust Velocity

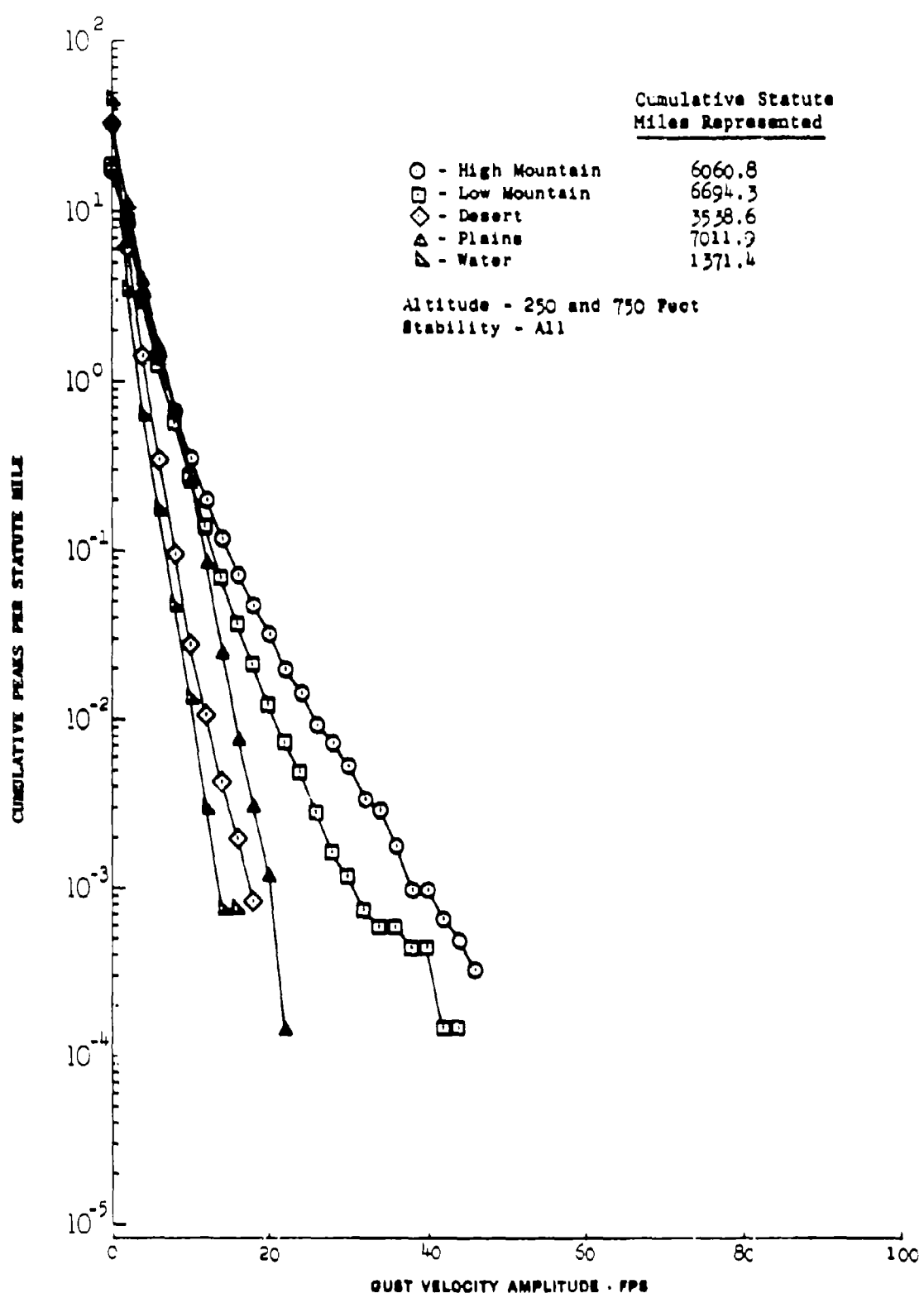


Figure 5.11 Terrain Effects on Longitudinal Gust Velocity Peaks

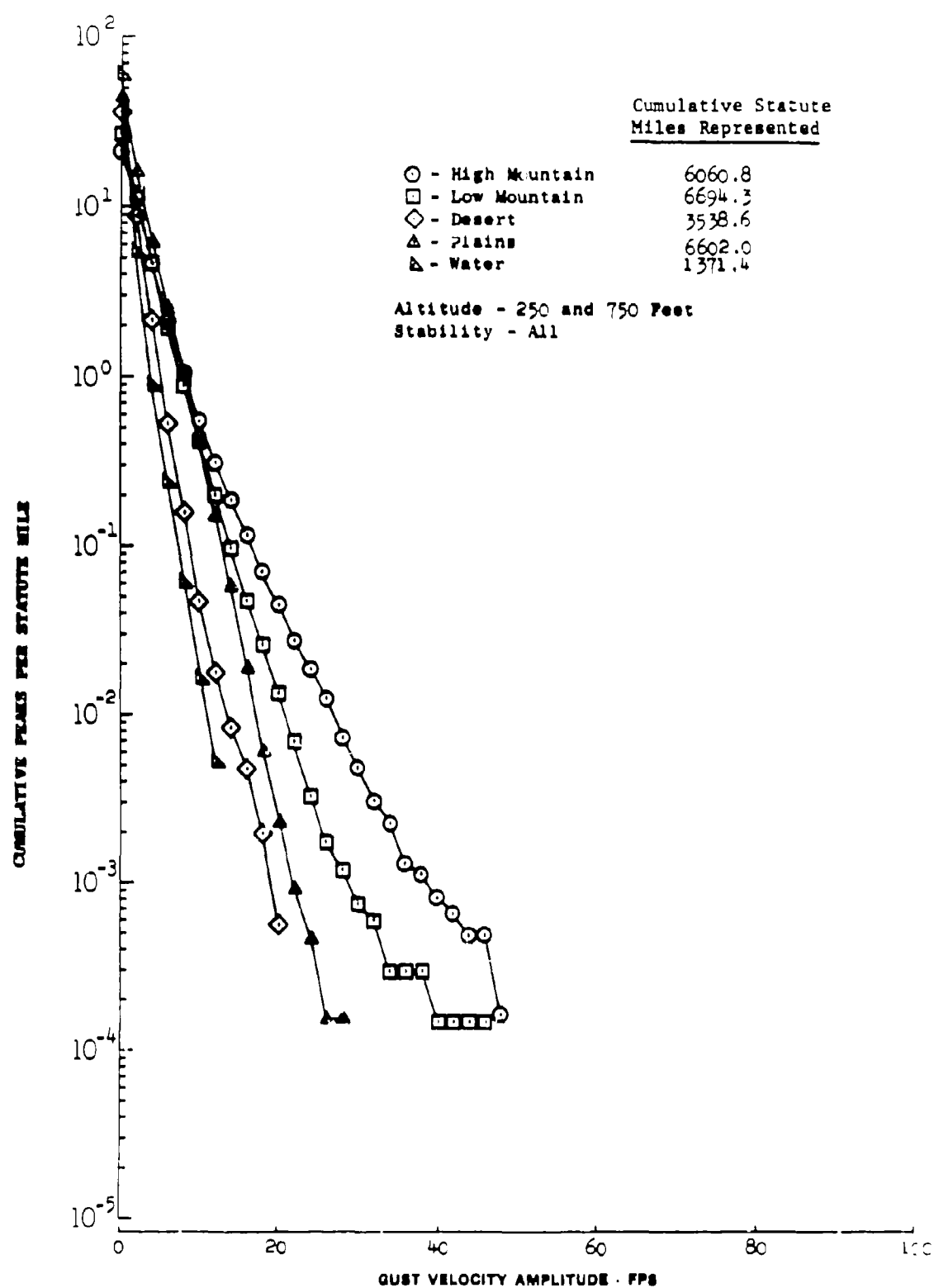


Figure 5.12 Terrain Effects on Lateral Gust Velocity Peaks

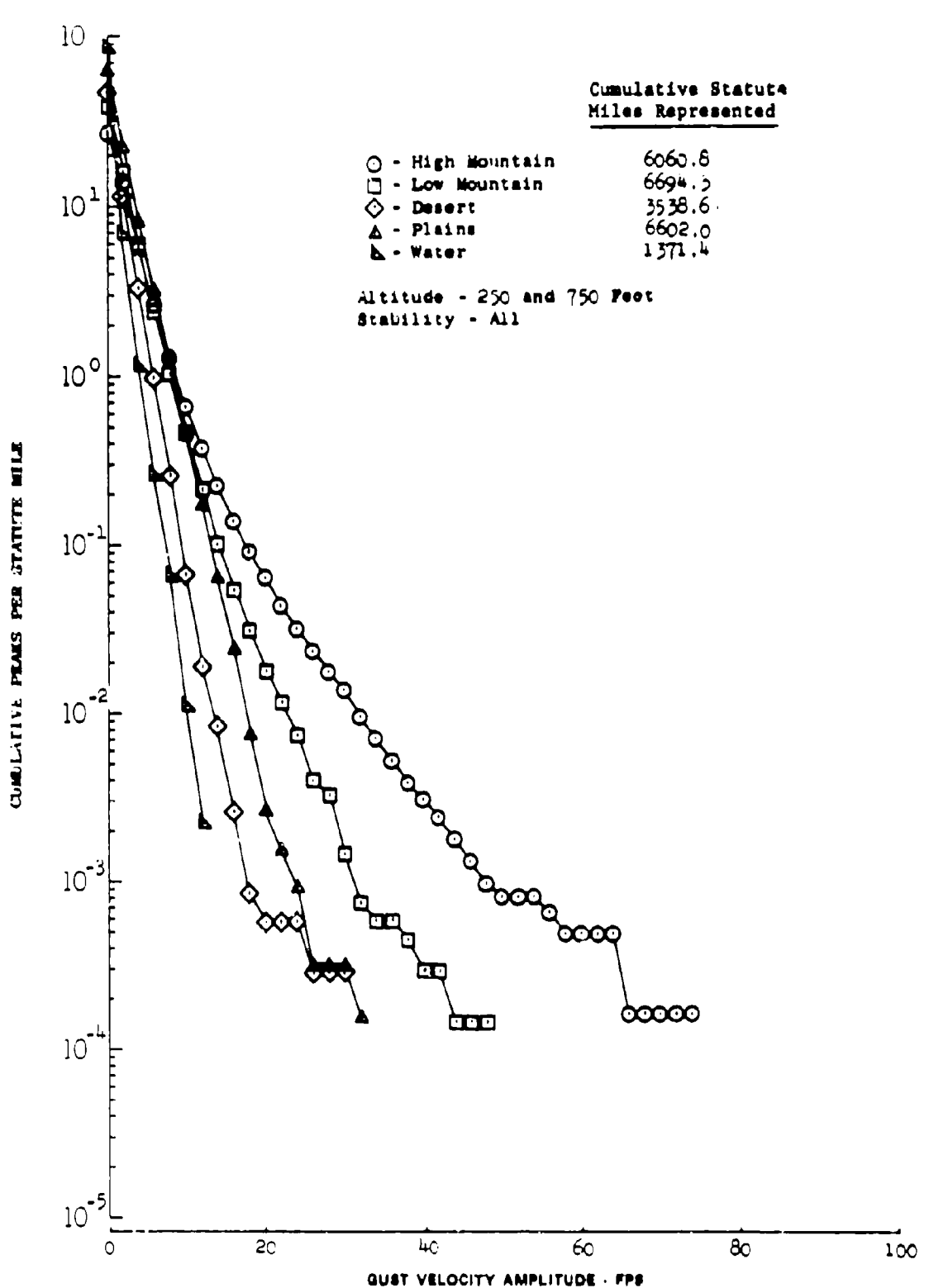


Figure 5.13 Terrain Effects on Vertical Gust Velocity Peaks

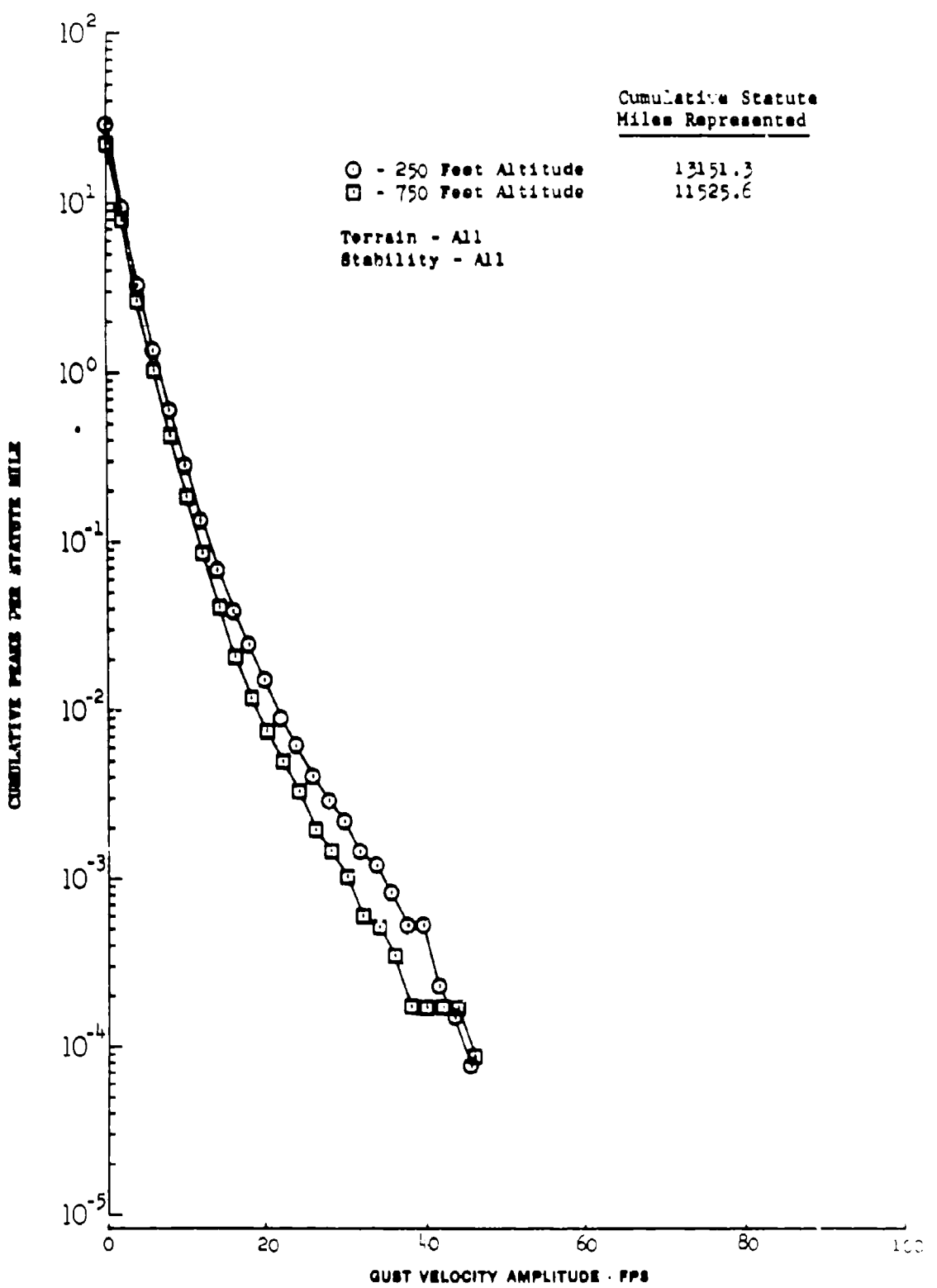


Figure 5.14 Altitude Effects on Longitudinal Gust Velocity Peaks

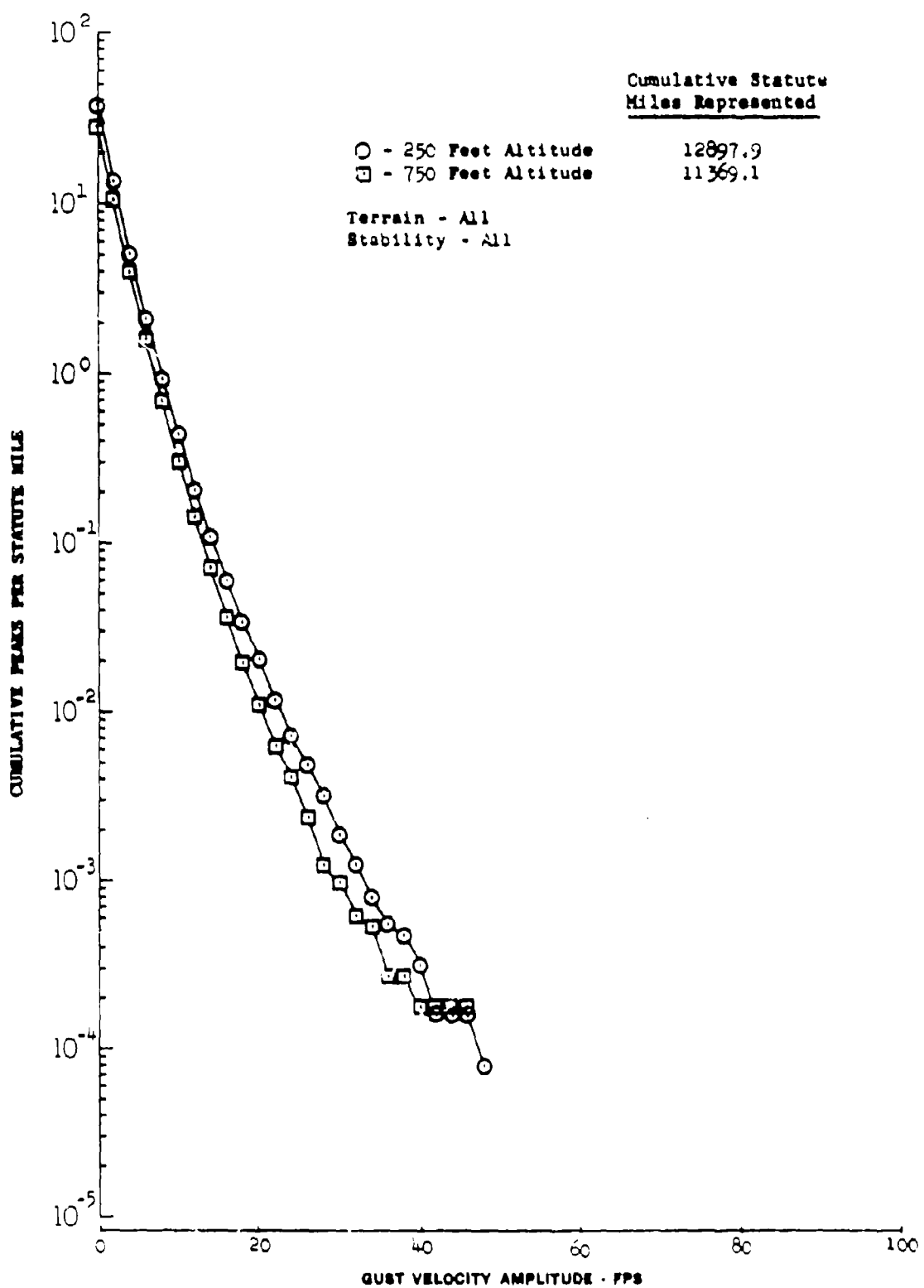


Figure 5.15 Altitude Effects on Lateral Gust Velocity Peaks

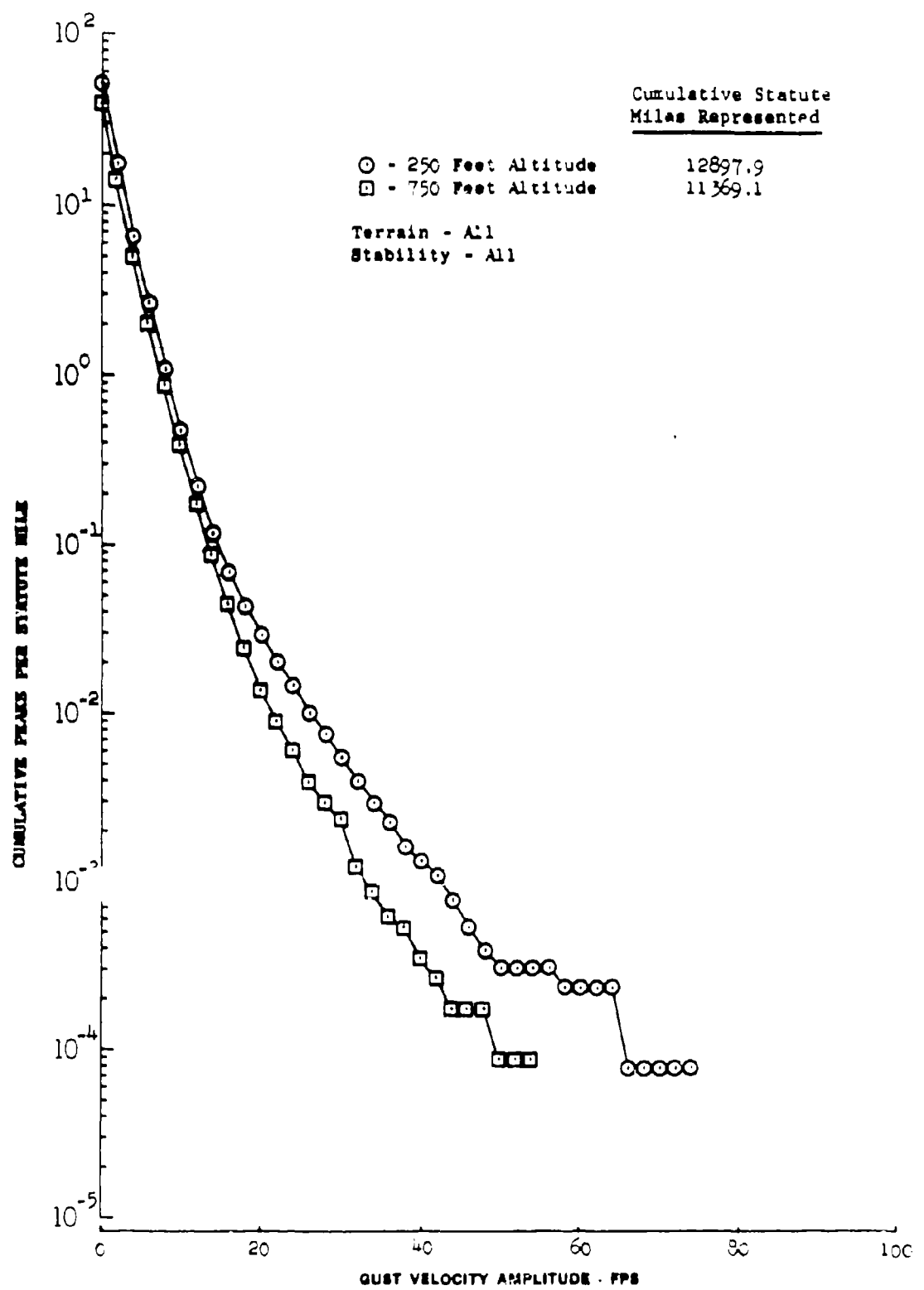


Figure 5.16 Altitude Effects on Vertical Gust Velocity Peaks

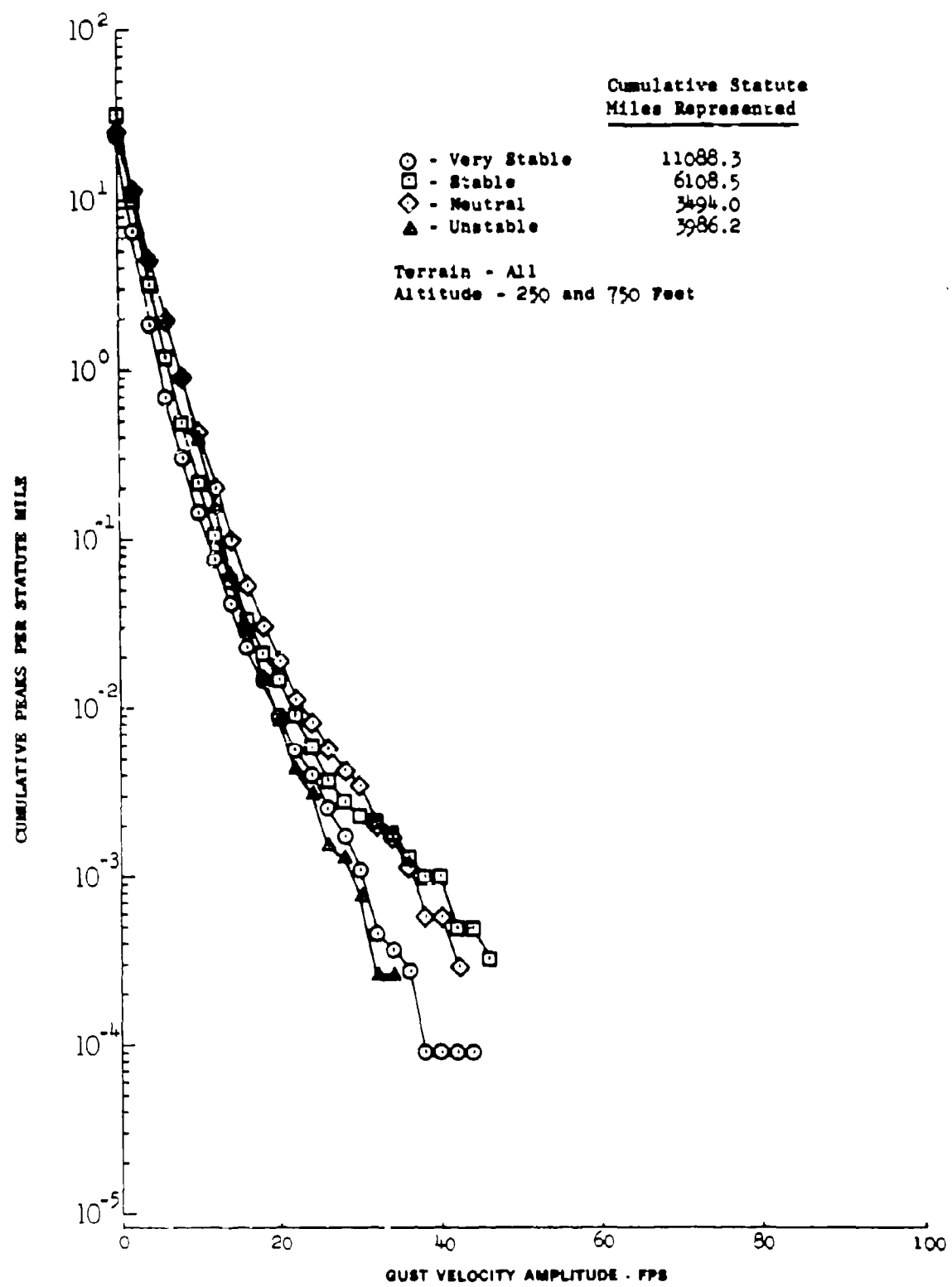


Figure 5.17 Stability Effects on Longitudinal Gust Velocity Peaks

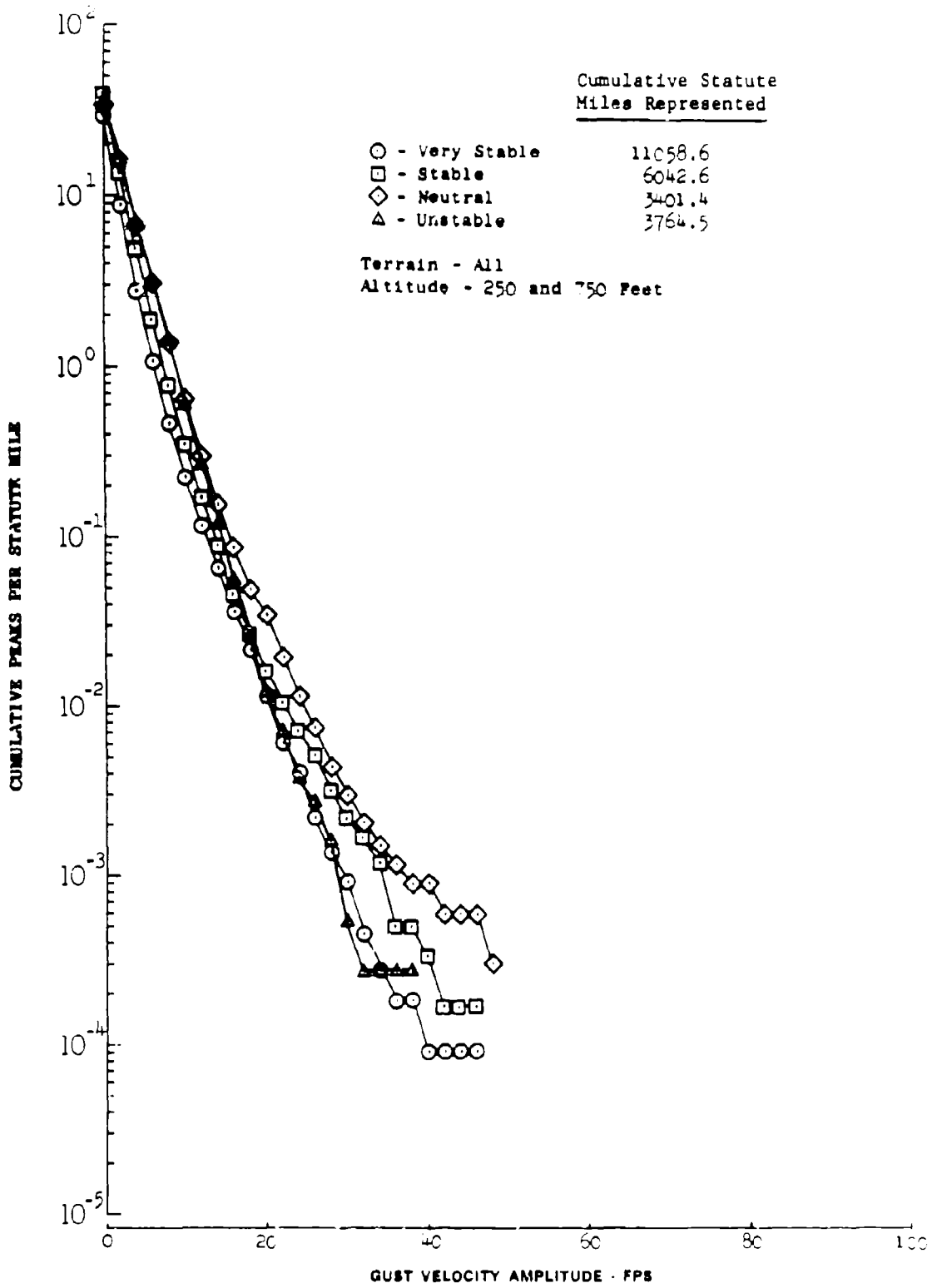


Figure 5.18 Stability Effects on Lateral Gust Velocity Peaks

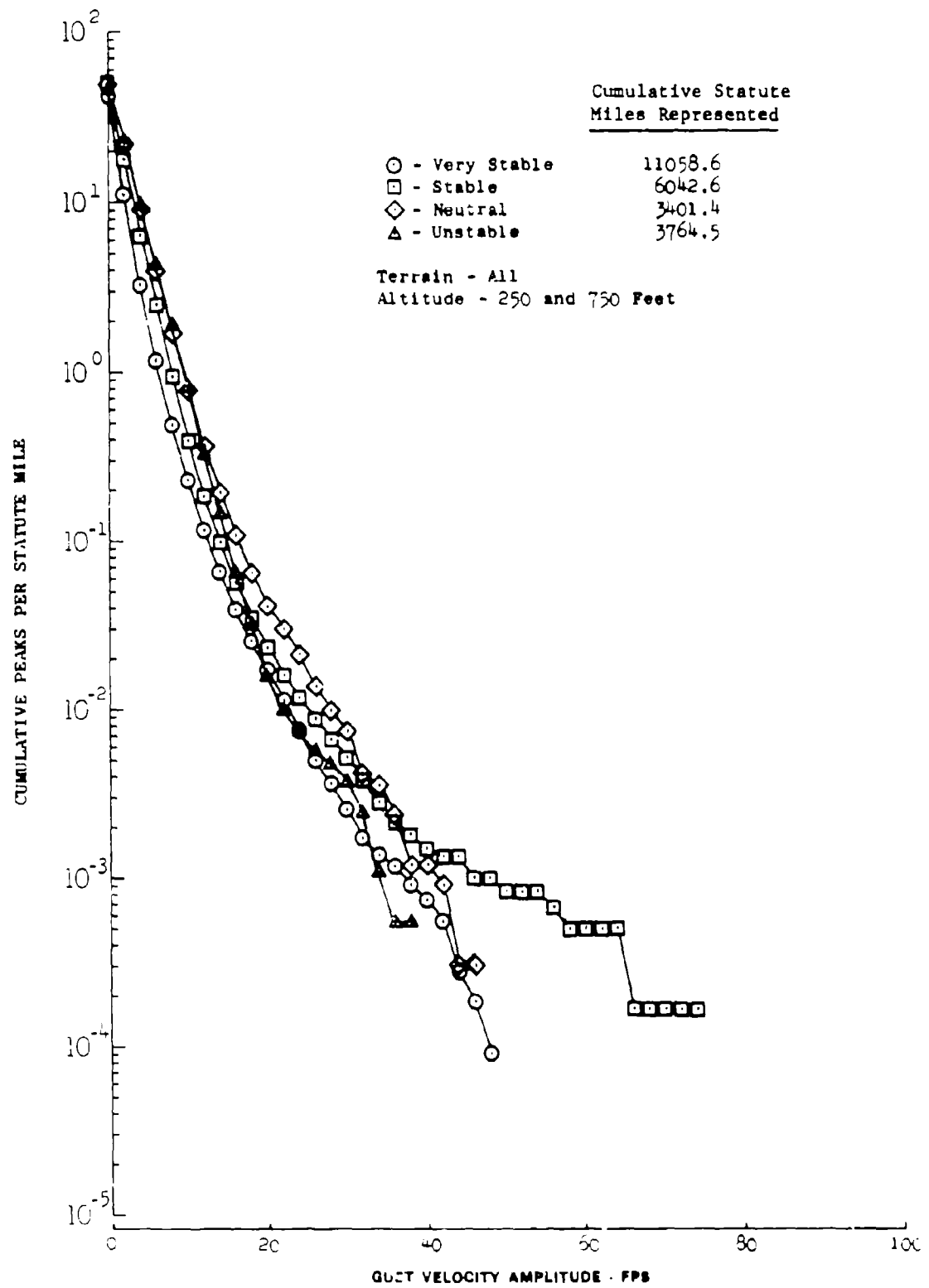


Figure 5.19 Stability Effects on Vertical Gust Velocity Peaks

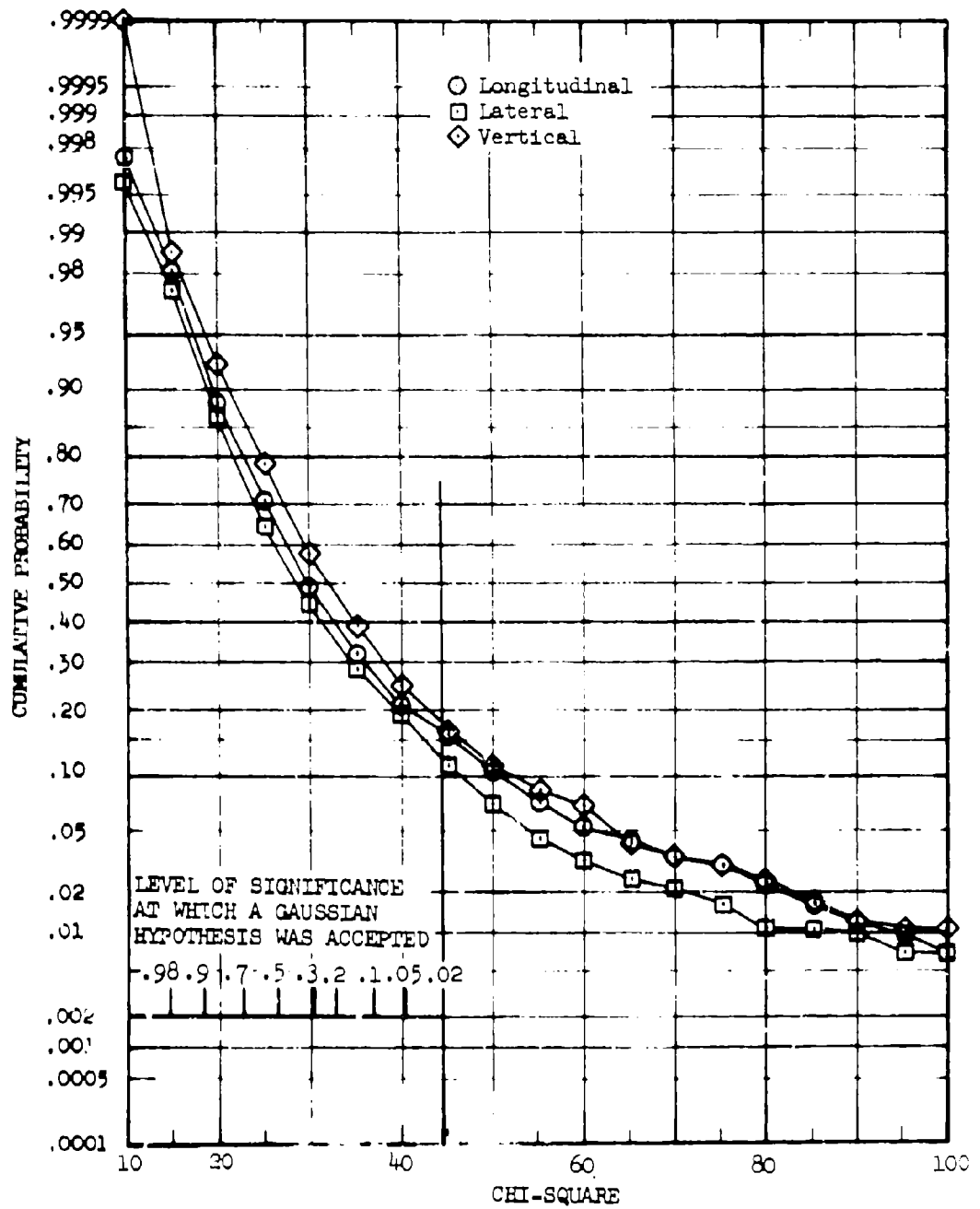


Figure 5.20 Chi-Square Test for Statistical Normality

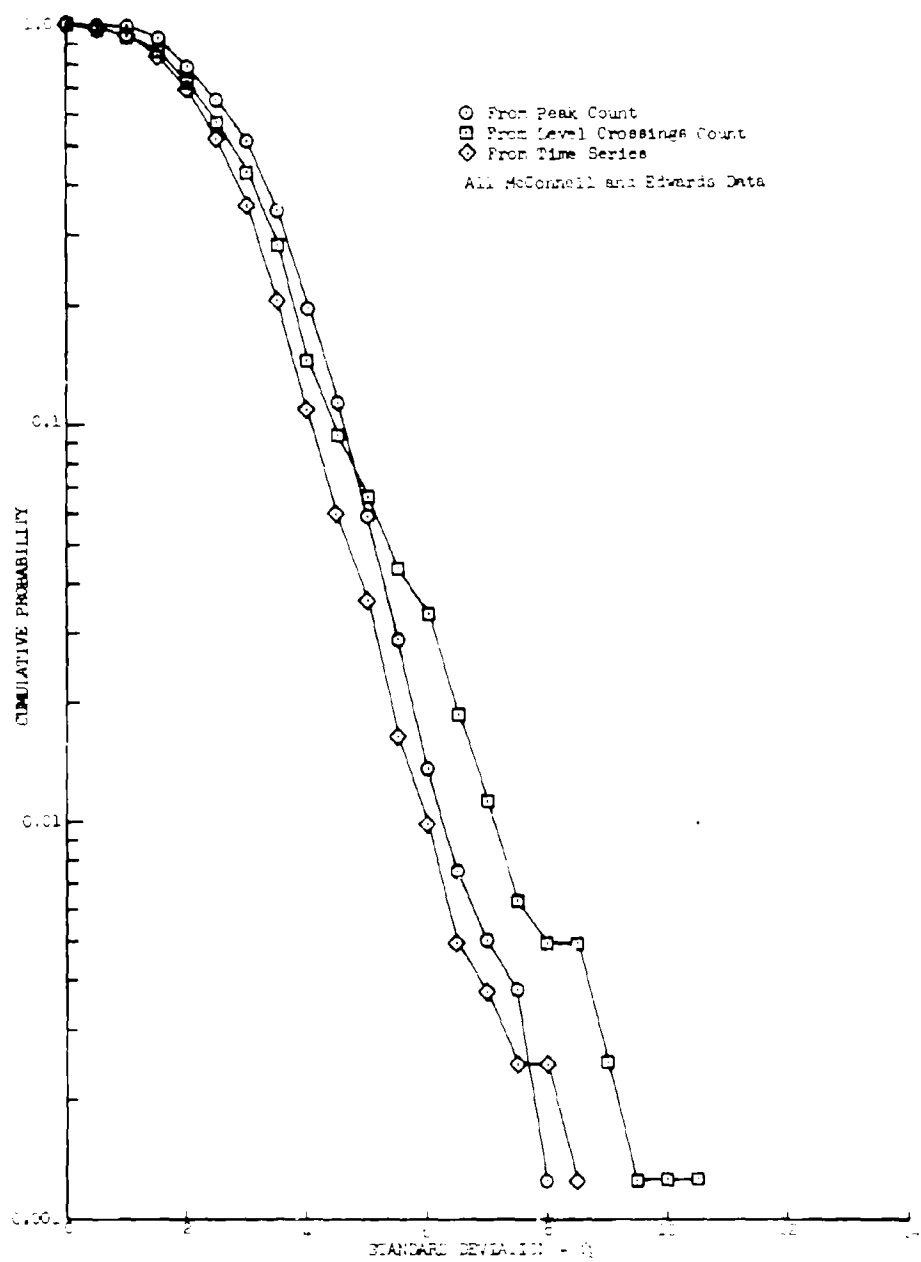


Figure 5.21 Comparison of Longitudinal Gust Velocity Standard Deviations Calculated by Different Techniques

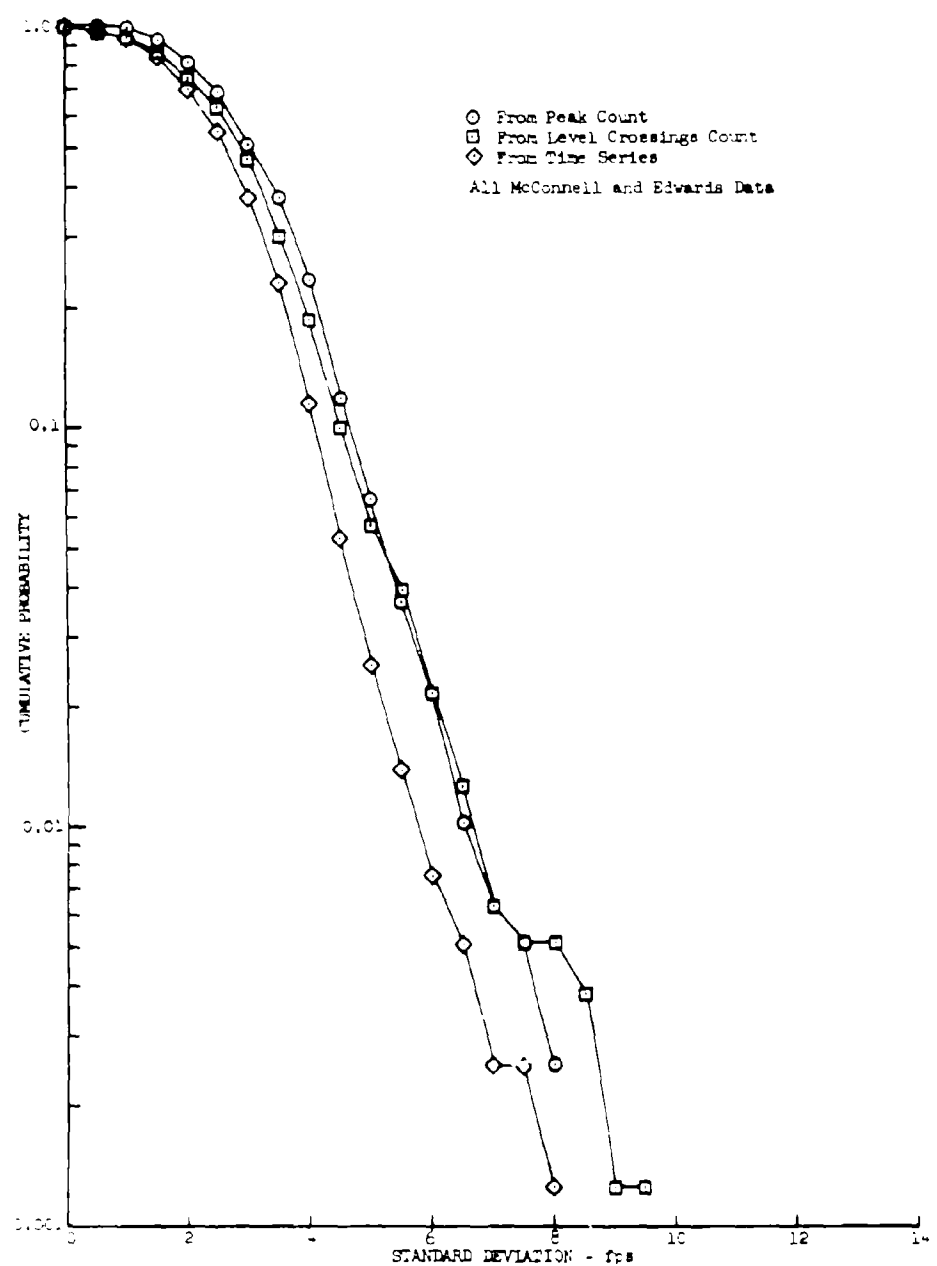


Figure 5.22 Comparison of Lateral Gust Velocity Standard Deviations Calculated by Different Techniques

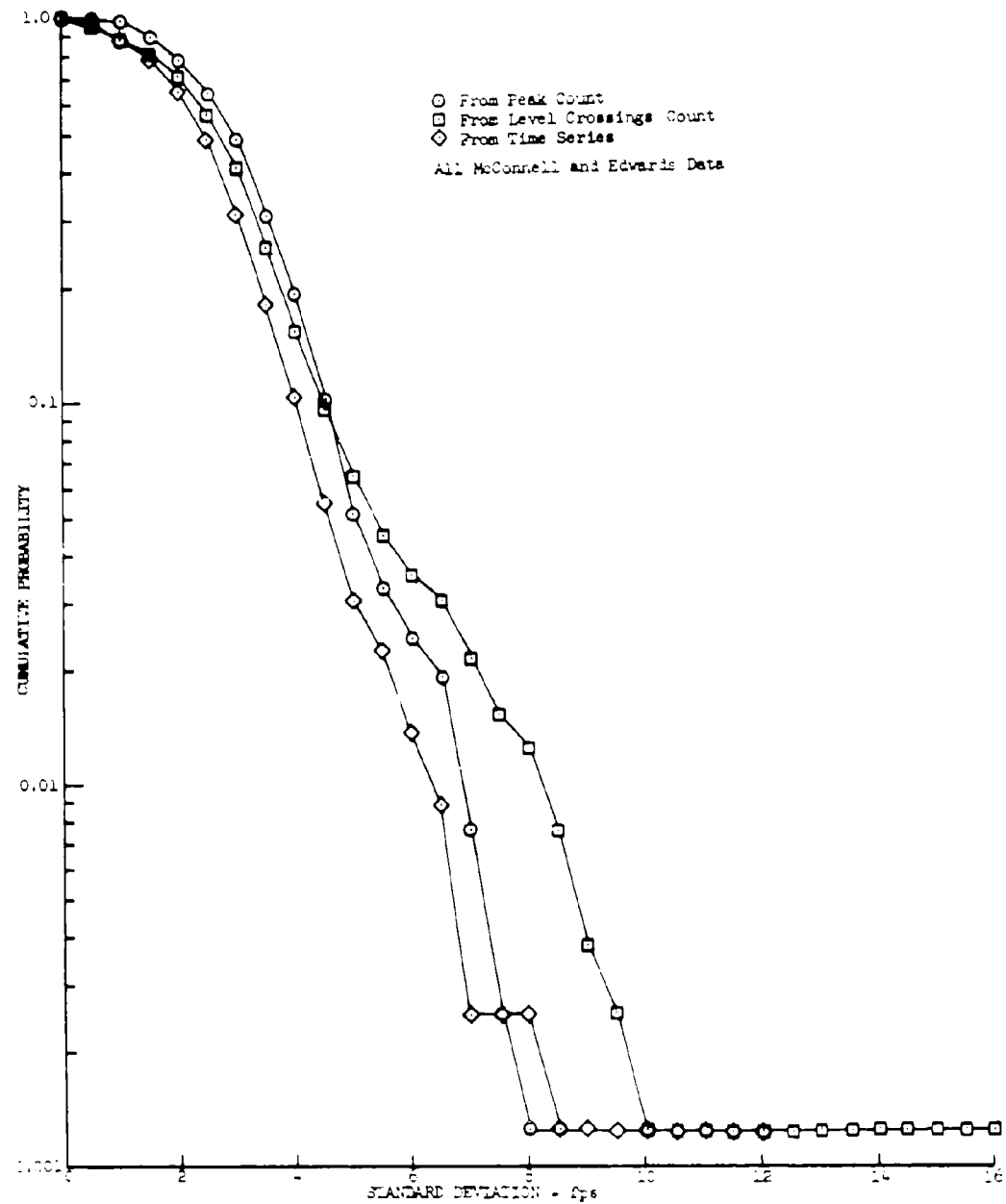


Figure 5.23 Comparison of Vertical Gust Velocity Standard Deviations Calculated by Different Techniques

Figure 5.24 Turbulence Spectra Data Calculated from Ensemble Average Time Function

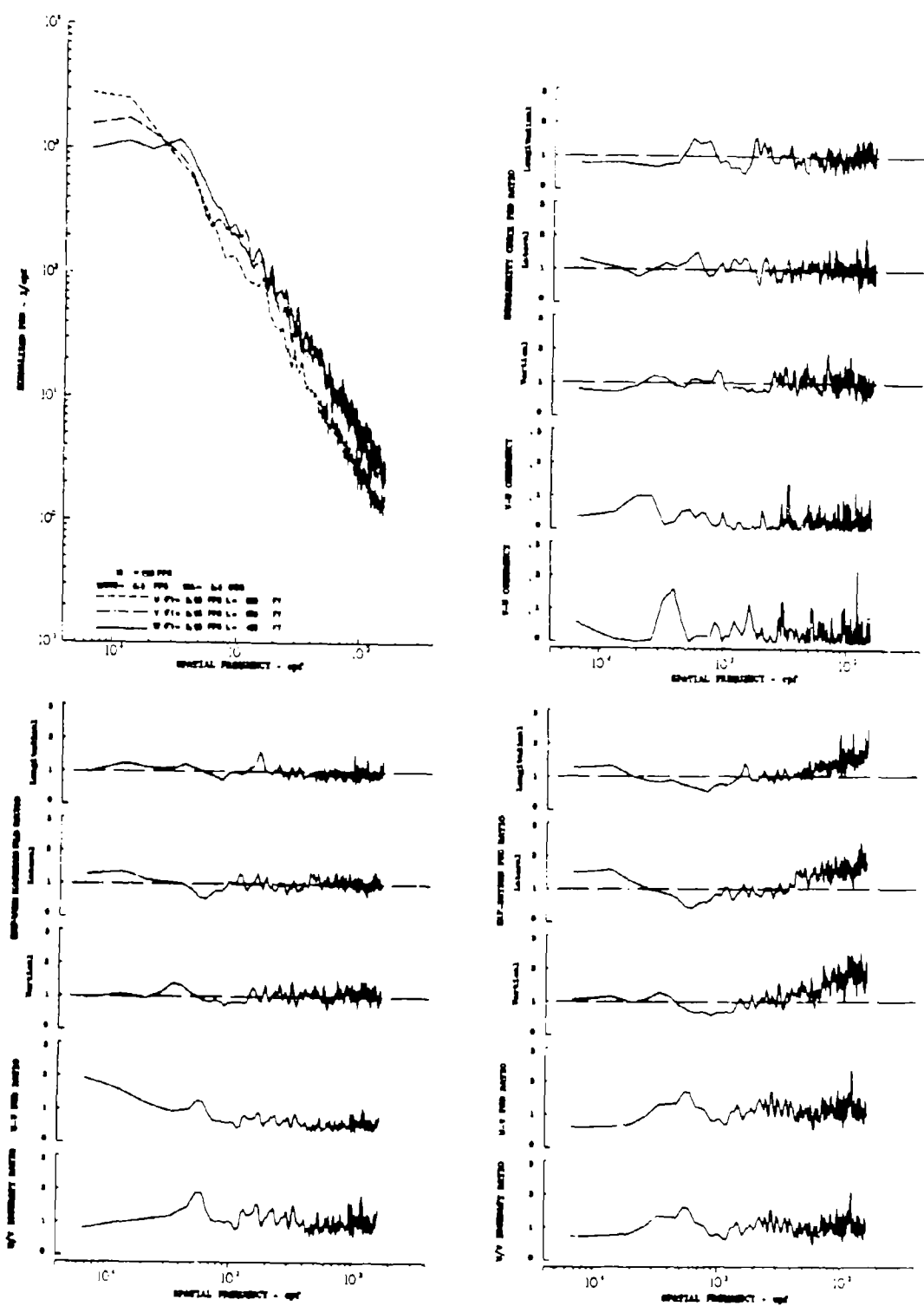


Figure 5.24 Turbulence Spectra Data Calculated from Ensemble Average Time Function

Test	87	Ambient Air Temp. (°F)	38.8	u_{max} (fps)	46.1
Date	11-13-69	True Airspeed (fps)	612.5	u_{min} (fps)	-41.4
Leg No.	3	Pilot Altitude (ft)	572	v_{max} (fps)	34.0
Category No.	112231	u_{ta} (fps)	8.59	v_{min} (fps)	-46.2
		u_{tv} (fps)	6.89	v_{max} (fps)	71.5
Wind Direction (deg)	No Data	u_{tw} (fps)	11.98	v_{min} (fps)	-65.0
Wind Velocity (fps)	No Data	u_{tw} (fps)			

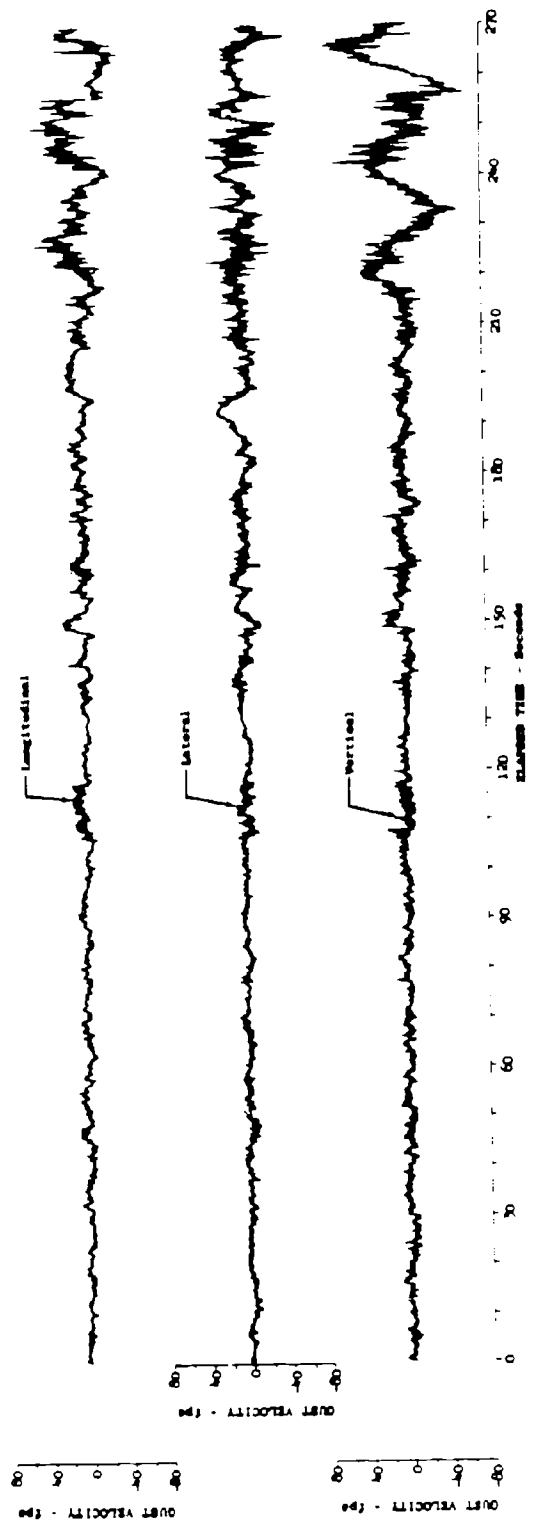


Figure 5.25 Time History of Gust Velocity Components - Severe Turbulence Encounter

Test	155	Ambient Air Temp (°F)	47.0	u_{\max} (fps)	40.8
Date	1-21-69	True Airspeed (fps)	622.5	u_{\min} (fps)	-35.4
Leg No.	7	Pilot Altitude (ft)	801	v_{\max} (fps)	54.6
Category No.	122243	σ_{t_u} (fps)	7.58	v_{\min} (fps)	-42.8
Wind Direction (deg)	247.1	σ_{t_v} (fps)	10.35	w_{\max} (fps)	42.0
Wind Velocity (fps)	31.1	σ_{t_w} (fps)	6.68	w_{\min} (fps)	-42.2

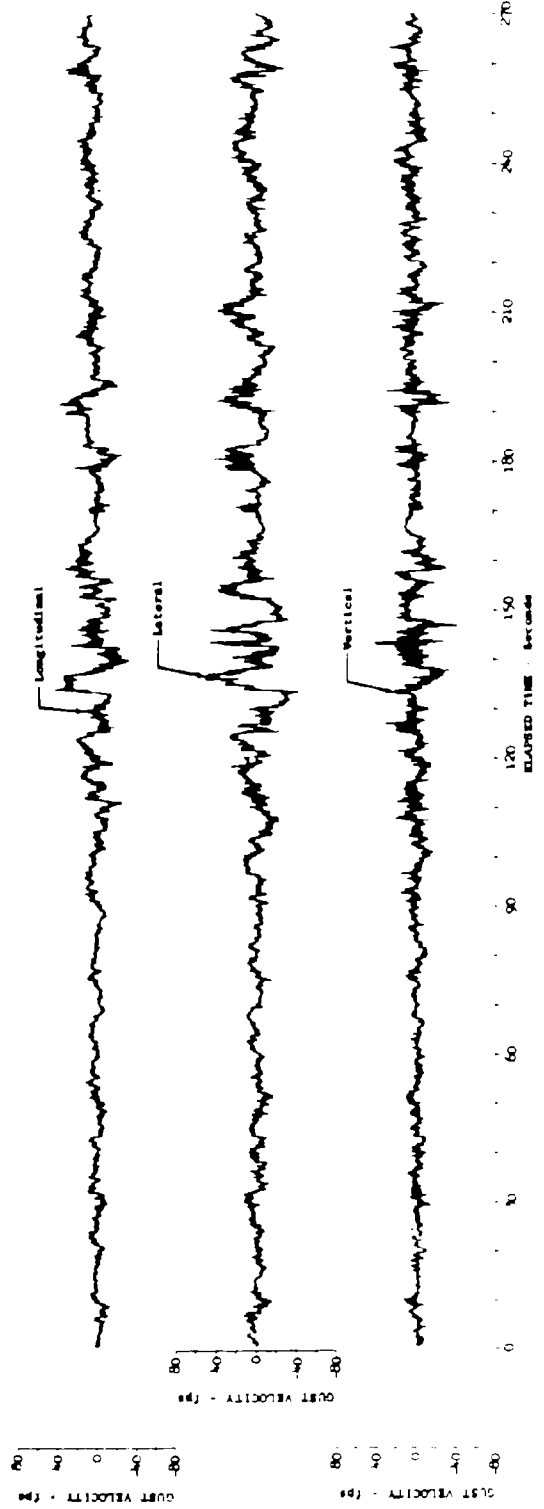


Figure 5.26 Time History of Gust Velocity Components - Severe Turbulence Encounter

Test	157	Ambient Air Temp. ($^{\circ}$ F)	35.0	U_{max} (fps)	51.1
Date	1-22-69	True Airspeed (fps)	639.0	U_{min} (fps)	-41.7
Leg No.	6	Polar Altitude (ft)	421	V_{max} (fps)	43.2
Category No.	113143	σ_{tu} (fps)	9.55	V_{min} (fps)	-55.0
Wind Direction (deg)	262.7	σ_{tv} (fps)	12.14	V_{max} (fps)	47.0
Wind Velocity (fps)	74.8	σ_{tv} (fps)	9.79	V_{min} (fps)	-42.4

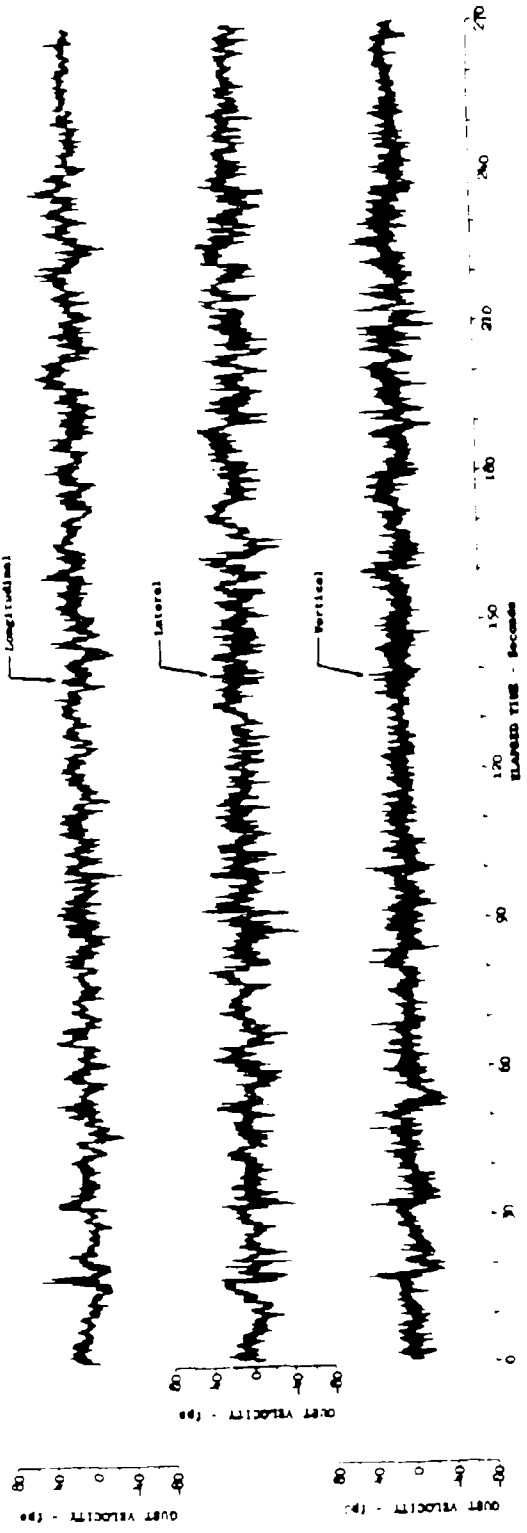


Figure 5.27 Time History of Gust Velocity Components - Severe Turbulence Encounter

Test	157	Ambient Air Temp (°F)	40.1	u_{max} (fps)	39.8
Date	1-22-69	True Airspeed (fps)	624.4	u_{min} (fps)	-47.2
Leg No.	7	Polar Altitude (ft.)	346	v_{max} (fps)	51.0
Category No.	113143	σ_{uu} (fps)	7.47	v_{min} (fps)	-63.8
Wind direction (deg)	251.4	σ_{vv} (fps)	10.10	w_{max} (fps)	37.3
Wind Velocity (fps)	42.5	σ_{ww} (fps)	6.79	w_{min} (fps)	-41.5

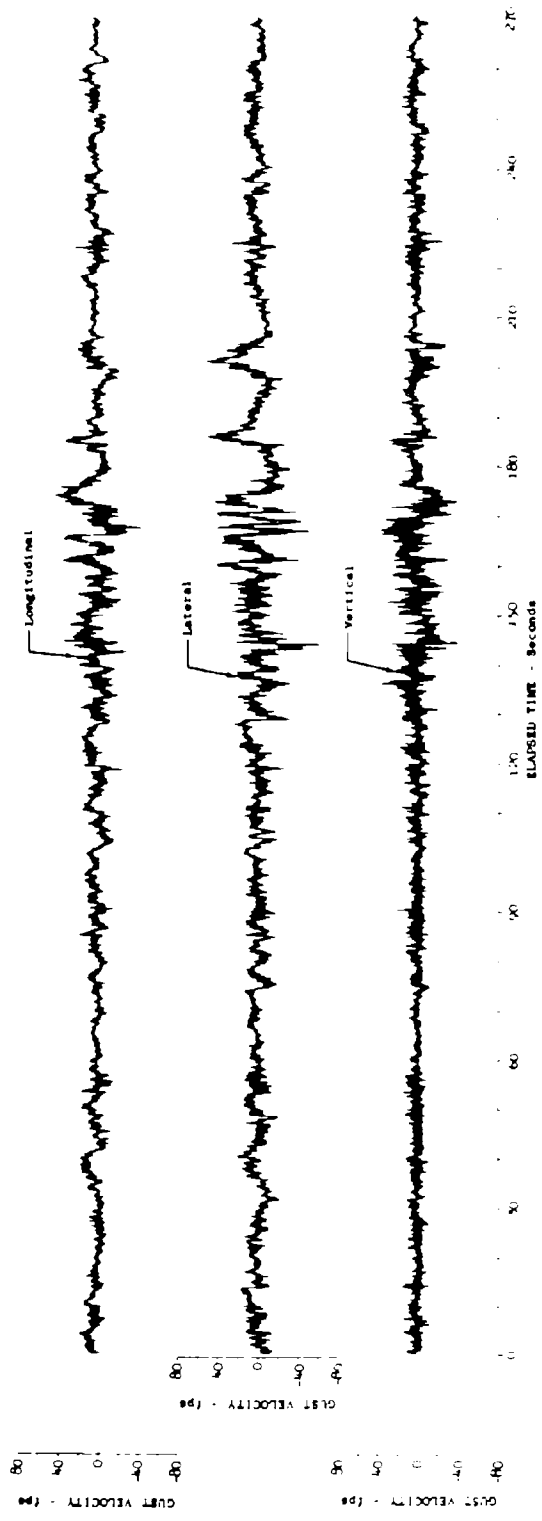


Figure 5.28 Time History of Gust Velocity Components - Severe Turbulence Encounter

Test	158	Ambient Air Temp (°F)	37.3	u_{\max} (fps)	34.8
Date	1-22-69	True Airspeed (fps)	619.2	u_{\min} (fps)	-44.2
Leg No.	6	Polar Altitude (ft)	406	v_{\max} (fps)	51.0
Category No.	113243	σ_{tu} (fps)	9.67	v_{\min} (fps)	-72.5
Wind Direction (deg)	269.8	σ_{tv} (fps)	13.12	w_{\max} (fps)	49.3
Wind Velocity (fps)	50.4	σ_{tw} (fps)	9.32	w_{\min} (fps)	-40.1

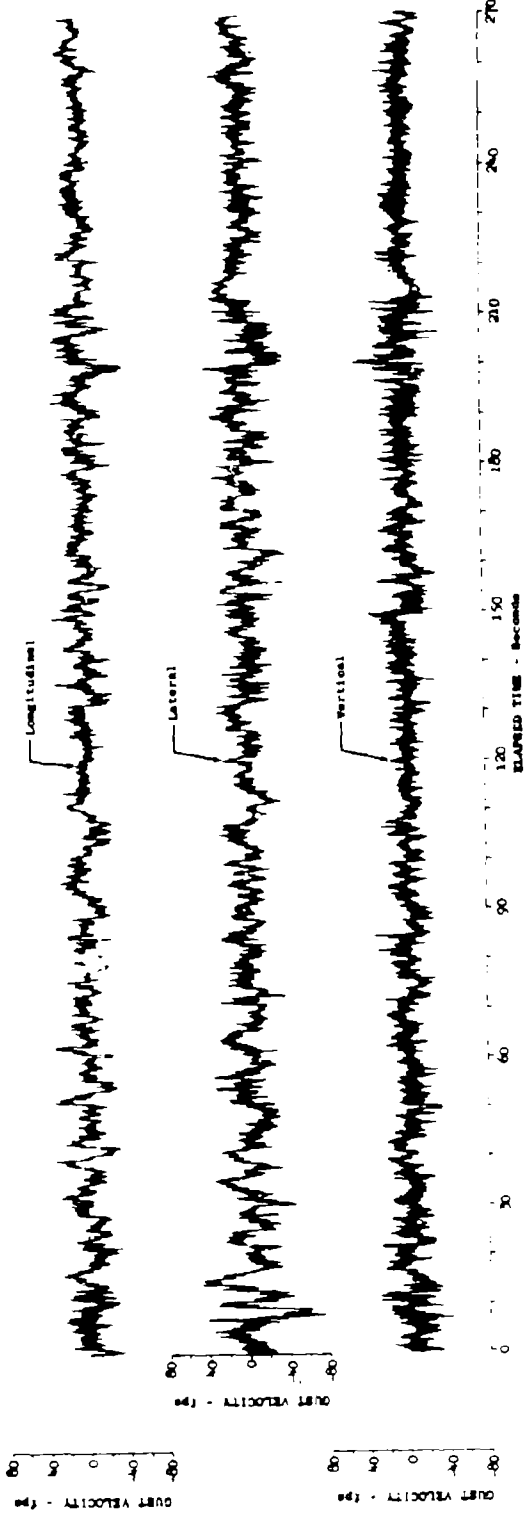


Figure 5.29 Time History of Gust Velocity Components - Severe Turbulence Encounter

Test	168	Ambient Air Temp (°F)	55.2	U_{max} (fps)	43.0
Date	2-5-69	True Airspeed (fps)	565.3	U_{min} (fps)	-55.1
Log No.	5	Pilot Altitude (ft)	No Data	V_{max} (fps)	69.8
Category No.	121143	U_{av} (fps)	6.77	V_{min} (fps)	-34.6
Wind Direction (deg)	258.3	U_{av} (fps)	11.01	V_{max} (fps)	57.4
Wind Velocity (fps)	59.8	U_{av} (fps)	9.06	V_{min} (fps)	-37.0

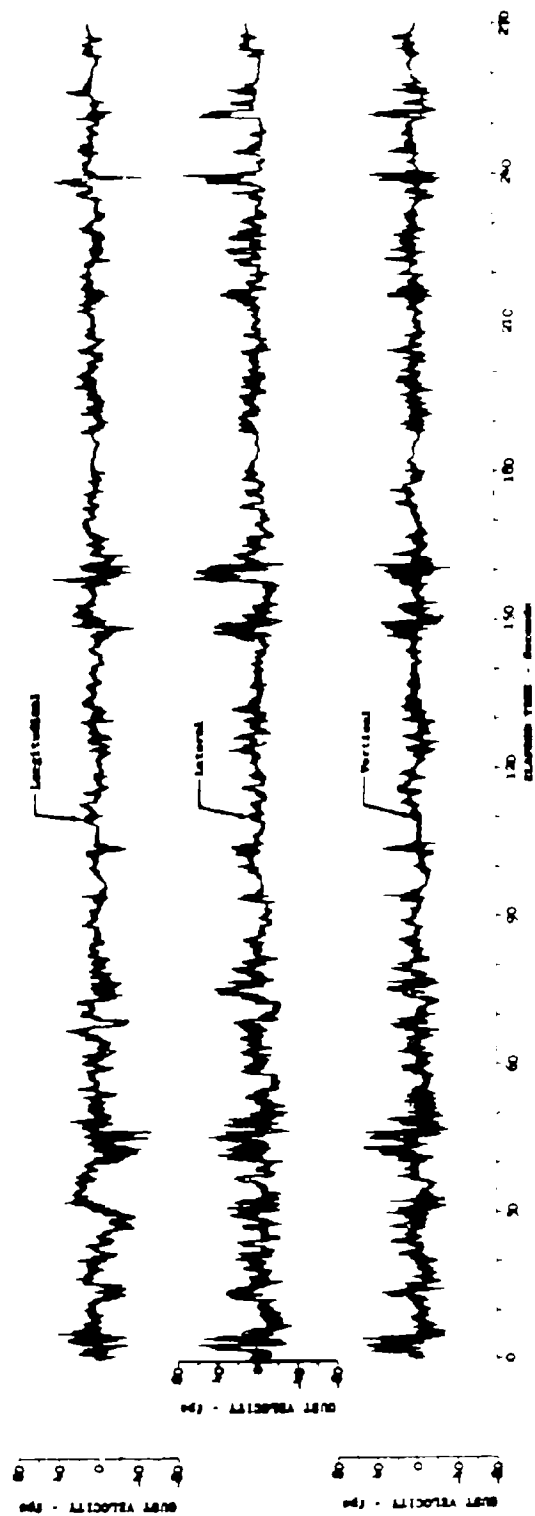


Figure 5.30 Time History of Gust Velocity Components - Severe Turbulence Encounter

Test	163	Ambient Air Temp. ($^{\circ}$ F)	37.5	u_{max} (fps)	42.5
Date	2-5-69	True Airspeed (fps)	599.4	u_{min} (fps)	-54.6
Leg No.	7	Pedar Altitude (ft)	No Data	v_{max} (fps)	54.9
Category No.	123143	σ_{tu} (fps)	8.95	v_{min} (fps)	-54.2
Wind Direction (deg)	240.5	σ_{tv} (fps)	11.80	w_{max} (fps)	36.1
Wind Velocity (fps)	44.9	σ_{tw} (fps)	7.30	w_{min} (fps)	-46.8

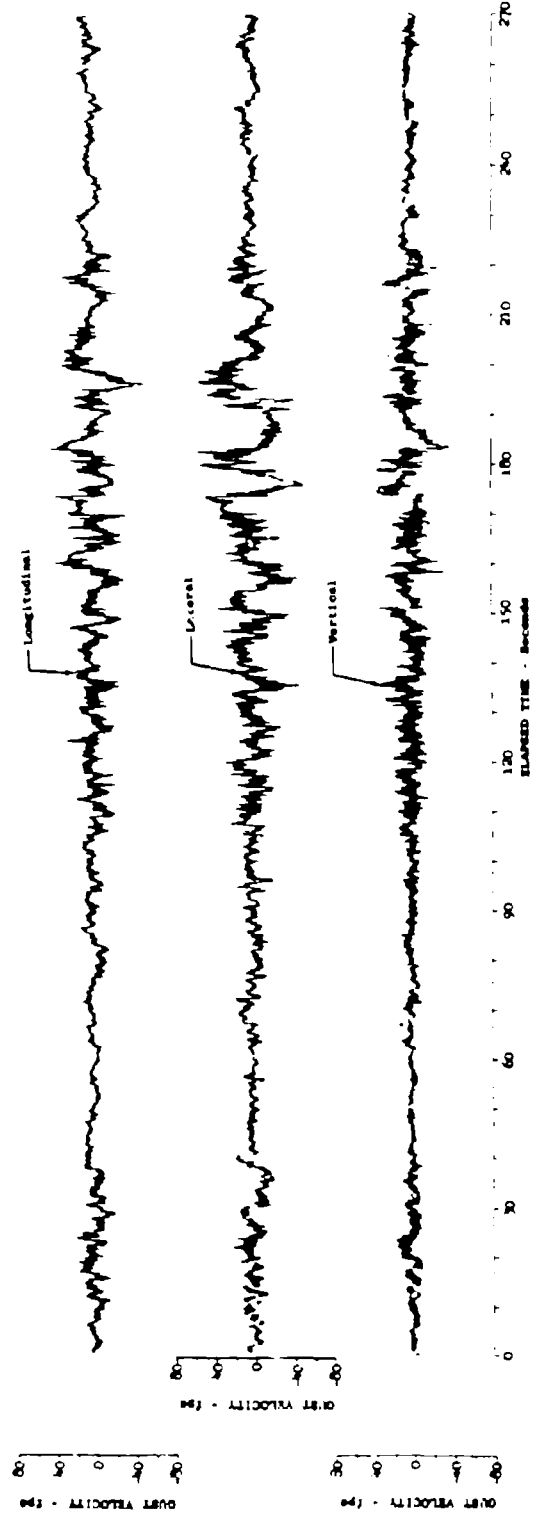


Figure 5.31 Time History of Gust Velocity Components - Severe Turbulence Encounter

Test	170	Ambient Air Temp. (°F)	27.6	u_{\max} (fps)	28.4
Date	2-6-69	True Airspeed (fps)	609.4	u_{\min} (fps)	-38.4
Leg No.	1	Polar Altitude (ft)	401	v_{\max} (fps)	29.6
Aircraft No.	12143	a_w (fps)	6.08	v_{\min} (fps)	-56.8
Wind Direction (deg)	216.0	a_{zv} (fps)	8.60	v_{\max} (fps)	37.1
Wind Velocity (fps)	50.2	a_{zv} (fps)	6.59	v_{\min} (fps)	-45.8

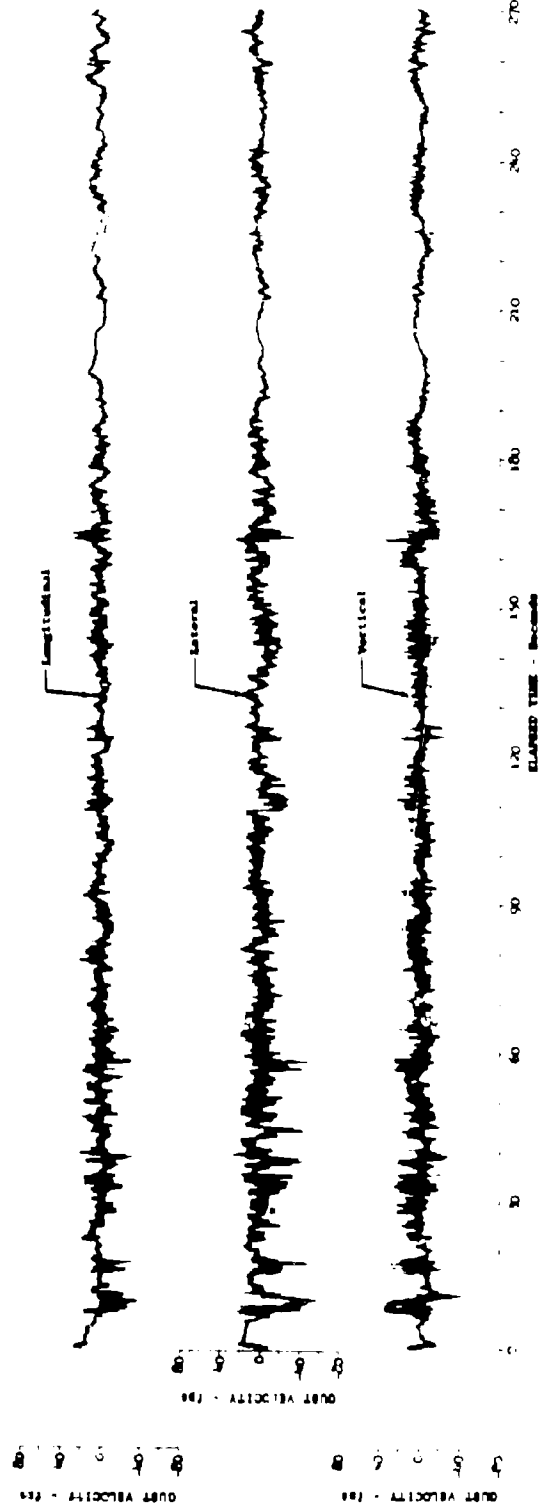


Figure 5.32 Time History of Gust Velocity Components - Severe Turbulence Encounter

	170	Ambient Air Temp (°F)	18.6	u_{\max} (fps)	36.6
Date	2-6-69	True Airspeed (fps)	598.3	u_{\min} (fps)	-55.0
Log No.	2	Pilot Altitude (ft)	389	v_{\max} (fps)	40.6
Category No.	1121b3	σ_{tu} (fps)	9.52	v_{\min} (fps)	-33.9
Wind Direction (deg)	No Data	σ_{tv} (fps)	7.28	v_{\max} (fps)	39.2
Wind Velocity (fps)	No Data	σ_{tw} (fps)	5.57	v_{\min} (fps)	-38.7

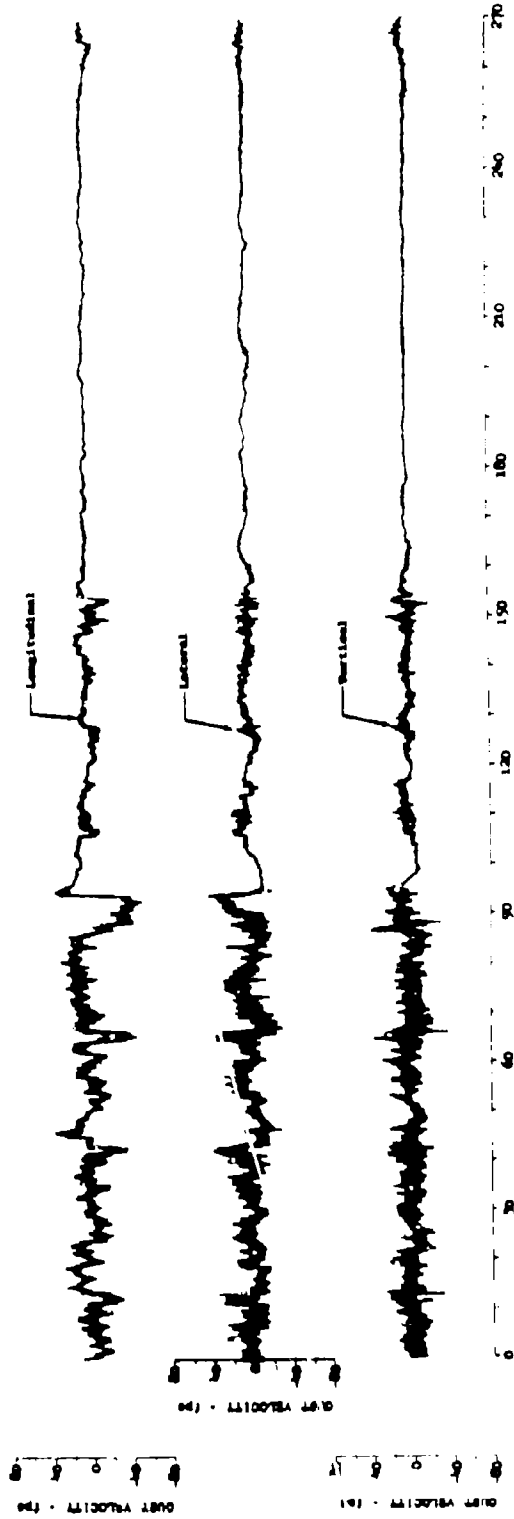


Figure 5.33 Time History of Gust Velocity Components - Severe Turbulence Encounter

Time	170	Ambient Air Temp (°F)	31.8	u_{\max} (fps)	40.1
Date	2-6-69	True Airspeed (fps)	566.3	u_{\min} (fps)	-37.0
Log No.	6	Pilot Altitude (ft)	386	v_{\max} (fps)	49.6
Survey No.	112043	σ_u (fps)	8.65	v_{\min} (fps)	-51.8
Wind Direction (deg)	260.9	σ_v (fps)	11.30	w_{\max} (fps)	31.9
Wind Velocity (fps)	76.9	σ_w (fps)	8.07	w_{\min} (fps)	-38.3

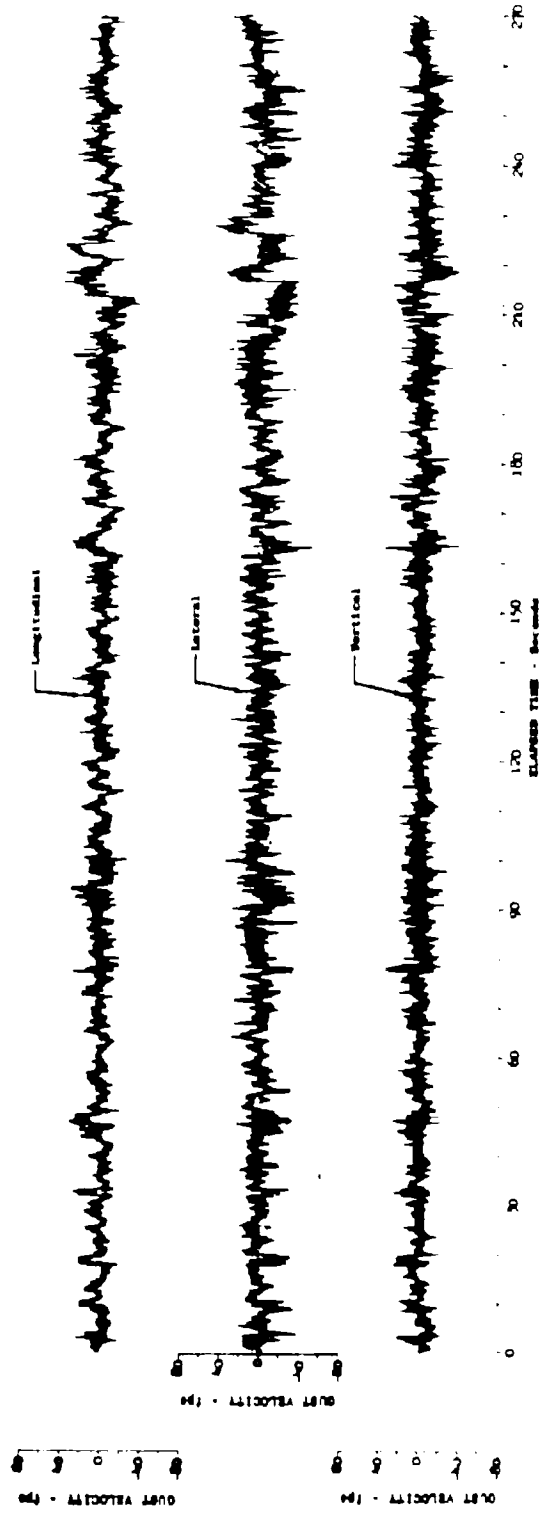


Figure 5.34 Time History of Gust Velocity Components - Severe Turbulence Encounter

Test	170	Ambient Air Temp (°F)	34.0	u_{\max} (fps)	45.7
Date	2-6-69	True Airspeed (fps)	567.4	u_{\min} (fps)	-37.5
Log No.	7	Polar Altitude (ft)	434	v_{\max} (fps)	32.5
Category No.	113143	σ_{u_0} (fps)	7.03	v_{\min} (fps)	-54.5
Wind direction (deg)	250.4	σ_{v_0} (fps)	8.42	v_{\max} (fps)	52.8
Wind Velocity (fps)	72.0	σ_{w_0} (fps)	7.05	v_{\min} (fps)	-47.4

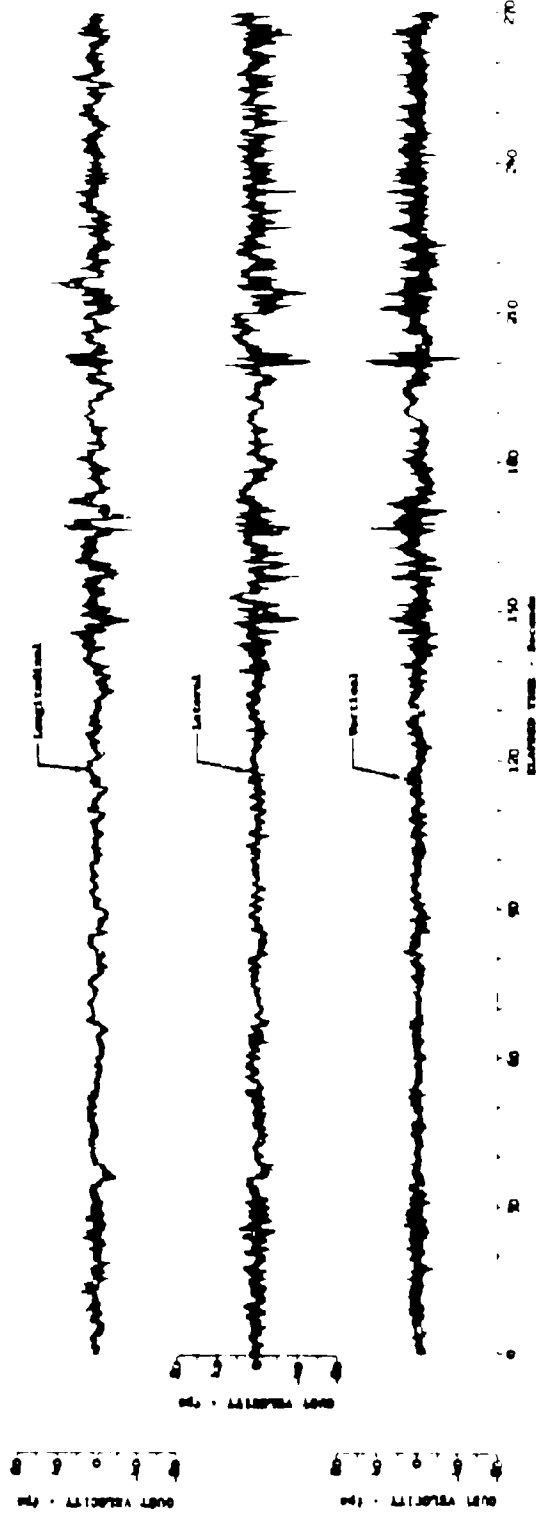


Figure 5-35 Time History of Gust Velocity Components - Severe Turbulence Encounter

Flight	171	Ambient Air Temp (°F)	32.4	u max (fps)	47.3
Date	2-6-69	True Airspeed (fps)	616.8	u min (fps)	49.4
Leg No.	1	Polar Altitude (ft)	389	v max (fps)	32.6
Category No.	114243	σ_{tu} (fps)	8.15	σ_v min (fps)	-55.4
Wind Direction (deg)	213.6	σ_{tv} (fps)	9.72	σ_v max (fps)	45.1
Wind Velocity (fps)	45.0	σ_{tw} (fps)	7.70	σ_w min (fps)	-43.0

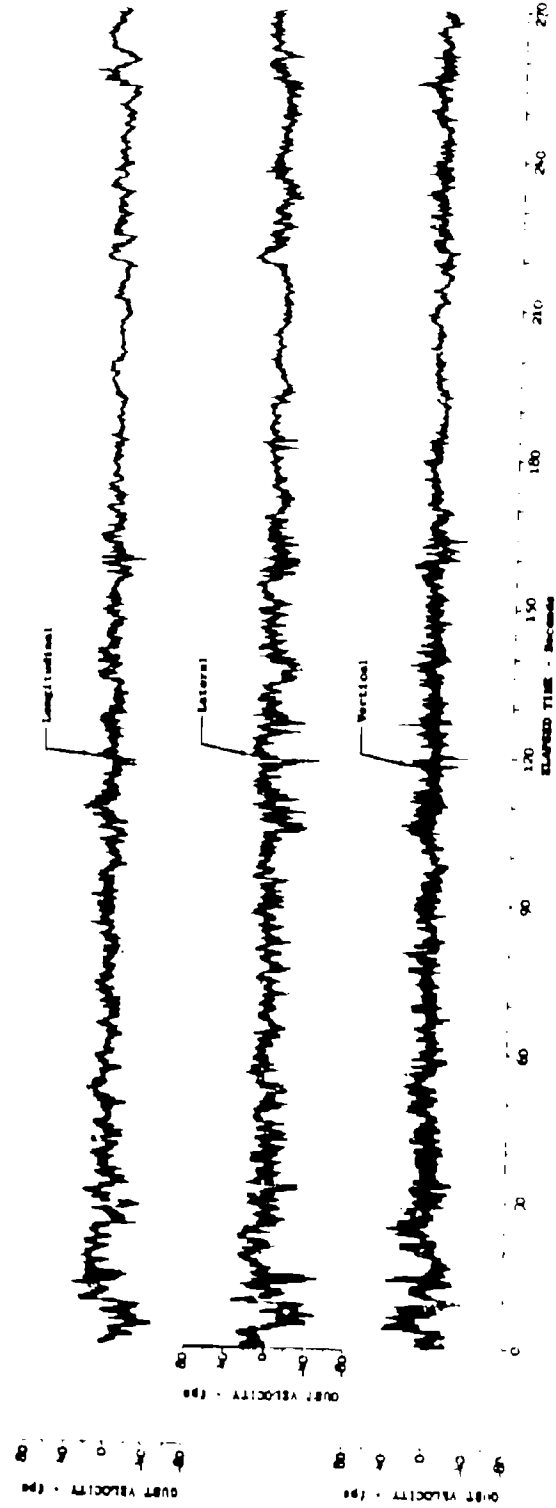


Figure 5.36 Time History of Gust Velocity Components - Severe Turbulence Encounter

TAC	171	Ambient Air Temp (°F)	23.5	v_{max} (fps)	59.0
Date	2-6-69	True Airspeed (fps)	617.1	v_{min} (fps)	-59.3
leg No.	2	Polar Altitude (ft)	No Data	v_{max} (fps)	48.2
Integrator No.	112243	v_{uw} (fps)	10.14	v_{min} (fps)	-40.1
Wind Direction (deg)		v_{uv} (fps)	7.88	v_{uw} (fps)	43.2
Wind Velocity (fps)		v_{uw} (fps)	7.77	v_{min} (fps)	-45.0

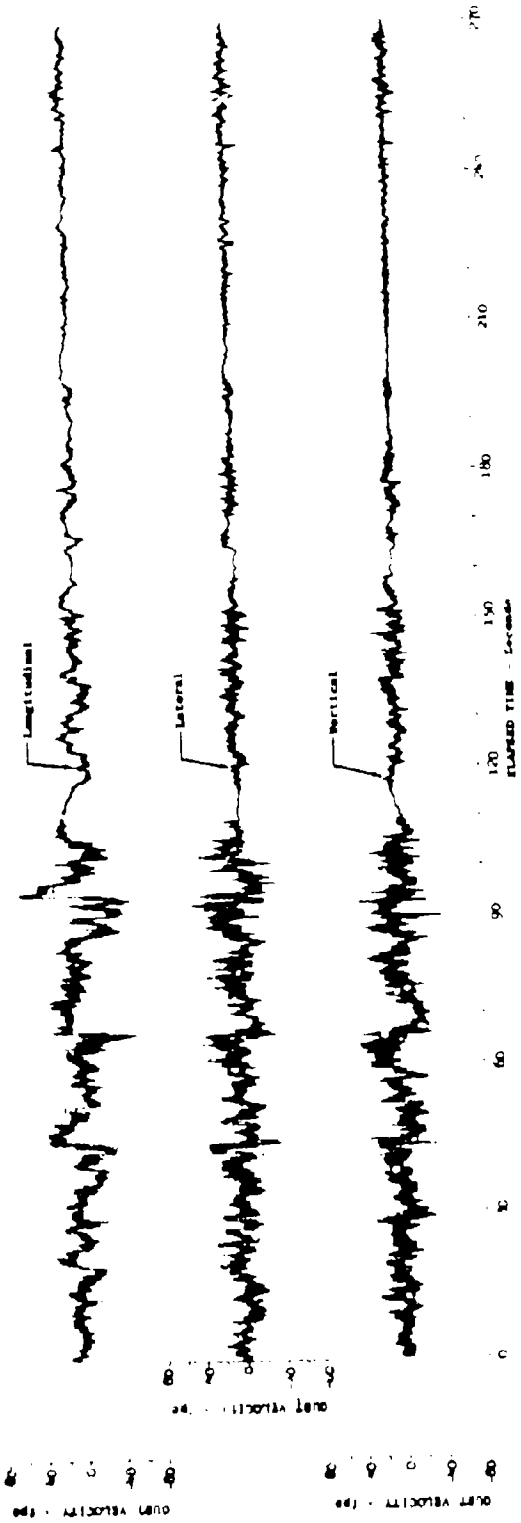


Figure 5-37 Time History of Gust Velocity Components - Severe Turbulence Encounter

Test	171	Ambient Air Temp (°F)	33.9	u_{\max} (fps)	68.6
Date	2-6-69	True Airspeed (fps)	584.3	u_{\min} (fps)	-40.4
Loc No.	6	Polar Altitude (ft)	366	v_{\max} (fps)	57.2
Category No.	1122A3	u_{av} (fps)	10.12	v_{\min} (fps)	-51.4
Wind Direction (deg)	258.7	v_{av} (fps)	11.39	w_{\max} (fps)	48.2
Wind Velocity (fps)	76.4	v_{av} (fps)	8.58	w_{\min} (fps)	-41.6

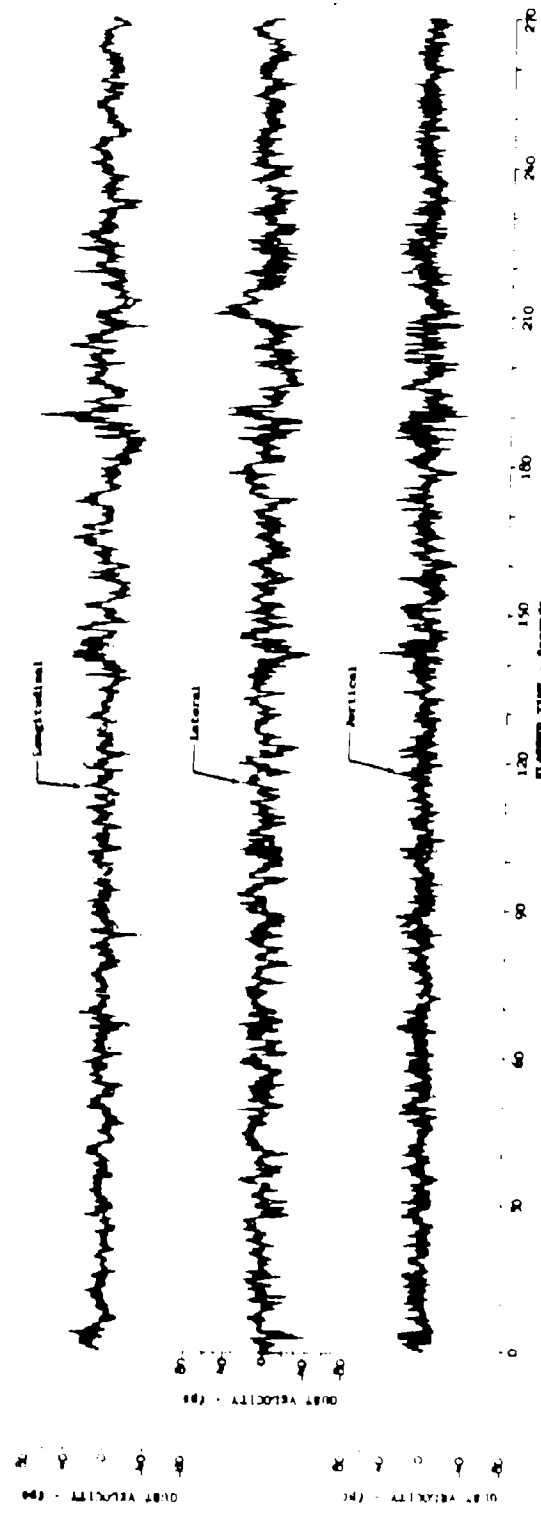


Figure 5.38 Time History of Gust Velocity Components - Severe Turbulence Encounter

Test	171	Ambient Air Temp (°F)	37.1	u _{max} (fps)	34.8
Date	2-6-69	True Airspeed (fps)	583.9	u _{min} (fps)	-40.8
Log No.	7	Pilot Altitude (ft)	422	v _{max} (fps)	33.0
Category No.	113243	• tu (fps)	8.20	v _{min} (fps)	-60.8
Wind Direction (deg)	251.0	• tv (fps)	9.20	v _{max} (fps)	41.3
Wind Velocity (fps)	81.5	• tw (fps)	8.07	v _{min} (fps)	-37.5

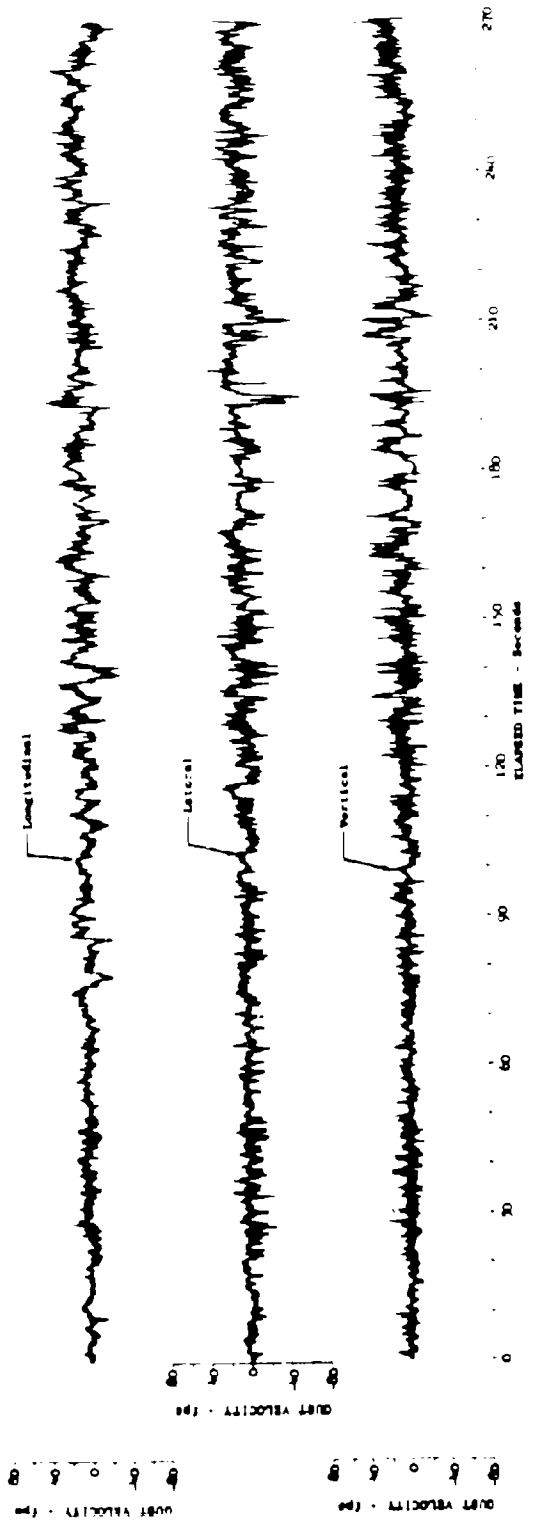


Figure 5.39 Time History of Gust Velocity Components - Severe Turbulence Encounter

Test	172	Ambient Air Temp (°F)	39.2	u_{\max} (fps)	33.5
Date	2-6-69	True Airspeed (fps)	624.8	u_{\min} (fps)	-33.8
Log No.	1	Flight Altitude (ft)	414	v_{\max} (fps)	32.5
Cat. No.	1123A3	a_{tu} (fps)	7.53	v_{\min} (fps)	-55.5
Wind Direction (deg)	No Data	a_{tv} (fps)	10.26	v_{\max} (fps)	45.1
Wind Velocity (fps)	No Data	a_{tv} (fps)	8.00	v_{\min} (fps)	-36.6

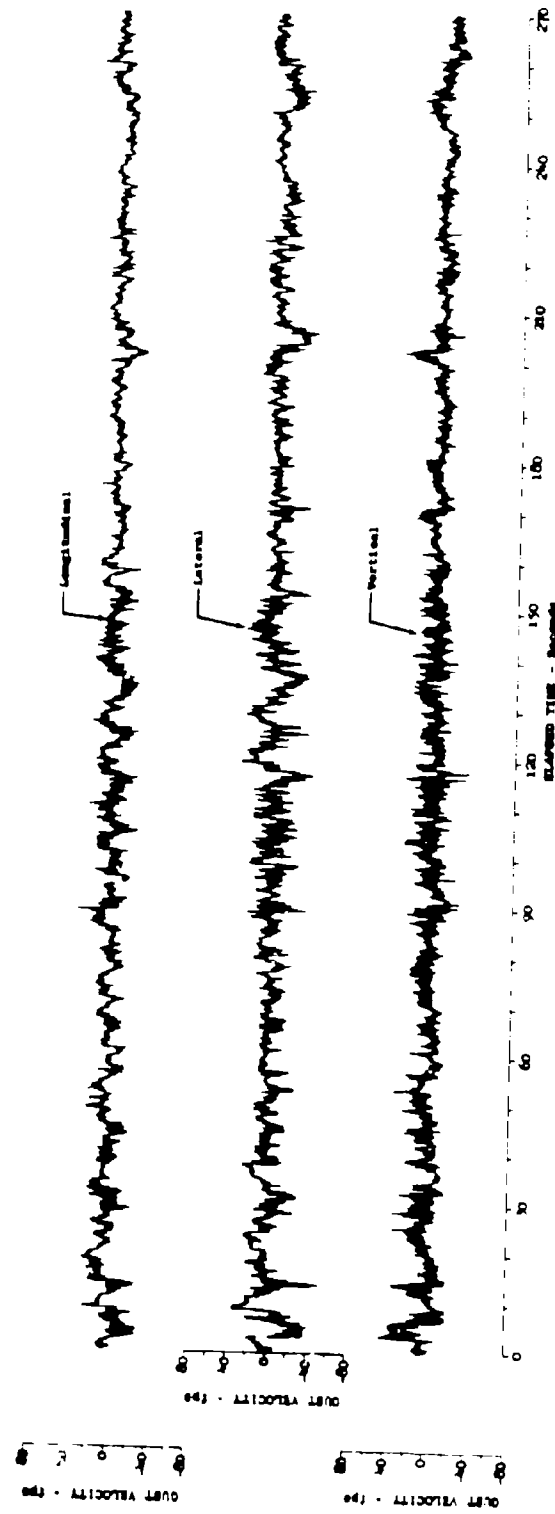


Figure 5.40 Time History of Gust Velocity Components - Severe Turbulence Encounter

Test	172	Ambient Air Temp (°F)	29.8	u _{max} (fps)	57.1
Date	2-6-69	True Airspeed (fps)	600.8	u _{min} (fps)	-53.4
Leg No.	2	Polar Altitude (ft)	405.0	v _{max} (fps)	41.8
Category No.	11k343	σ_u (fps)	8.58	v _{min} (fps)	-34.1
Wind direction (deg)	No Data	σ_v (fps)	6.74	v _{max} (fps)	34.3
Wind Velocity (fps)	No Data	σ_w (fps)	6.34	v _{min} (fps)	-40.2

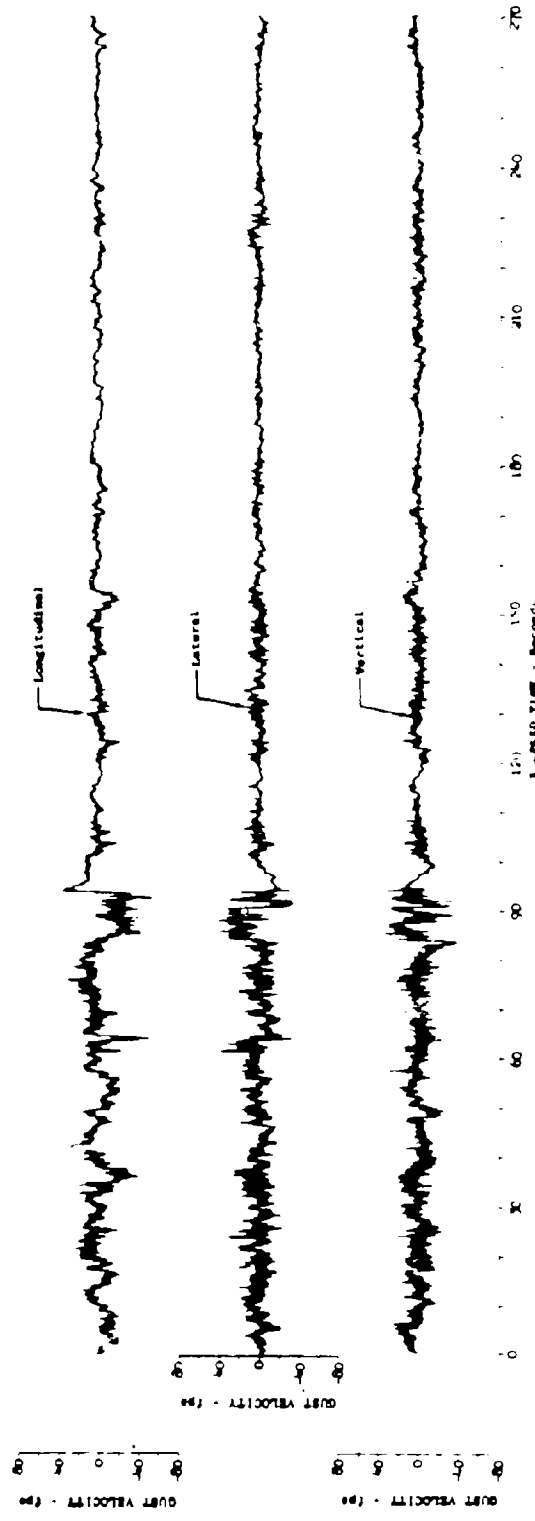


Figure 5.41 Time History of Gust Velocity Components - Severe Turbulence Encounter

Test	172	Ambient Air Temp (°F)	36.9	u_{\max} (fps)	48.6
Date	2-6-69	True Airspeed (fps)	580.7	u_{\min} (fps)	-31.4
Leg No.	6	Pilot Altitude (ft)	345.7	v_{\max} (fps)	38.0
Category No.	112343	σ_u (fps)	7.14	v_{\min} (fps)	-40.1
Wind Direction (deg)	259.9	σ_w (fps)	9.74	w_{\max} (fps)	36.9
Wind Velocity (fps)	71.5	σ_w (fps)	7.68	w_{\min} (fps)	-54.6

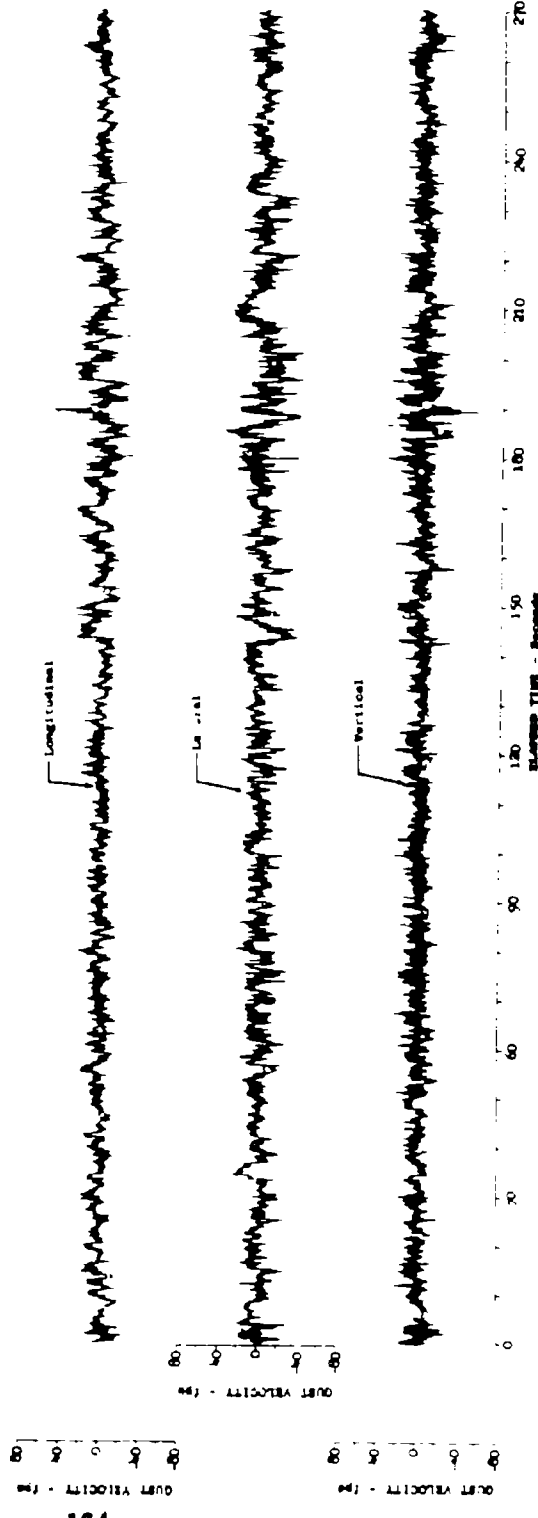


Figure 5.42 Time History of Gust Velocity Components - Severe Turbulence Encounter

Test	181	Ambient Air Temp ($^{\circ}\text{F}$)	34.5	u_{\max} (fps)	52.1
Date	2-13-69	True Airspeed (fps)	626.7	u_{\min} (fps)	-45.3
Leg No.	5	Pedair Altitude (ft)	438	v_{\max} (fps)	48.1
Category No.	113343	u_w (fps)	9.34	v_{\min} (fps)	-41.1
Wind Direction (deg)	307.6	s_{uv} (fps)	12.71	w_{\max} (fps)	61.9
Wind Velocity (fps)	24.8	s_{uw} (fps)	8.96	w_{\min} (fps)	-47.5

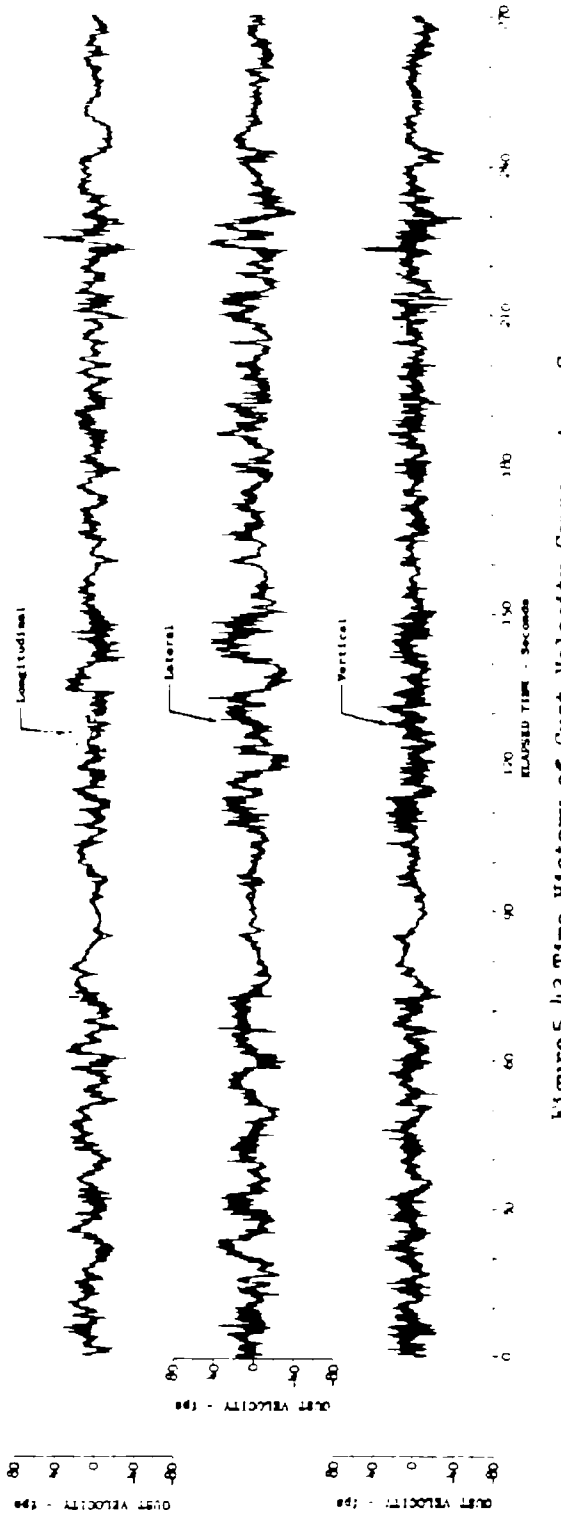


Figure 5.43 Time History of Gust Velocity Components - Severe Turbulence Encounter

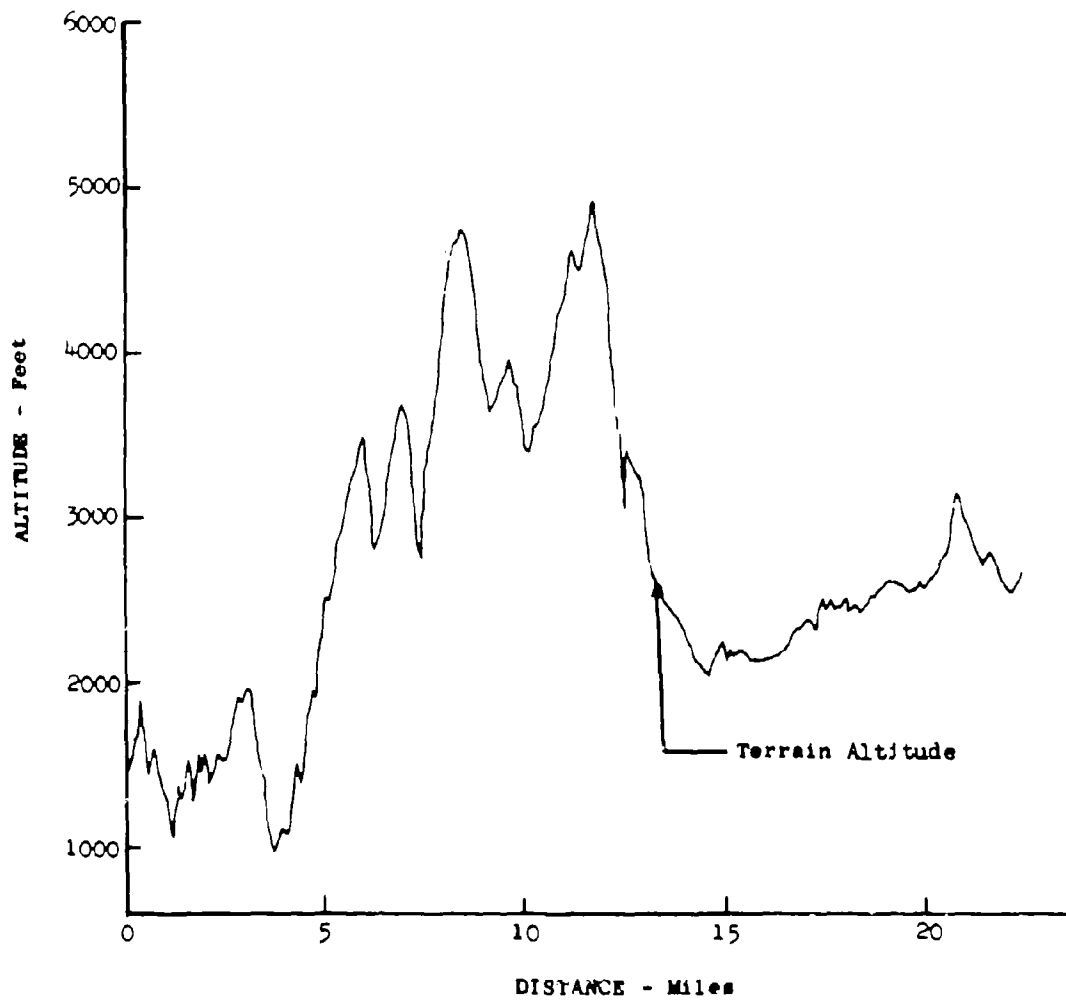


Figure 5.44 Terrain Profile of Leg 2 - Peterson Field Route

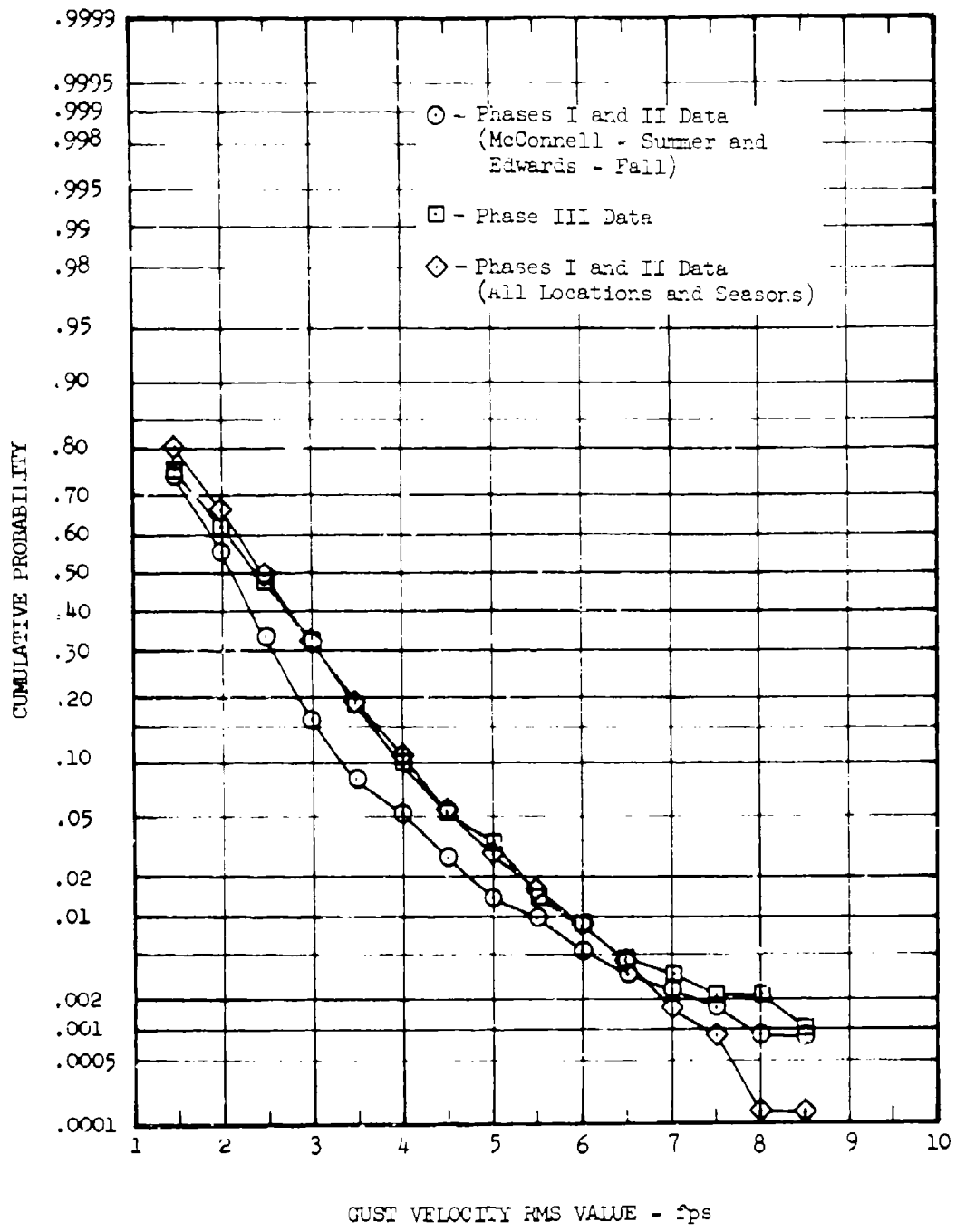


Figure 5.45 Longitudinal Gust Velocity RMS Cumulative Probability During Various Phases of LO-LOCAT

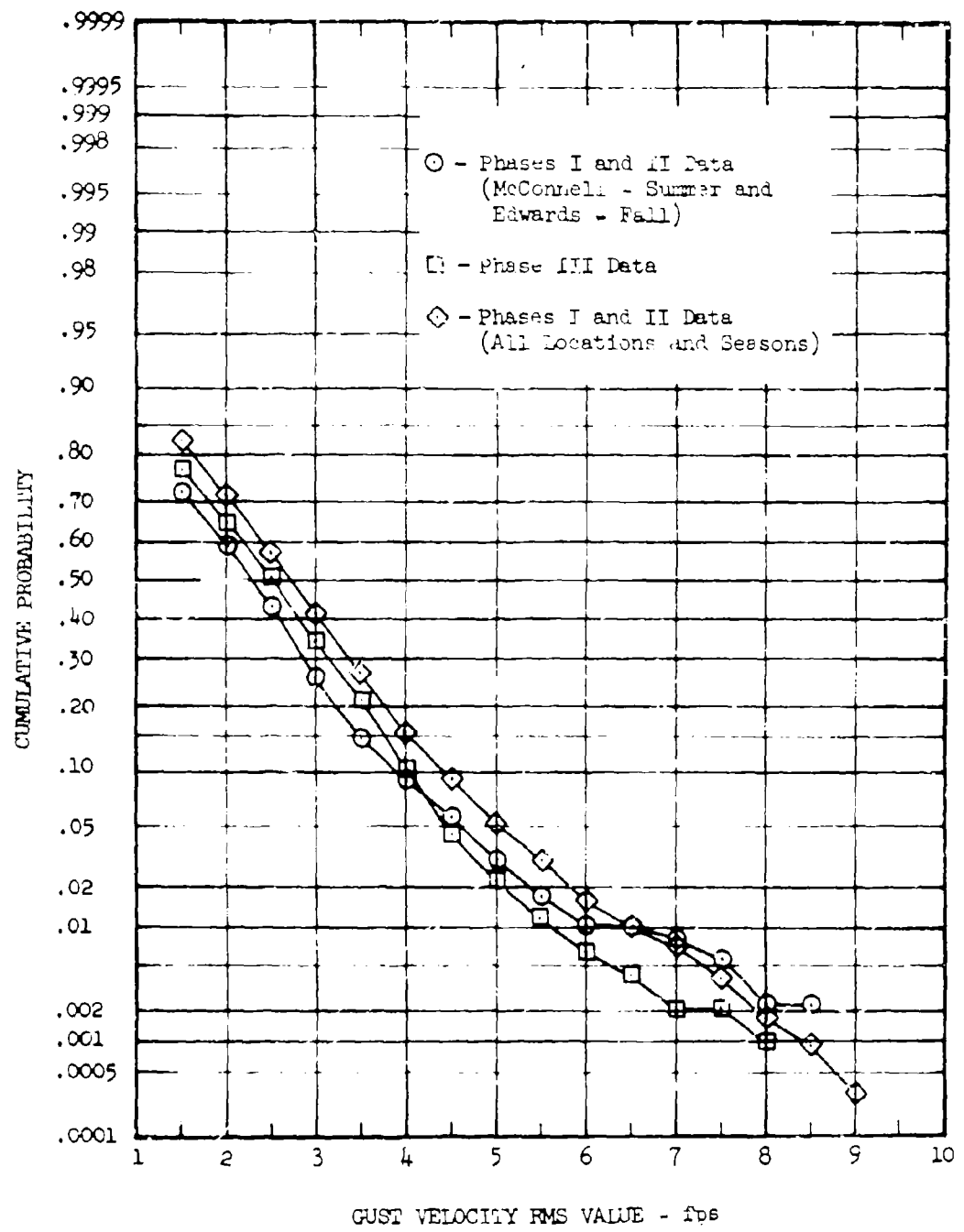


Figure 5.46 Lateral Gust Velocity RMS Cumulative Probability During Various Phases of LO-LOCAT

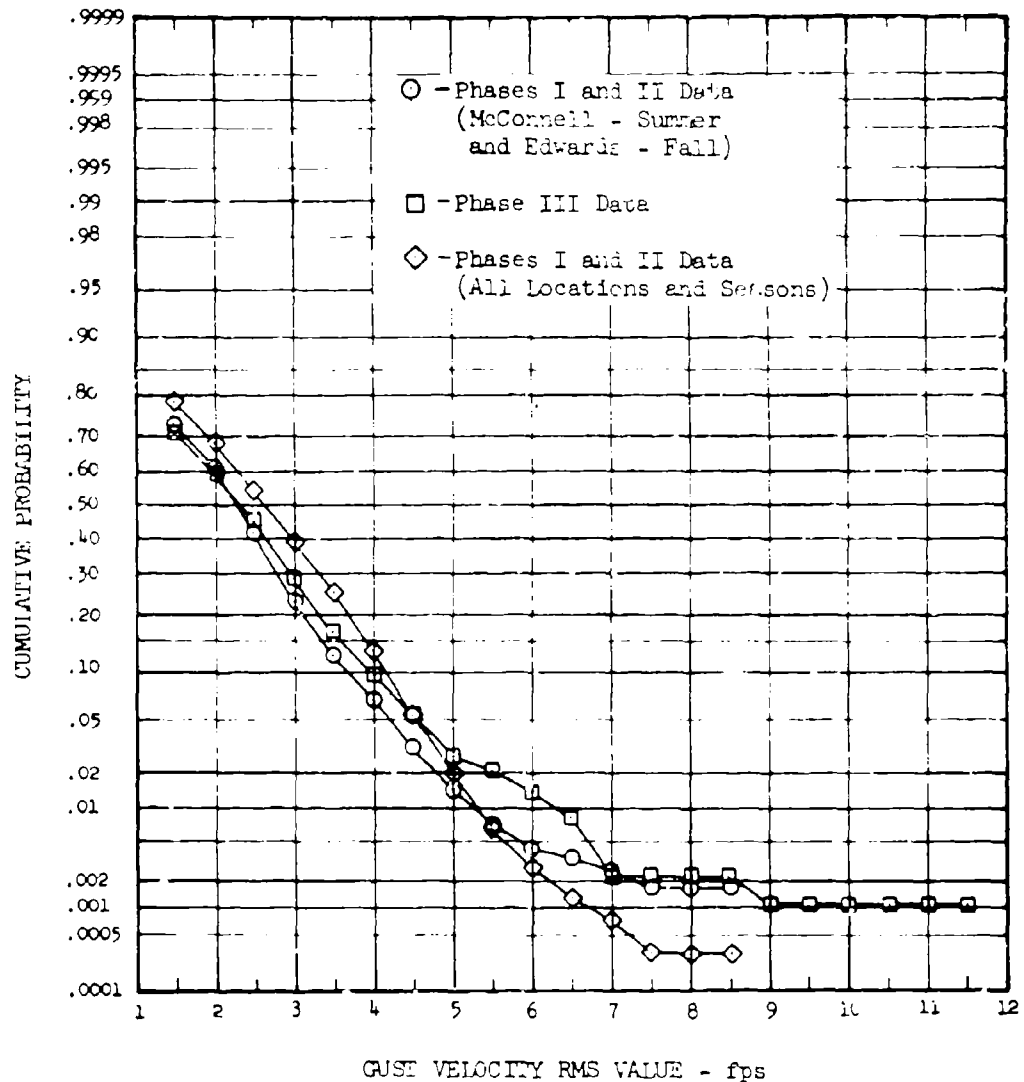


Figure 5.47 Vertical Gust Velocity RMS Cumulative Probability During Various Phases of LO-LOCAT

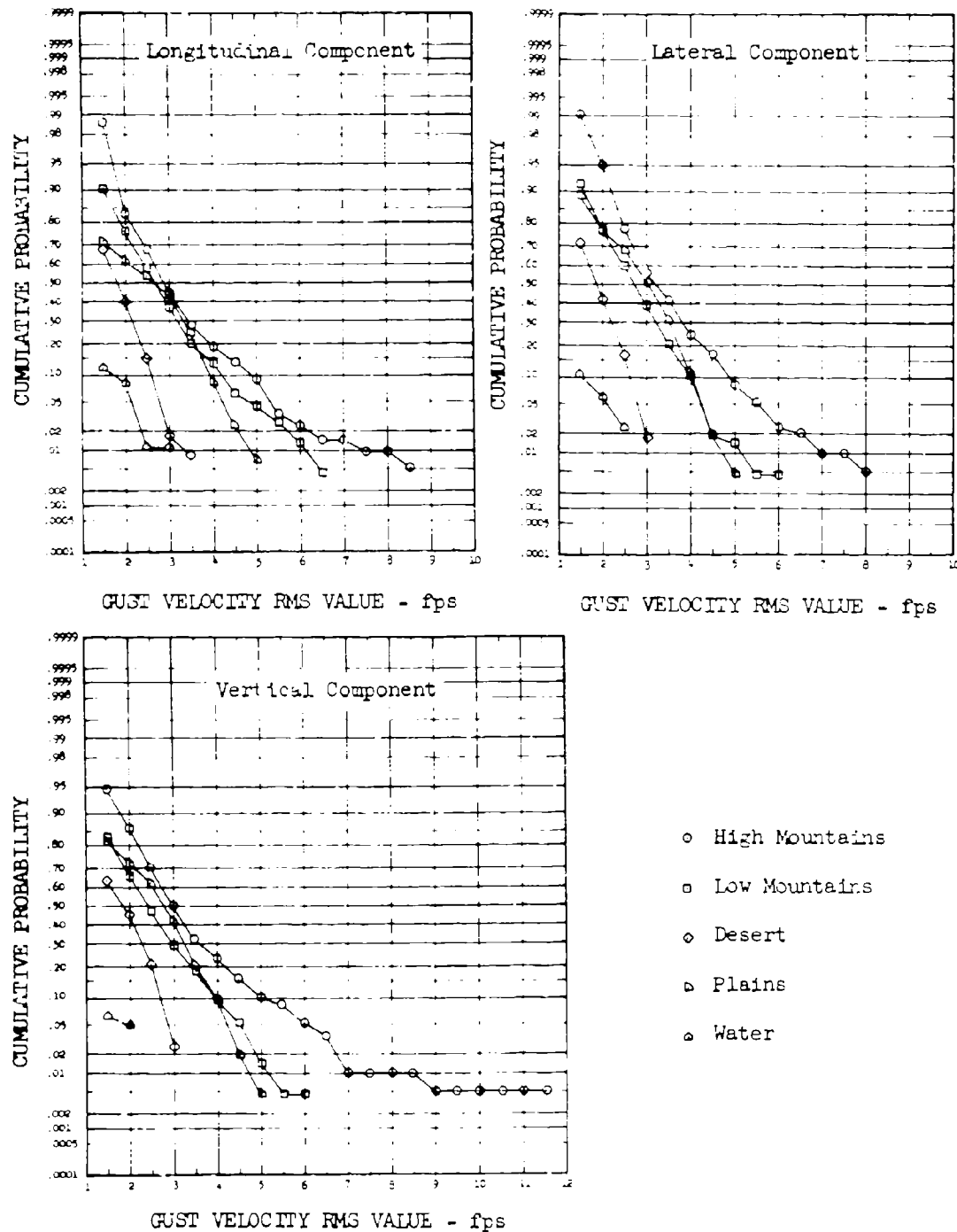


Figure 5.48 Gust Velocity RMS Cumulative Probability Associated with Terrain

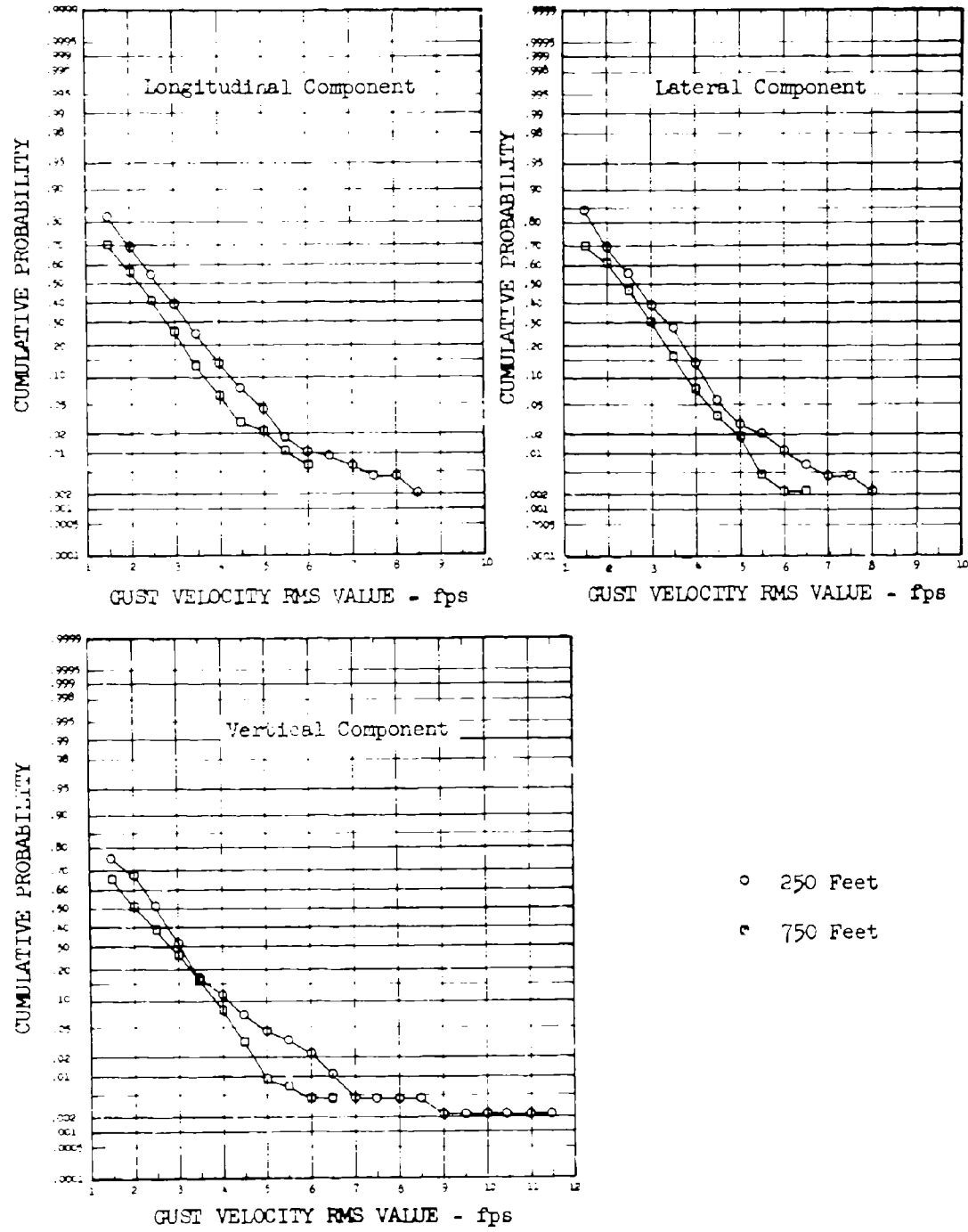


Figure 5.49 Gust Velocity RMS Cumulative Probability Associated with Altitude

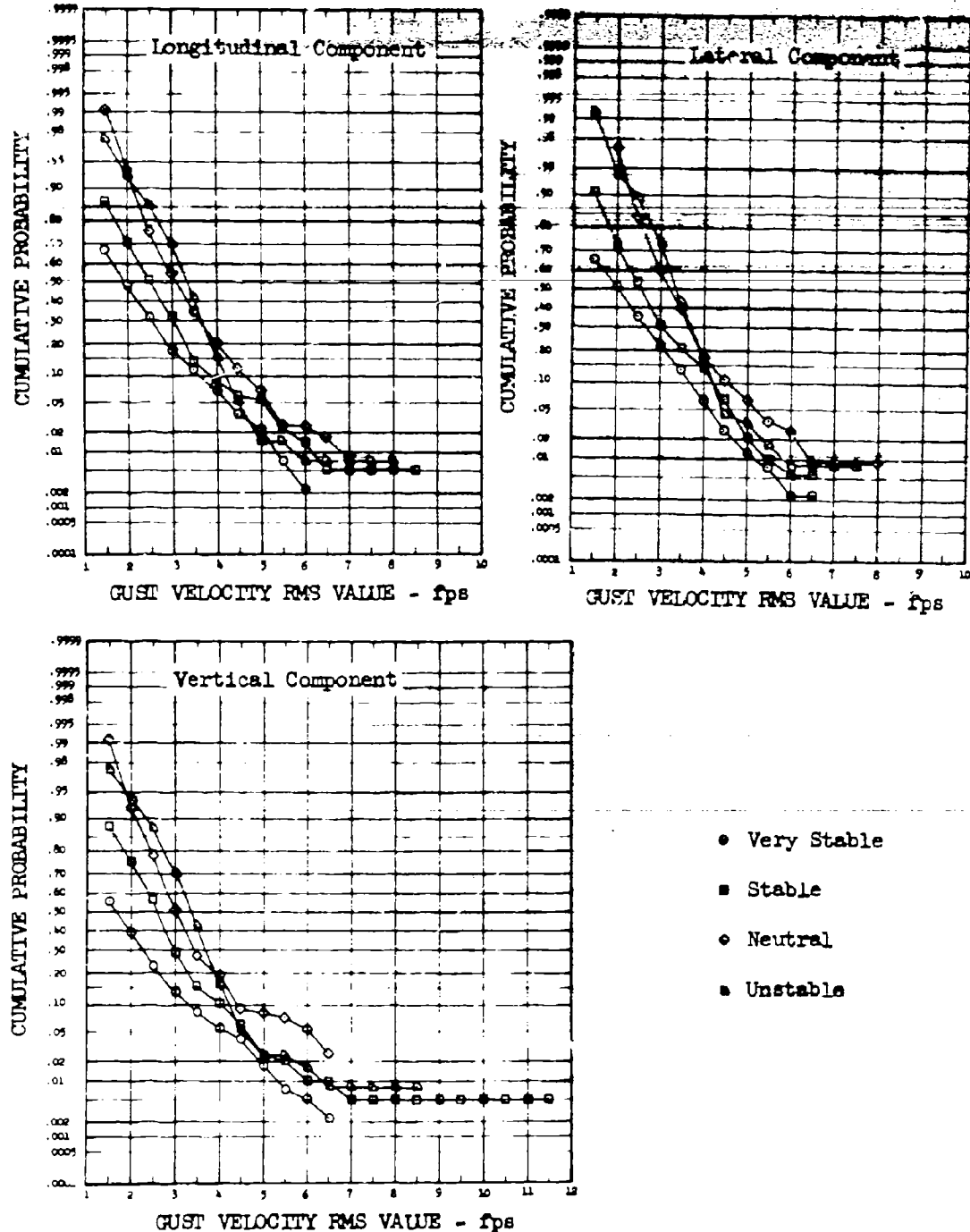


Figure 5.50 Gust Velocity RMS Cumulative Probability Associated with Atmospheric Stability

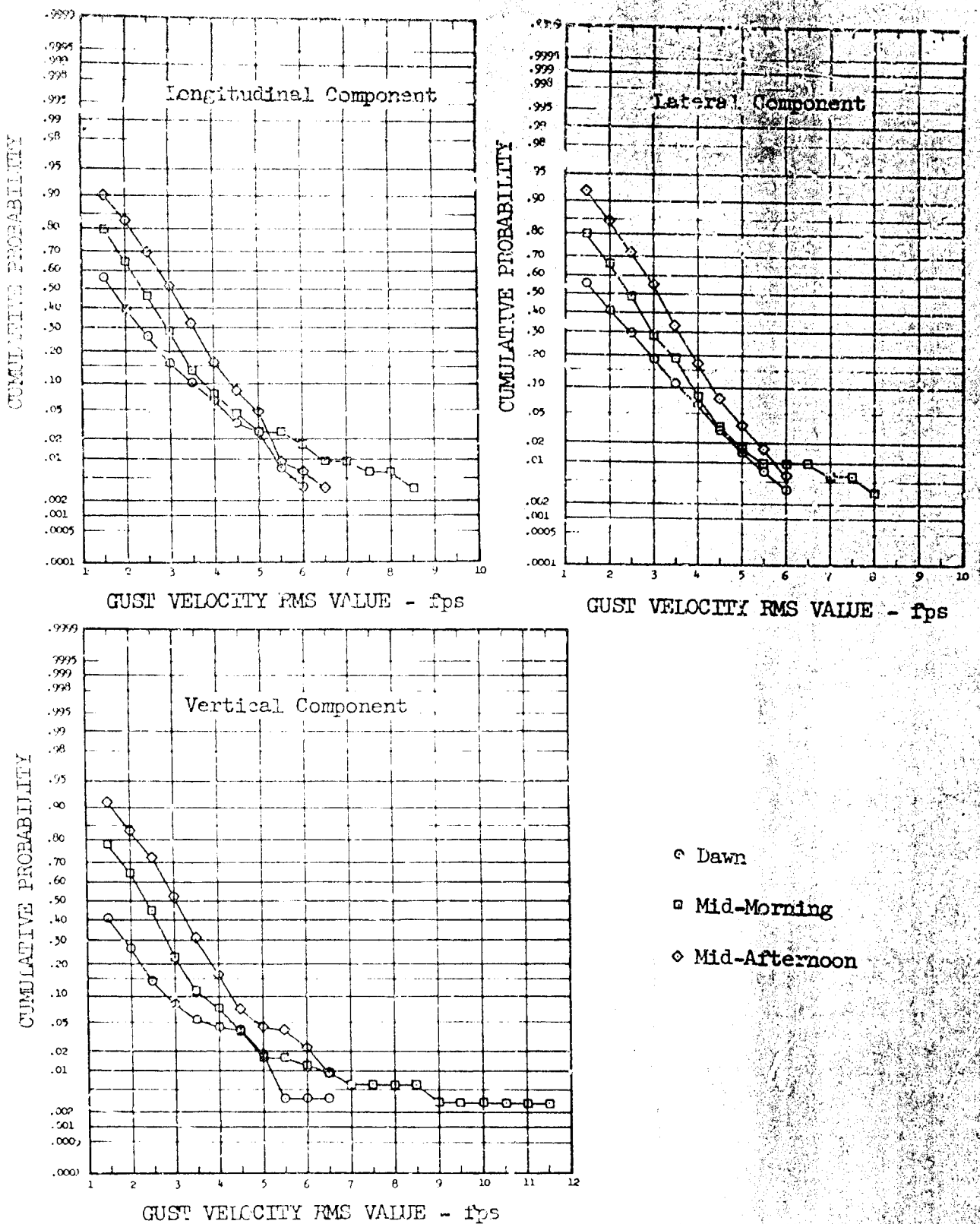


Figure 5.51 Gust Velocity RMS Cumulative Probability Associated with Time-of-Day

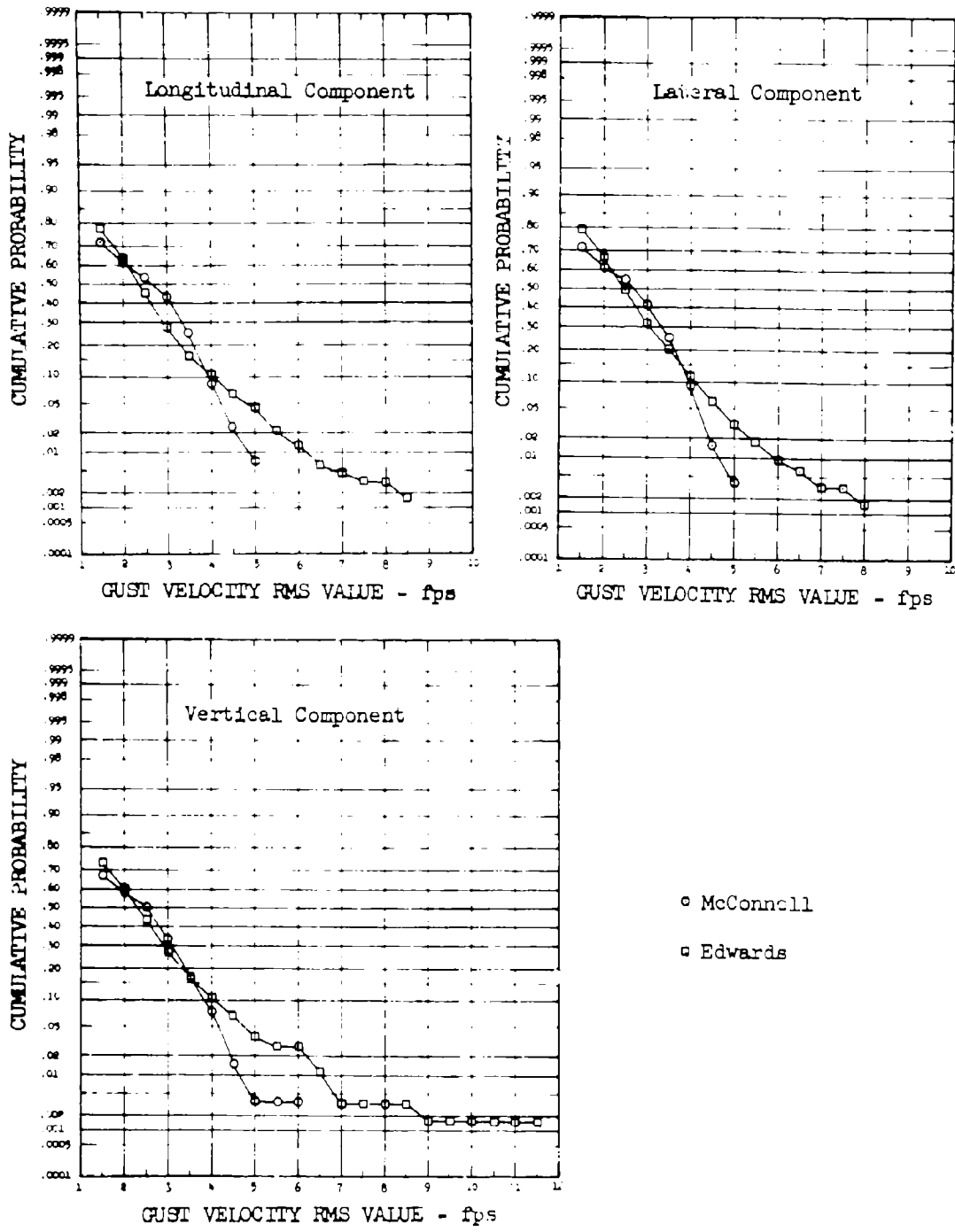


Figure 5.5 Gust Velocity RMS Cumulative Probability Associated with Location

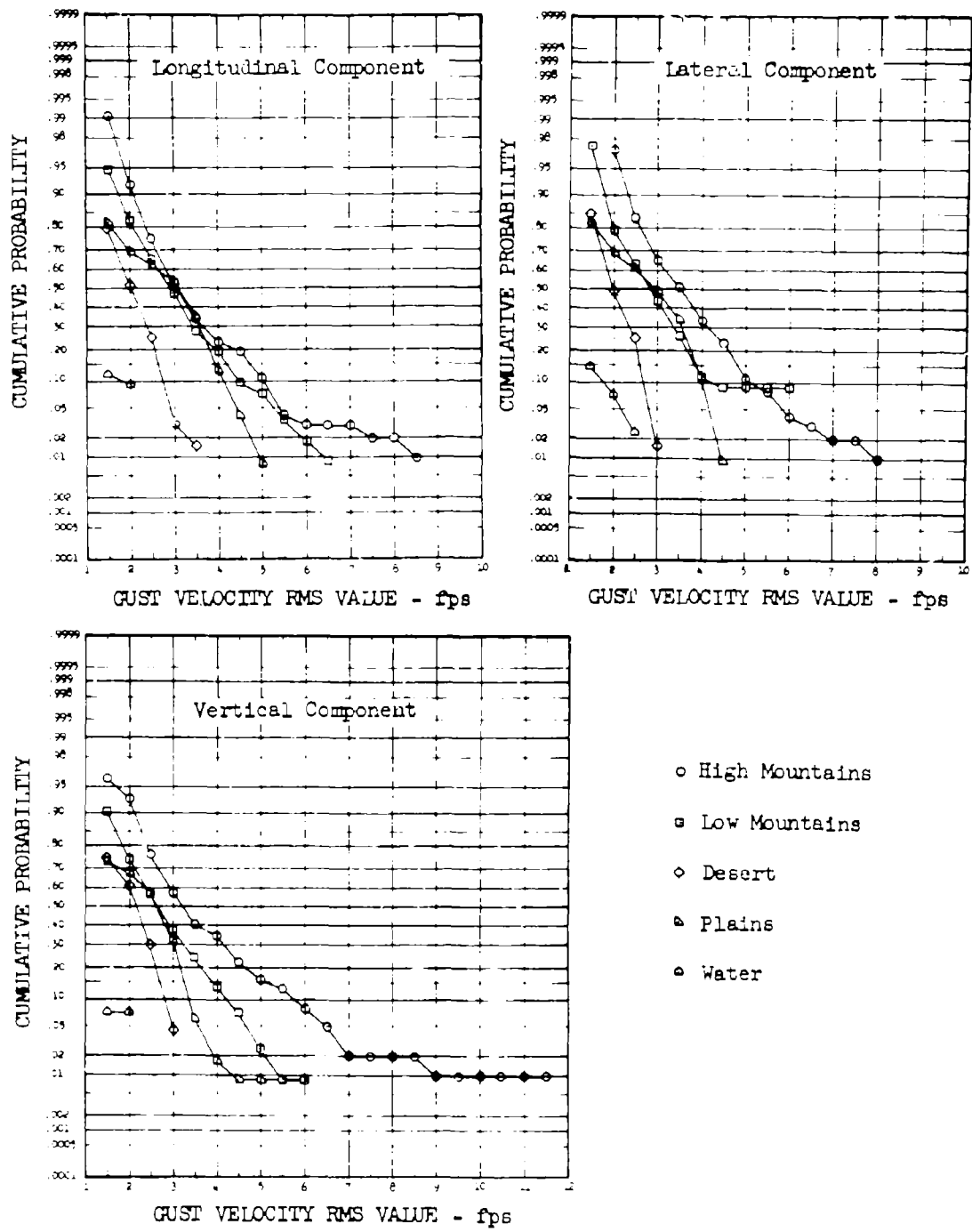


Figure 5.53 Effects of Terrain on Cumulative Probability of Gust Velocity RMS Values Obtained at 250 Feet

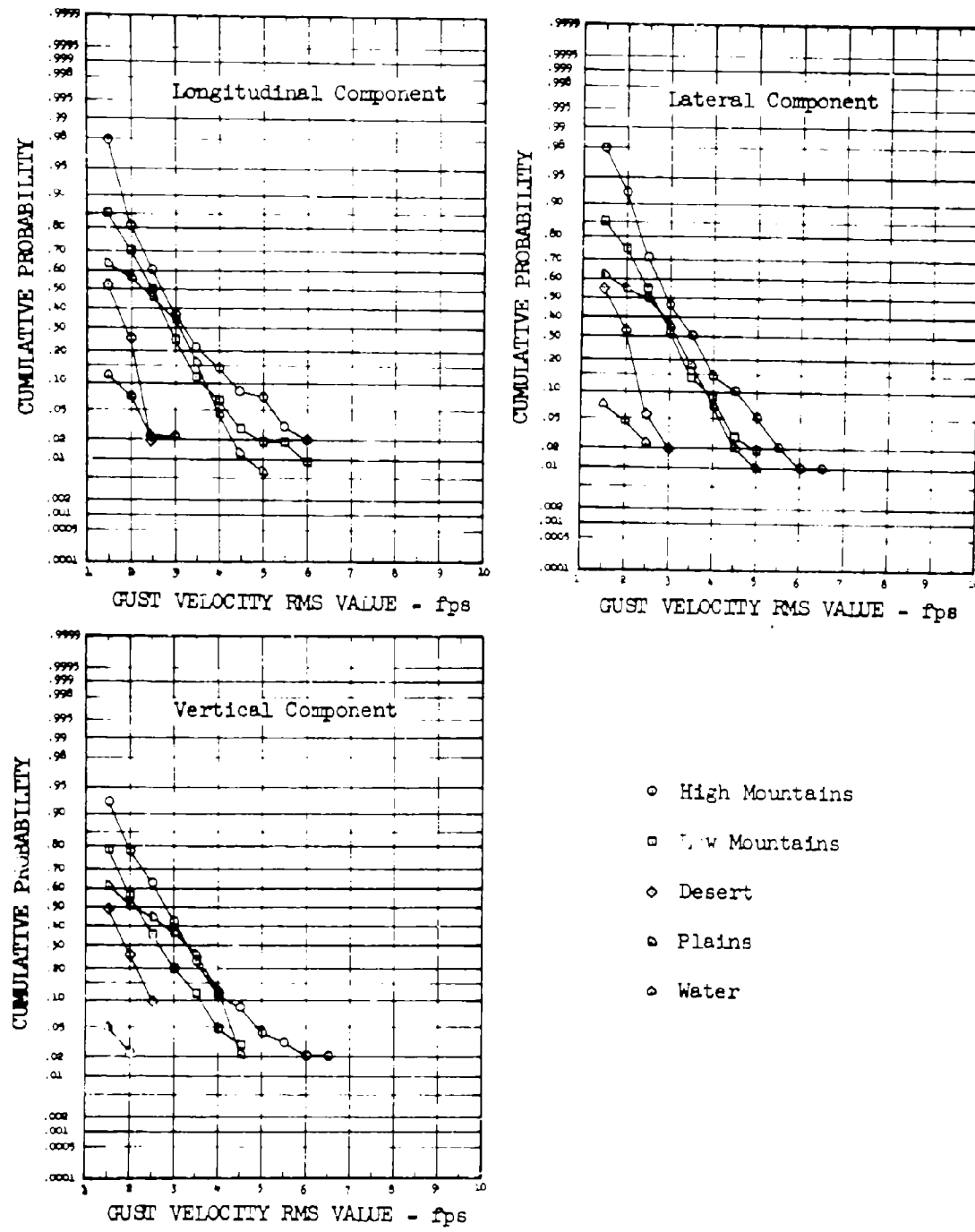


Figure 5.54 Effects of Terrain on Cumulative Probability of Gust Velocity RMS Values Obtained at 750 Feet

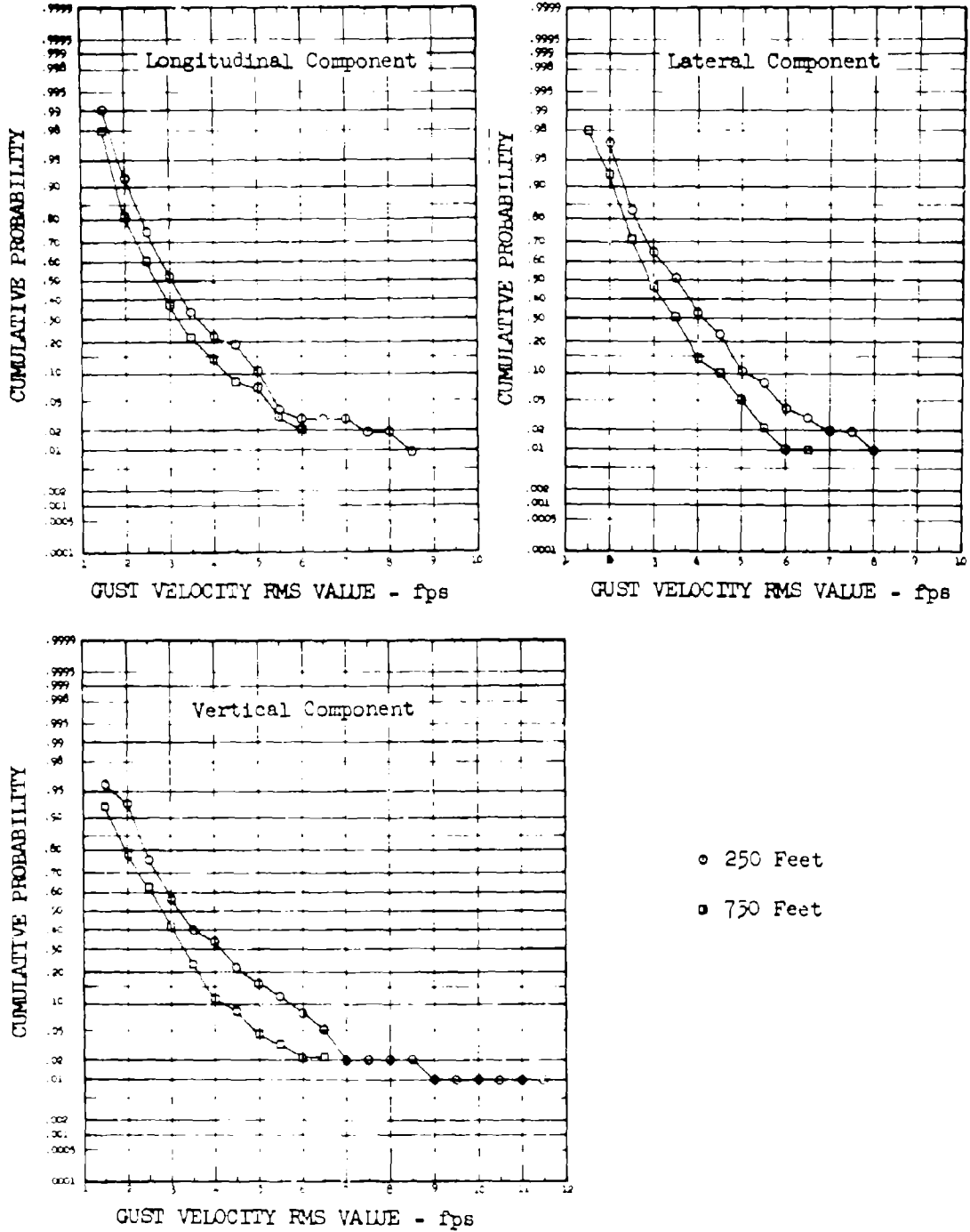


Figure 5.55 Effects of Altitude over High Mountains on Gust Velocity RMS Cumulative Probability

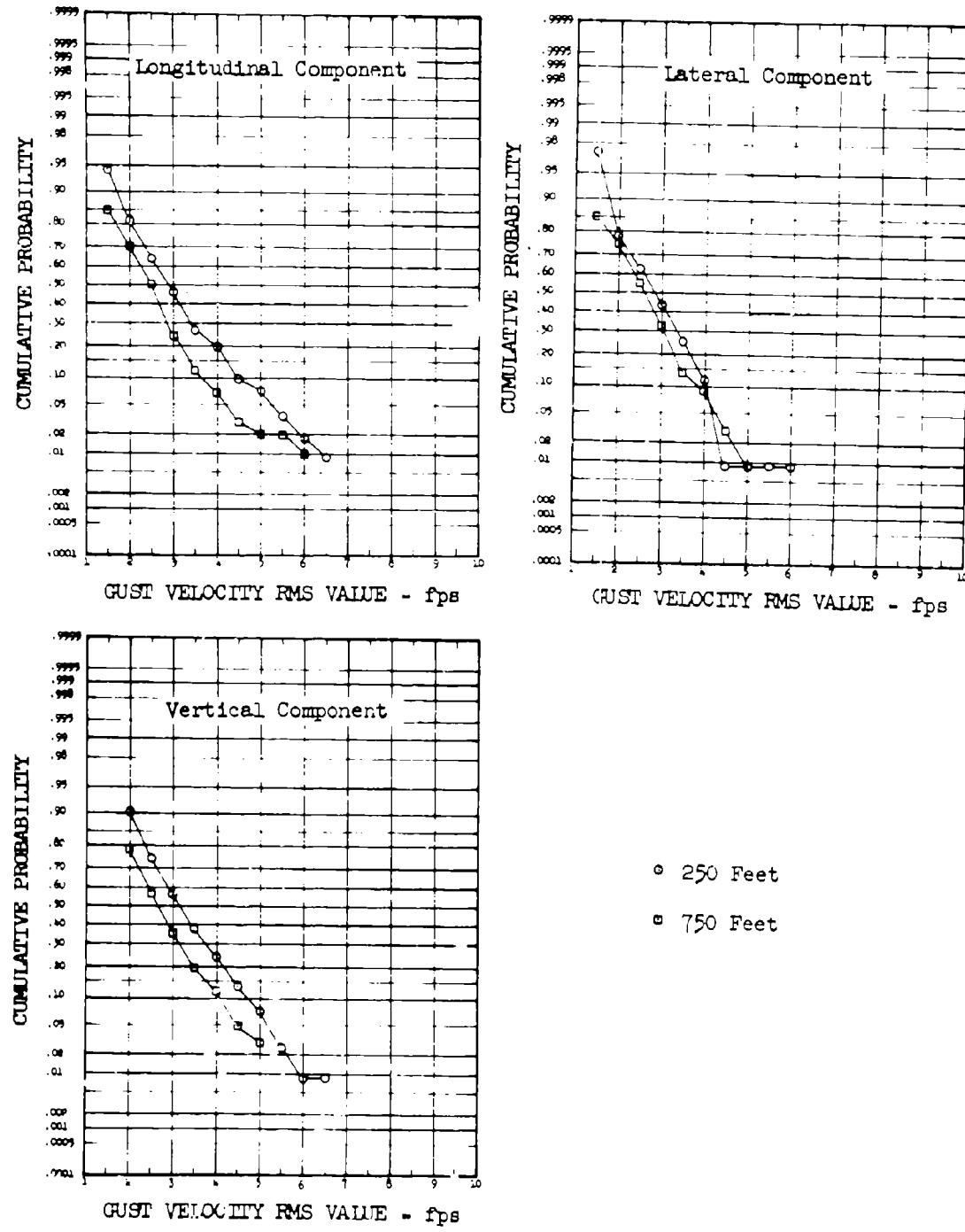


Figure 5.56 Effects of Altitude over Low Mountains on Gust Velocity RMS Cumulative Probability

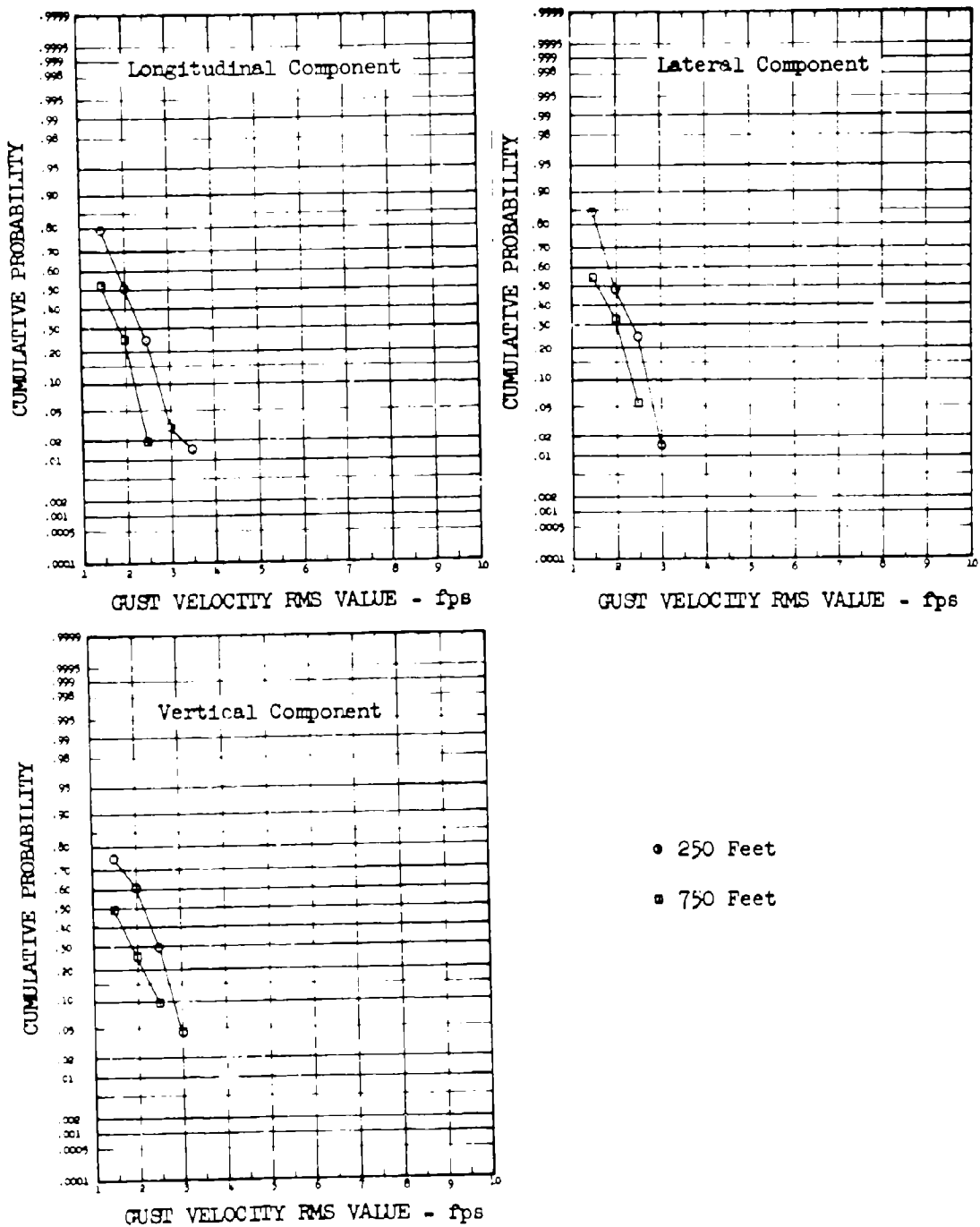


Figure 5.57 Effects of Altitude over Desert Terrain on Gust Velocity RMS Cumulative Probability

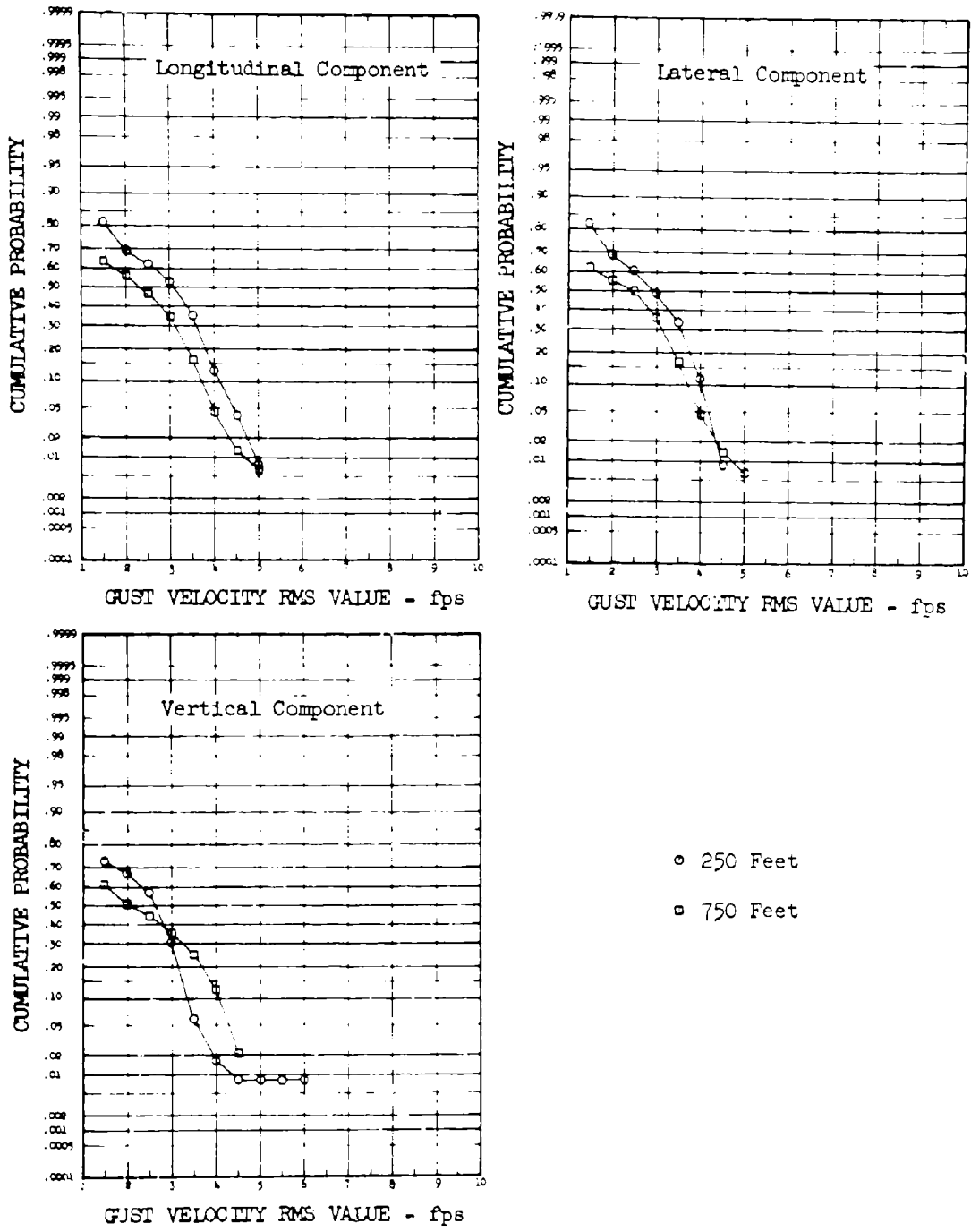


Figure 5.58 Effects of Altitude over Plains on Gust Velocity RMS Cumulative Probability

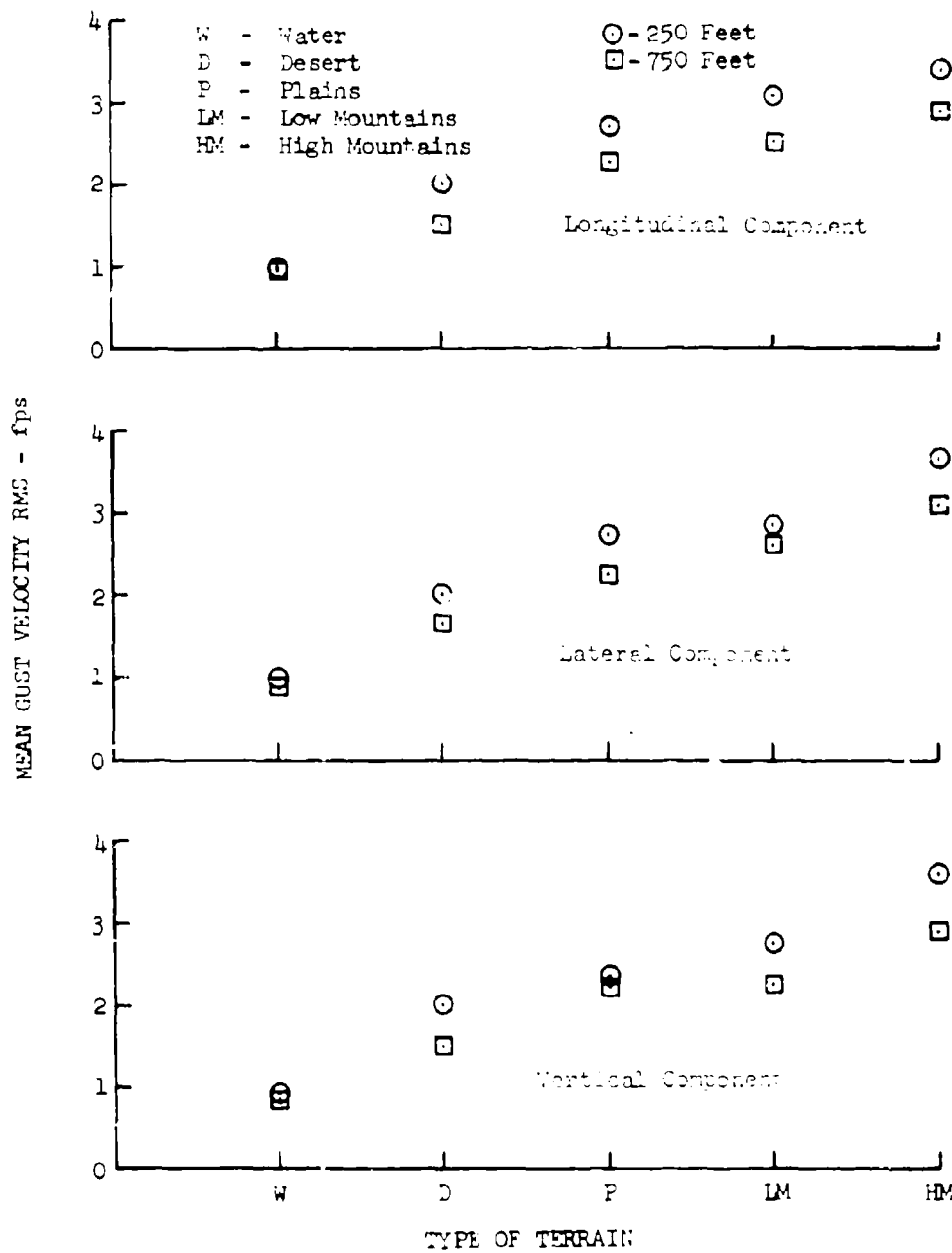


Figure 5.59 Variation of Gust Velocity RMS Mean Values with Terrain and Altitude

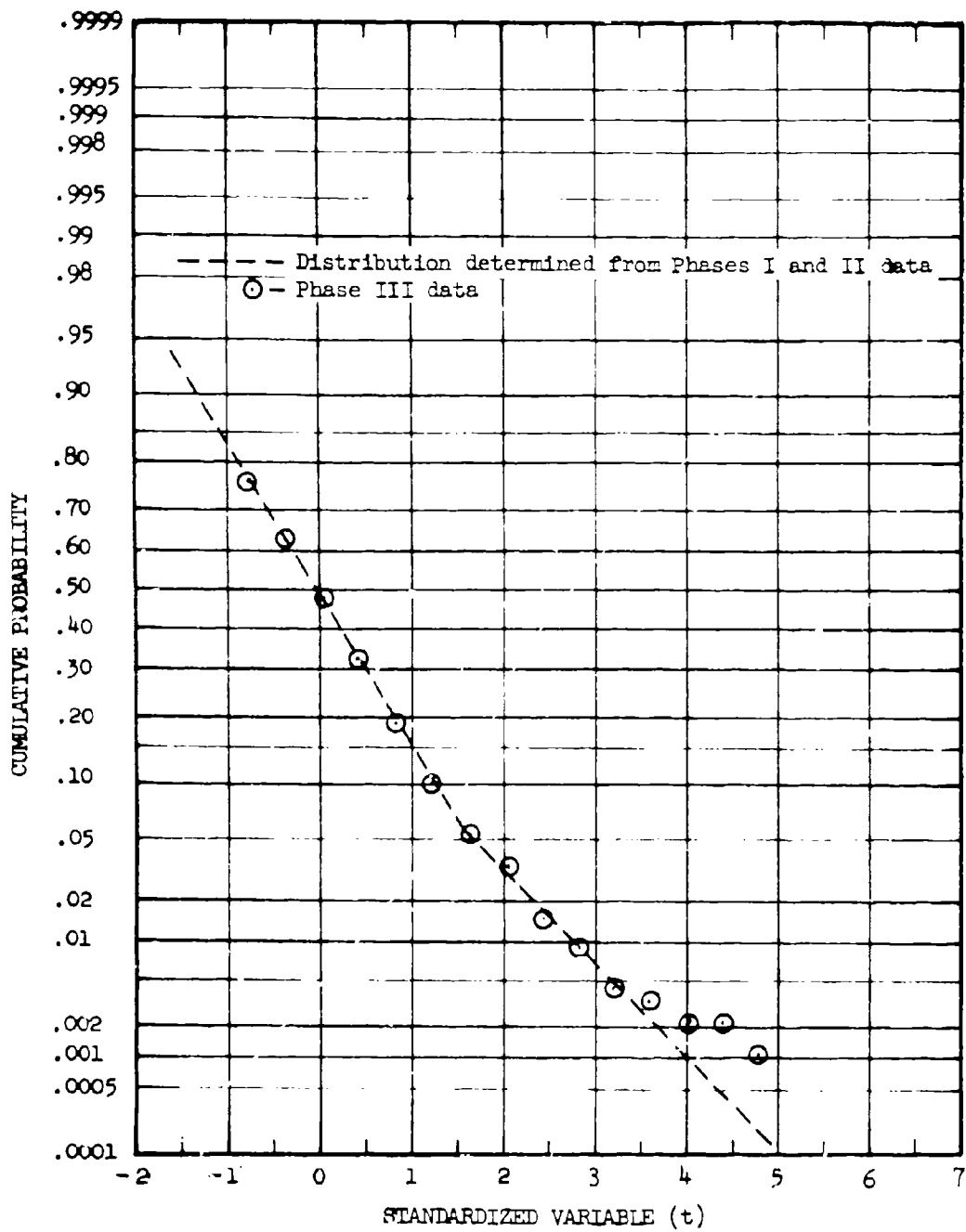


Figure 5.60 Standardized Longitudinal Gust Velocity RMS Cumulative Probability Distribution.

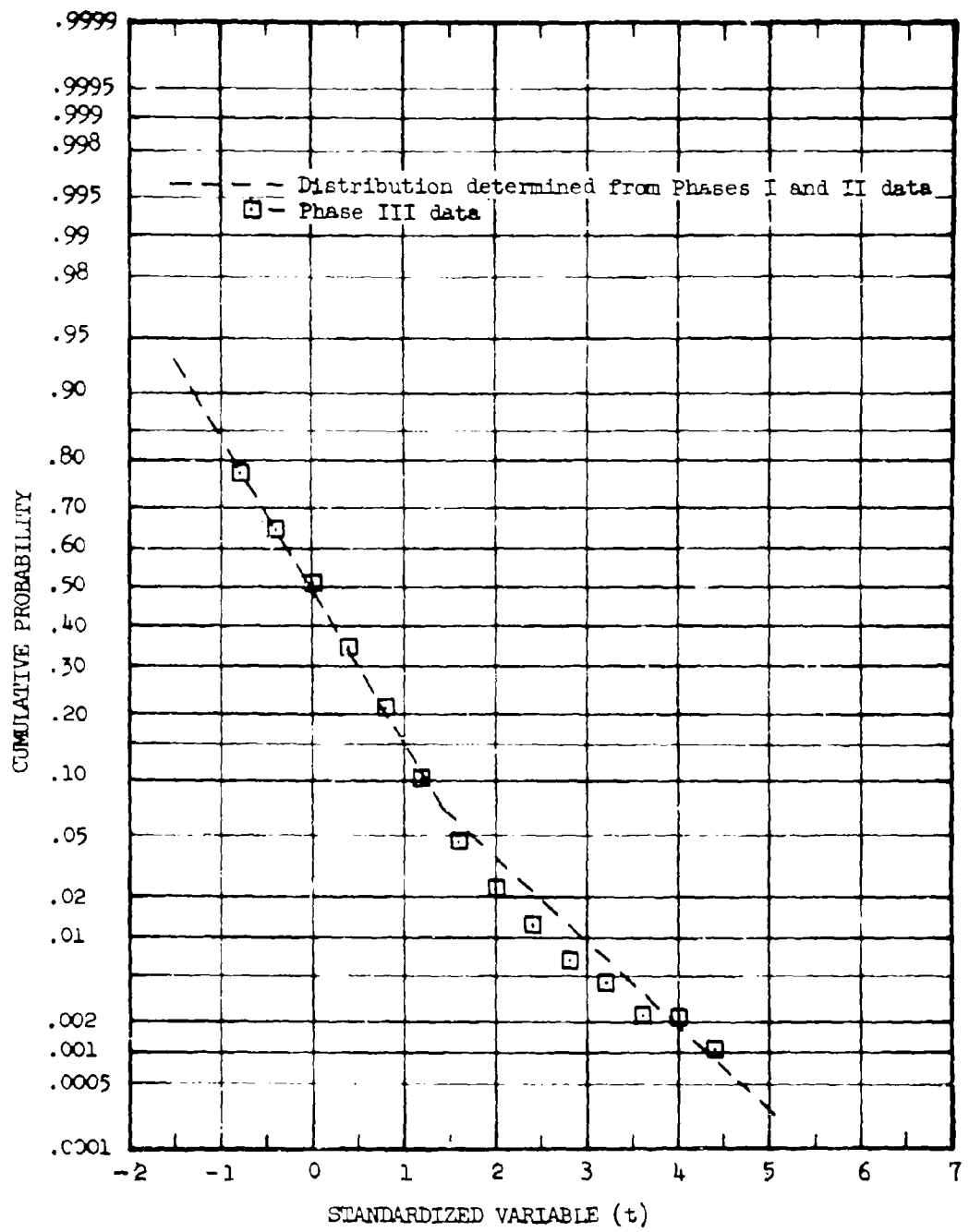


Figure 5.61 Standardized Lateral Gust Velocity RMS Cumulative Probability Distribution

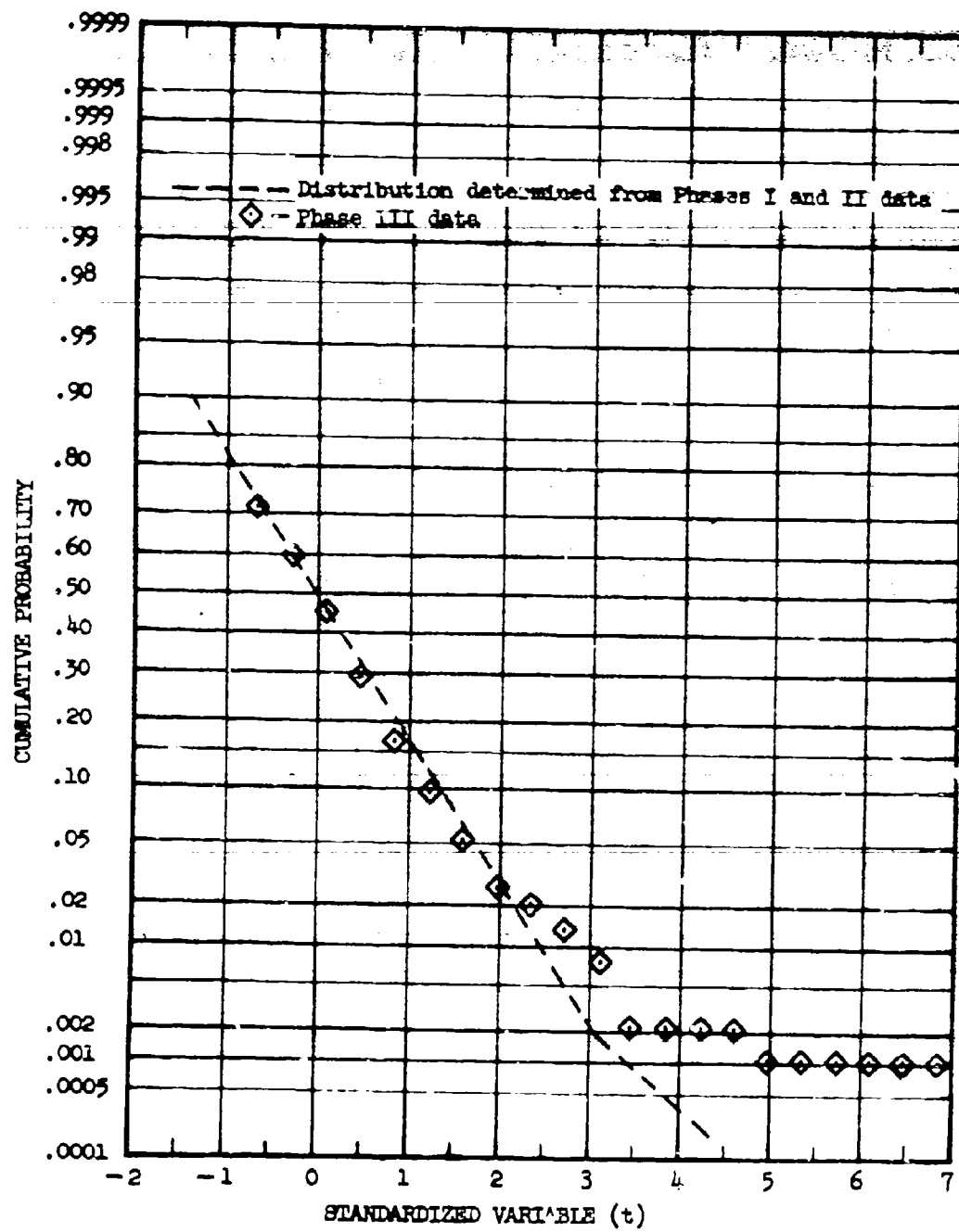


Figure 5.62 Standardized Vertical Gust Velocity RMS Cumulative Probability Distribution

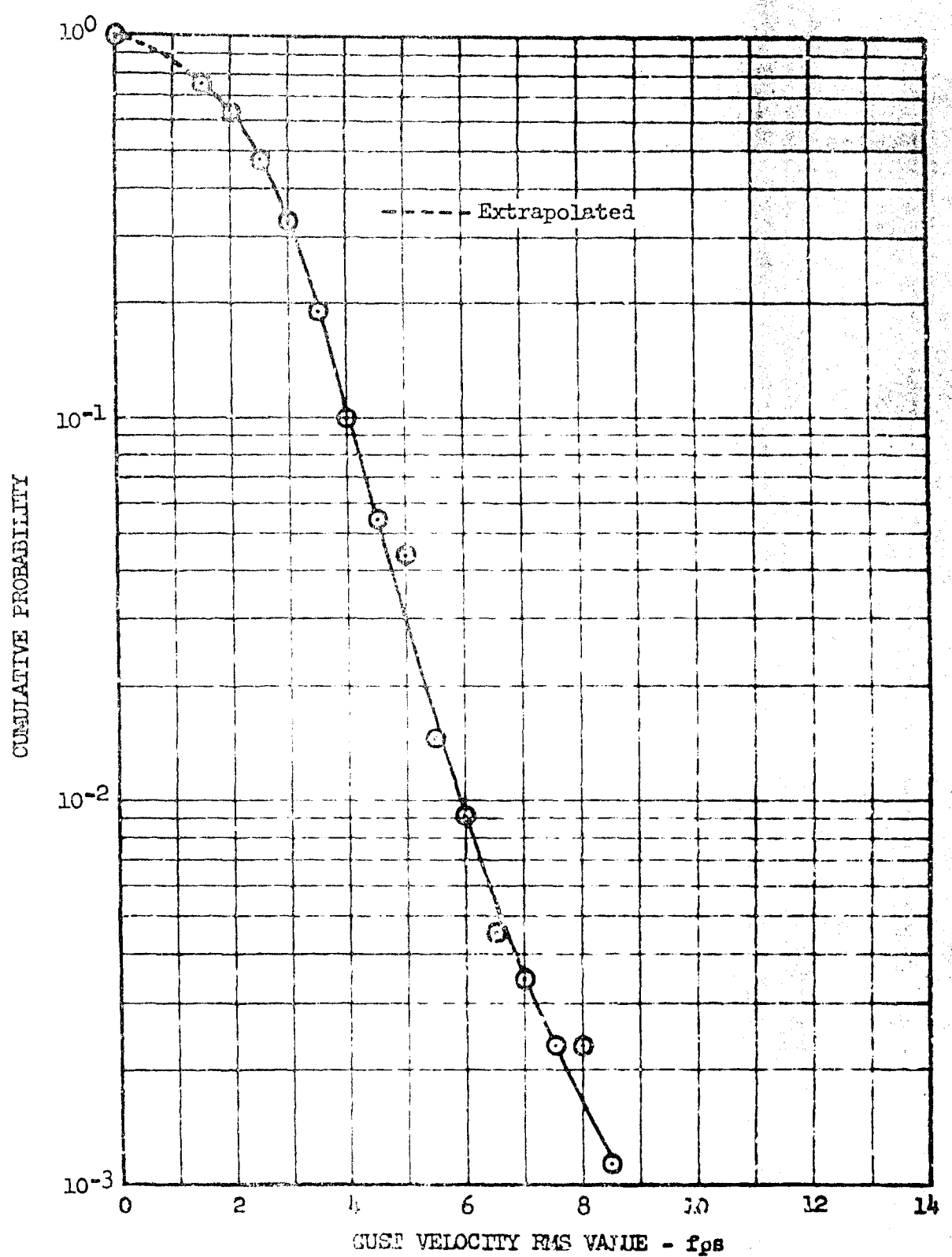


Figure 5.63 Extrapolated Longitudinal Gust Velocity RMS Cumulative Probability

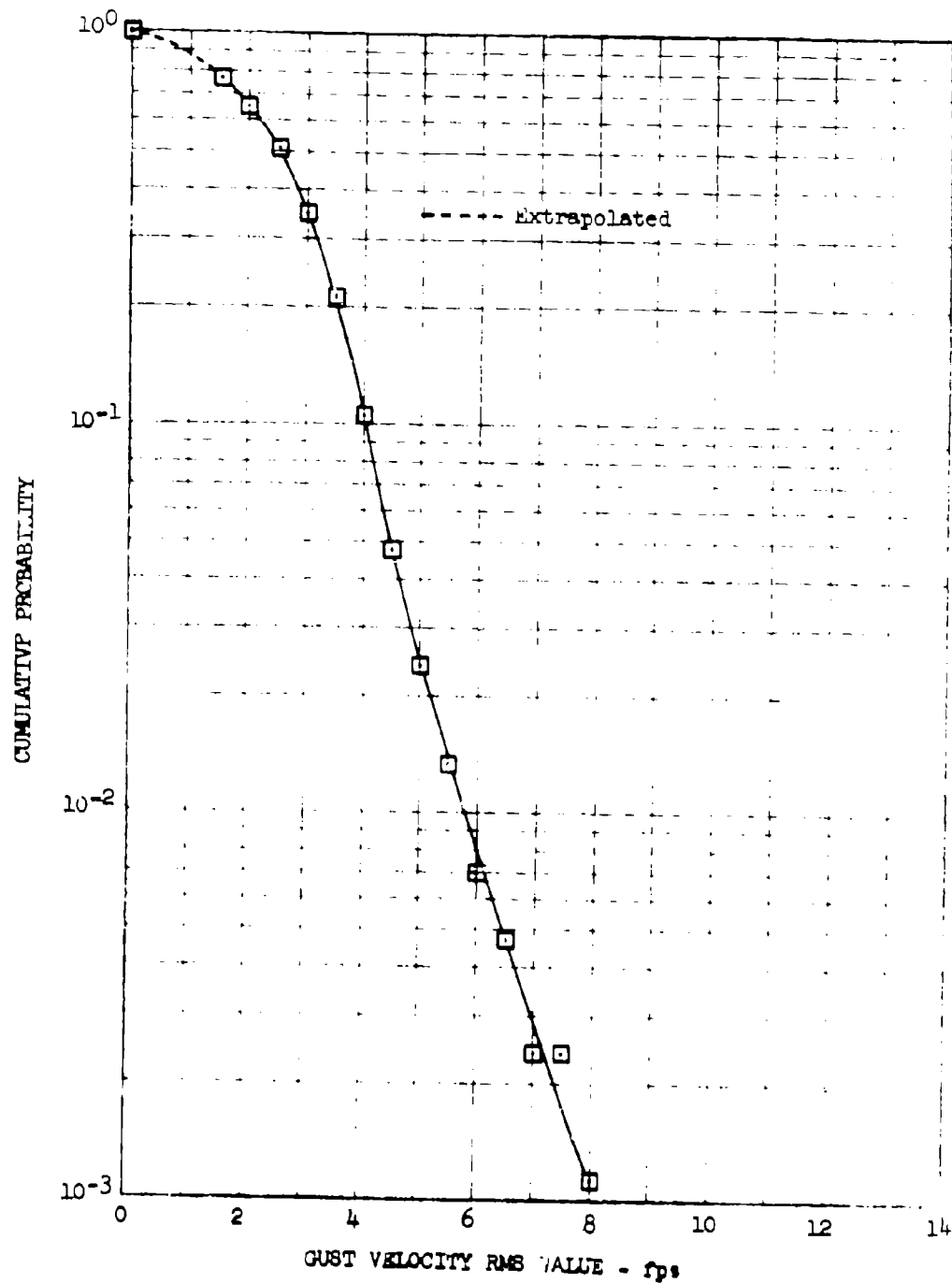


Figure 5.64 Extrapolated Lateral Gust Velocity RMS Cumulative Probability

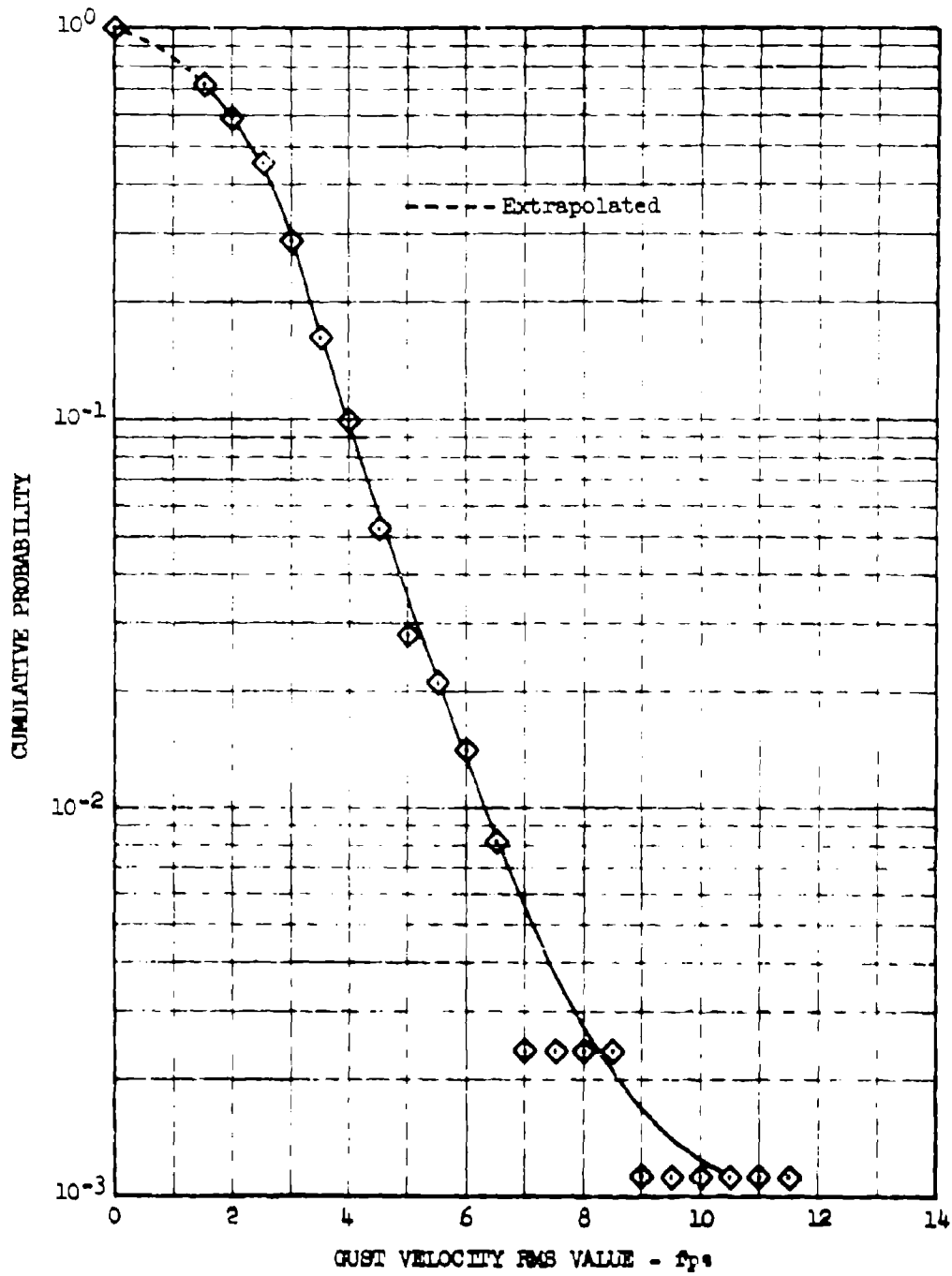


Figure 5.65 Extrapolated Vertical Gust Velocity RMS Cumulative Probability

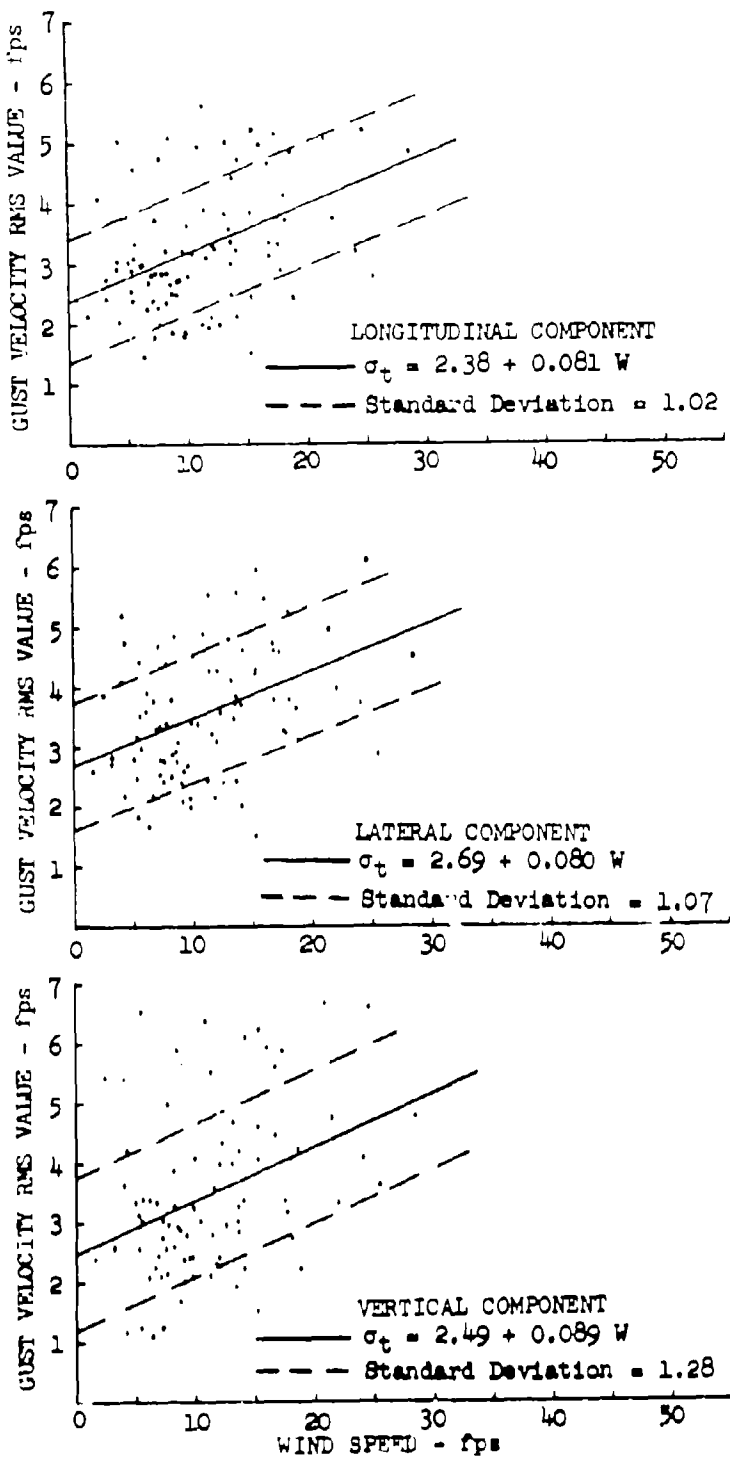


Figure 5.66 Gust Velocity RMS Values versus Wind Speed at 250 Feet Over High Mountains

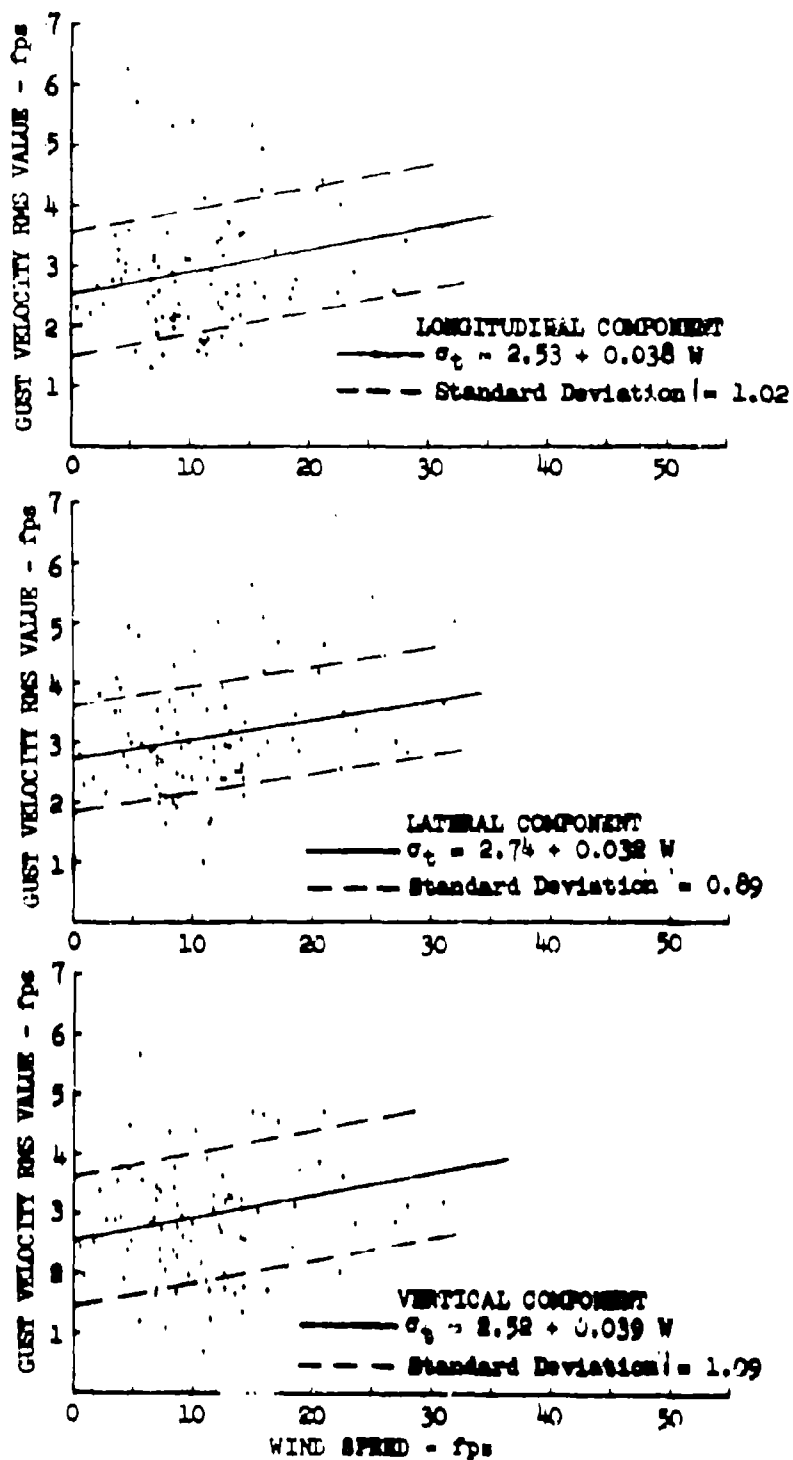


Figure 5.67 Gust Velocity RMS Values versus Wind Speed at 750 Feet Over High Mountains

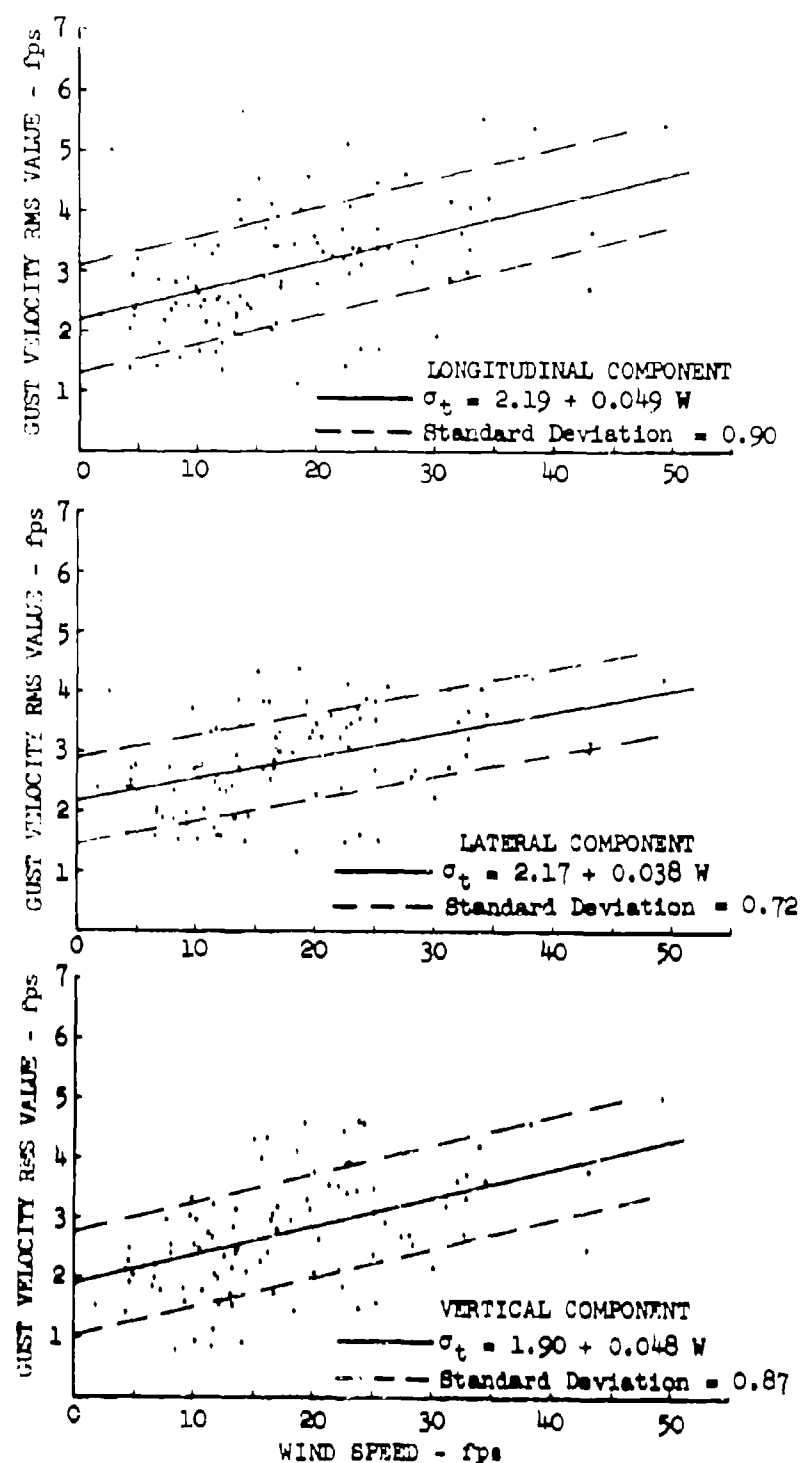


Figure 5.68 Gust Velocity RMS Values versus Wind Speed at 250 Feet Over Low Mountains

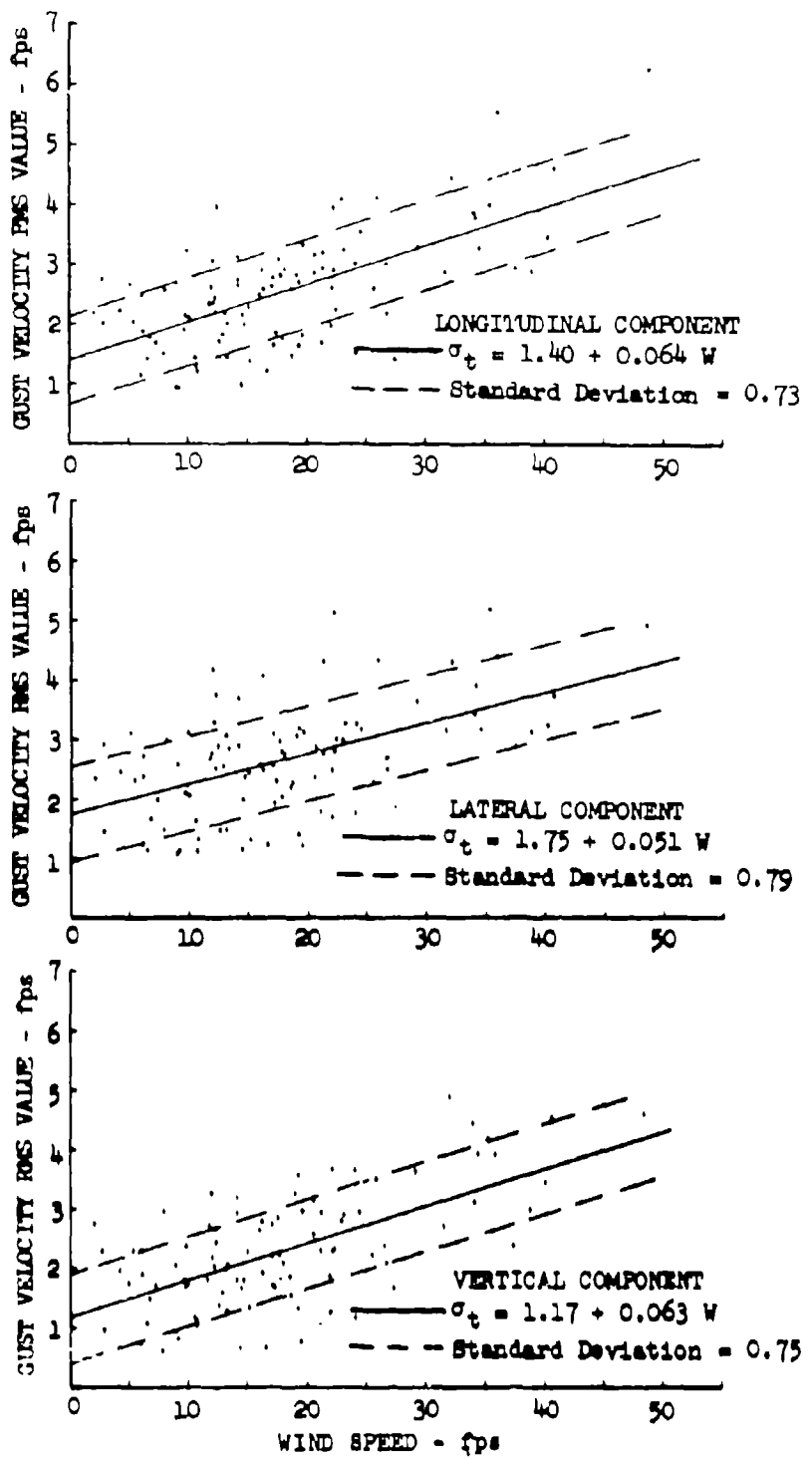


Figure 5.69 Gust Velocity RMS Values versus Wind Speed at 750 Feet Over Low Mountains

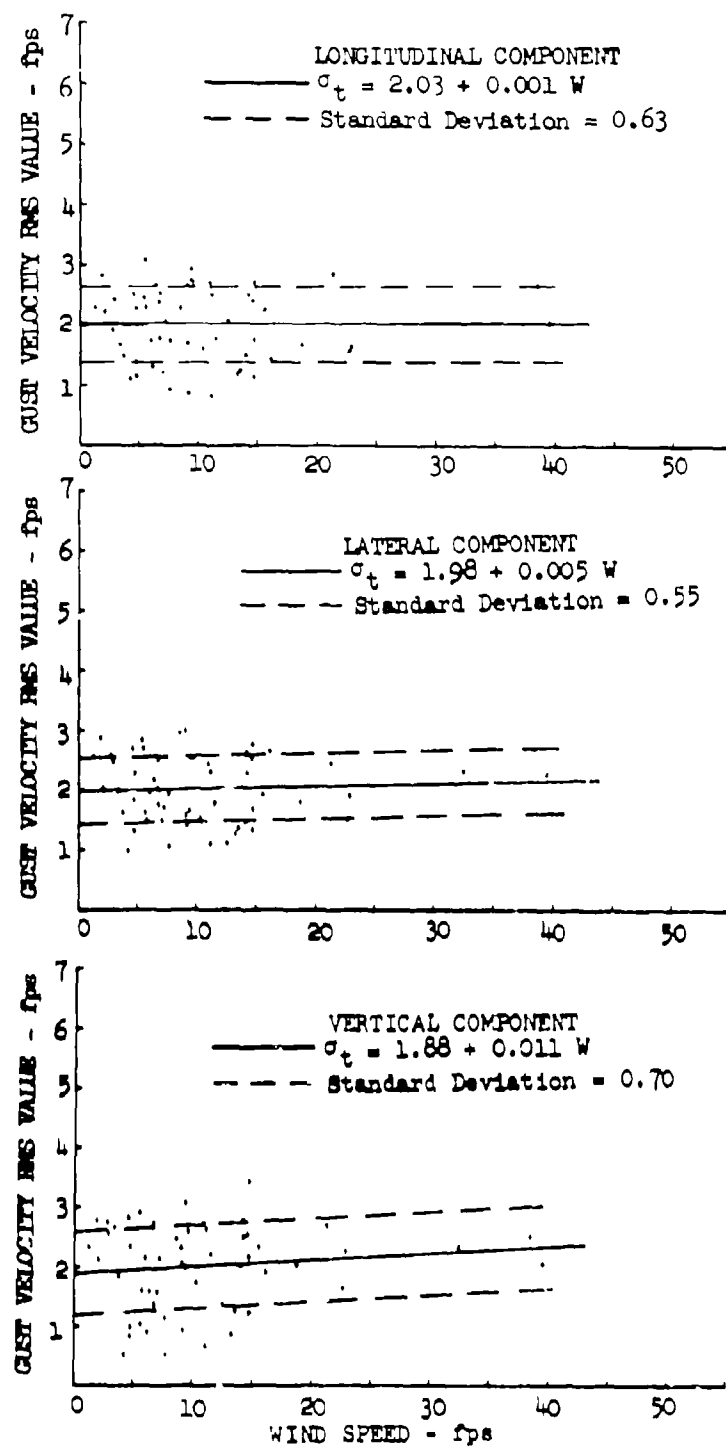


Figure 5.70 Gust Velocity RMS Values versus Wind Speed at 250 Feet Over Desert

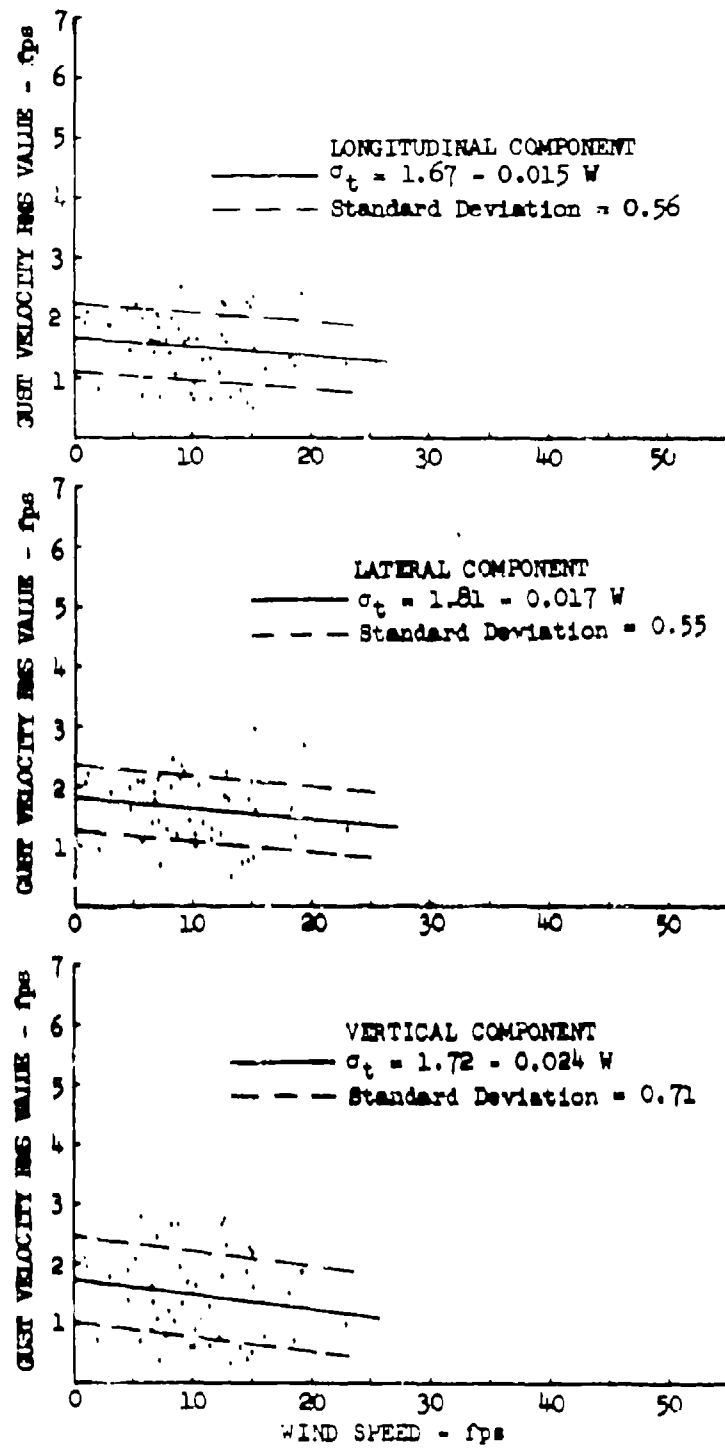


Figure 5.71 Gust Velocity RMS Values versus Wind Speed at 750 Feet Over Desert

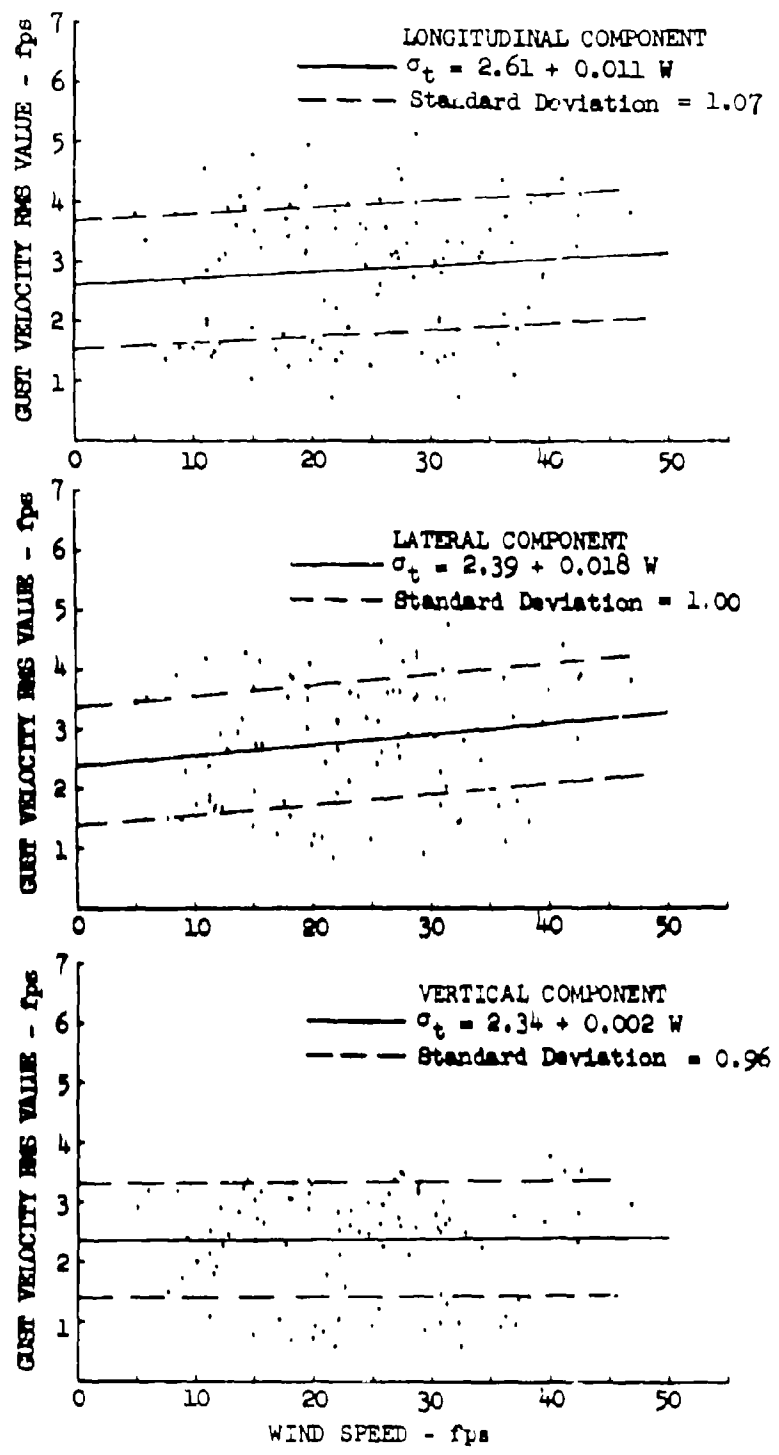


Figure 5.72 Gust Velocity RMS Values versus Wind Speed at 250 Feet Over Plains

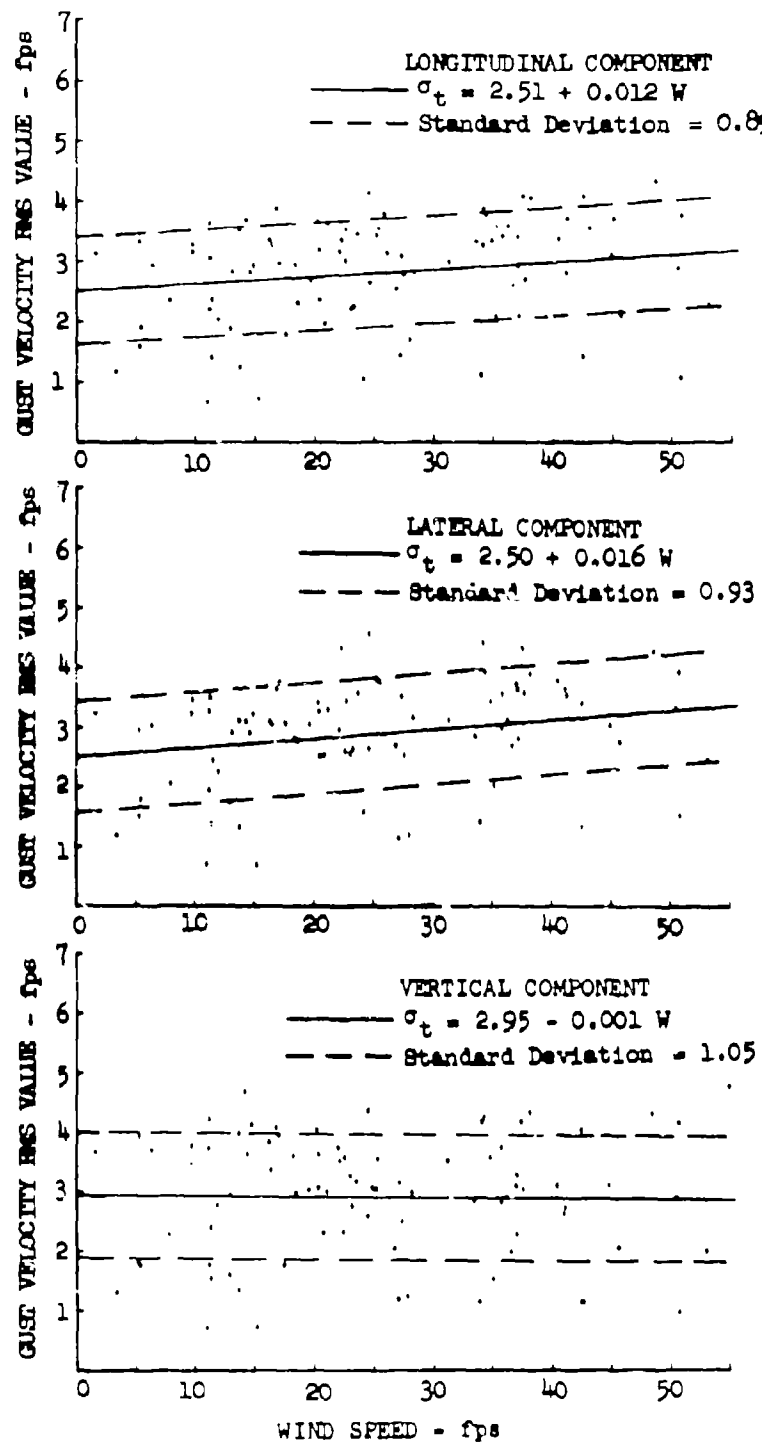


Figure 5.73 Gust Velocity RMS Values versus Wind Speed at 750 Feet Over Plains

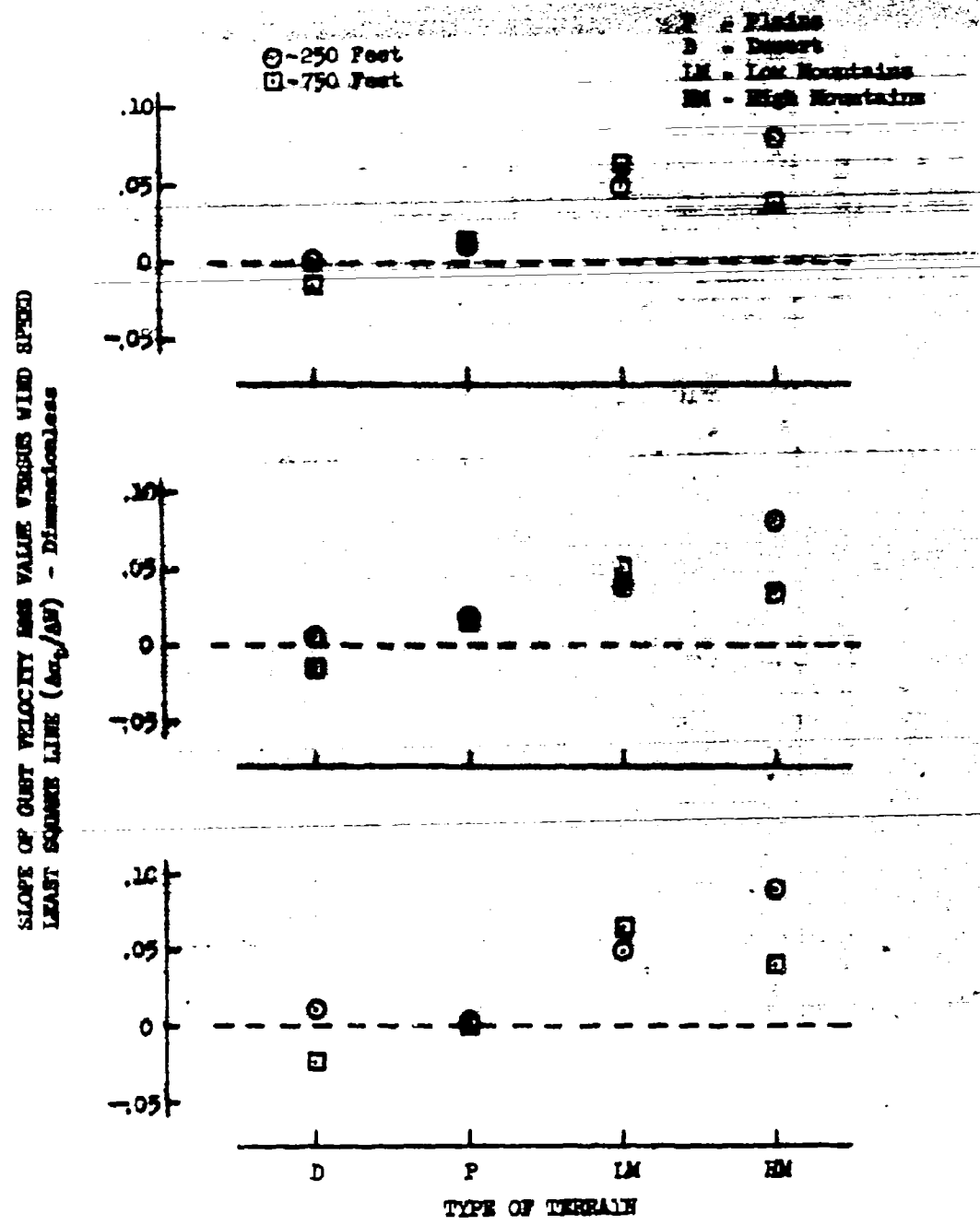


Figure 5.74 Correlation of Gust Velocity RMS Values with Wind Speed as a Function of Terrain and Altitude

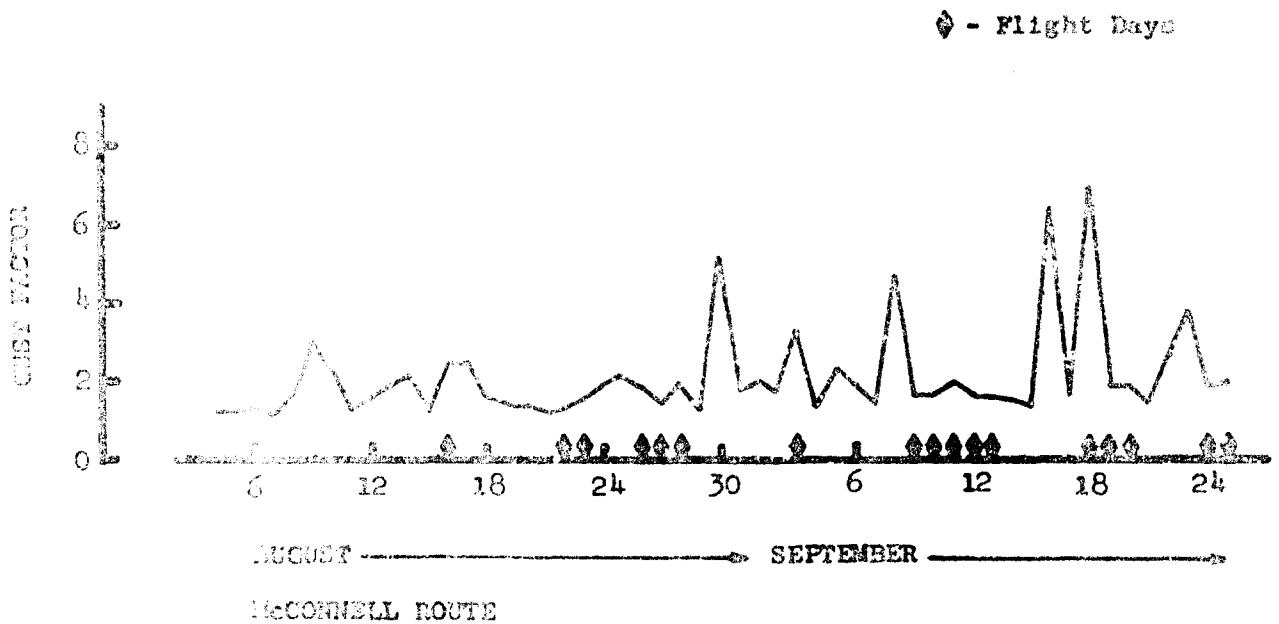


Figure 5.75 Time Histories of Gust Factor

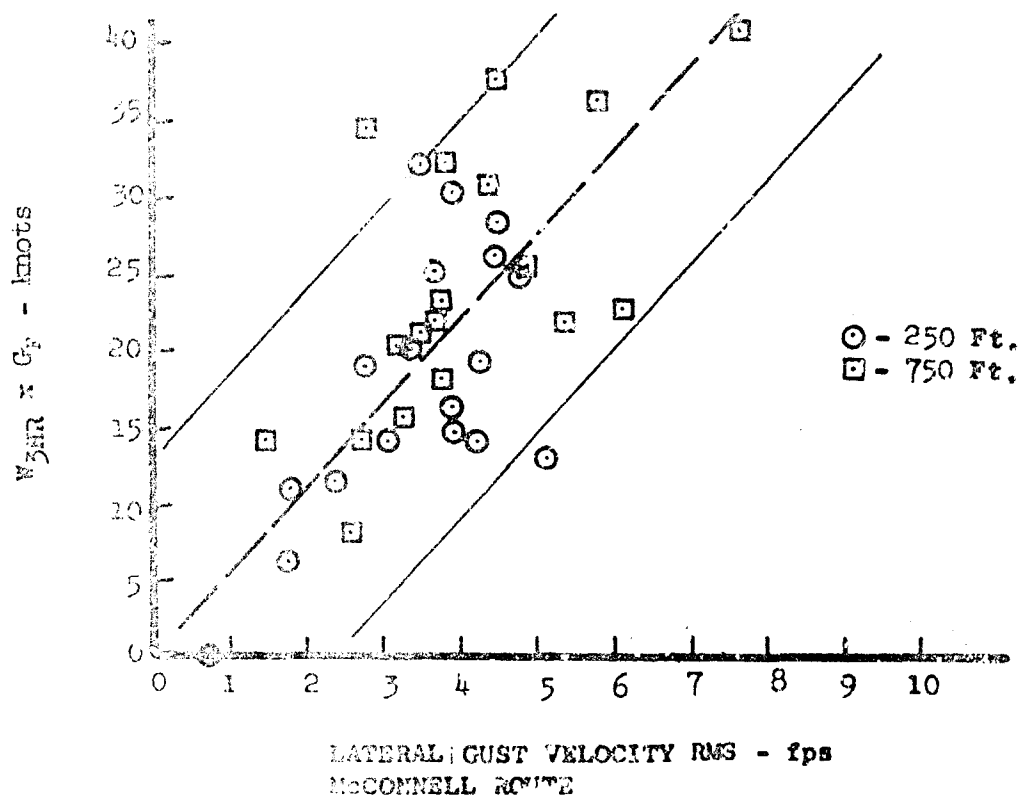


Figure 5.76 Lateral Gust Velocity RMS Versus Corrected Surface Winds

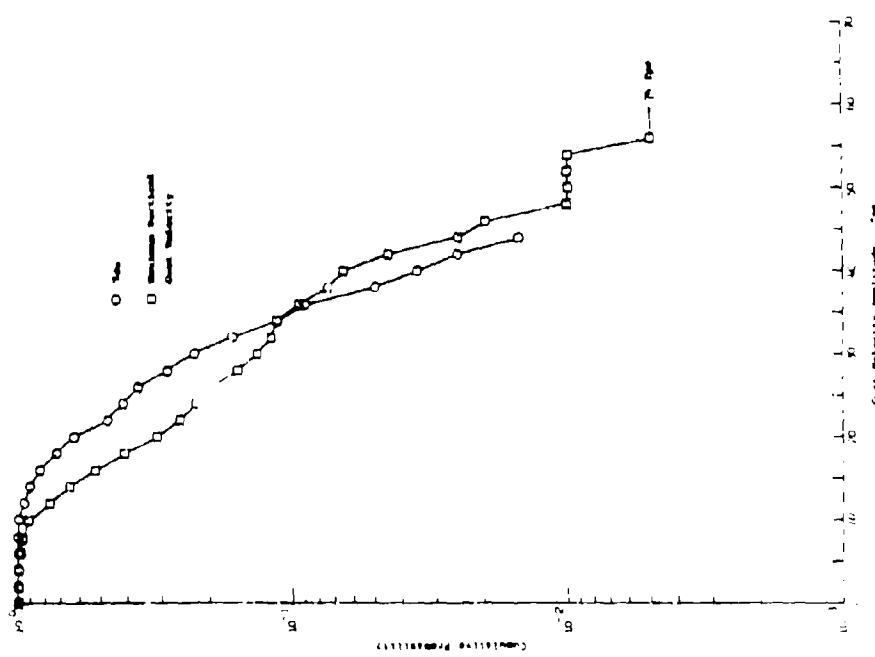


Figure 5.77 Cumulative Probability of U_{de} and Maximum Vertical Gust Velocity - High Mountains

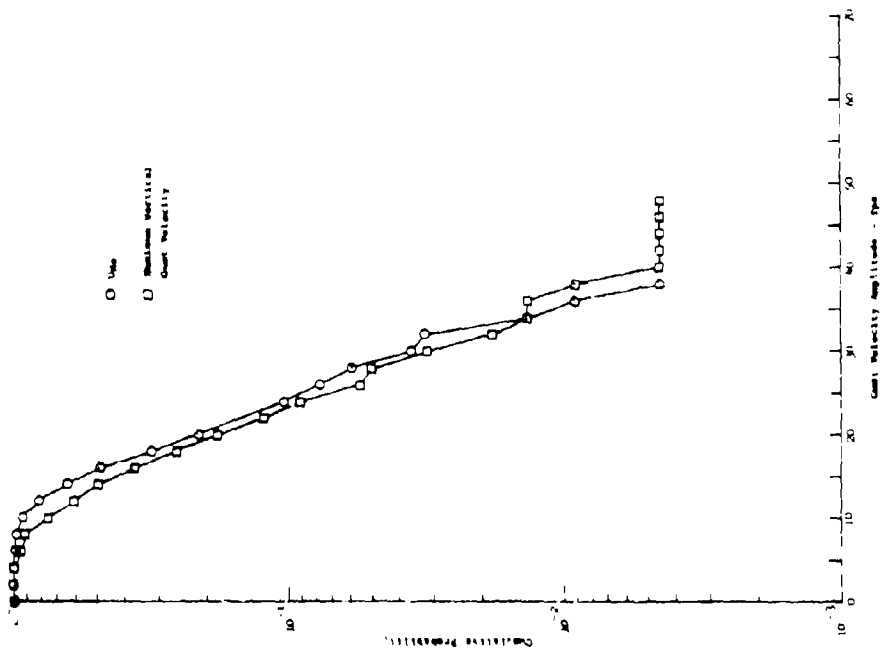
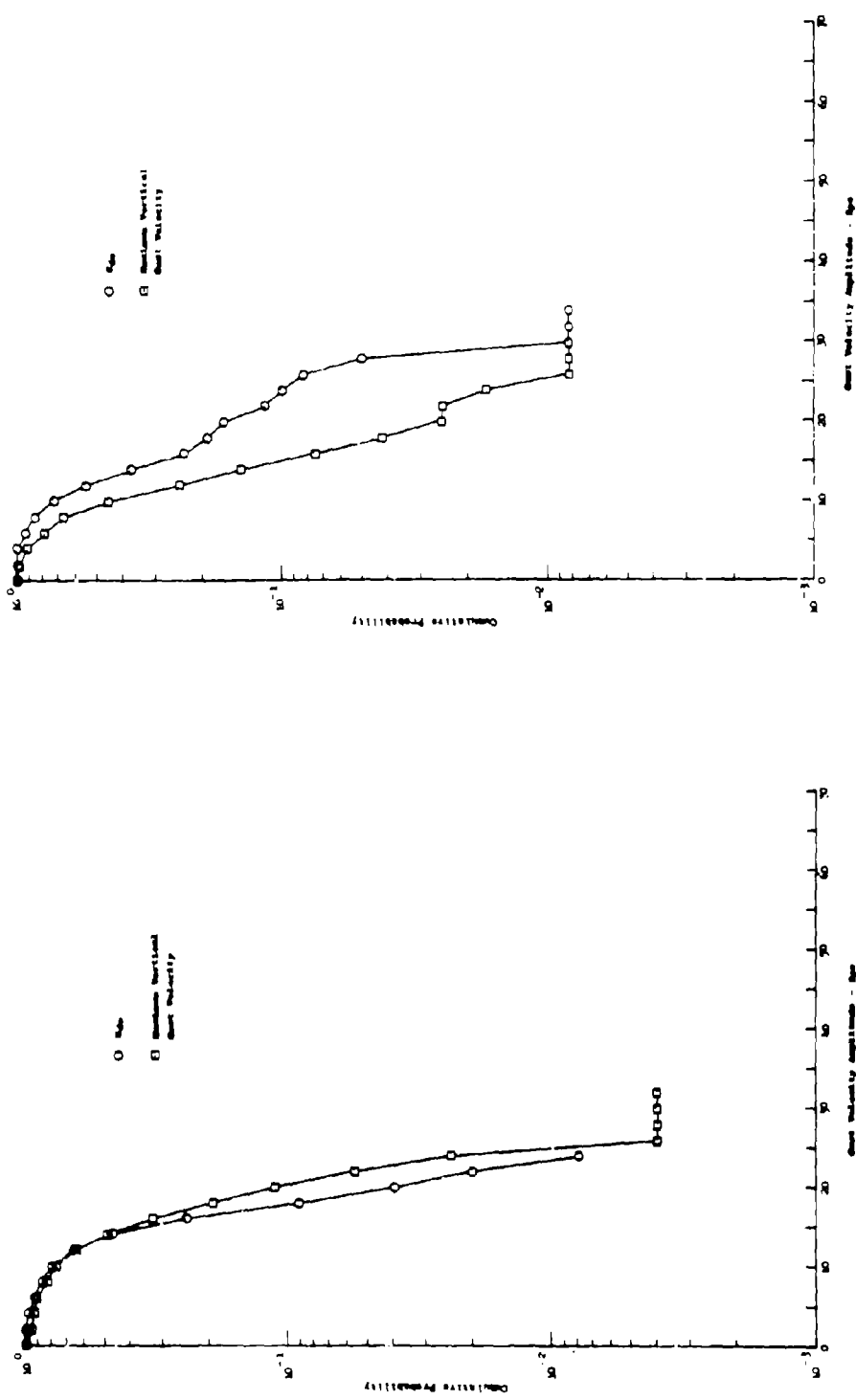


Figure 5.78 Cumulative Probability of U_{de} and Maximum Vertical Gust Velocity - Low Mountains



199

Figure 5.79 Cumulative Probability of U_{de} and Maximum Vertical Gust Velocity - Plains

Figure 5.80 Cumulative Probability of U_{de} and Maximum Vertical Gust Velocity - Desert

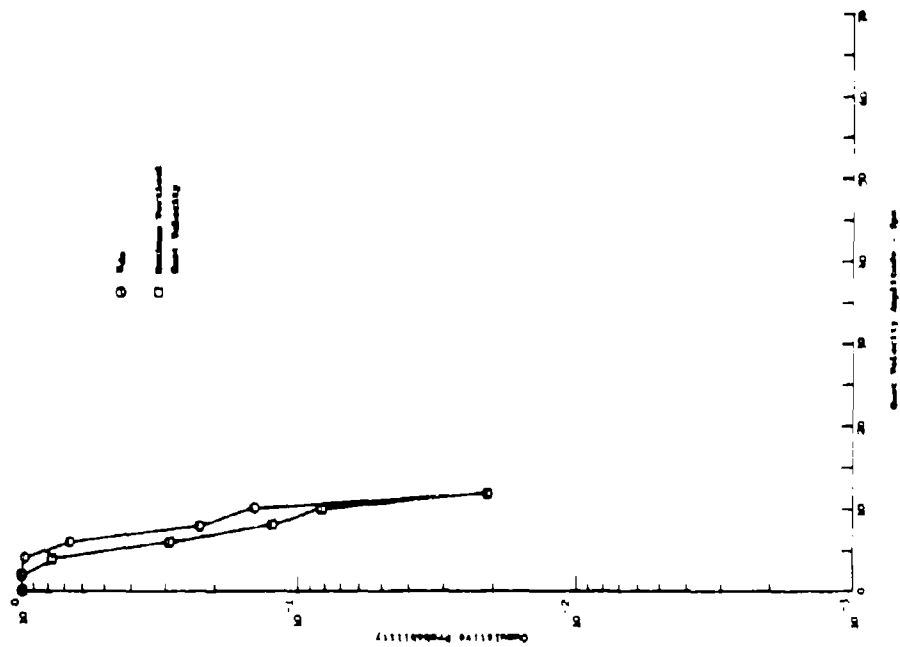


Figure 5.81 Cumulative Probability of U_{de} and Maximum Vertical Gust Velocity - Water

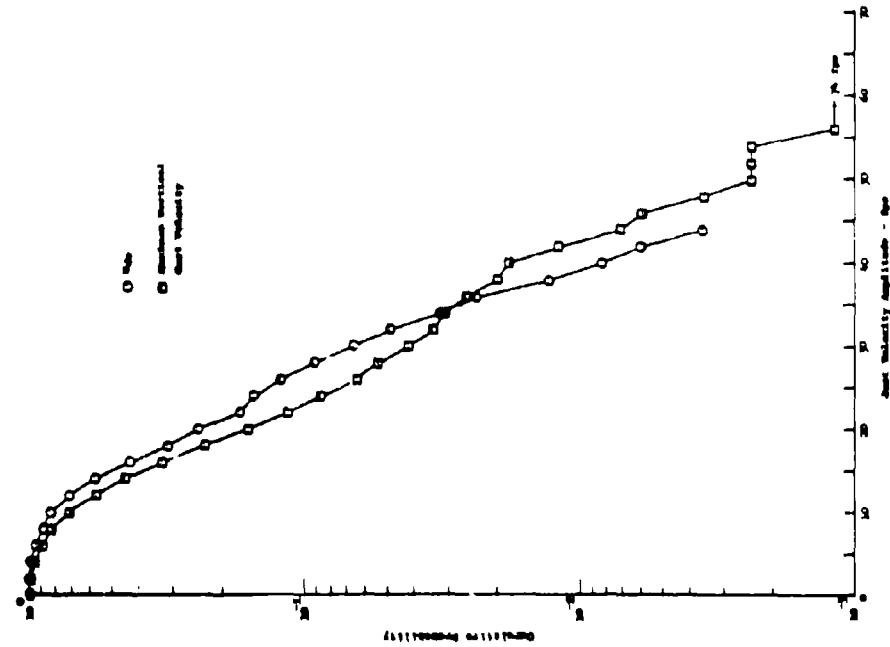


Figure 5.82 Cumulative Probability of U_{de} and Maximum Vertical Gust Velocity - All Terrain

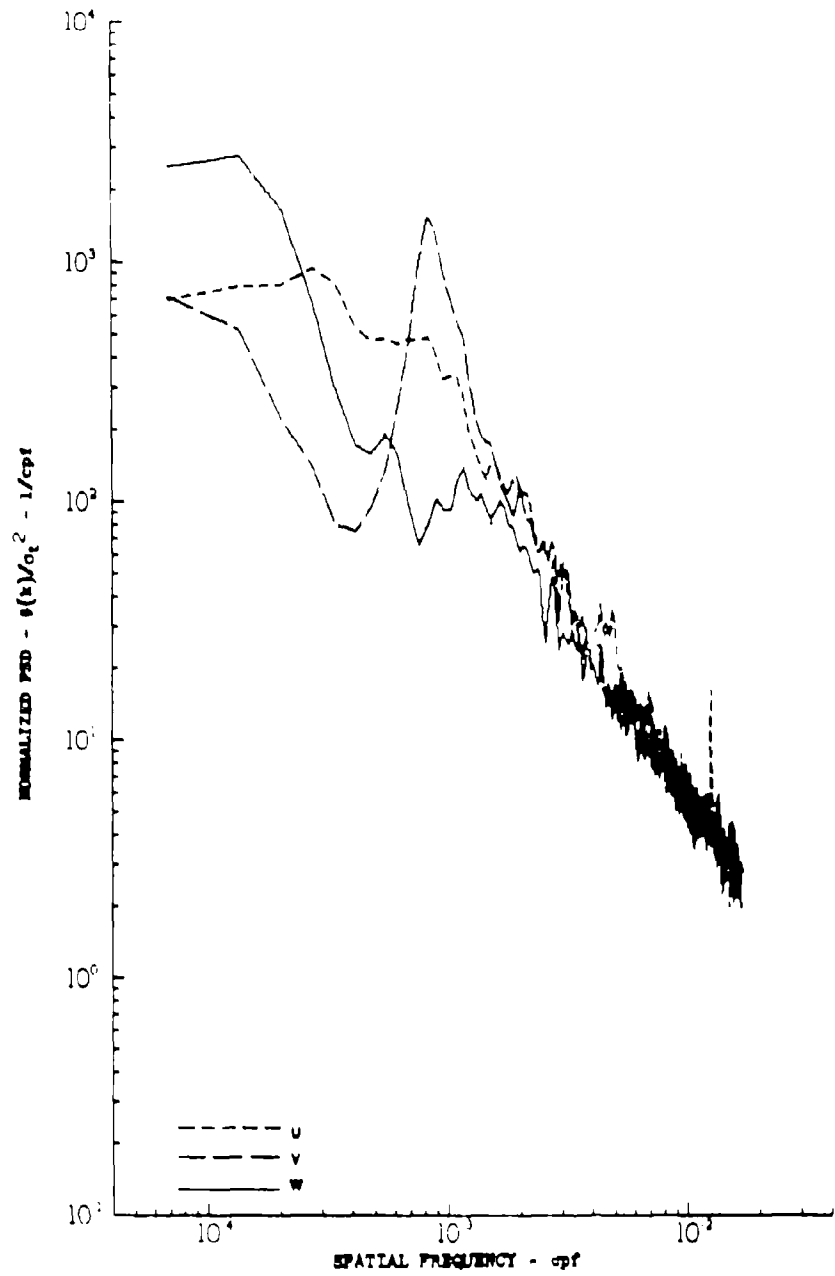


Figure 5.33 Gust Velocity Power Spectra of a Data Sample Containing Suspected Instrumentation Irregularities

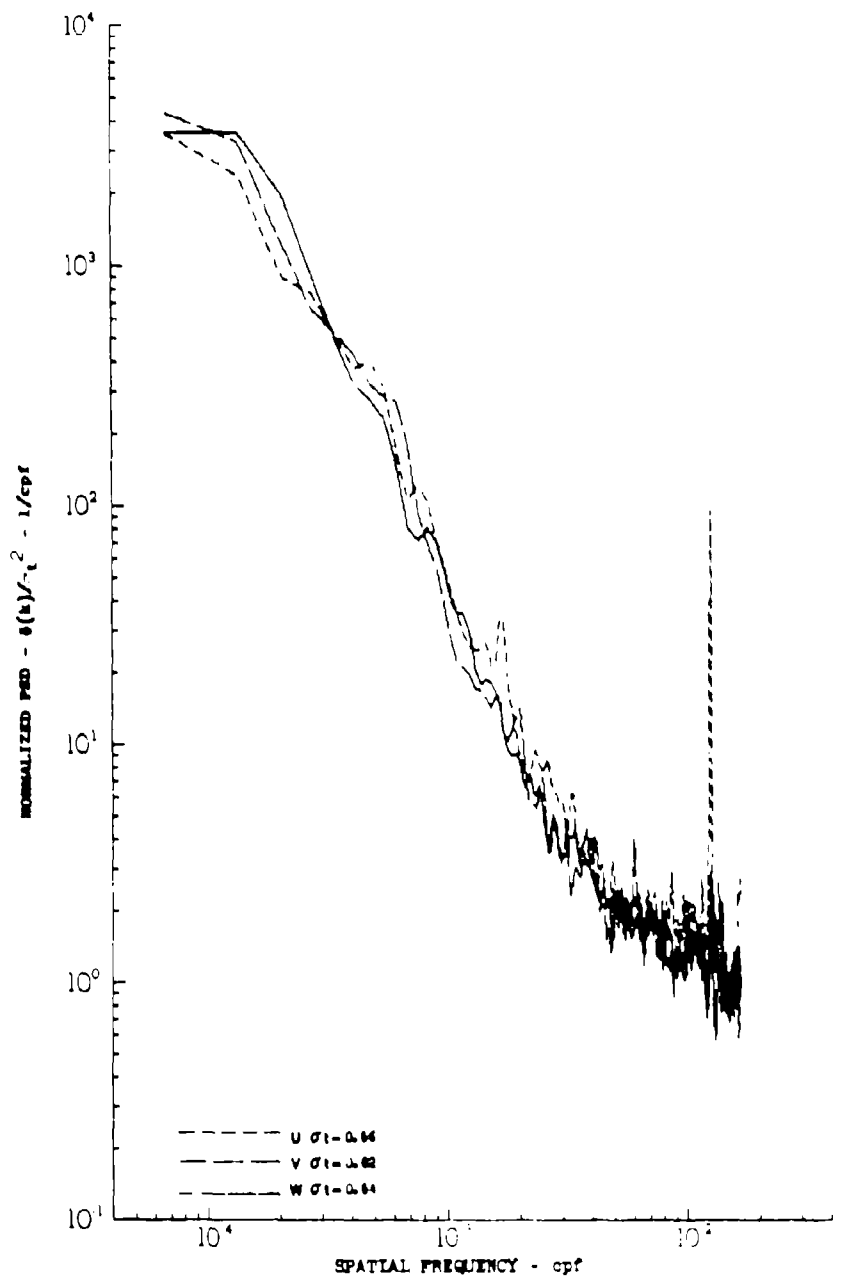


Figure 5.84 Gust Velocity Power Spectra of a Data Sample Having Insufficient Signal-To-Noise Ratio

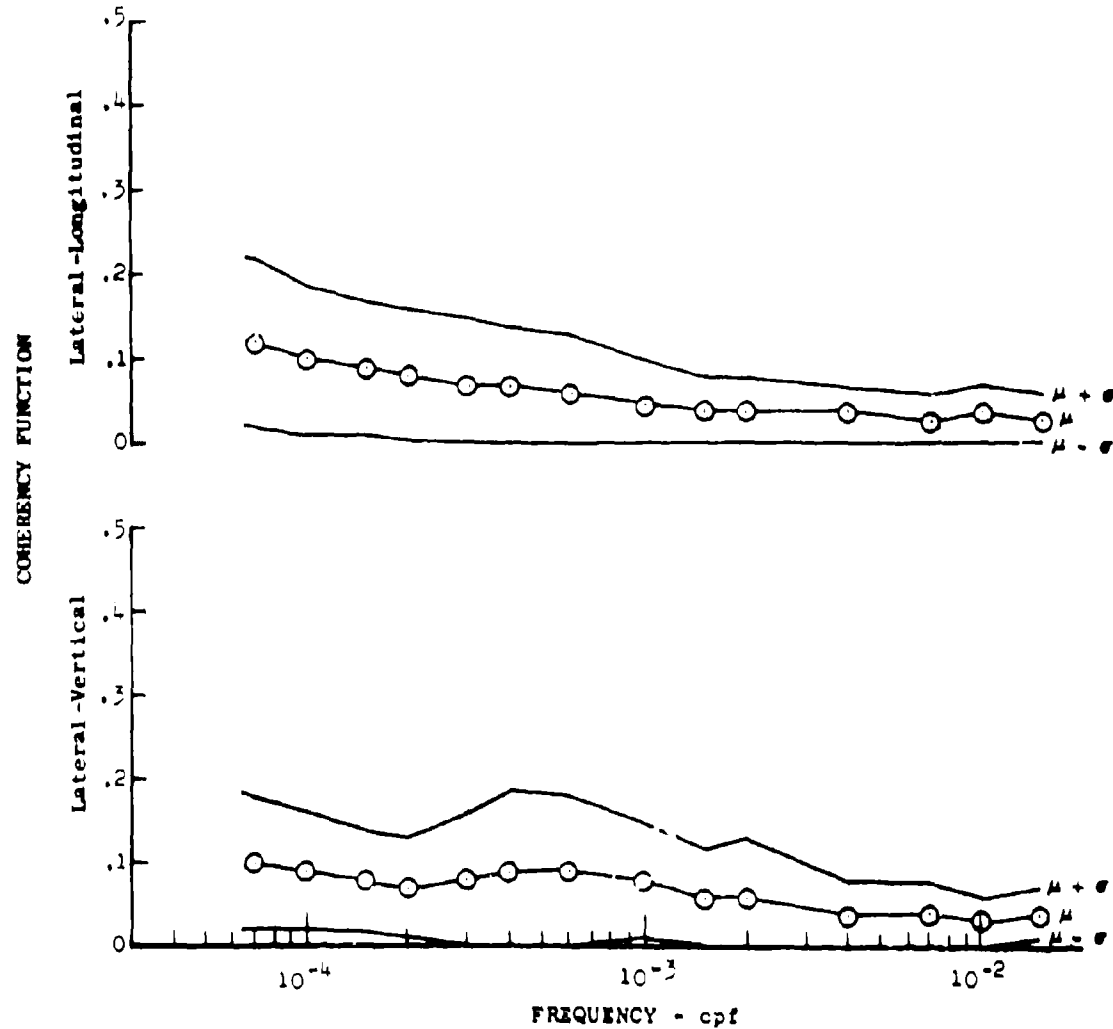


Figure 5.85 Average Gust Velocity Coherency Characteristics

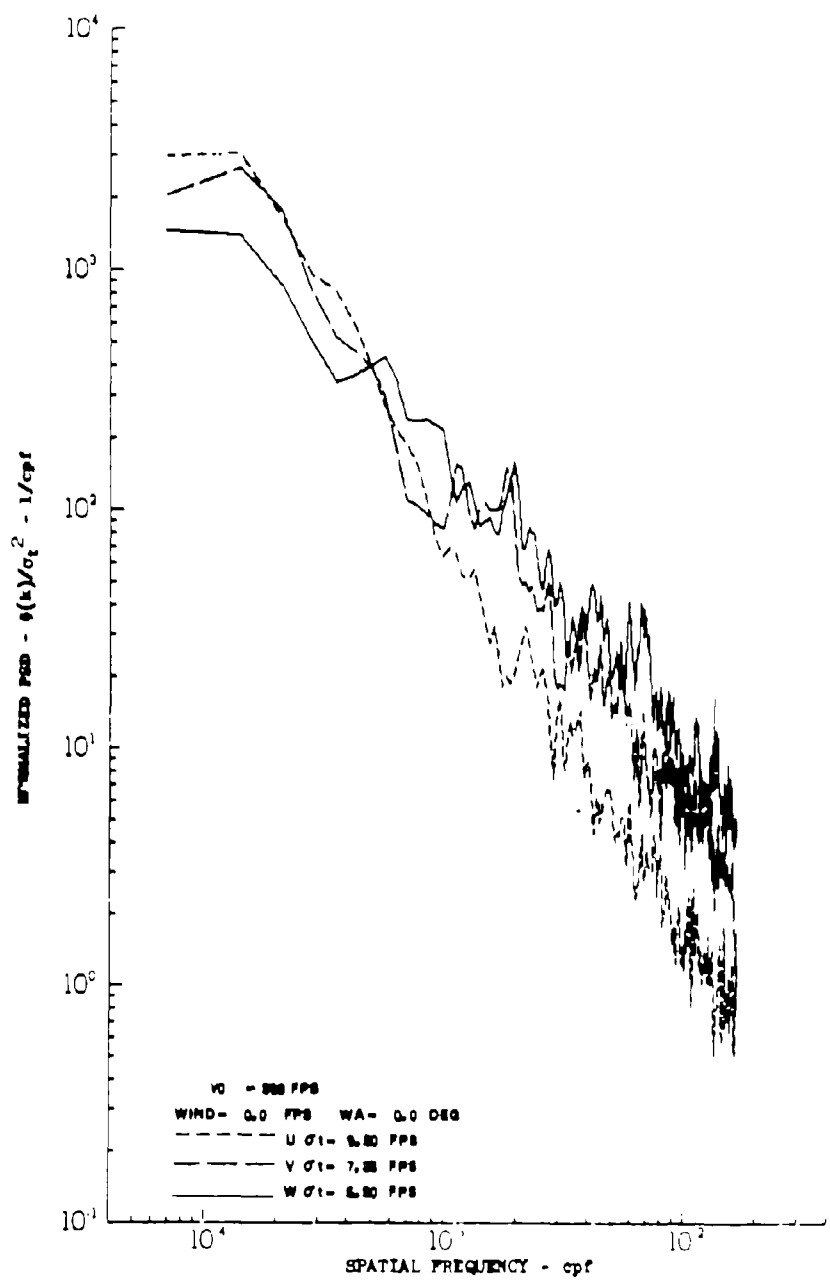


Figure 5.86 Gust Velocity Power Spectra of Non-Homogeneous Turbulence - Test 170 Leg 2, Category 112143

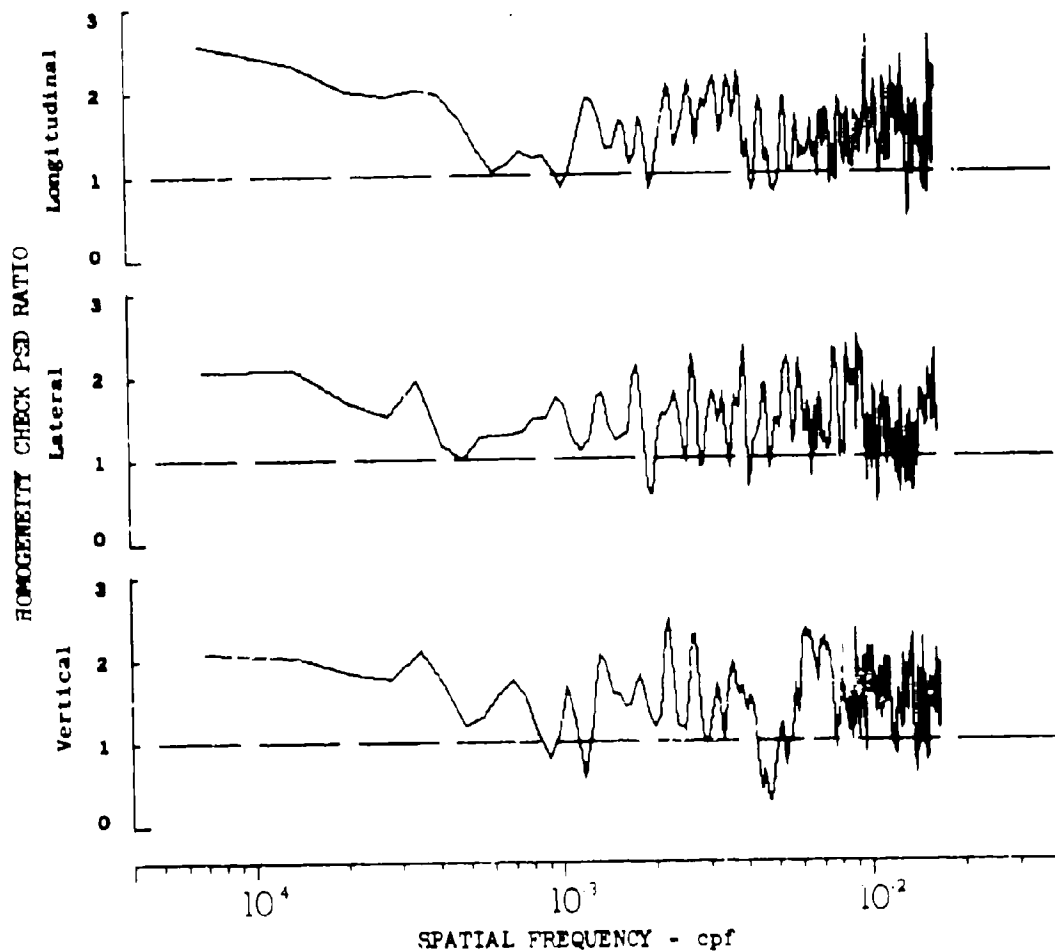


Figure 5.87 Turbulence Homogeneity Characteristics - Test 170 Leg 2,
Category 112143

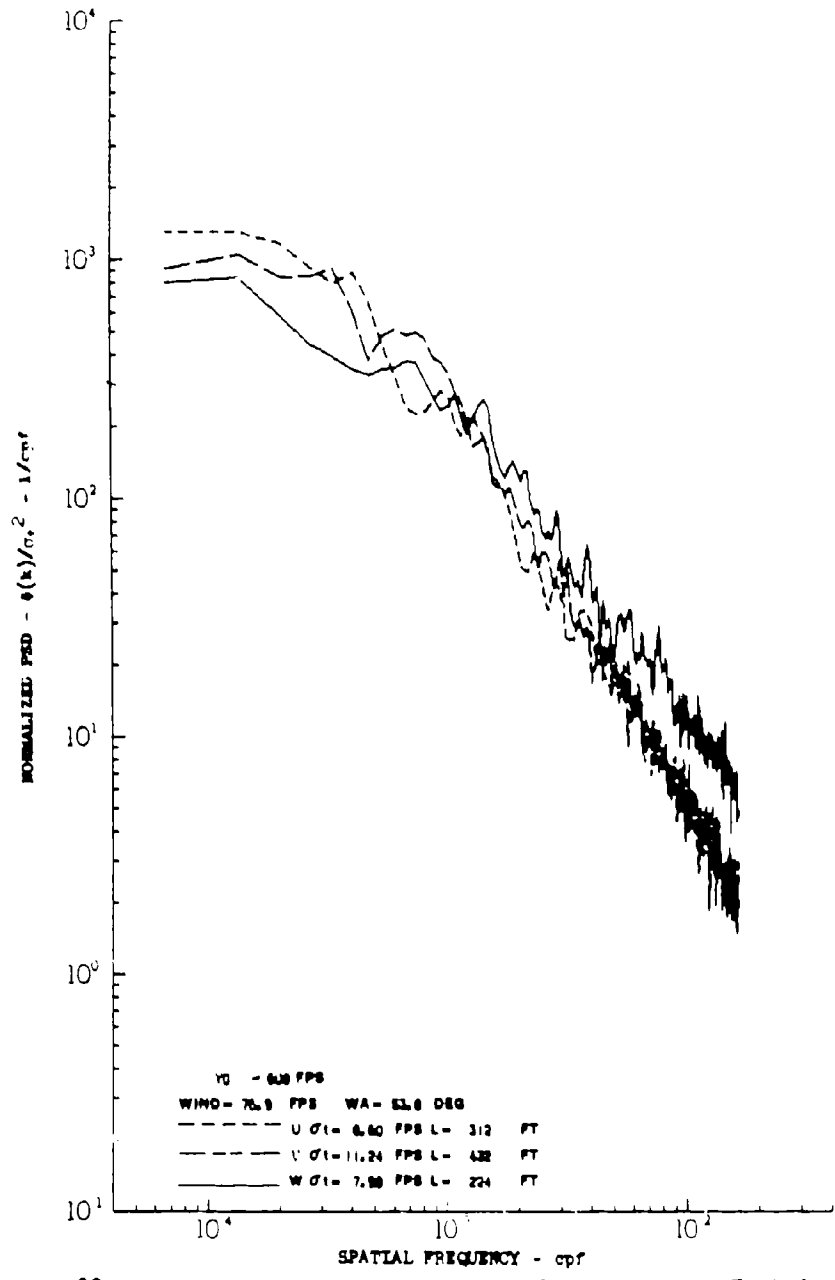


Figure 5.88 Gust Velocity Power Spectra of Homogeneous Turbulence - Test 170 Leg 6, Category 112143

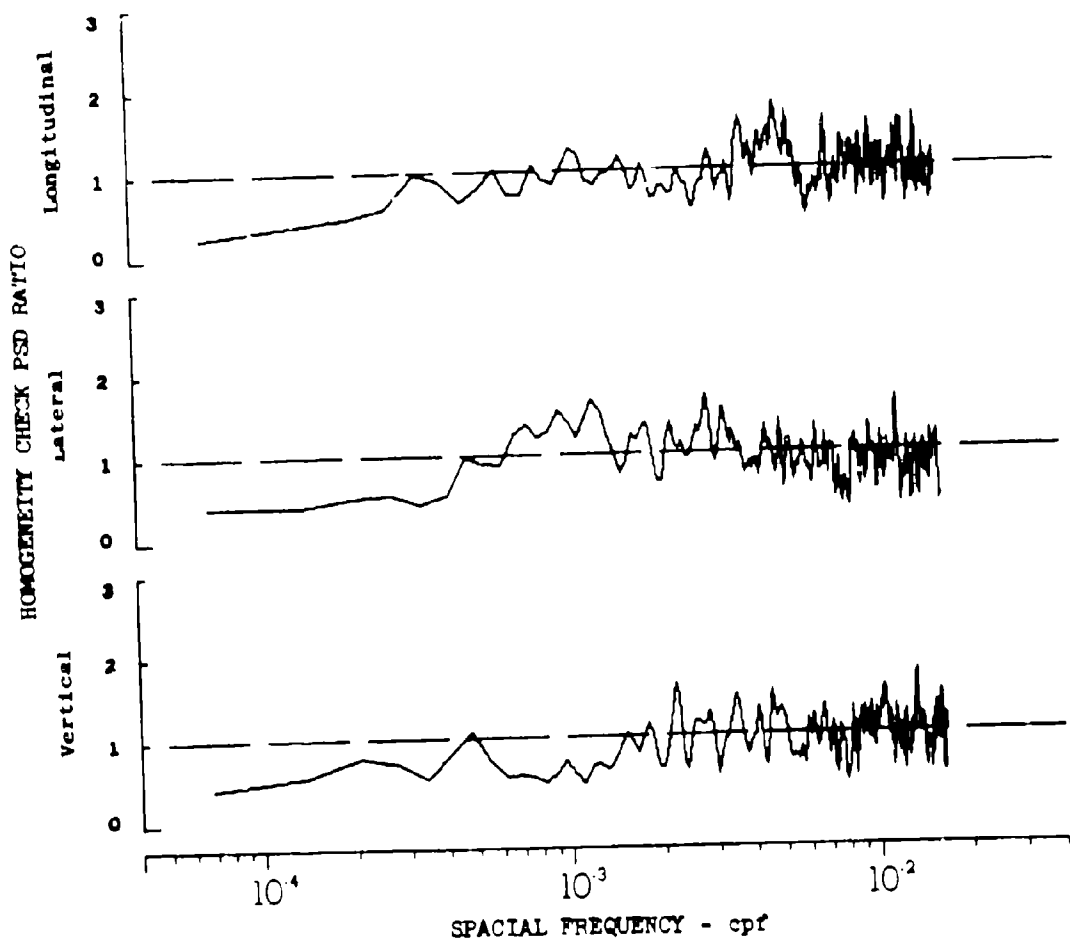


Figure 5.89 Turbulence Homogeneity Characteristics - Test 170 Leg 6,
Category 112143

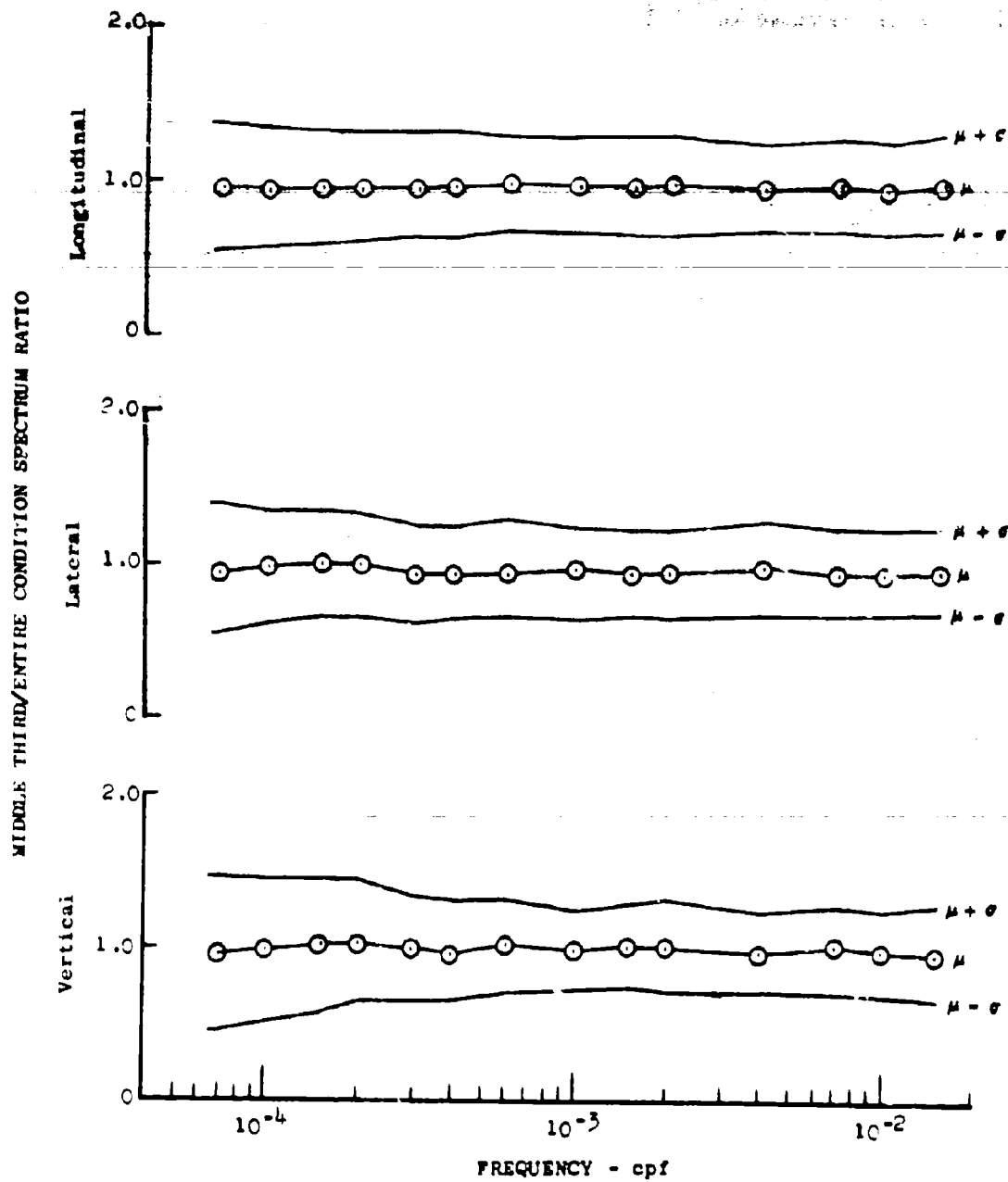


Figure 5.90 Average Homogeneity Characteristics

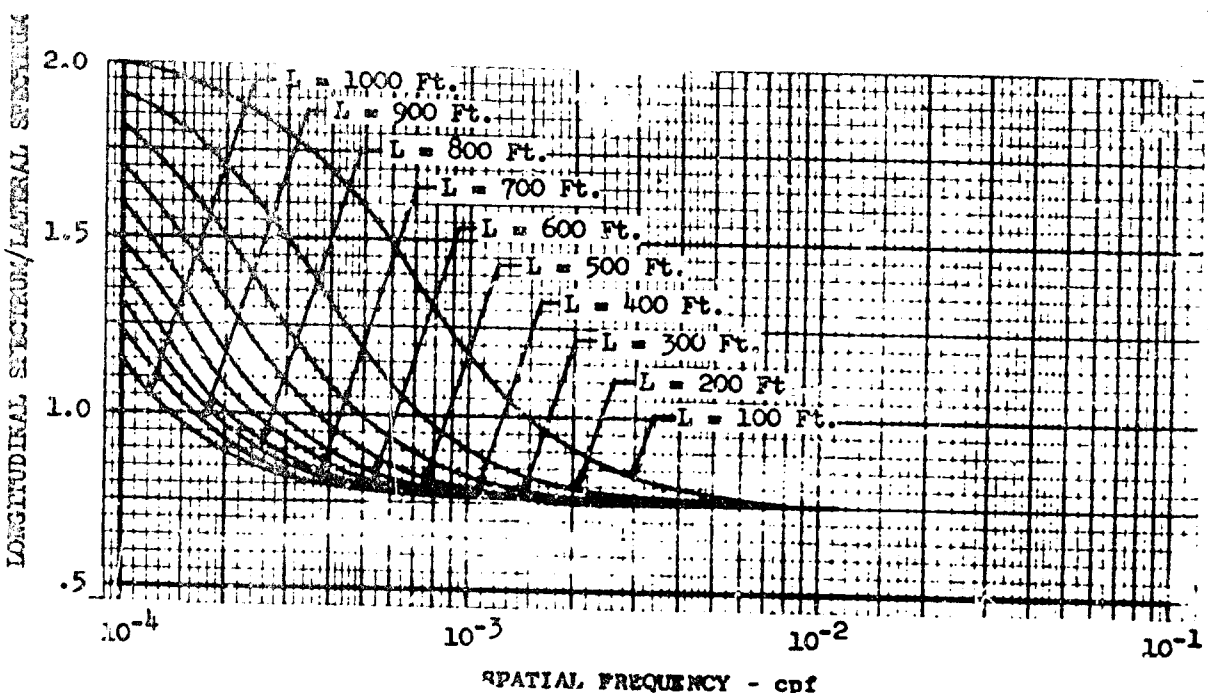


Figure 5.91 Isotropy Based on von Karman Expressions

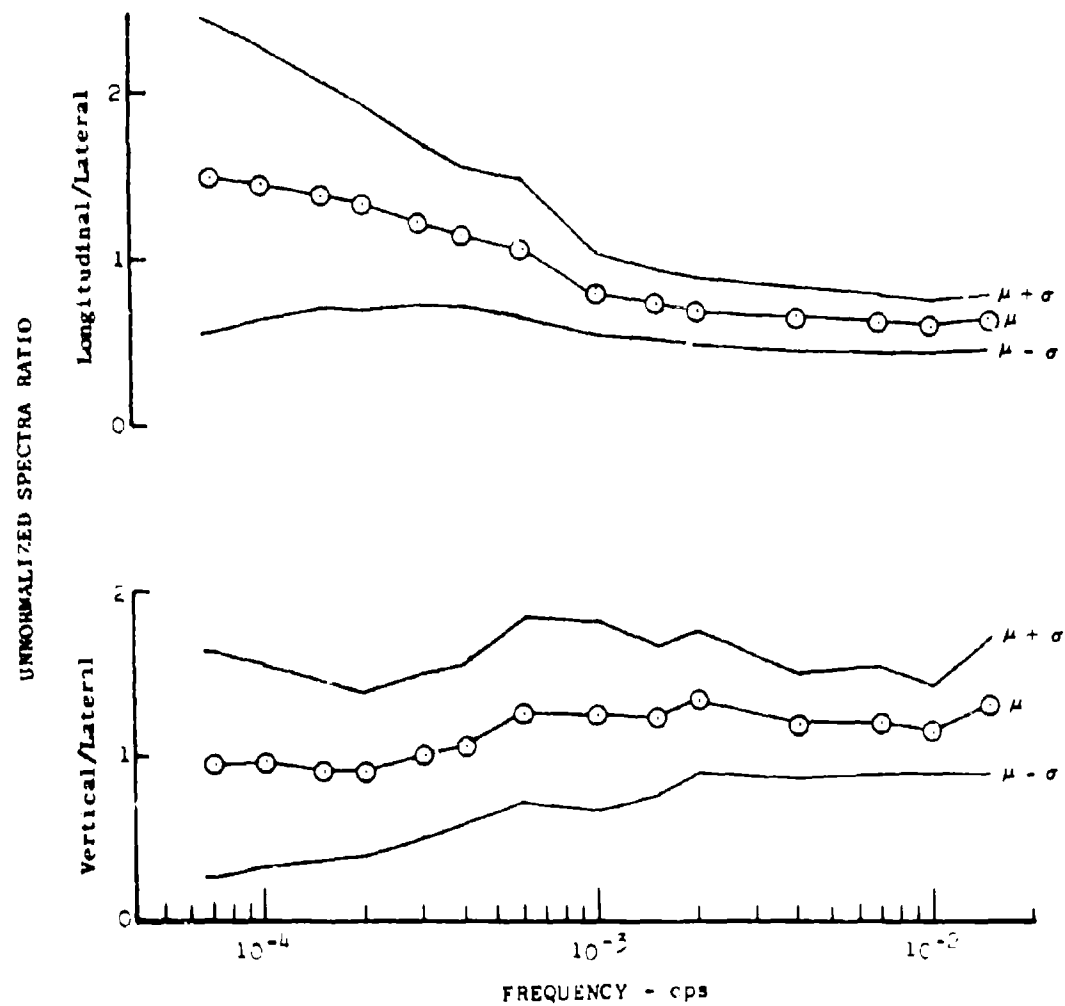


Figure 5.92 Average Isotropy Characteristics

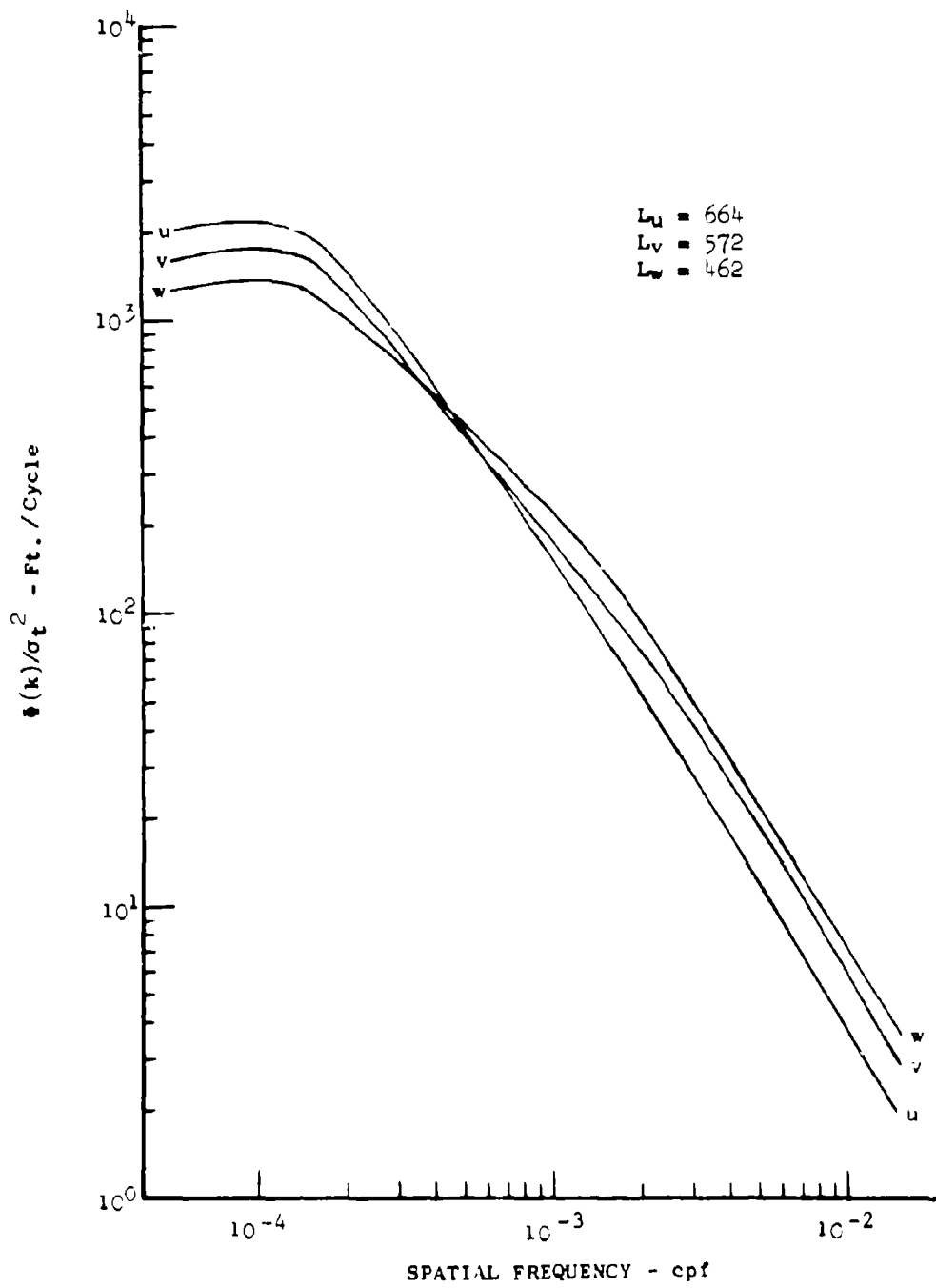


Figure 5.93 Gust Velocity Average Power Spectra Normalized by σ_t^2

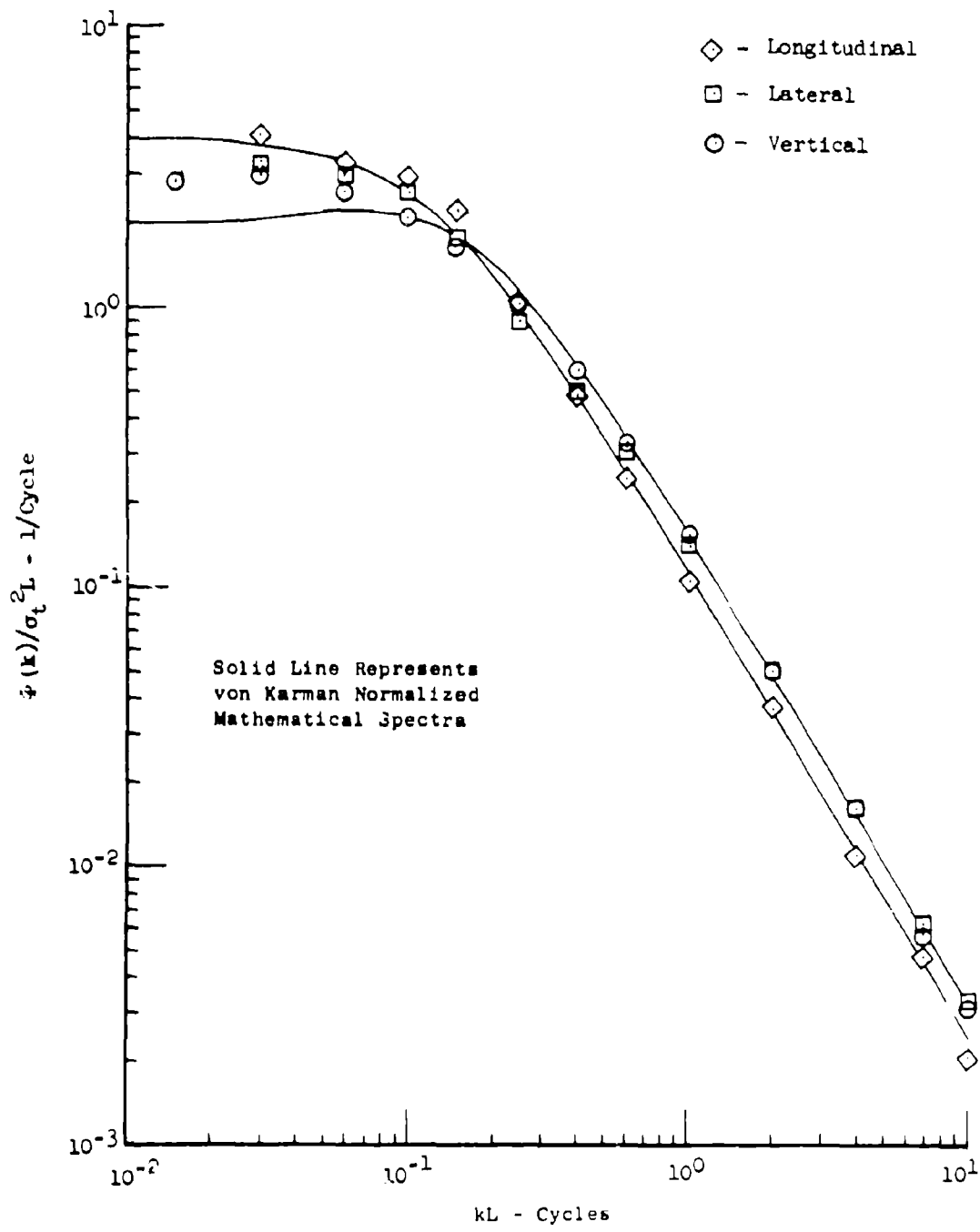


Figure 5.94 Gust Velocity Average Power Spectra Normalized by $\sigma_t^2 L$

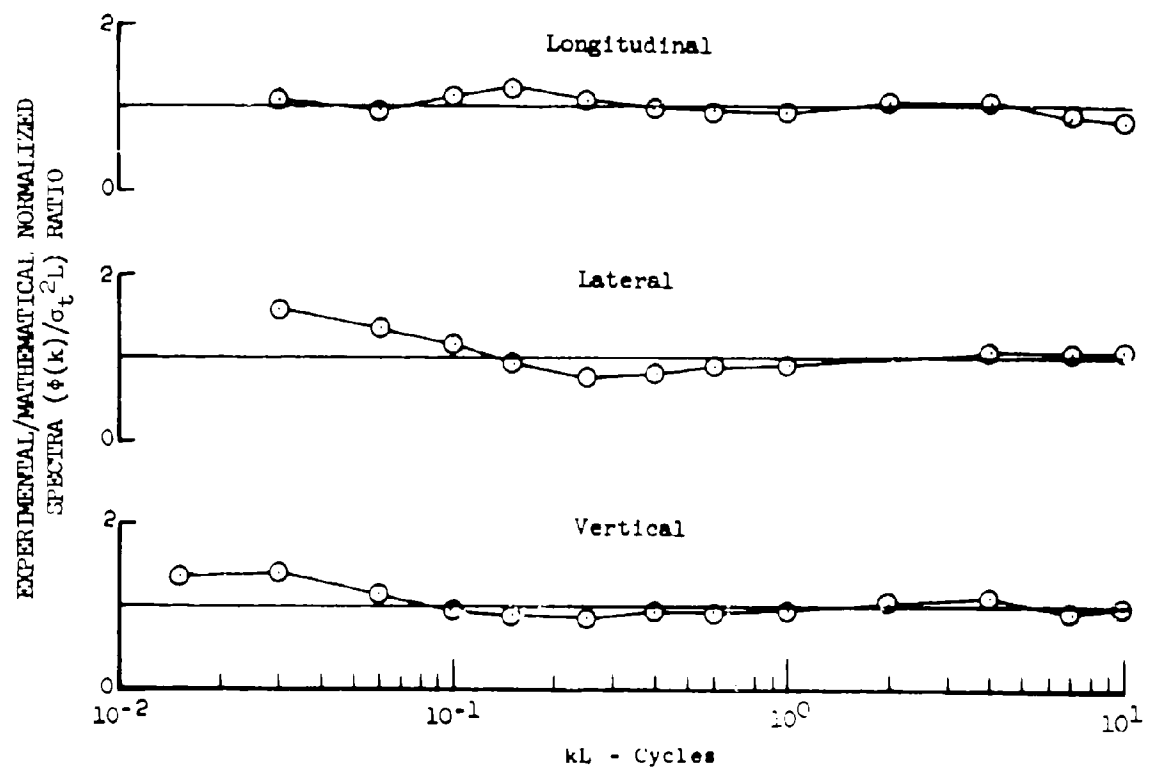


Figure 5.95 Experimental Gust Velocity Power Spectra/von Karman Mathematical Power Spectra - Normalized by $\sigma_t^2 L$

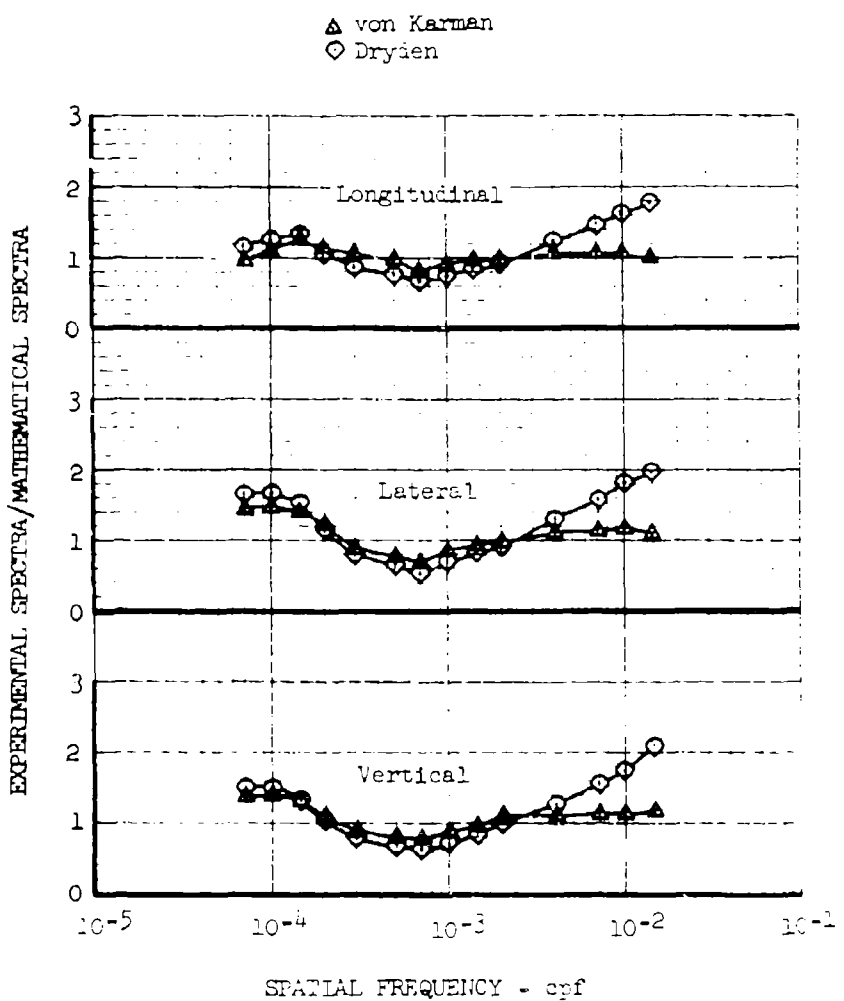


Figure 5.4 Experimental Power Spectra/Dryden and von Karman Mathematical Power Spectra Comparisons

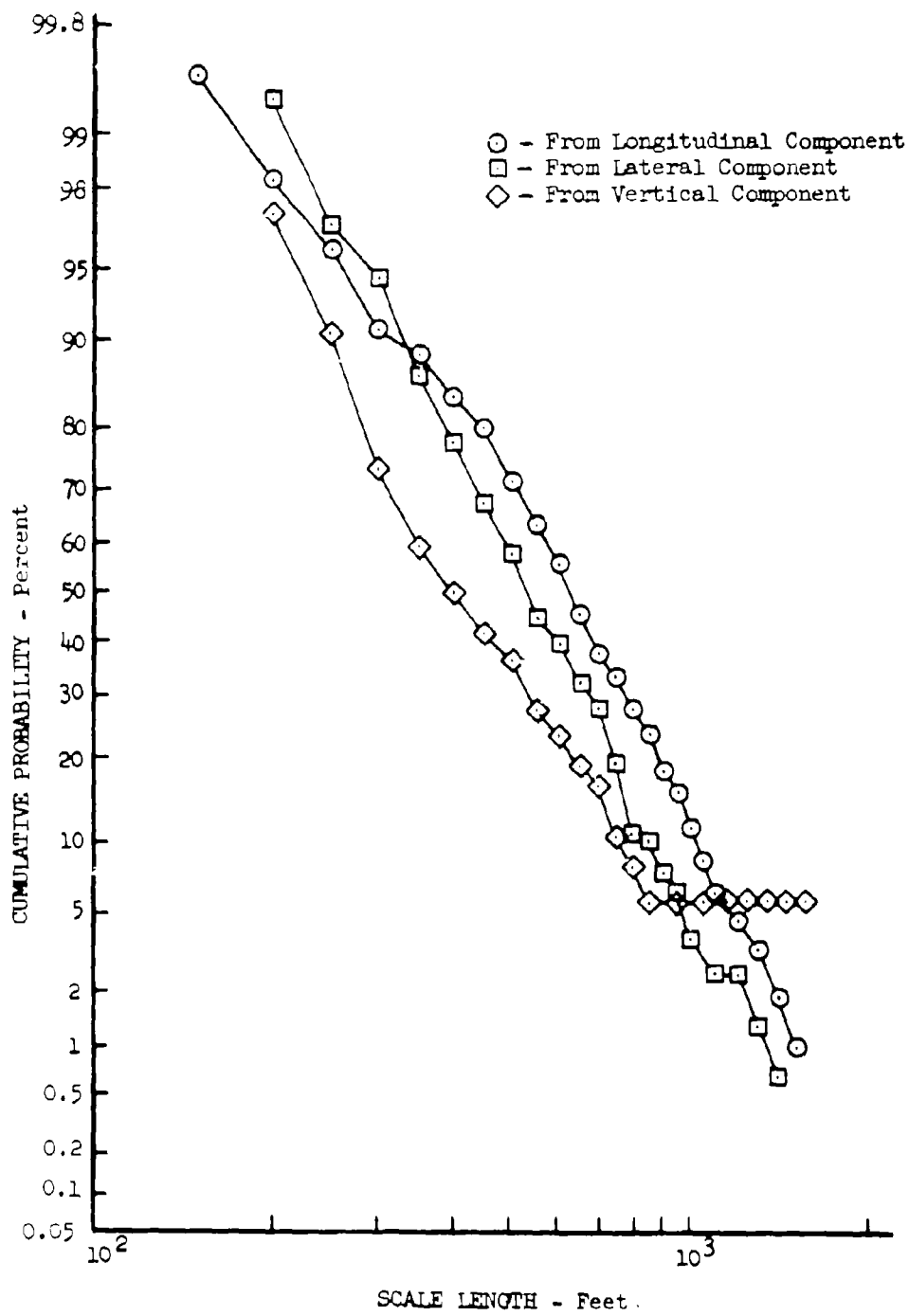


Figure 5.97 Von Karman Longitudinal Scale Length Cumulative Probability

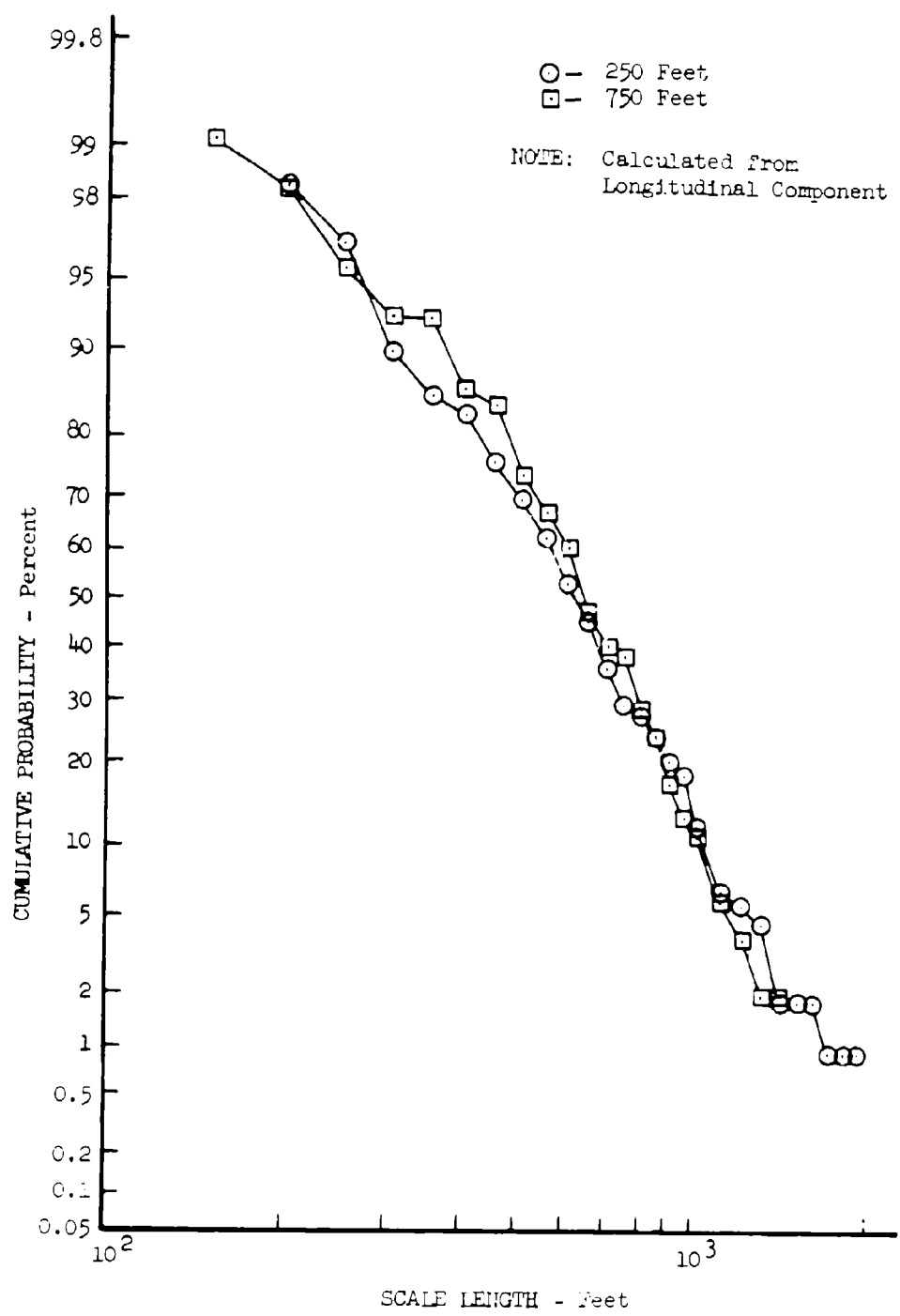


Figure 5.98 Effects of Altitude on von Karman Longitudinal Scale Length

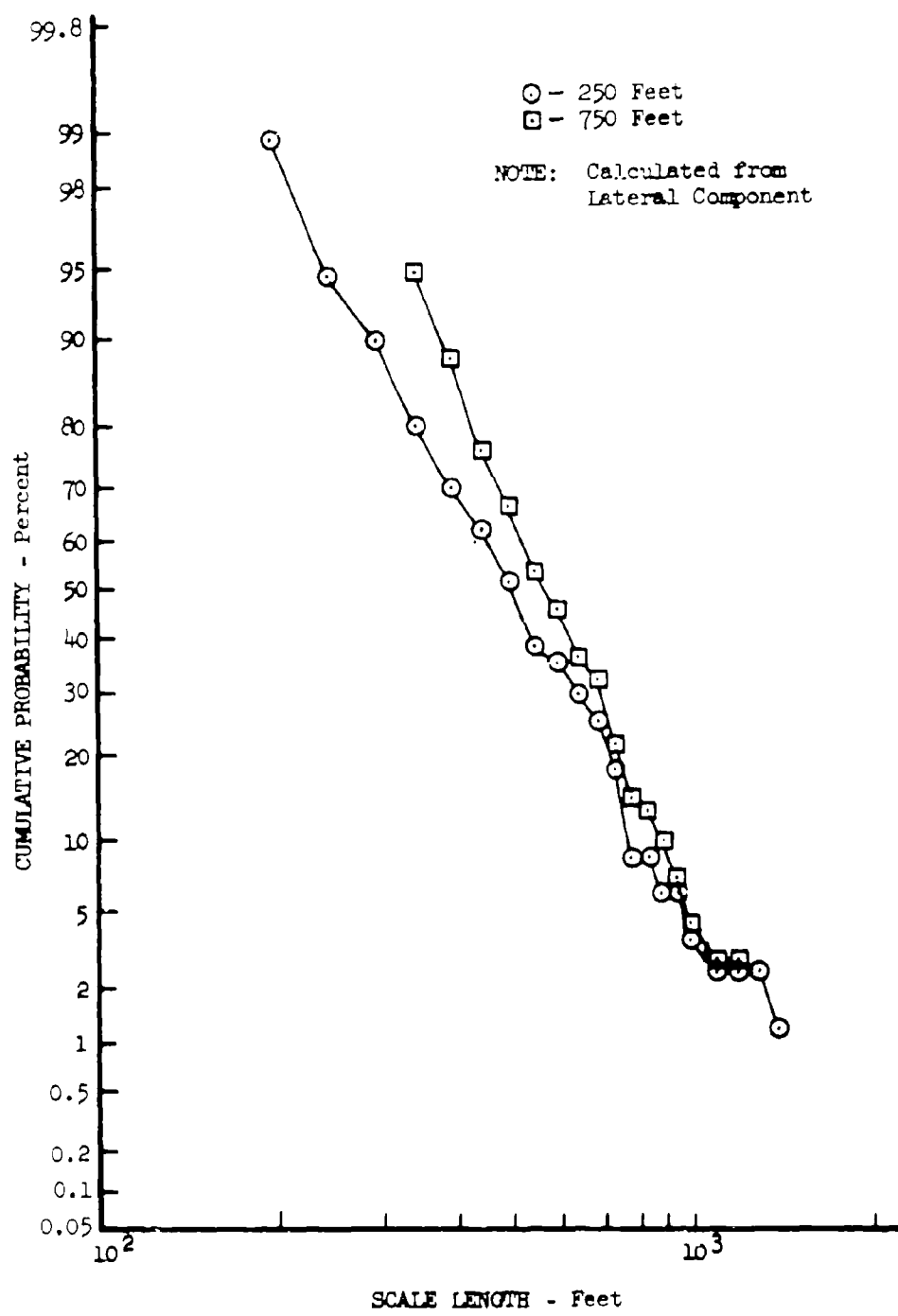


Figure 5.99 Effects of Altitude on von Karman Longitudinal Scale Length

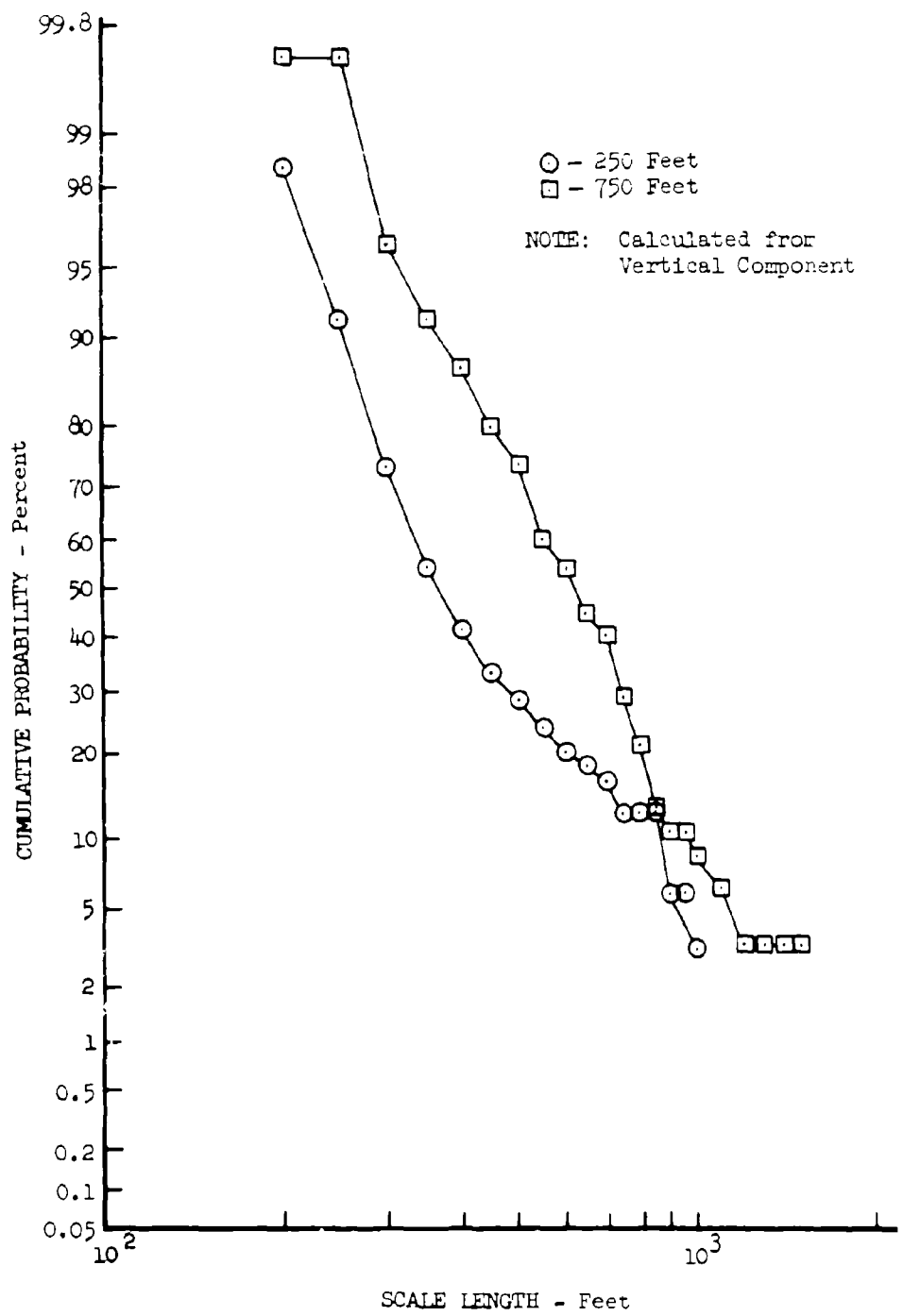


Figure 5 100 Effects of Altitude on von Karman Longitudinal Scale Length

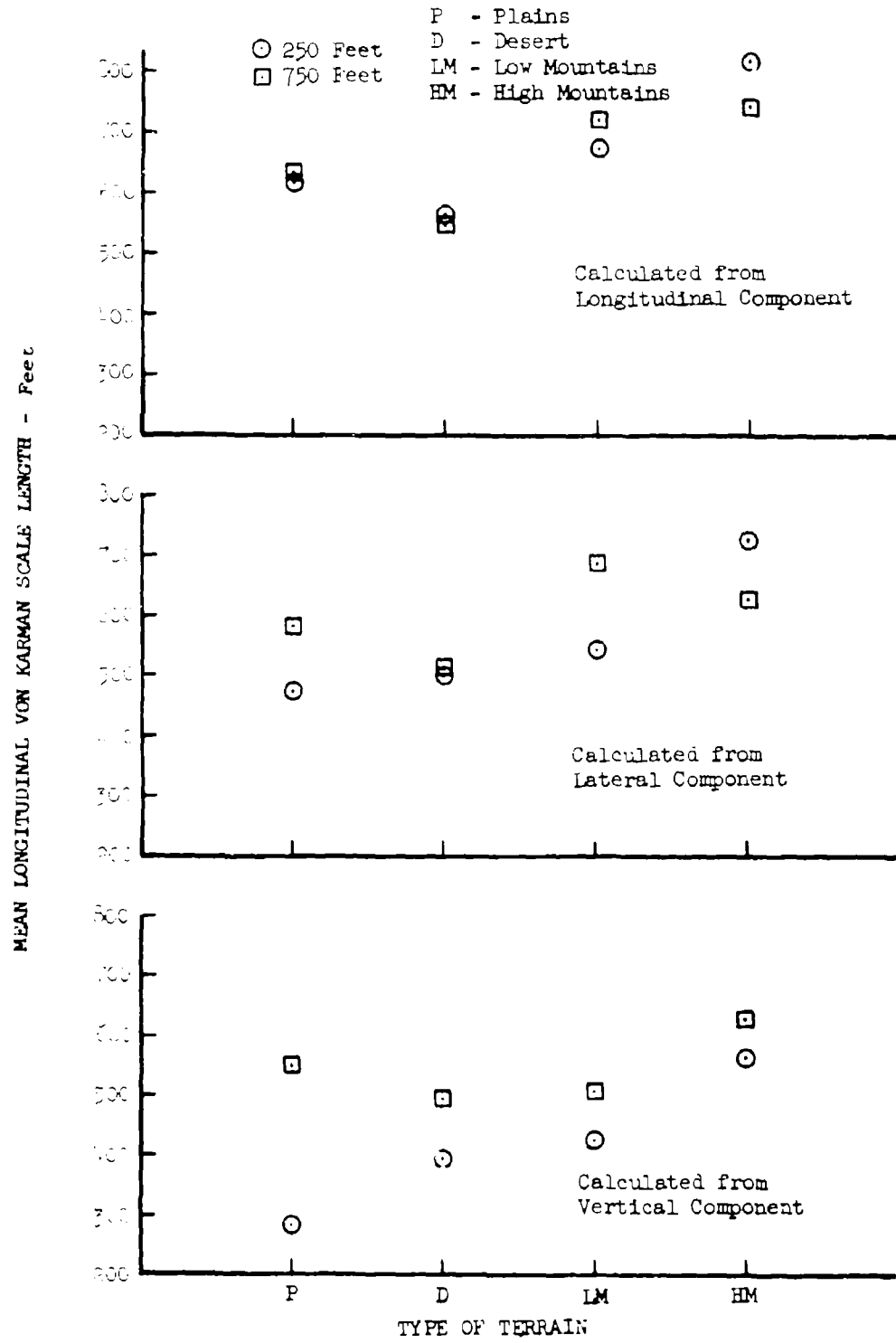


Figure 5.101 Variation of von Karman Longitudinal Scale Length with Altitude and Terrain

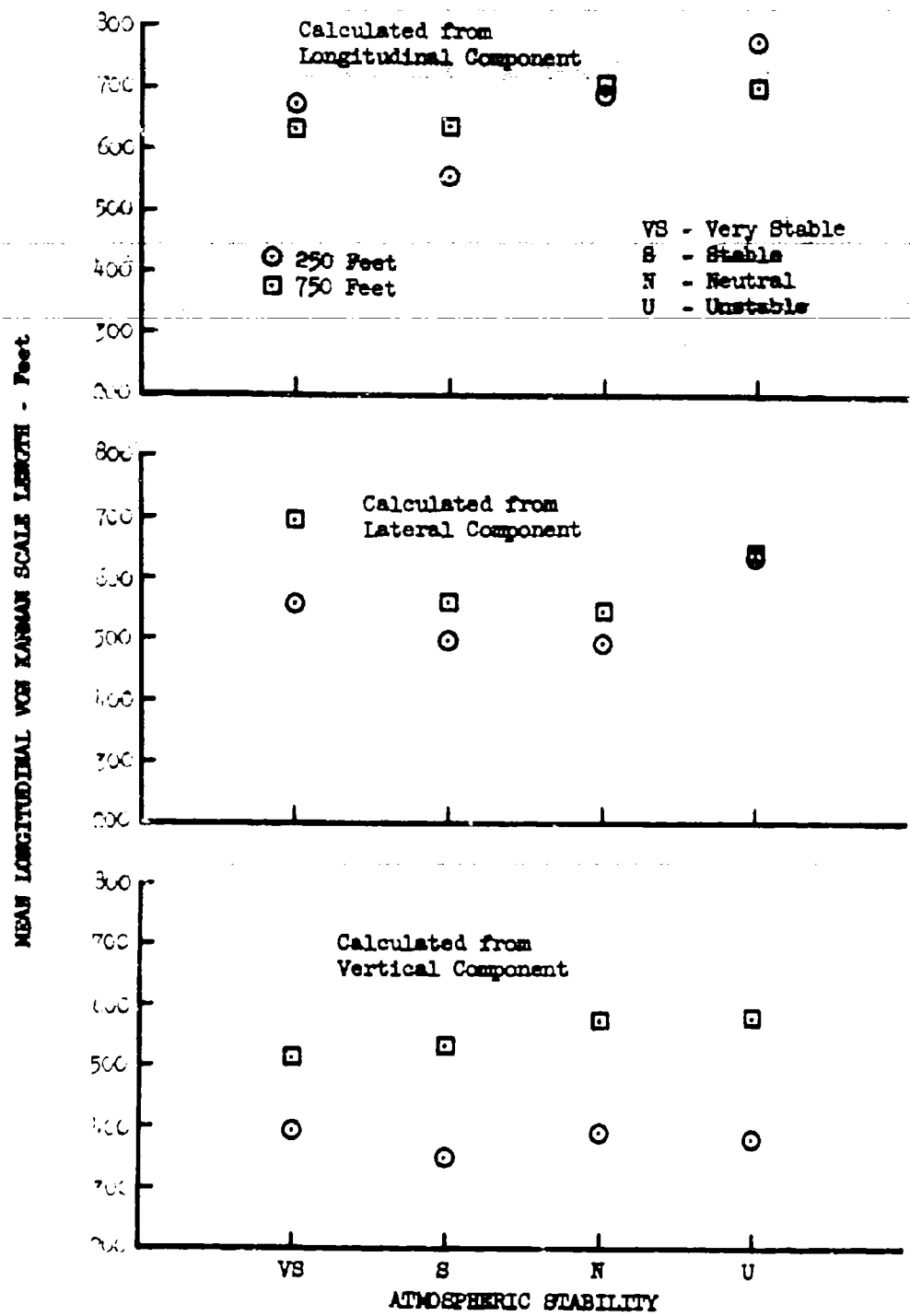


Figure 5.102 Variation of von Karman Longitudinal Scale Length with Altitude and Stability

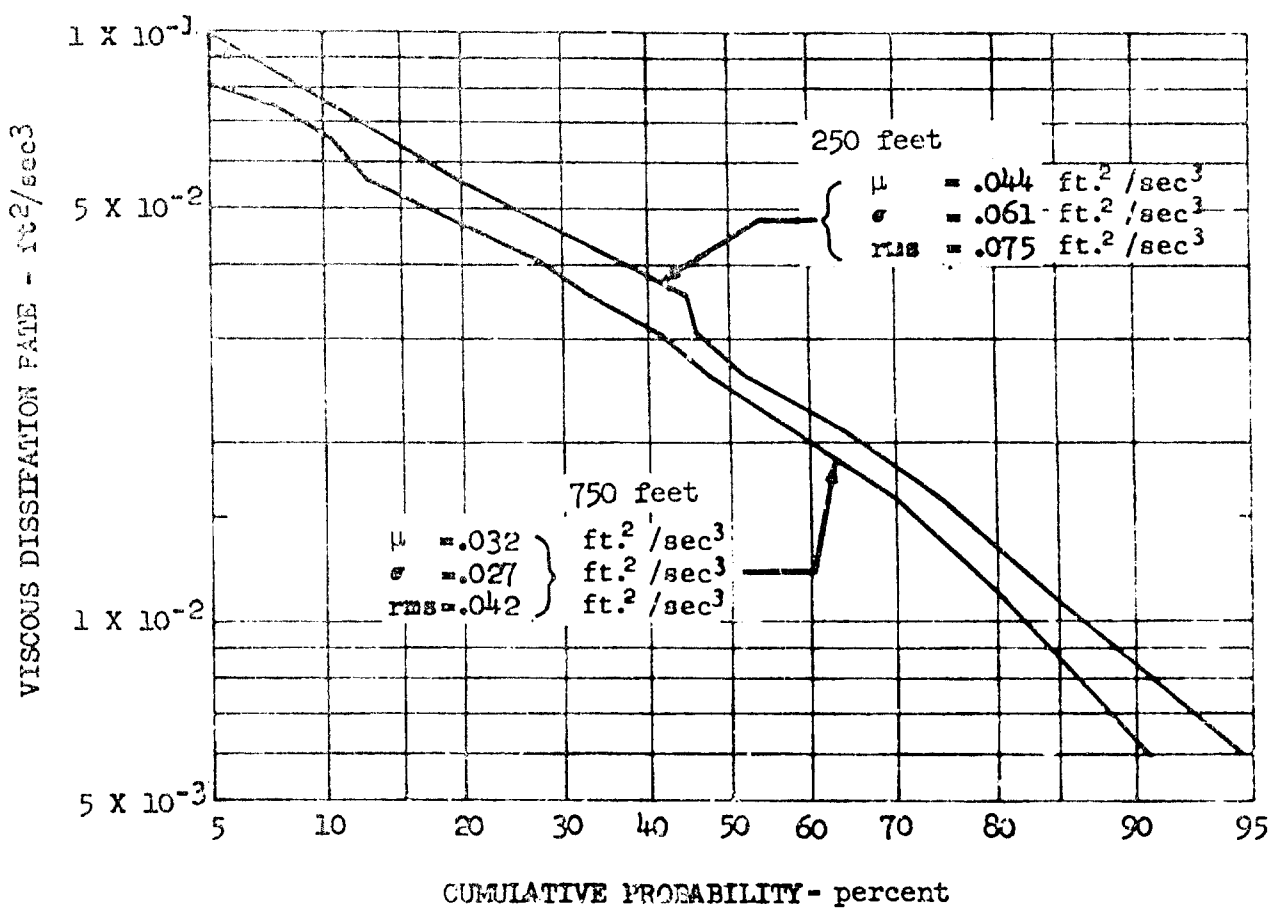


Figure 5.103 Viscous Dissipation Rate Statistics for 750 Foot and 250 Foot Altitudes

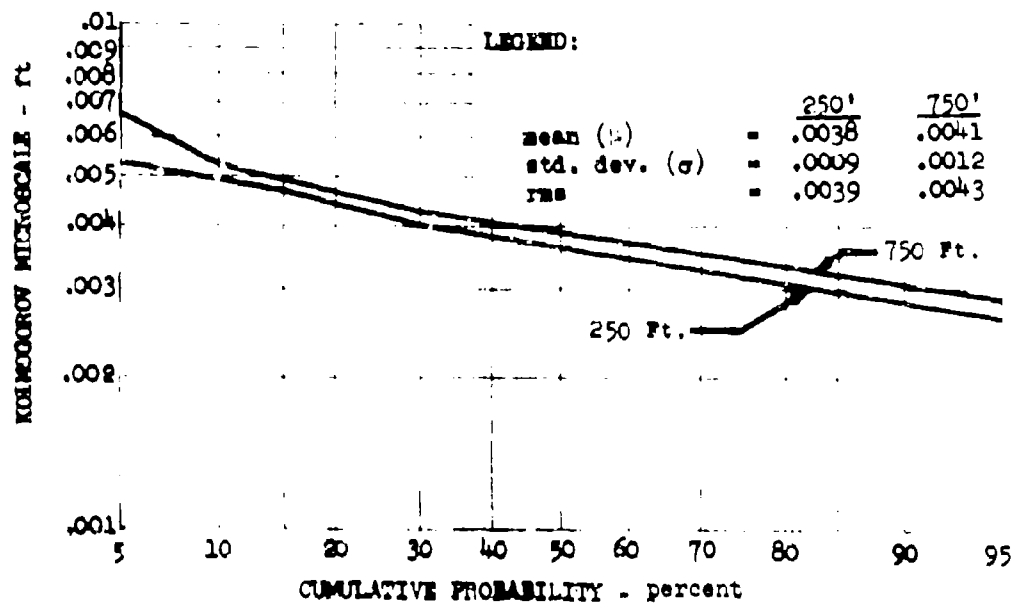


Figure 5.104 Kolmogorov Microscale Statistics for 750 Foot and 250 Foot Altitudes

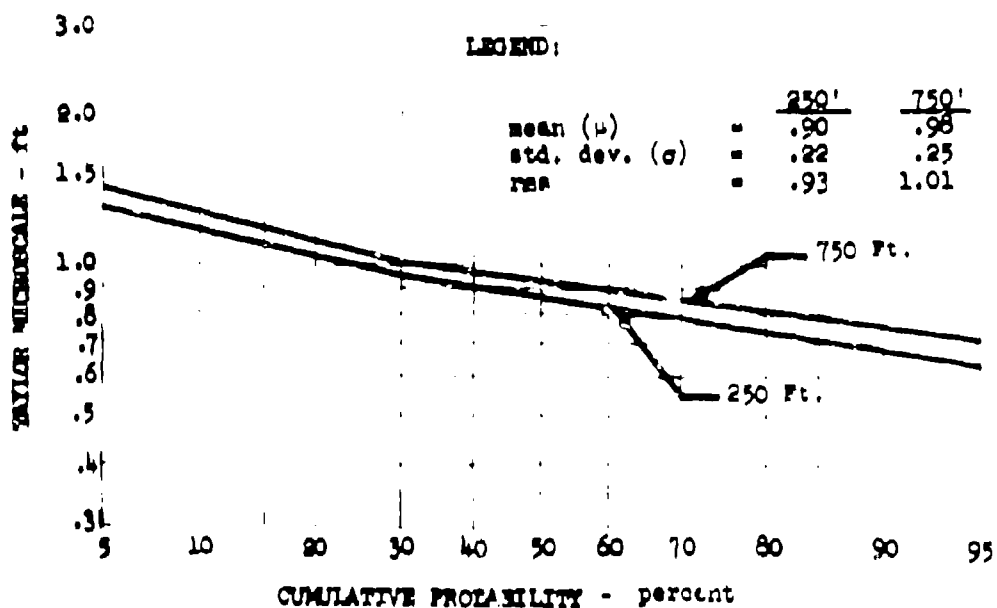


Figure 5.105 Taylor Microscale Statistics for 750 Foot and 250 Foot Altitudes

SECTION VI

BREN TOWER FLYBY

The test airplane was flown by AEC's BREN tower near Jackass Flats, Nevada (Figure 6.1) on 8 January 1969. The purpose of this flyby was to compare turbulence data obtained from the tower with the turbulence data obtained from the airplane. BREN tower is located in a restricted area identified as area number R-4808. The tower is 1520 feet high and is instrumented to record temperature and wind at various levels. At the time of this flyby, only the 565 foot level instrumentation was operational. The terrain surrounding the tower is rolling desert and hills, with mountains located on the east side. The Shoshone mountains are directly north of the tower.

Eight passes, each approximately nine miles in length, were made on alternate 60 degree and 240 degree magnetic headings. The wind was reported to be northerly at 27 fps. The pilot reported that the turbulence was light during the passes. Subsequent data processing has revealed a maximum gust velocity during the test to be approximately 31 fps, with the average of the maximum values for all 8 passes being less than 15 fps. Table 6.1 lists the average meteorological values for two of the passes.

Atmospheric survey data were obtained prior to each flyby flown on a 60 degree heading. These surveys were conducted by flying the airplane over a fixed point at 100 feet and 1000 feet above the terrain. Survey data were used to determine the vertical gradients which were then employed to describe the state of the atmosphere for the following flyby.

The first and seventh passes were chosen for spectral analysis because of the good homogeneity and isotropy characteristics of the turbulence. Time histories of the gust velocity components for each of these flybys are shown in Figures 6.2 and 6.3.

The power spectral densities are shown in Figures 6.4 and 6.5. The von Karman scale lengths were approximately 600 feet. The homogeneity, isotropy, and coherency characteristics are also shown in Figures 6.4 and 6.5.

The flybys selected for PSD analysis are representative low-level turbulence samples and should provide a good basis for evaluation of the tower data when they become available.

TABLE 6.1
BREN TOWER FLYBY DATA

Variable	Pass No. 1	Pass No. 7
σ_t (fps)	3.36	3.52
σ_t (fps)	3.52	3.56
σ_t (fps)	3.31	3.77
W (fps)	27	26
$\Delta W/\Delta H$ (fps/ft)	.024	.067
R	.266	-.007
T _g (°F)	80	.84
OAT (°F)	44	49
H _p (ft)	5000	4100
V _r (fps)	490	472
τ (miles)	8.72	7.96

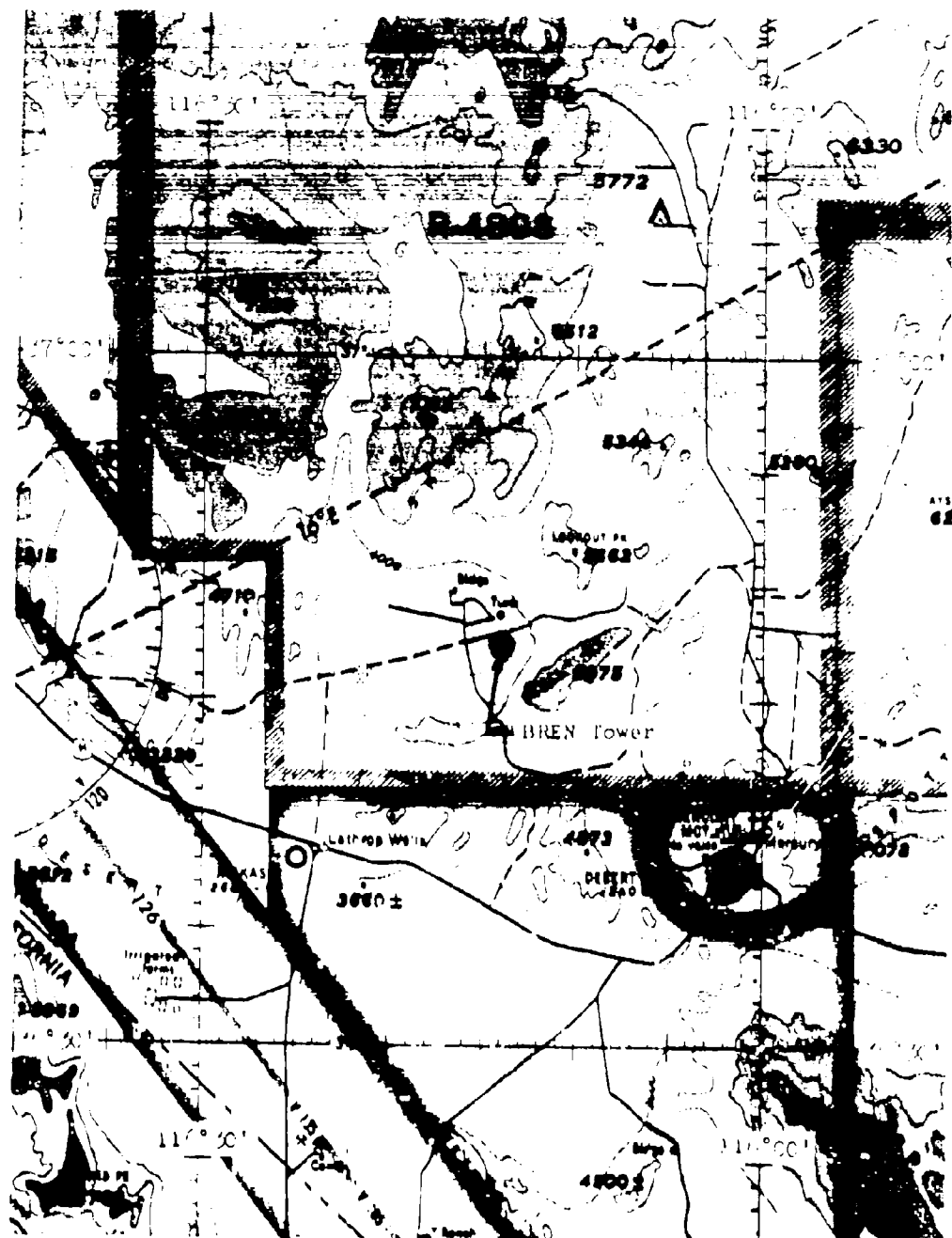


Figure 5.1 BREN Tower Location

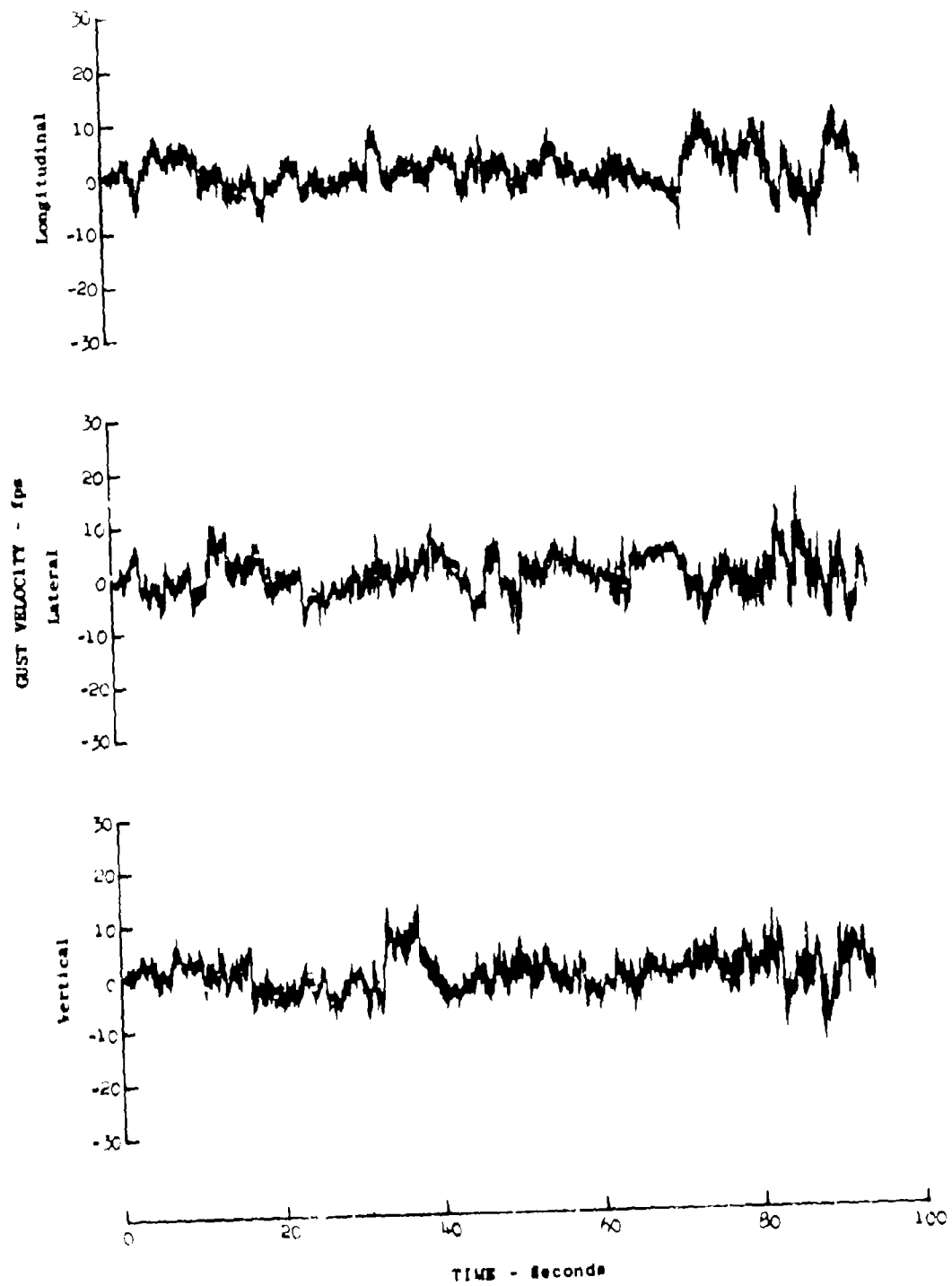


Figure 8.2 Gust Velocity Time History for BREN Tower Flyby No. 1

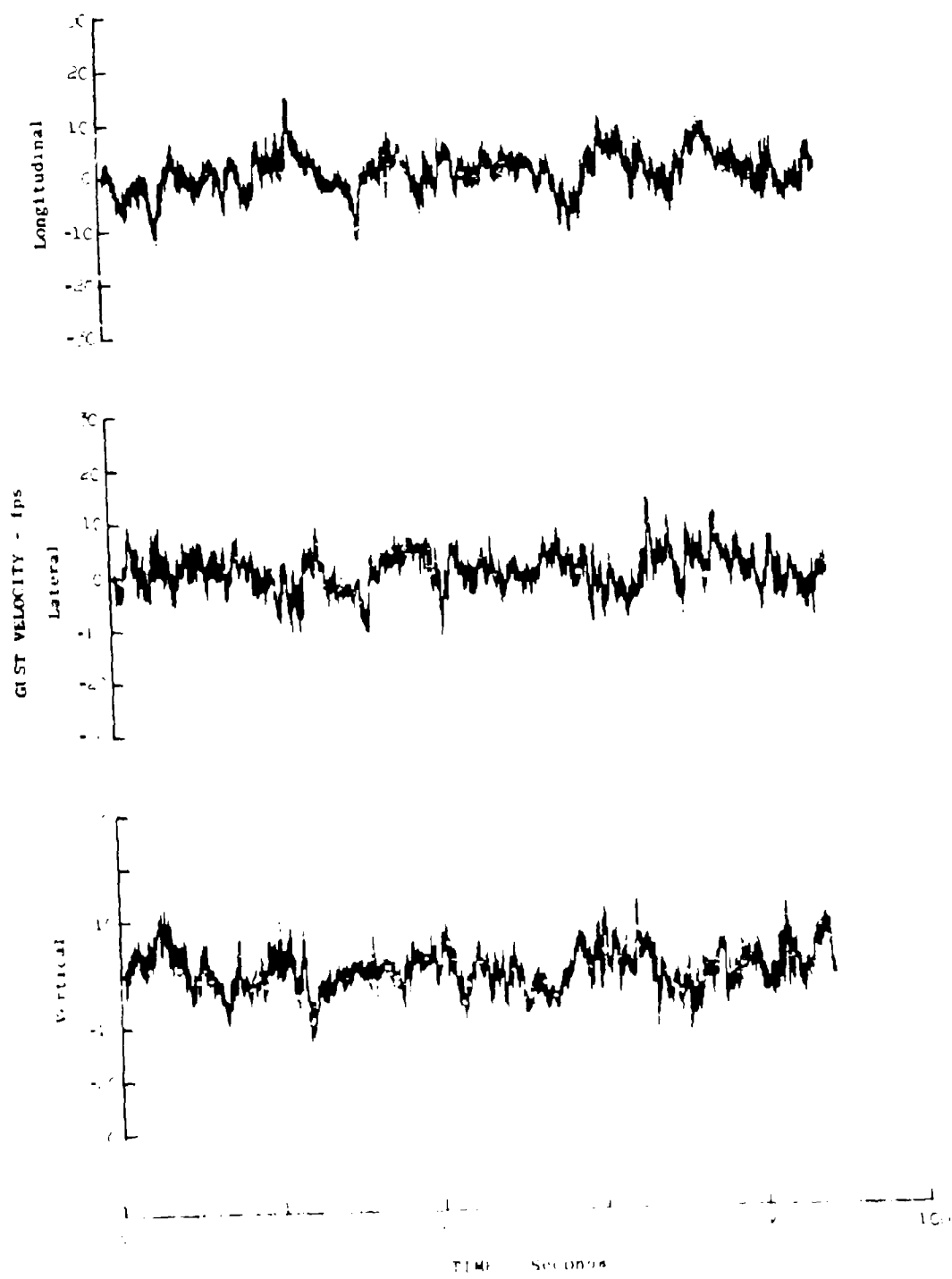


Figure 13. GIST Velocity Time History for B-52N Tower Flyby No. 1

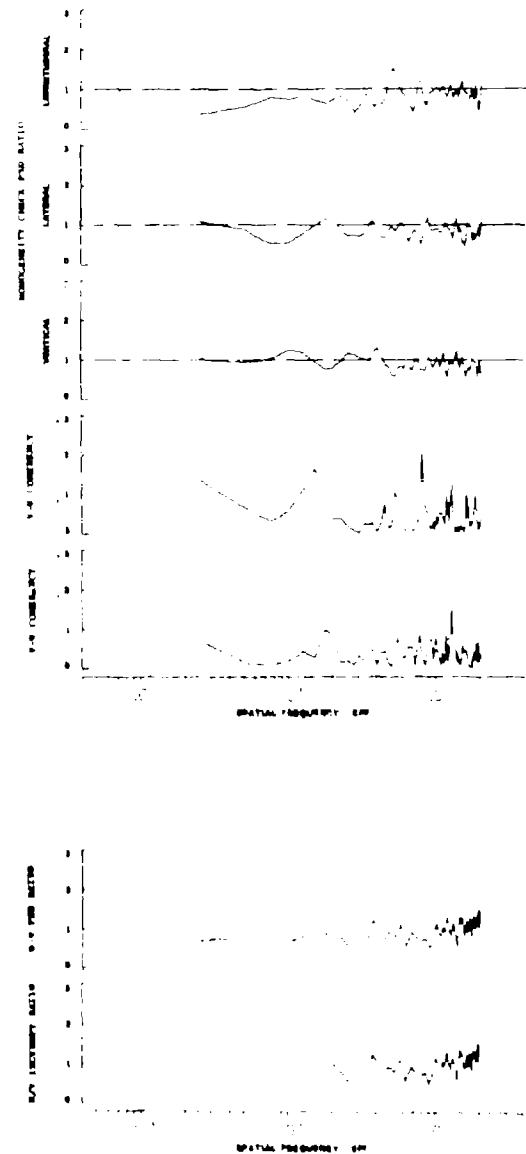
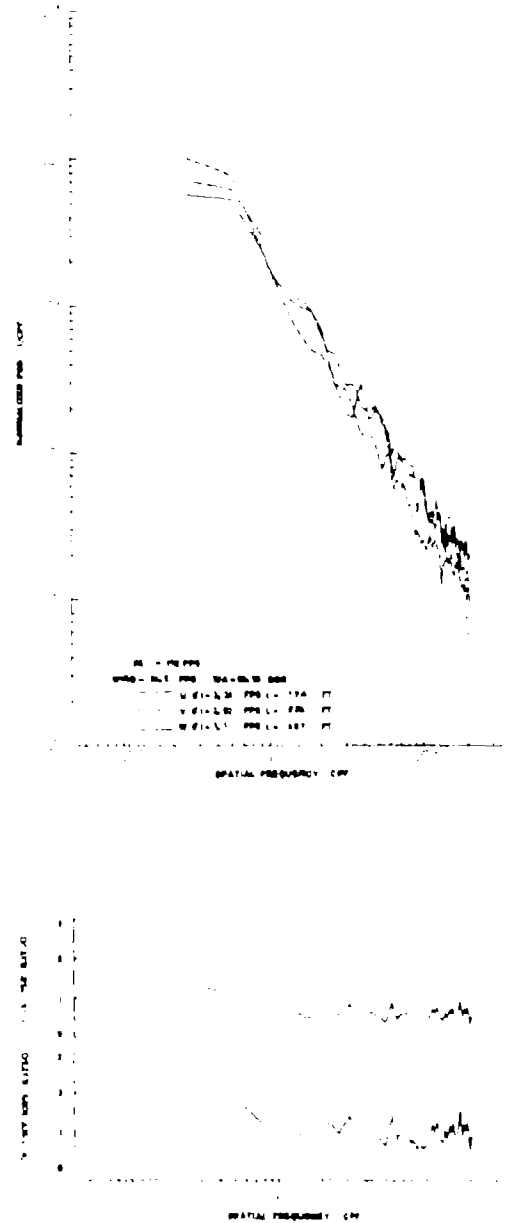


Figure 6.6 Turbulence Spectra Data for BREN Tower Flyby No. 1

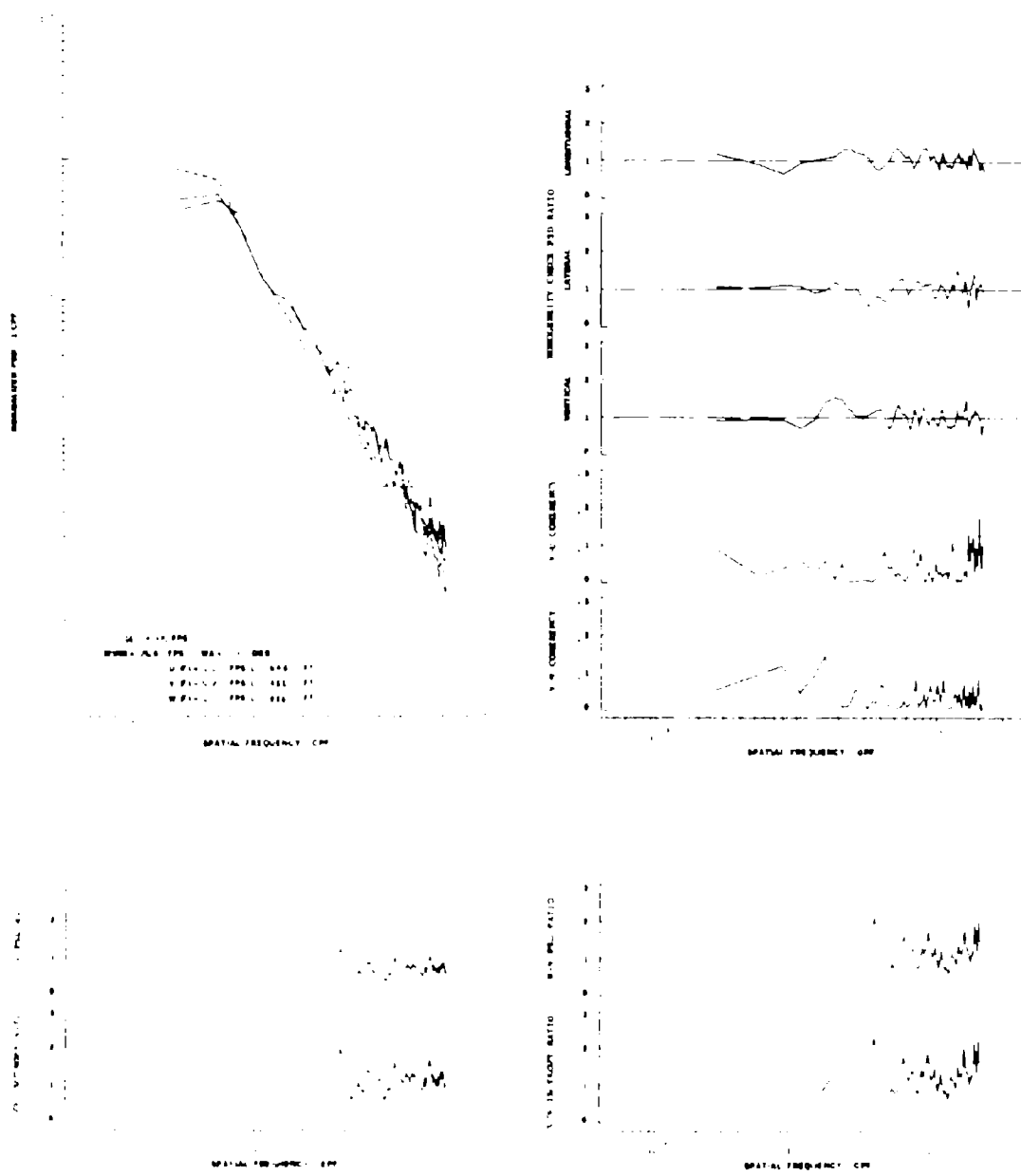


Figure 6.5 Radiation Spectra Data for BIRL Tower Flap, No. 1

SECTION VII

SUMMARY

Conclusions regarding low-level atmospheric turbulence would be untimely at this interim point in the LC-LOCAT Phase III program. A number of observations are made, however, to summarize the accomplishments and results achieved to date.

The most distinguishing characteristic of the Phase III data when compared to data obtained during Phases I and II is the incidence, on the average, of higher rms values, longer scales of turbulence, longer Taylor microscales, higher gust velocity magnitudes, and lower viscous dissipation rates. This is due to the fact that longer wavelength turbulence is being sensed during Phase III. Long wavelength (14,000 feet) turbulence being recorded during Phase III at 0.04 cps would have appeared at 0.02 cps during Phases I and II, since the C131B airplanes were flown at one-half the speed of the T-33A. This 0.02 cps data was below the useful range of the instrumentation causing gust velocity rms values to be reduced and hence the scale length, Taylor's microscale, etc. Phase III data are illustrating the fact that low altitude turbulence wavelengths longer than 7000 feet are significant. In addition, the following observations were noted:

- Comparison of Phase III time series statistical distributions with those from Phases I and II shows that the Phase III distributions tend to increase or level off at the higher gust velocities. This is also attributed to the use of the higher speed Phase III test airplane which permits measurement of longer wavelength turbulence.
- Increased gust velocity rms values are associated with decreased altitude and increased terrain roughness. The only exception occurs for data recorded over the plains. These data exhibit rms values of greater magnitude than those obtained over desert, even though the desert terrain is rougher than the plains.
- Surface winds recorded near the flight routes can be related to the rms gust velocity by a scale factor based on the ratio of maximum to average wind speeds.
- There is greater correlation between gust velocity rms values and recorded inflight wind speed over the rougher types of terrain.
- The experimental spectra show good correlation with spectra computed from the von Karman expressions. It was noted that experimental spectra estimates tended to be somewhat higher than von Karman estimates at very low values of kL . The Dryden expressions do not give as good a representation of the data. This is particularly true in the inertial subrange where these expressions have a -2 logarithmic slope rather than the -5/3 slope of the data.
- The average longitudinal integral scale length of turbulence, as calculated from the von Karman expressions, is approximately 570 feet. Scale lengths are higher for Phase III data than for data recorded during Phases I and II.

- The probability of increased gust velocity peak values with increasing terrain roughness, decreased altitude, and decreased atmospheric stability (with the exception of the unstable category) is indicated by the data.
- Gust velocity peak count probability distributions were found to compare reasonably well with corresponding amplitude count and level crossing probability distributions.
- Calculated values of derived equivalent vertical gust velocity (U_{eq}) from the T-33A airplane, overestimate the maximum measured true vertical gust velocity component at the low true gust velocity values and underestimate at the higher true gust velocity values.
- The maximum discrete gust velocity encountered as of 15 February 1969 was 74.5 fps for the vertical component and occurred over high mountainous terrain on leg 3 of the Edwards route. The maximum gust velocity rms was 13.1 fps for the lateral component and occurred on leg 6 of the Peterson route.
- Characteristic frequencies calculated from both peak count and power spectra data compared favorably.
- As in the past, drift existed in all computed, unfiltered gust velocities. The drift was not characterized by constant amplitude or frequency, but varied in amplitude and frequency from sample to sample.
- Approximately 86 percent of the 4-1/2 minute turbulence samples were determined to be normally distributed based on gust velocity amplitude statistics.
- LO-LOCAT Phase III signal-to-noise ratio is at an acceptable level when $\sigma_t \geq 1.4$ fps. Standard deviations of gust velocity (data + noise computed from data obtained in smooth air) as low as .28 fps were obtained.
- Probable errors in the calculation of LO-LOCAT gust velocities are ± 2 fps with maximum errors of ± 4 fps.
- Winds recorded at McConnell during Phase III compare well with those recorded at McConnell during Phases I and II. Winds recorded at Edwards are slightly less for Phase III than for Phases I and II. The highest winds recorded so far were obtained over the plains legs at McConnell.
- Climatological variance during the first two flight periods (at the McConnell and Edwards routes) was approximately normal, with the exception of higher than normal precipitation amounts.
- Viscous dissipation rates calculated for Phase III of the LO-LOCAT program are lower than obtained during Phases I and II. A comparison of Taylor microscales indicates an increase, but near the expected value. Kolmogorov microscales are approximately one millimeter.

- Data recorded and processed from the BREN tower flyby provides an opportunity for evaluation of data from this tower based on airplane measured gust velocities.

REFERENCES

- 1.1 Neal V. Loving, "Clear Air Turbulence (CAT) Measurement for Structural Design Criteria," AIAA Paper No. 65-510, American Institute of Aeronautics and Astronautics, Easton, Pa., July, 1965.
- 1.2 D. E. Gunter, et al., Low Altitude Atmospheric Turbulence LO-LOCAT Phases I and II, being published by the Air Force as an Aeronautical Systems Division Technical Report. ASD-TR-69-12, Wright-Patterson Air Force Base, Ohio, February, 1969.
- 1.3 J. Gault, et al., Dynamic Loads Survey - B-52 with ECP 1050 (WFT 1217), B-52 Flight Test Activities Report, Boeing Document D-13273-361A, The Boeing Company, Wichita, Kansas, May, 1966.
- 1.4 Test Operations Unit, High Speed Low Level Investigation - B-52G and H (WFT 1286), B-52 Flight Test Activities Report, Boeing Document D-13273-365A, The Boeing Company, Wichita, Kansas, September, 1966.
- 1.5 Test Operations Unit, Prototype Stability Augmentation and Flight Control System Evaluation - B-52G and H (WFT 1301), B-52 Flight Test Activities Report, Boeing Document D-13273-379A, The Boeing Company, Wichita, Kansas, November, 1967.
- 2.1 R. J. Neimann, Instrumentation Technical Report, Low Level Turbulence Program, Boeing Document D3-7329, The Boeing Company, Wichita, Kansas, December, 1968.
- 3.1 G. T. Tucker and J. Gault, Low-Level Critical Air Turbulence Technical Progress - Monthly Report, Boeing Document D3-7087-10, The Boeing Company, Wichita, Division, Wichita, Kansas, February, 1967.
- 5.1 U. O. Lappe, A Climatological Wind Turbulence Model for Estimating Low Altitude Gust Loads, AFFDL-TR-67-122, Wright-Patterson Air Force Base, Ohio, January, 1968.
- 5.2 R. V. Martin, An Analysis of the Correlation Between Turbulences Encountered During B-52 G/H Low Level Operations and Synoptic Meteorological Data, D3-6649, The Boeing Company, February 26, 1965.
- 5.3 J. O. Hinze, Turbulence, An Introduction to its Mechanism and Theory, McGraw-Hill Book Co., Inc., 1959.
- 5.4 John C. Houbolt, et al., Dynamic Response of Airplanes to Atmospheric Turbulence Including Flight Data on Input and Response, NACA Report TR R-199, Langley Research Center, Langley Station, Va., June, 1964.
- 5.5 T. von Karman, "Progress in the Statistical Theory of Turbulence," Turbulence Classic Papers on Statistical Theory, Interstate Publishers, Inc., 1961, pp 162-173.
- 5.6 H. L. Dryden, "A Review of the Statistical Theory of Turbulence," Turbulence Classic Papers on Statistical Theory, Interstate Publishers, Inc., 1961, pp 115-150.

5.7 J. Taylor, Manual on Aircraft Loads, AGARDograph 83, Pergamon Press Ltd., New York, N.Y., 1965.

5.8 U. O. Lappe, Design of a Low Altitude Turbulence Model for Estimating Gust Loads on Aircraft, AFFDL-TR-64-170, Research and Technology Division, Wright-Patterson Air Force Base, Ohio, March, 1965.

5.9 MIL-F-008785A, "Flying Qualities of Piloted Airplanes," (MSC Project 345-10), October, 1968

5.10 O. G. Sutton, Micrometeorology, McGraw-Hill Book Co., Inc., 1953.

5.11 J. L. Lumley and H. A. Panofsky, The Structure of Atmospheric Turbulence, Interscience Monographs and Texts in Physics and Astronomy, Vol. XII, John Wiley and Sons, 1964.

5.12 Francis K. Davis and Herman Newstein, "The Variation of Gust Factors with Mean Wind Speed and with Height," Journal of Applied Meteorology, Vol. 7, No. 3, American Meteorological Society, June 1968.

UNCLASSIFIED

DOCUMENT CONTROL DATA - R & D		
(Security classification of title, body of abstract and indexing annotation must be entered when the overall report is classified)		
1. ORIGINATING ACTIVITY (Corporate author) The Boeing Company Wichita Division Wichita, Kansas 67210		2a. REPORT SECURITY CLASSIFICATION Unclassified
		2b. GROUP
3. REPORT TITLE Low Altitude Atmospheric Turbulence LO-LOCAT Phase III Interim Report Volume I		
4. DESCRIPTIVE NOTES (Type of report and inclusive dates) R&D Interim Report - 17 April 1968 to 8 January 1969		
5. AUTHOR(S) (First name, middle initial, last name) K. R. Monson, G. W. Jones, R. H. Mielke, et al.		
6. REPORT DATE August 1969		7a. TOTAL NO. OF PAGES 233
8a. CONTRACT OR GRANT NO. F33615-68-C-1468		9a. ORIGINATOR'S REPORT NUMBER(S) NONE
b. PROJECT NO.		
c. ADP682E		9b. OTHER REPORT NO(S) (Any other numbers that may be assigned this report) AFFDL-TR-69-63, Volume I
d.		
10. DISTRIBUTION STATEMENT This document is subject to special export controls and each transmittal to foreign governments or foreign nationals may be made only with prior approval of Air Force Flight Dynamics Laboratory (FDTE), Wright-Patterson AFB, Ohio 45433		
11. SUPPLEMENTARY NOTES		12. SPONSORING MILITARY ACTIVITY Air Force Flight Dynamics Laboratory FDTE Wright-Patterson AFB, Ohio 45433
13. ABSTRACT The contents of this report describe accomplishments during the first half of the Low-Level Critical Air Turbulence (LO-LOCAT) Phase III program. Data that were obtained during flight over routes near McConnell Air Force Base, Kansas, and Edwards Air Force Base, California, are presented. Also included are time histories of some of the larger magnitude gust velocities recorded over the Peterson Field, Colorado route. Approximately 72 hours of low-level (0-1000 feet) turbulence and associated meteorological data recorded from August 16, 1968, through January 8, 1969, are presented. The turbulence environment is analyzed in terms of gust velocity primary peaks, amplitude samples, rms values, maximum values and derived equivalent gusts. Mathematical expressions for turbulence spectra and scale length statistics, and correlations between atmospheric gust velocities and meteorological and geophysical phenomena are shown. The most predominant characteristics of these data are the increases in rms values, scale lengths, Taylor micro scales and maximum gust values as compared to the LO-LOCAT Phases I and II data. These differences are attributed to the increased speed of the Phase III airplane which is providing a better definition of the longer wavelengths of atmospheric turbulence. This report consists of two volumes. Volume I contains a discussion of data acquisition and quality, along with a preliminary analysis of turbulence and meteorological data. Instrumentation details, calibrations and checks, data processing, gust velocity data (power spectra, peak and amplitude count, etc.) and test logs are presented in Volume II.		
(Distribution of this abstract is unlimited)		

DD FORM 1 NOV 65 1473

UNCLASSIFIED

Security Classification

UNCLASSIFIED

Security Classification

14 KEY WORDS	LINK A		LINK B		LINK C	
	HOLE	WT	ROLE	WT	ROLE	WT
LO-LOCAT (Low-Low Altitude Critical Atmospheric Turbulence) Low Level Turbulence (0-1000 feet) Clear Air Turbulence Gust Velocity Statistics Gust Velocity Power Spectra Low Level Turbulence Models Meteorology (Turbulence) Turbulence Forecasting						

UNCLASSIFIED

Security Classification